CHARACTERIZATION OF GAS-LIQUID TWO-PHASE FLOW IN A PROTON EXCHANGE MEMBRANE FUEL CELL

by

Ryan Anderson

B.S., Bucknell University, 2007

B.A., Bucknell University, 2007

A THESIS SUBMITTED IN PARTIAL FULFILLMENT OF

THE REQUIREMENTS FOR THE DEGREE OF

DOCTOR OF PHILOSOPHY

in

THE FACULTY OF GRADUATE STUDIES

(Chemical and Biological Engineering)

THE UNIVERSITY OF BRITISH COLUMBIA

(Vancouver)

June 2012

Abstract

This thesis explores two-phase flow phenomena relevant to water management in PEM fuel cells. Particularly, pressure drop hysteresis is explored in depth, which occurs when the gas and liquid flow rates are increased and decreased along a set path but exhibit different pressure drops. The hysteresis effect is explored here experimentally in three studies: non-operating cold model to study hydrodynamics, non-operating hot model at fuel cell operating conditions to study increasingly relevant hydrodynamics, and an operating study to explore pressure drop hysteresis in an active cell. This is the first time pressure drop hysteresis has been studied in a PEM fuel cell. A specially designed visualization fuel cell, allowing for observation into the cathode flow field channels, is utilized to further understand these results. The pressure drop hysteresis occurs because liquid water accumulates in the cathode flow channels during the descending approach. The cathode air stoichiometry and temperature play a major role, as lower stoichiometries and lower temperatures lead to more water accumulation in the channels, which increases the hysteresis problem. The gas diffusion layer is not a main parameter affecting pressure drop hysteresis. Additionally, several other variables are studied through the three experimental setups to understand the hysteresis behavior. This thesis then examines anode water removal (AWR) as a diagnostic tool to determine maximum fuel cell performance in the absence of mass transfer limitations on the cathode. By exacerbating cathode flooding and using a variety of cathode GDLs, large voltage increases occur through the AWR process when the cathode GDL is under flooding conditions. Larger voltage gains occur during the AWR process with the use of GDLs without an MPL when the cathode gas stream is fully humidified. Both studies, pressure drop hysteresis and AWR, improve overall fuel cell performance by better understanding water

management in PEM fuel cells. Understanding the pressure drop hysteresis is important to limit the parasitic power losses associated with higher pressure drops, and AWR is a novel tool researchers can use to evaluate new GDLs in terms of their ability to prevent voltage losses due to flooding.

Preface

Chapter 2 is based on a review paper written by our research group under the supervision of Dr. David Wilkinson and Dr. Xiaotao Bi. This work was published: R. Anderson, L. Zhang, Y. Ding, M. Blanco, X. Bi, D.P. Wilkinson, A critical review of two-phase flow in gas flow channels of proton exchange membrane fuel cells, J. Power Sources 195 (2010) 4531-4553. I was responsible for writing the following sections: 'Introduction', 'Experimental visualization techniques', 'Ex-situ experimental two-phase flow studies relevant to PEM fuel cells', and 'Summary and outlook'. Dr. Lifeng Zhang wrote the section 'In-situ experimental two-phase flow studies in PEM fuel cells', PhD candidate Yulong Ding wrote the 'CFD simulations of two-phase flow in PEM fuel cell flow channels' (which has been placed in Appendix A), and Dr. Mauricio Blanco wrote 'Water mitigation strategies' (which has been condensed here). I was also in charge of editing all of the sections and revising each individual contribution into one document before publication. This chapter also includes more references to reflect the literature since the publication of our review paper.

Chapter 4 is based on experimental work that I collected, analyzed, and wrote. Section 4.2 was published: R. Anderson, D.P. Wilkinson, X. Bi, L. Zhang, Two-phase flow pressure drop hysteresis in parallel channels of a proton exchange membrane fuel cell, J. Power Sources 195 (2010) 4168-4176. The co-authors provided feedback on the experimental approach, analysis, and subsequent paper. Section 4.3 was presented at the 217th Electrochemical Society (ECS) meeting in Vancouver. The resulting publication was in the conference proceedings: R. Anderson, D.P. Wilkinson, X. Bi, L. Zhang, Two-phase flow pressure drop hysteresis under typical operating conditions for a proton exchange membrane fuel cell, ECS Trans. 28 (2010) 127-137. I was responsible for the

data collection and analysis, along with the conference presentation and paper. The co-authors provided feedback throughout the process.

Chapter 5 is based my on experimental work and was published: R. Anderson, D.P. Wilkinson, X. Bi, L. Zhang, Two-phase flow pressure drop hysteresis in an operating proton exchange membrane fuel cell, J. Power Sources 196 (2011) 8031– 8040. I was responsible for the data collection, analysis, and paper preparation. The co-authors provided feedback and insight throughout this process. The data for the Lockhart-Martinelli approach was also used for publication in: L. Zhang, X.T. Bi, D.P. Wilkinson, R. Anderson, J. Stumper, H. Wang, Gas-liquid two-phase flow behavior in minichannels bounded with a permeable wall, Chem. Eng. Sci. 66 (2011) 3377-3385. I provided the data and analysis for Figure 10b in that paper.

Chapter 6 is based on an additional study in PEM fuel cell water management, anode water removal. I was assisted by UBC summer student Gary Wang and CERC volunteer Shehin Rahemtulla on data collection, and this work was done in collaboration with Dr. Mauricio Blanco and Dr. David Wilkinson. I was responsible for establishing the experimental procedure, determining which experiments to perform, and analyzing the experimental results. Part of this chapter has been accepted at ASME's 10th Fuel Cell Science, Engineering and Technology Conference.

Table of Contents

List of Tables

List of Figures

List of Symbols and Abbreviations

A	area, cm^2
A	advancing contact angle, ^{o}
A	refers to anode
C	refers to cathode
C	Chisholm parameter, dimensionless
c_p	specific heat, J $g^{-1}K^{-1}$
D_h	hydraulic diameter, m
D	diffusivity, m^2 s^{-1}
F	Faraday's constant, 96,485.339 C mol^{-1}
F_x	Force from contribution x, N
g	gravity, m s^{-2}
g	gas
h_m	mass transfer coefficient, m s^{-1}
I	current, amps
i	current density, amps cm^{-2}
k	ratio of specific heats (diatomic gas = 1.4)
L	characteristic length, m
l	liquid
M	molecular weight, g mol^{-1}
$\dot{m}$	mass flow rate, g s^{-1}
$\dot{n}$	molar flow rate, mol s^{-1}
N_{needed}	required molar gas flow at a given current density, mol s^{-1}

$N_{supplied}$	supplied molar gas flow at a given current density, mol s^{-1}
ΔP	pressure drop, Pa
P	pressure, Pa
r_{H2O}	volume fraction water vapor in a gas, dimensionless
R	receding contact angle, ^{o}
s	solid
t	time, s
T	temperature, K
T_c	critical temperature, K
$\bar{v}$	superficial velocity, m s^{-1}
v	vapor
V	voltage, volts
W	power, watts
x	distance from channel inlet

Greek letters

α	water transfer coefficient, dimensionless
α	half angle, degree ^{o}
β	inclination angle, degree ^{o}
Δ	change in value, dimensionless
γ	surface tension, N m^{-1}
η	efficiency, dimensionless
θ	contact angle, ^{o}
λ_i	stoichiometric ratio of gas i, dimensionless

λ	membrane saturation
μ	viscosity, Pa s
ρ	density, g cm^{-3}
$\varphi_{2\text{-phase}}$	two-phase flow multiplier, dimensionless
$\Phi_{\Delta P}$	pressure drop multiplier, dimensionless
χ^2	Martinelli parameter, dimensionless

Abbreviations

↑↓	ascending and descending, respectively
2-phase	two-phase system, liquid water and gas
1-phase	single-phase system, gas only
ascending	path of increasing current density (increasing gas and liquid flow rates)
act	active
comp	compressor
descending	path of decreasing current density (decreasing gas and liquid flow rates)
dp	dew point
gl	gas and liquid (two-phase)
min:sec	time, minutes and seconds
$O_{2,need}$	required oxygen demand at a given current density
$O_{2,inlet}$	supplied oxygen demand at a given current density
sim	simulated current density in non-operating experiments
stoich	stoichiometry

Dimensionless numbers

Bo	Bond number

Ca	Capillary number
Re	Reynolds number
Sc	Schmidt number
Sh	Sherwood number
Su	Suratman number
We	Weber number

Acronyms

CCM	catalyst coated membrane
FC	fuel cell
GDL	gas diffusion layer
LM	Lockhart-Martinelli
MEA	membrane electrode assembly
MPL	microporous layer
PEM	proton exchange membrane
PTFE	polytetrafluoroethylene

Acknowledgements

I would first like to thank my family for their support. I would not be where I am today without your encouragement of my studies and doing whatever you had to do to make sure I could be successful at every level. Thank you all for always being there for me.

I would like to thank my supervisors, Dr. David Wilkinson and Dr. Xiaotao Bi. Your complimentary approaches toward graduate student supervision have made me a stronger student and more thoughtful researcher. I would also like to thank my committee members, Dr. Jürgen Stumper and Dr. Fariborz Taghipour, for their advice and insight into my investigation. Thank you also to the University of British Columbia for the Four Year Fellowship funding.

Thank you fellow students in the two-phase flow research group: Cyrus Yau, Yulong Ding, Dr. Mauricio Blanco, and Dr. Lifeng Zhang. Lifeng, thank you for assisting me in developing my project, helping me define a project scope, and editing our papers. Mauricio, thank you for training me in the art of fuel cells and for being a supportive friend and lab-mate.

I'd also like to extend a thank you to the members of CHBE 2624: Dr. Alfred Lam, Ross McCulloch, Dave Bruce, James Butler, and Tyler Lewis, along with Iwan Townson and Nagu Daraboina. We've accumulated more Craic points than we may want to admit, but you're all 'worth it'. A special thanks to Dave and Alfred in this respect, where the team often worked on lab related problems on napkins over Hatchet. I'd also like to thank Mahony and Sons and Benny's Bagels.

Thank you BCFC, you've been mediocre. And frankly, I wouldn't and couldn't have it any other way. Thank you co-founders and only members, Arlie Krauchek and Mike Weigley, for trying so hard.

Thank you Whistler-Blackcomb. The ride has been sublime. And thank you British Columbia, for the never-ending sources of backcountry exploration that serve to sustain the soul.

Thank you CHBE community, in particular Naoko Ellis, Serge Milaire, Helsa Leong, and Joanne Dean. Thank you fellow graduate students for making CHBE a great place to work.

And thank you Ella Anderson for being my partner and wife. Your constant support has been a blessing. Thank you for being my compliment. Thank you for keep me in check. And thank you for your unwavering commitment to us…'Of all the gin joints in all the towns in all the world, she walks into mine.'

To all of my educators-in all walks of life and in all types of lessons-I extend my most sincere and humble thanks.

1 Introduction

Fuel cells offer a way to turn the stored chemical energy in a fuel, such as methanol or hydrogen, into electricity. Unlike a battery, electricity continues to be produced as long as fuel is continually supplied to the fuel cell. The proton exchange membrane (PEM) fuel cell has received much attention in recent decades as a clean and efficient way to generate power for various applications due to its high energy efficiency, low operating temperature, and low to zero emissions during its operation. In particular, it has been considered one of the most promising alternatives to fossil-based fuel engines for automotive applications. The electrochemical reaction between hydrogen fuel and oxygen oxidant produces electricity, with the only emissions being excess heat and water. The PEM fuel cell is thus an environmentally viable option that is also capable of achieving high power density and high efficiency. Proton exchange membrane fuel cells (PEMFC) refer to a class of fuel cells that utilize a conductive ionomer membrane as electrolyte. PEM fuel cells have the advantages of high power density, good start-stop capabilities, and low temperature operation well suited for portable applications. However, disadvantages include an expensive platinum catalyst, an expensive membrane, water management issues, and strict fuel requirements (i.e. avoiding carbon monoxide in the hydrogen stream)[1].

The following half reactions and overall reaction occur in the PEM fuel cell that operates with hydrogen.

Anode:

$$H_2 \rightarrow 2H^+ + 2e^- \qquad E^o = 0\ V \qquad (1)$$

Cathode:

$$\frac{1}{2}O_2 + 2H^+ + 2e^- \rightarrow H_2O \qquad E^o = 1.23\ V \qquad (2)$$

Overall:

$$H_2 + \frac{1}{2}O_2 \rightarrow H_2O + \text{heat} \qquad E^o = 1.23\ V \qquad (3)$$

The PEM fuel cell is comprised of seven main layers in a ‘sandwich’: the air/oxygen (oxidant) flow field channel, the cathode gas diffusion layer (GDL), the cathode catalyst layer, the polymer electrolyte membrane (PEM), the anode catalyst layer, the anode gas diffusion layer, and the hydrogen (fuel) flow field. The combination of the GDLs, catalyst layers, and membrane is commonly referred to as the membrane electrode assembly (MEA). A schematic of this setup is shown in Figure 1. The number of layers is reduced to five with the inclusion of a catalyst coated membrane (CCM), where the catalyst layers are included on the membrane. The gases diffuse perpendicular to the direction of the channel flow through the respective gas diffusion layers to reach the catalyst layers, where the reactions take place. Protons move through the membrane from the anode toward the cathode, and electrons move through an external circuit. The protons and electrons react with oxygen at the cathode to form water. The product water also diffuses through the GDL to reach the flow channels where it can be removed.

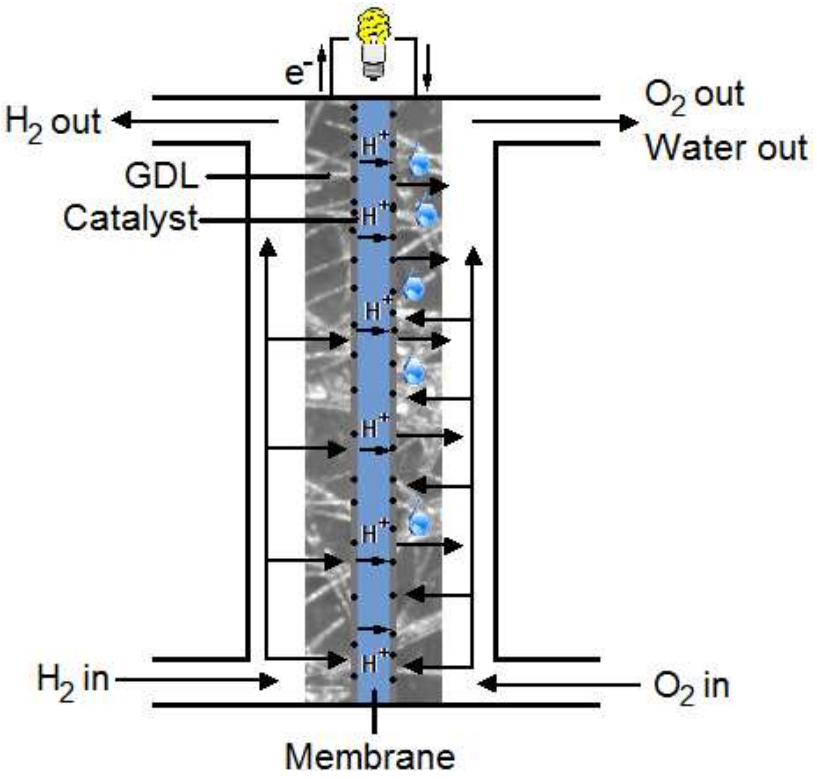

Figure 1. Schematic of a PEM fuel cell's components highlighting the gas flows, gas diffusion layers, catalyst layers, and membrane

The theory and background presented here explain PEM fuel cells in terms of basic thermodynamics, sources of voltage losses, the fuel cell's components, typical operating conditions, and flow channel pressure drop. The scope is intentionally broad and aims to be largely applicable to PEM fuel cell water management, one of the current disadvantages in PEM fuel cells. The scope is then focused and water management issues are covered more extensively in the literature review presented in Chapter 2.

1.1 Fuel cell thermodynamics

This overall reaction in Eqn. 3 is exothermic, and the heat of reaction can be determined by:

$$\Delta H = (h_f)_{H_2O} - (h_f)_{H_2} - 1/2(h_f)_{O_2} \quad (4)$$

For liquid water formation at 25°C, this value is -286 kJ mol^{-1} (using hydrogen's higher heating value) at standard conditions. However, not all of the energy can turn into electricity due to entropy. The total potential energy in fuel cell operation is the Gibbs free energy, where only -238 kJ mol^{-1} can turn into electricity (ΔG) and the rest (due to ΔS) is lost to heat:

$$\Delta G = \Delta H - T\Delta S \tag{5}$$

The electrical work can also be related to the Gibbs free energy. The electrical work (J mol^{-1}) is:

$$W_{el} = qE = -\Delta G \tag{6}$$

where q is charge (Coulombs mol^{-1}) and E is potential (Volts). The charge is expressed as:

$$q = nN_{Av}q_{el} = nF \tag{7}$$

where n is the number of electrons per molecule of H_2, N_{Av} is Avogadro's number (6.022×10^{23} molecules/mol), q_{el} is the charge of an electron (1.602×10^{-19} Coulombs/electron), and F is Faraday's constant (96,485 Coulombs/electron-mol). Thus, the electrical work expression is:

$$W_{el} = nFE \tag{8}$$

Thus, $W_{el} = -\Delta G$ is the theoretical hydrogen/oxygen fuel cell potential. At 25°C and 1 atm, this maximum voltage is the equilibrium cell potential:

$$E^{o} = \frac{-\Delta G}{nF} = \frac{237{,}340\ \mathrm{J\,mol^{-1}}}{2 \times 96{,}485\ \mathrm{A\,s\,mol^{-1}}} = 1.23\ \mathrm{V} \tag{9}$$

1.1.1 Effect of temperature on theoretical fuel cell potential

The theoretical potential, E, can be substituted in for the Gibbs Free Energy expression to give:

$$E = -\left(\frac{\Delta H}{nF} - \frac{T\Delta S}{nF}\right) \tag{10}$$

This means that an increase in cell temperature will decrease the theoretical cell potential. This result is true because ΔH and ΔS are both negative. The enthalpy and entropy can also be solved for as a function of temperature, both of which increase (become less negative) with temperature, by knowing how the heat capacity changes with temperature. The change in E^o from 25^{o}C to 100^{o}C is a loss of 0.063 V (63 mV), a 5% decrease.

1.1.2 Effect of pressure on theoretical fuel cell potential

For an isothermal process, the change in Gibbs free energy can be expressed as

$$dG = V_m dP \tag{11}$$

where V_m is the molar volume and P is the pressure. The ideal gas law is the simplest basis to use (PV_m=RT), which after integration leads to:

$$G = G_0 + RT\ln\frac{P}{P_0} \tag{12}$$

For the general reaction $jA + kB \rightarrow mC + nD$, the Gibbs free energy can be written as $\Delta G = mG_C + nG_D - jG_A - kG_B$. As a function of pressure, this is:

$$G = G_0 + RT\ln\left[\frac{\left(\frac{P_C}{P_0}\right)^m\left(\frac{P_D}{P_0}\right)^n}{\left(\frac{P_A}{P_0}\right)^j\left(\frac{P_B}{P_0}\right)^k}\right] \tag{13}$$

which is the Nernst equation (P_0 is 1 atm). When applied to the hydrogen/oxygen fuel cell, this expression becomes:

$$E = E^0 + \frac{RT}{nF} \ln \frac{P_{H_2} P_{O_2}^{0.5}}{P_{H_2O}} \tag{14}$$

The P_{H2O} term is 1 if the water is liquid, and the partial pressure of oxygen in air is 0.21, which reduces the theoretical potential by 0.012 V (12 mV). When combined with the expression for how E^0 changes with T, one has a final expression for the cell potential as a function of temperature and pressure.

$$E_{T,P} = -\left[\frac{\Delta H}{nF} - \frac{T\Delta S}{nF}\right] + \frac{RT}{nF} \ln \frac{P_{H_2} P_{O_2}^{0.5}}{P_{H_2O}} \tag{15}$$

1.1.3 Theoretical efficiency

One of the benefits of PEM fuel cells is the potential for high efficiency, where the maximum efficiency at standard conditions is:

$$\eta = \frac{\Delta G}{\Delta H} = \frac{237.34 \frac{kJ}{mol}}{286.02 \frac{kJ}{mol}} = \frac{-\Delta G}{-\Delta H} = \frac{\frac{-\Delta G}{nF}}{\frac{-\Delta H}{nF}} = \frac{1.23\,V}{1.482\,V} = 0.83 \tag{16}$$

This uses the higher heating value of hydrogen, which is more thermodynamically correct because the ΔH term accounts for all of the available energy coming into the system. The Gibbs free energy term decreases more than the enthalpy with temperature, which means the efficiency of the fuel cell will decrease up to 100°C. The efficiency lowers from ~83% to ~78% when the temperature is increased from 25°C to 100°C. However, for an operating fuel cell where the oxygen is always supplied in excess, water vapor can form in addition to the liquid water. While this would make the theoretical efficiency look

artificially higher (lower ΔH), it also realistically limits the total potential in an operating fuel cell.

1.2 Voltage losses

The difference between the electrode potential and the reversible potential (determined from thermodynamics) is the overpotential. Even at no current the cell does not exist at the equilibrium cell potential (1.23 V at 25^{o}C, 1 atm) because of fuel crossover. The resulting open circuit voltage (OCV) during operation at zero current is therefore lowered, with typical values ranging from 0.95-1 V [1].

Once current is drawn, the electrode potential decreases depending on three different losses: activation (kinetics), ohmic (resistance), and mass transport. Though each loss can occur at all current densities, as the current increases, the main (controlling) loss mechanism changes. The voltage as a function of current density is referred to as a polarization curve. An example of a polarization curve with the controlling loss mechanism highlighted is shown in Figure 2.

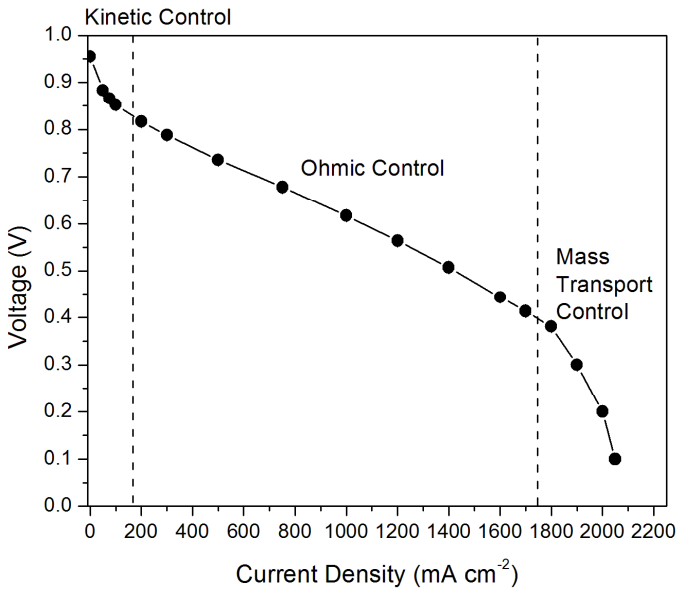

Figure 2. Polarization curve schematic showing kinetic, ohmic, and mass transport losses control regions

The derivation of each loss mechanism is provided in the following sections.

1.2.1 Activation polarization

The reactions happen on an interface between the ionically conductive electrolyte and the electrically conductive electrode. The speed of the reaction is the rate at which the electrons are released or "consumed", which is the electrical current. Faraday's Law gives the current density (current normalized by reaction area) produced:

$$i = n \cdot F \cdot j \tag{17}$$

where i is the current density, nF is the charge transferred (Coulombs mol^{-1}) and j is the flux of reactant per unit surface area (mol $s^{-1}cm^{-2}$).

The local kinetic rate expression for an electrochemical system is the Butler-Volmer Equation (BVE), which can be simplified to:

$$i = i_0 \left\{ \exp\left(\frac{-\alpha_{Rd} F(E - E_r)}{RT} \right) - \exp\left(\frac{\alpha_{Ox} F(E - E_r)}{RT} \right) \right\} \tag{18}$$

where i_0 is the exchange current density, α is the transfer coefficient for either the reduction or oxidation reaction, and $(E-E_r)$ is the activation overpotential. The expression is considered local since the oxygen content can decrease down the length of the flow field channel, changing the local concentration of oxygen at the catalyst sites. The exchange current density is a measure of the equilibrium reaction rate, where a higher values means faster reaction kinetics. The transfer coefficient is a dimensionless value that reflects the 'symmetry' of the forward and reverse reaction's activation barrier. Typical values are 0.2-0.5. The Butler-Volmer (BV) expression can be written for the anode and the cathode, but the cathodic current is the limiting reaction due to slow oxygen reduction reaction kinetics. The exchange current density of the anode is much higher than the cathode by several orders of magnitude. A higher i_0 means lower energy barrier to reaction and more current is generated at any overpotential, so the overpotential on the cathode is much larger than the anode. Neglecting the anodic contributions, the BV expression can be simplified to:

$$i_c = i_{0,c}\exp\left(\frac{-\alpha_{Rd,c}F(E_c - E_{r,c})}{RT}\right) \tag{19}$$

Solved for the voltage loss due to activation, the BV equation becomes:

$$\Delta V_{act,c} = E_{r,c} - E_c = \frac{RT}{\alpha_c F}\ln\left(\frac{i}{i_{0,c}}\right) \tag{20}$$

A simplified form of this is the Tafel equation:

$$\Delta V_{act,c} = a + b\log(i) \tag{21}$$

where $a = -2.3\frac{RT}{\alpha F}\log(i_0)$ and $b = 2.3\frac{RT}{\alpha F}$.

The Tafel slope is b. Higher Tafel slopes means lower performance (lower α means higher Tafel slope). An additional problem at low currents is fuel crossover, where hydrogen can diffuse directly through the membrane without reacting, which lowers the cell potential. The total current is the sum of external (useful) current and current due to losses ($i = i_{ext} + i_{loss}$), which means the expression for E_{cell} at lower current densities for losses due to activation is:

$$E_{cell} = E_r - \frac{RT}{\alpha F}\log\left(\frac{i_{ext} + i_{loss}}{i_0}\right) \tag{22}$$

1.2.2 Ohmic losses

Ohmic losses are due to resistance to the flow of ions in the electrolyte and the flow of electrons through the conductive fuel cell components. Ohm's Law relates the voltage drop to the current and resistance:

$$\Delta V_{ohm} = iR_T \tag{23}$$

The total resistance is the sum of all the internal resistances: ionic, electronic, and contact:

$$R_T = R_i + R_e + R_c \tag{24}$$

The electronic resistance is almost negligible, while the ionic and contact resistances are the same order of magnitude (typical R_T values are 0.1-0.2 ohms-cm^2).

1.2.3 Concentration polarization

Concentration or mass transfer limited polarization occurs when a reactant is rapidly consumed at the electrode by the electrochemical reaction. An expression for this loss is:

$$\Delta V_{con} = \frac{RT}{nF} \ln\left(\frac{C_B}{C_S}\right) \tag{25}$$

where B refers to the bulk and S refers to the surface concentration (mol cm^{-3}). Fick's Law equates flux and concentration gradient:

$$N = \frac{D \cdot (C_B - C_S)}{\delta} A \tag{26}$$

where N = the flux of reactants (mol s^{-1}), D = the diffusion coefficient ($cm^2 s^{-1}$), A = electrode surface area, and δ = diffusion distance. Combining with Faraday's law at steady state, the consumption rate is equal to the diffusion flux, which means:

$$i = \frac{n \cdot F \cdot D \cdot (C_B - C_S)}{\delta} \tag{27}$$

The surface concentration is zero when consumption exceeds diffusion, which occurs at the limiting current density:

$$i_L = \frac{n \cdot F \cdot D \cdot C_B}{\delta} \tag{28}$$

This result means the concentration polarization is:

$$\Delta V_{con} = \frac{RT}{nF} \ln\left(\frac{i_L}{i_L - i}\right) \tag{29}$$

This equation accounts for the sharp drop in cell potential at the limiting current density, as shown in Figure 2.

1.2.4 Overall expression for cell voltage

A simplified version of the polarization curve subtracts the three loss mechanisms (kinetic, ohmic, mass transport) from the equilibrium cell potential at a given temperature and pressure:

$$E_{cell} = E_{T,P} - \underbrace{\frac{RT}{\alpha F}\ln\left(\frac{i}{i_0}\right)}_{\text{Kinetic}} - \underbrace{iR_T}_{\text{Ohmic}} - \underbrace{\frac{RT}{nF}\left(\frac{i_L}{i_L - i}\right)}_{\text{Mass Transport}} \quad (30)$$

This expression assumes there are no anodic contributions to any of the loss mechanisms.

1.3 Properties of PEM fuel cell components

As discussed and shown schematically in Figure 1, the PEM fuel cell consists of separate oxidant and fuel flow field channels, anode and cathode gas diffusion layers, anode and cathode catalyst layers, and the polymer electrolyte membrane (PEM). This section discusses these main components.

The membrane must be a high proton conductor, barrier to fuel and reactant gas mixing, and chemically and mechanically stable. The membranes are typically made of perfluorocarbon-sulfonic acid ionomer (PSA), which is a copolymer of tetrafluorethylene (TFE) and perfluorosulfonate monomers. Proton conductivity is a function of membrane water content, so the membrane must be well hydrated. Water transport can occur through the membrane by three main mechanisms, each of which is a function of membrane hydration, λ[1]:

1. Electroosmotic drag (anode to cathode)

$$N_{H_2 0,drag} = \zeta(\lambda)\frac{i}{F} \quad (31)$$

2. Diffusion (cathode to anode, usually)

$$N_{H_2 0,diff} = D(\lambda)\frac{\Delta c}{\Delta z} \quad (32)$$

3. Hydraulic permeation (high pressure on cathode forces water to anode)

$$N_{H_2 0,hyd} = k_{hyd}(\lambda)\frac{\Delta P}{\Delta z} \quad (33)$$

[1]N.B. This λ should not be confused with the gas stoichiometry, which is mentioned often in the rest of the thesis and is explained in Section 1.4.

The membrane hydration is the ratio of the number of water molecules to charged $SO_3^-H^+$ sites, with values ranging from 0 (dry) to 22 (full saturation) [1]. Depending on the relative magnitude of each term, which depends on the operating conditions, water can favor net flux toward the anode or the cathode. In general, the net water transport to the cathode is the difference between the electroosmotic drag term and the diffusion term.

The electrode is a thin catalyst layer between the ionomer and the porous electrically conductive substrate, where the reaction takes place on the catalyst surface (usually platinum). Current Pt loadings are 0.3-0.4 mg cm^{-2}.

The gas diffusion layers (GDLs) are responsible for several roles in PEM fuel cell operation, including:

- Pathway for reactant gas from the flow field to the catalyst layer
- Pathway for product water back to the flow field channel from the catalyst layer
- Electrically connects the catalyst layer to the bipolar plate
- Conducts heat from the reaction to the bipolar plate for heat removal
- Mechanical support of the MEA to stop intrusion into the flow field

Required properties include being porous to allow gas and water flow, electrically and thermally conductive (in-plane and through-plane), and sufficiently rigid. Typical thickness ranges from 70-400 μm, with a porosity between 70-80%. They are also usually PTFE treated (5-20% by weight) to increase the hydrophobicity and thus reduce flooding. Some GDLs include a microporous layer (MPL) for better electrical contacts with the catalyst layer and increased water management capabilities.

Typical flow field designs include parallel, serpentine, and interdigitated channels, and these flow fields are generally made of metals or graphite plates. The flow field plates must also satisfy many requirements:

- Connect cells electrically in series (must be conductive)
- Separate the gases in adjacent cells (must be impermeable)

- Structural support (must be strong but lightweight)

Parallel channels are advantageous because of the low flow channel pressure drop but are susceptible to flooding and reactant maldistribution. Single-serpentine channels are common in small active areas but have a higher pressure drop due to the numerous bends. In interdigitated designs, gas is forced from the inlet to the outlet through the porous GDL, which can increase cell performance, but has trouble removing liquid water from inlets. The channel's shape, dimensions, and spacing are also important considerations. Typical channels are ~1 mm in width. Wider channels allow more reactant gas to touch the GDL and give more area for water removal, but if they are too wide the GDL will bend into the flow field. Wider spacing (landing areas) facilitates conduction of heat and electricity, but the GDL is less exposed to gases and water can accumulate below the landing areas.

1.4 Fuel cell operating conditions

The main operating conditions in a PEM fuel cell are the pressure, temperature, gas flow rates, and the relative humidities of the gas streams.

Increasing pressure increases cell potential via two reasons, the Nernst equation and an increase in the exchange current density due to increased gas concentrations at the electrodes. For example, increasing the cell operating pressure from 101.3 kPa to 200 kPa can result in a 34 mV gain. However, the increase in voltage due to an increase in pressure may be offset due to parasitic losses from the compressor. The pressure is also related to water management, which can have varying impacts on the fuel cell performance.

Typical fuel cell operation occurs at ~75^{o}C, which means the cell must be heated. Like pressure, the energy required to keep the cell temperature up may offset the electrochemical gains of elevated temperature. However, the reaction is exothermic so a cooling system is needed to maintain the proper temperature. Measuring the temperature can be ambiguous as it can typically be measured at the outer surface, exiting air, or exiting coolant. The complex geometries and electrochemical reaction often mean temperature gradients will be present in the cell.

Faraday's Law (Eqn. 17) dictates all of the flow rates based on the current, which for hydrogen, oxygen, and water are:

$$\dot{N}_{H_2} = \frac{I}{2F} \qquad \dot{N}_{O_2} = \frac{I}{4F} \qquad \dot{N}_{H_2O} = \frac{I}{2F} \tag{34}$$

These can all be corrected for T and P with the ideal gas law when determining the gas velocity in the flow channel. Also, the actual flow rate of supplied reactant is always more than needed, and the ratio of supplied gas to needed gas is the stoichiometric ratio:

$$\lambda_i = \frac{N_{supplied}}{N_{needed}} \tag{35}$$

An increase in the stoichiometry (stoich) helps remove product water from the flow field channels and keeps the oxygen concentration high. Typical stoichiometries are 2 for the cathode and 1.5 for the anode.

The reactants are typically humidified to ensure the membrane remains well hydrated. Relative humidity (RH) is the ratio between the water vapor partial pressure and the saturation pressure (saturation pressure is only a function of temperature). Some systems can capture heat and water generated by the cell to humidify the incoming air. However, even if enough water is generated most of the air will stay under-saturated (RH < 100%)

1.5 Pressure Drop in PEM fuel cell flow channels

The Darcy–Weisbach equation can be used to approximate the pressure drop of incompressible flow in pipes:

$$\Delta P = \underbrace{f \frac{L}{D_H} \rho \frac{\bar{v}^2}{2}}_{\text{1st order with v}} + \underbrace{\sum K_L \rho \frac{\bar{v}^2}{2}}_{\text{2nd order with v}} \tag{36}$$

where f is the friction factor, $\bar{v}$ is the average velocity, ρ is the density and K is local resistances (bends and expansion /contraction etc.) In PEM fuel cells, there are deviations from normal pipe flow such as the roughness of the GDL being different than the walls, the gas participates in the reaction and therefore the flow rate varies down the channel length, the temperature may not be uniform, and liquid water impacts the pressure drop.

The presence of liquid water in the flow channels is an example of two-phase flow, and this increases the pressure drop. The two-phase flow multiplier provides useful insight into the impact of the two-phase flow pressure drop. The two-phase flow multiplier, $\varphi_{2\text{-phase}}$, is defined as:

$$\varphi_{2-\text{phase}} = \frac{\Delta P_{2-\text{phase}}}{\Delta P_{1-\text{phase}}} \tag{37}$$

A higher two-phase flow multiplier indicates a larger influence of water on the overall pressure drop. This is relevant to PEM fuel cells since an increase in the pressure drop is an increase in the parasitic power loss of the system.

2 A review of two-phase flow in PEM fuel cell flow channels[2]

As has been discussed, PEM fuel cells have received extensive study and interest due to its high energy efficiency, low operating temperature, and low to zero emissions during its operation [2]. However, several technical issues still exist that impede the further use of fuel cells in practical applications. One major issue that has received a great deal of attention is proper water management in the fuel cell, and this issue continues to play an important role in the understanding of fuel cells. In a perspective piece published by AIChE Journal, Benziger [3] stated "Recent results suggest that better engineering designs of PEM fuel-cell reactors may be more important to the commercial success of fuel cells that developing better membranes and catalysts, which has been the focus of the DOE road map." The key problem, he notes, is how to manage water. An excellent review by Jiao and Li [4] was published in 2011 furthering the topic of water transport in a fuel cell. Their comprehensive review (430 papers) covers the state of water in each layer of the fuel cell, the various transport mechanisms, experimental and numerical work, cold start operation, and high temperature PEM fuel cells. Their outlook for future experimental work is for researchers to simultaneously measure more parameters while avoiding major modifications to the fuel cell.

PEM fuel cell water management is particularly important because too little water will cause membrane dehydration, which limits proton conductivity, and too much water can flood the fuel cell, causing less reactant to reach active catalyst sites. Both cases consequently decrease the cell performance. Another recent review [5] detailed issues associated with water management, which described the role of each layer of the PEM

[2] A portion of this chapter was published in [2]: R. Anderson, L. Zhang, Y. Ding, M. Blanco, X. Bi, D.P. Wilkinson, A critical review of two-phase flow in gas flow channels of proton exchange membrane fuel cells, J. Power Sources 195 (2010) 4531-4553.

fuel cell and how each area is prone to flooding. The paper also detailed mitigation strategies based on 1) engineering principles and changing operating conditions and 2) modification of materials. While comprehensive in the overall picture of water management, little emphasis is placed on gas-liquid two-phase flow issues in the flow field channel itself.

Trabold [6] noted the importance of two-phase flow research in PEM fuel cells, and explained that the gas-liquid flow within the flow channels is complex and requires an understanding of electrochemistry, heat and mass transfer, and fluid mechanics. Knowing the air and liquid velocity in the channel allows one to develop flow regime maps, which have been studied in traditional two-phase flow research. Different operating conditions can lead to different flow patterns though, which can lead to flow maldistribution among multiple channels to satisfy the equal pressure drop between a single inlet and outlet of the manifold. Thus, many competing variables are noted in PEM fuel cell two-phase flow. Two-phase flow also represents a higher overall pressure drop, which lowers the total system efficiency.

In addition to experimental efforts, many attempts have been made to model and simulate the two-phase transport phenomena in PEM fuel cells. In particular, computational fluid dynamics (CFD) is considered to be a very powerful tool in fuel cell design and operation optimization. In the literature, the earliest PEM fuel cell models date back to the early 1990s by Springer et al. [7] and Bernardi and Verbrugge [8]. Increasingly complex and detailed models have been developed since, from one-dimensional, single-phase flow, isothermal, steady state and single layer models to three-dimensional, two-phase flow, non-isothermal, transient and multiple layer models.

However, due to the various complicated phenomena in PEM fuel cells, the modeling and simulation of PEM fuel cells still remains a challenge. Complications include two-phase flow, electrochemical reaction, charge transport, diffusion in porous media, and coupling different length scales (such as the nanometer components of catalysts, the micrometer heterogeneous pores in the gas diffusion layers (GDLs), and the millimeter dimensions of flow field channels), and experimental validation. Numerical studies are reviewed in Appendix A.

This chapter presents a review of two-phase flow in PEM fuel cell flow channels. The relevance of this topic is demonstrated by the number of papers published related specifically to ‘two-phase flow’ and ‘PEM fuel cells’ continuing to increase, which is shown in Figure 3. While this shows 207 cumulative citations since 1994, it is also interesting to note that in the same time publications relating to ‘water management’ and ‘PEM fuel cells’ numbered 431 citations via the same database.

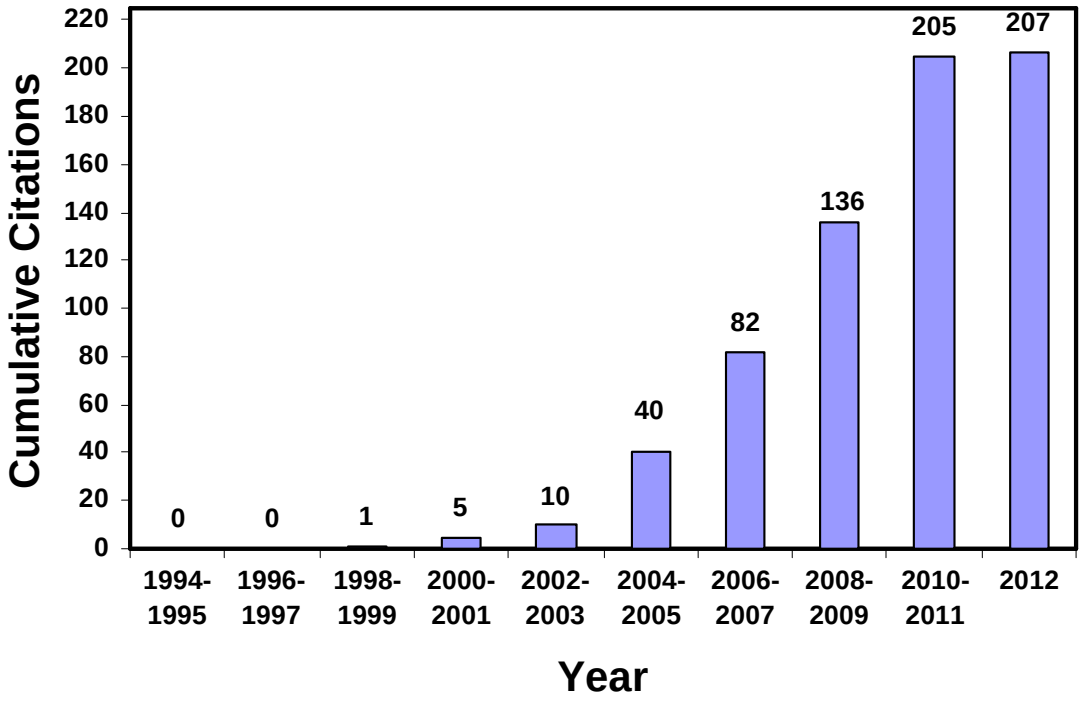

Figure 3. Cumulative number of papers published for keywords "two-phase flow" and "PEM fuel cells" since 1994 in the Compendex Engineering Village 2 database

This review emphasizes gas-liquid two-phase flow in minichannels or microchannels ($D_{microchannel} \leq 1$ mm) related to PEM fuel cell applications. The focus is on PEM fuel cells under normal operating conditions (ambient temperature to 100^{o}C operation) and neglects two-phase flow issues related to startup or shutdown. The experimental approaches and results of researchers in both active fuel cells (in-situ; operating) and in channels designed to mimic operational fuel cells (ex-situ; non-operating) are considered. Mitigation strategies specific to water flooding in channels via material modifications and operating conditions are also presented.

2.1 Experimental visualization techniques

This section reviews techniques for detecting water in PEM fuel cell minichannels, focusing on direct optical visualization while referencing other methods reported in the

literature. A discussion of the uses and the results of these techniques in active fuel cells is given in Section 2.2.

2.1.1 Optical visualization

The most common technique to observe flow field two-phase flow is to use a transparent fuel cell. A typical schematic diagram of a transparent fuel cell is shown in Figure 4.

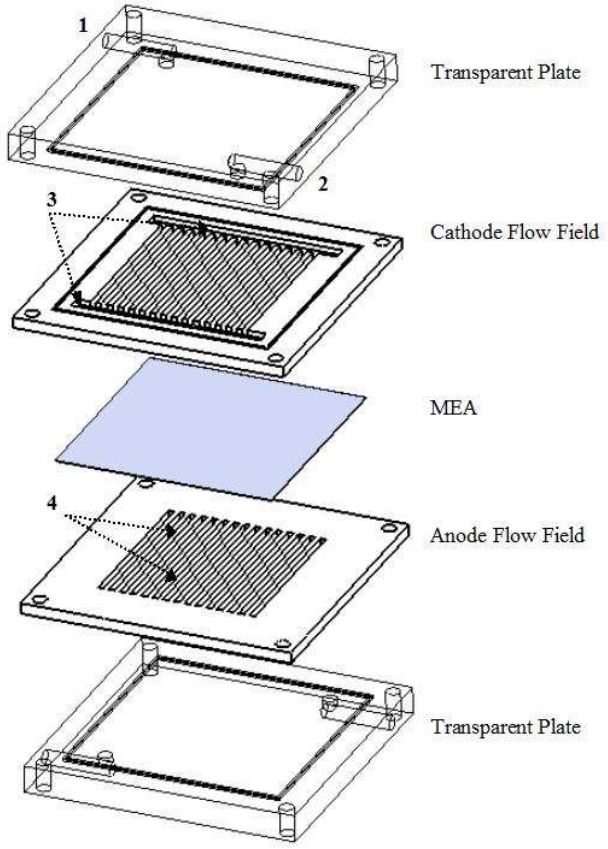

Figure 4. Schematic of a typical transparent PEM fuel cell (reprinted from Anderson et al. [2] with permission from Elsevier)

The membrane electrode assembly (MEA) is sandwiched between flow field plates and transparent endplates for viewing. Not shown are the means to collect current, plates for heating (either electrically or via cooling water), or compression plates since these are common to all fuel cells and are not novel in regards to a transparent fuel cell. Machining

the flow field directly through a metal plate allows the flow field plate to also act as the current collector. In Figure 4, gas enters via port 1 and exits via port 2. The manifolds (labeled 3) distribute the gas to the flow channels (labeled 4). The flow field plates in this schematic are symmetrical about the MEA. This design is not the only means of creating a transparent cell but contains the components commonly found in the literature. Tüber et al. [13] conducted a highly cited work on transparent fuel cells. A steel rib was placed between an MEA and a Plexiglas end plate, with the rib defining the depth and the landing width of two channels. Gas was introduced from the Plexiglas above via one common inlet hole. The unit was compressed with screws, and a copper wire was attached to the rib for current collection. Different phenomena to be studied lead to specific designs for a transparent fuel cell, and Table 1 summarizes the designs of several research groups, including relevant channel dimensions, materials, and flow field design.

Table 1 Typical transparent fuel cell designs with a focus on flow field type, flow field material, channel dimension, and transparent plate material (reprinted from Anderson et al. [2] with permission from Elsevier)

Author	Flow Field Type	Flow Field Material	Channel Dimensions (l x w x d)	Transparent plate material
Zhang et al. [9]	7 Parallel Channels	Gold Coated Stainless Steel	100x 1x 0.5 mm Active Area = 14 cm^2	Antifogging polycarbonate
Liu et al. [10]	9 Parallel Channels (vertical orientation)	Gold Coated Stainless Steel	22.4x0.8x1mm	Plexiglas
Ous and Arcoumanis [11]	13 Serpentine Channels	Graphite	655 x1.5 x 1.5mm	Plexiglas
Masuda et al. [12]	Single Straight Channel	Gold Coated Stainless Steel	30 x 1.6 x 1 mm	Glass
Tüber et al. [13]	2 Parallel Channels	Stainless Steel	50 x 1.5 x 1 mm	Plexiglass
Hakenjos et al. [14]	Single Serpentine	Graphite	1 x 1 mm (w x d) Active Area = 20.25 cm^2	Zinc Selenide
Weng et al. [15]	Two Serpentine Channels	Brass	2 x 2 mm (w x d) Active Area = 10 cm^2	Acrylic
Spernjak et al. [16]	Single Serpentine	Stainless Steel 316	0.8 x 1 mm (w x d) Active Area = 10 cm^2	Polycarbonate
Ge and Wang [17]	(a) 7 Parallel Channels (b) 4 Serpentine Channels	Gold Plated Stainless Steel	(a) 1 x 0.5 mm (w x d) Active area =14 cm^2 (b) 70 x 1 x 0.5 mm Active area=5 cm^2	Polycarbonate
Theodorakakos et al. [18]	Single Serpentine	Plexiglas	1.46 x 0.28 mm (w x d)	Plexiglas
Shimoi et al. [19]	3 Parallel Channels	Brass	100 x 3 x 1 mm	Sapphire (Al_2O_3)
Kim et al. [20]	35 Serpentine Channels	Carbon	0.7 x 1 mm (w x d) Active Area = 25 cm^2	Acrylic
Sugiura et al. [21]	Single Serpentine 14 Parallel	--	1.6 x 0.8 mm (w x d) Active Area = 25 cm^2	Polycarbonate
Ma et al. [22]	Single Straight Channel	Graphite	125 x 1.5 x 1 mm Active Area = 5 cm^2	
Yang et al. [23]	7 Parallel Channels	Gold Coated Stainless Steel	100x 1x 1 mm Active Area = 14 cm^2	Polycarbonate

As shown in Table 1, metals are often used for flow field plates. Weng et al. [15] showed that a brass plate could be used for the anode and cathode flow fields with extension areas included for electric heating or convective cooling. Clear acrylic plates acted as endplates on the cathode and anode side, allowing for visualization of either side of the cell. Stainless steel is a common flow field material in transparent cells [9, 10,12,13,16,17,23], and the plates are often gold plated to avoid corrosion and to increase conductivity. When clear acrylic end plates are used they are prone to fogging, and it can be difficult to discern between liquid water emerging into the channels and liquid water condensing on the clear plate if humidified reactants are used. One solution to this problem is to use an antifogging coating [9], though this solution causes the clear polycarbonate plate to be very hydrophilic, which is not representative of commercially used graphite flow field plates that are less hydrophilic. Another interesting choice for an optical plate is zinc selenide, as used by Hakenjos et al. [14]. Zinc selenide is transparent to optical light for direct visualization and IR irradiations for the determination of the temperature distribution with an IR camera. A barium fluoride plate is also transparent to IR light and can be used to determine temperature distributions [24].

One drawback of transparent cells is the lack of quantitative information provided. Viewing the channel from the top does not offer depth resolution, and the true volume of films, slugs, and droplets in the channel cannot be analyzed. The reflective GDL background also complicates image processing [16]. The images are often usefully correlated with pressure or voltage data, but this correlation provides only qualitative details about the cell [25]. The subjective nature of these qualitative correlations makes it difficult to standardize between authors. Another issue associated with transparent cells is

the material of construction. The surface properties are very important in analyzing two-phase flow, especially contact angles, and little consideration is given to this problem in the literature. For instance, specific results found in a cell with a Plexiglas end plate may differ from the results found in a cell using traditional graphite plates. Since transparent cells define flow channels with an optical plate top, flow field plate walls, and a GDL bottom, three contact angles must be considered when analyzing the surface properties and droplet dynamics. Another potentially important parameter is the surface roughness of the flow field plates [26]. Despite these drawbacks, visualization cells provide a method to validate existing models and to further understand the influence of key operating variables. As pointed out by Chang et al. [27], this validation is particularly important in incorporating two-phase flow into existing models. Coupling the optical visualization with other techniques to monitor liquid water also enhances the use of transparent cells [28].

Recently, an in-situ technique was coupled with advanced image processing techniques to quantitatively determine the water content in the flow fields of the anode and cathode in an operating visualization fuel cell [29]. Depending on the GDL, stoichiometries, and current density, the water coverage and type of flow pattern (film or slug) changed. While the image processing filtered out droplets on the transparent wall via condensation, it is unclear what role the condensation played in growing the slugs and films reported. However, this is still the most quantitative statement of flow channel flooding yet made via optical visualization. This work also points out the excess water accumulation at low current densities and low gas flows, which are conditions a fuel cell may often operate at for high efficiency.

Flow channel water visualization and oxygen partial pressure have also been studied together in a triple-serpentine fuel cell [30]. An oxygen sensitive porphyrin luminescent dye film coated the channel walls, and from this the oxygen partial pressure can be determined. At water blockages, the partial pressure of oxygen approaches zero. The partial pressure results also show oxygen can pass through the GDL from the other channels to the blocked channel, which is one reason the serpentine configuration shows high electrochemical performance. Further, this result showed an interesting link between channel flooding and catalyst layer flooding, and mitigation strategies should reflect both flooding processes.

2.1.2 Other visualization systems

Other methods to visualize two-phase flow include neutron radiography and magnetic resonance imaging (MRI). Neutron radiography can be used to obtain 2-D images of liquid water [31, 32], and this allows the user to gain greater quantitative information. Recent reviews of water visualization and measurements by these methods and others are discussed in greater detail [28,33]. These methods help validate the qualitative information derived from optical visualization cells, and also help validate the results of numerical models. A review by Tsushima and Hiraiu [34] extensively covers these topics, as in-situ imaging techniques are also becoming more readily available to study water transport in PEM fuel cells. Though these methods have improved in the last few years, the authors still note that better spatial and temporal resolution is needed, especially to consider water transport in the catalyst layers and MPLs. Also, physical properties from these studies should be used in new numerical simulations for more accurate models. The connection between the emergence of liquid water in the flow field channels and the cell

voltage has been noted, but like Jiao and Li [4], the authors note that the visualization results should be validated in a more realistic setup that does not rely on clear plates and metal current collectors.

In an MRI system, Dunbar et al. [26] attempted to mimic actual materials used in typical flow fields. Ferromagnetic materials like iron or nickel are unsuitable due to the magnetic field, so Teflon® flow fields coated with a graphite layer (Aquadag) to represent the hydrophobicity of commercially available graphite flow fields were used to avoid complications in the MRI. A neutron imaging technique was used to study purging, a possible mitigation strategy, when using super-hydrophilic (13.5^{o}) and super-hydrophobic (152.5^{o}) channels [35]. Each coating offered a benefit, as the super-hydrophilic channels helped remove more water from the GDL, while the super-hydrophobic channels increased convective water removal from the channels. Lu et al. [62] also noted benefits to using hydrophilic channels in promoting film flow on the channel walls. Additional work needs to be done to determine an optimized solution.

2.2 In-situ experimental two-phase flow studies in PEM fuel cells

In active PEM fuel cells, the presence of liquid water has been observed by the visualization techniques described in Section 2.1. This section describes two-phase flow studies in operational PEM fuel cells, which is an important distinction because two-phase flow in fuel cells is different from traditional two-phase flow in other applications [36]. One such difference is that the water content changes along the length of the channel as water is introduced to the channels from the GDL after reaction at the catalyst surface. This introduction method means water droplet generation and removal at the GDL surface into the channel must be considered. This issue is further complicated by

the location of the emerging droplet because the removal process depends on whether the droplet is created on the GDL surface towards the center or the wall of the channel [11]. As discussed, the surfaces of the channel also have dissimilar contact angles, since the transparent plates, flow field plates, and the GDL have different contact angles, which influences droplet behavior. A schematic showing these three surfaces is shown Figure 5.

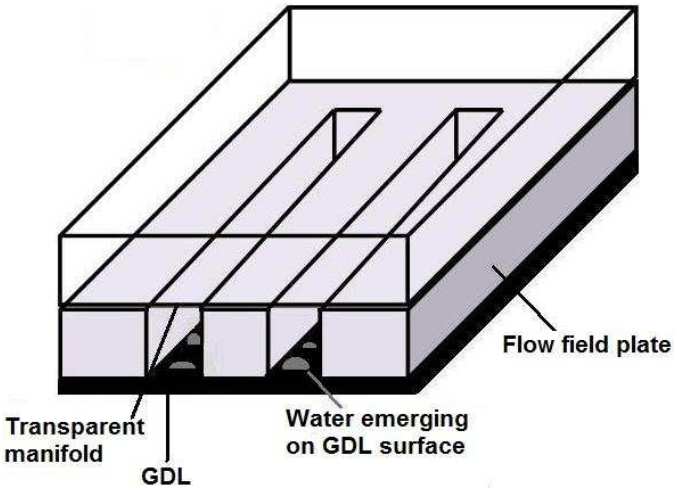

Figure 5. Schematic of three distinct channel surfaces in a transparent fuel cell (modified from Anderson et al. [2] with permission from Elsevier)

Once the droplet is removed from the GDL surface, it can coalesce with droplets downstream, changing the behavior of the two-phase flow. Also, the two-phase flow in fuel cell flow channels is characterized by a large gas to liquid flow ratio and a decreasing mole fraction of the reactant gas down the length of the channel due to consumption. Non-uniform temperature distributions created by local hotspots can also change the amount of water that will remain in the gas phase, which affects the water balance in the flow channel [24]. Non-uniform current distribution, which changes the amount of water being produced locally, can also lead to non-uniform distribution of the water product in the channels.

2.2.1 Gas channel two-phase flow: causes and problems

Liquid product water is transported in the fuel cell by various mechanisms, and a review of the PEM fuel cell water balance has recently been published [37]. Also, water can condense in the flow field channel from the inlet gas due to decreased operating temperature, increased pressure, or increased gas humidification if the saturation vapor pressure is reached. The water that eventually enters the cathode flow field channels is therefore a function of condensation, evaporation, and the contributions of electroosmotic drag and water back diffusion. Electroosmotic drag carries water from the anode to the cathode via protons moving through the electrolyte. Back diffusion occurs when the product water establishes a concentration gradient between the cathode and anode, causing water to diffuse toward the anode. These terms are defined explicitly in Section 1.3.

The product water must diffuse through the GDL to reach the flow field channels. Once liquid water enters the channels, several problems can emerge, and major issues associated with gas channel flooding include [36]:

- Blockage of the channel by liquid water, which can increase the pressure drop in the channel.
- Non-uniform current distribution and reactant distribution.
- Blockage of reactant gas transport to the active reaction sites due to the formation of a liquid film on the GDL surface.

2.2.2 Flow patterns

In an operating fuel cell, two-phase flow patterns impact the pressure drop and liquid water distribution in the flow channel, which can alter the PEM fuel cell performance. Research has shown that liquid water holdup is a particular concern for low Bond number ($10^{-4} \leq Bo \leq 10^{-1}$) and low Suratman number ($10^{3} \leq Su \leq 10^{5}$) environments [10]. The Bond

number is the ratio of gravitational force (body force) to surface tension and the Suratman number is the ratio of surface tension to viscous forces. The equations for these dimensionless groups are shown below:

$$Bo = \frac{\Delta \rho g L^2}{\gamma} \tag{38}$$

$$Su = \frac{\gamma \rho L}{\mu^2} \tag{39}$$

where ρ is the density, $\Delta \rho$ is the density difference between phases, g is the acceleration due to gravity, L is a characteristic length such as the drop radius, γ is the surface tension, and μ is the dynamic viscosity. For low Bo and low Su conditions, the noted flow patterns are slug flow, core-annular, and transition flows [10]. Typical flow patterns in operating fuel cells can be seen in Figure 6 from the work of Hussaini and Wang [38].

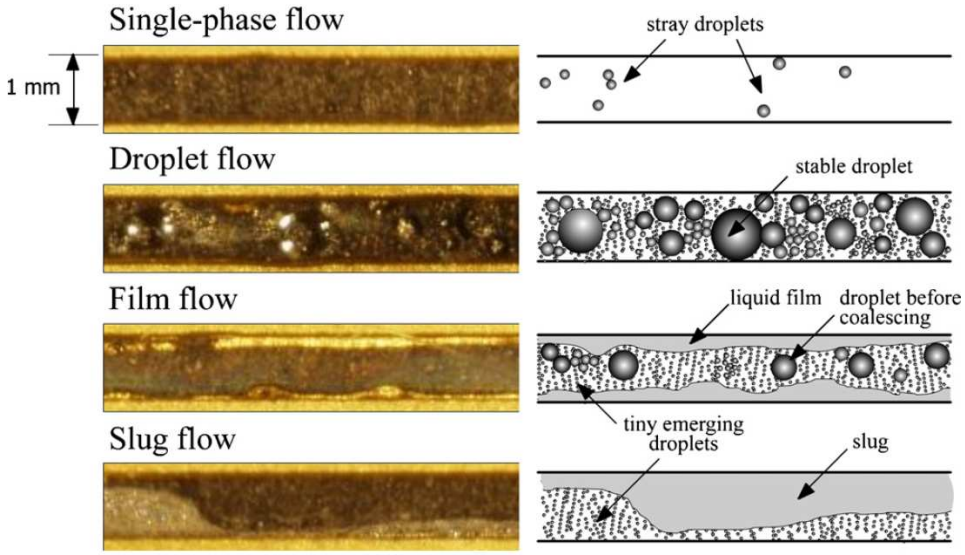

Figure 6. Typical flow patterns in PEM fuel cell flow channels including single-phase flow, droplet flow, film flow, and slug flow (reprinted from Hussaini et al. [38] with permission from Elsevier)

Not all two-phase flow studies show the same flow patterns and the lack of consistency highlights the difficulty in understanding and characterizing two-phase flow in operational cells. Additionally, the schematic in Figure 6 contains stray droplets in the description of single-phase flow, which would be more accurately described as mist flow

(if enough stray droplets are noted) or as a pseudo-homogenous flow. Mist flow has been identified in an operating fuel cell but at an air stoichiometry of 10, which may be unrealistic for a fuel cell due to high parasitic power losses [9]. Further complicating the identification of flow patterns, fuel cells operate at different relative humidities and temperatures (affecting water removal capacity), with different flow channel configurations, different flow rates, and different surfaces (GDL and channel). Individual results are thus noted for specific setups, and no work has been done to determine the effect of such operating conditions on two-phase flow in a general sense.

Flow patterns maps are useful because it shows how superficial air and liquid velocity can be exploited to give a particular flow regime. Hussaini and Wang [38] constructed a flow map showing different regions at different superficial gas and liquid velocities.

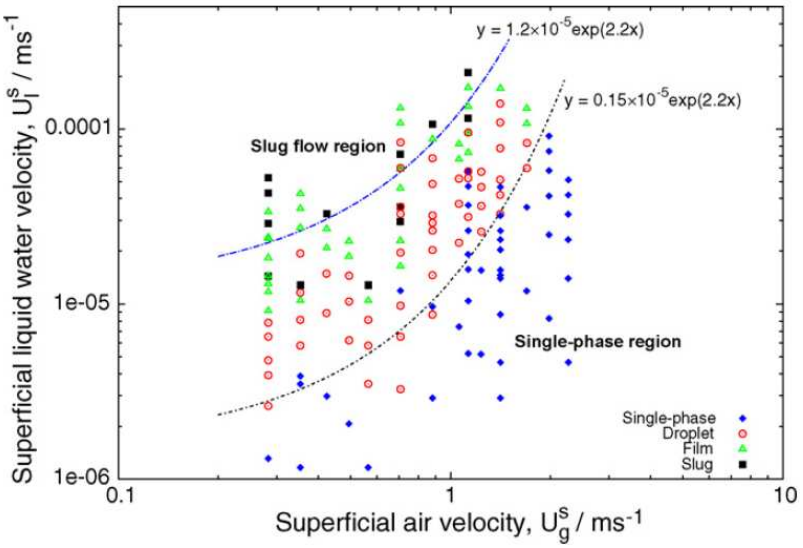

Figure 7. Flow map in an active PEM fuel cell based on superficial gas and liquid velocities showing different flow regimes (reprinted from Hussaini et al. [38] with permission from Elsevier)

Trabold [6] recommends operating the channels in the annular flow regime, which would require a superficial gas velocity of 5 to 6 m s^{-1}. This regime allows water to be removed on the channel walls while leaving the GDL surface available for gas transport. To

maintain this regime, though, specific operating conditions would have to be met at a given current density and stoichiometry (λ_i). In practical systems, the parasitic load or energy required for gas delivery is directly related to the pressure, flow rate, and pressure drop. It is therefore desirable to keep the stoichiometric ratio as low as possible while sufficiently high for effective water management [39]. Since the GDL, flow field, and operating conditions can shift the transitions between flow regimes, the results presented in Figure 7 are valid for that specific experimental setup only. Multiple factors in addition to superficial velocities have to be understood in order to operate the fuel cell in the desired flow regime.

2.2.3 Pressure drop (characteristics under active cell operating conditions)

The pressure drop is considered to be an indicator of liquid water build-up in flow field channels of a PEM fuel cell. The pressure drop increases with current density, which is explained by the higher reactant flow rates and higher water production rates in accordance with Faraday's law. Higher water production can mean a higher degree of channel flooding and thus a higher pressure drop. The pressure drop will continue to increase with time as liquid water accumulates in the channels, which varies with flow rate and flow field design [40]. The flow regime also plays an important role in determining the overall pressure drop, where a liquid slug can completely block a channel before being removed, causing a sudden spike in the pressure drop measurement. Liu et al. [41] have shown that the different flow patterns can be identified based on the total pressure drop. Pressure measurements can also be used to obtain information about how much water enters the cathode. Differential pressure between the cathode to anode can be used to determine the water saturation in the GDL, which affects how much water is

transported into the channel and directly affects the liquid flow rate into the flow channels [42].

The pressure drop can also be used as a diagnostic tool, which is seen by comparing the cathodic pressure drop signal to the voltage signal, as shown in Figure 8 [6]. As the voltage decreases, the pressure drop increases and fluctuates to a greater extent, providing a sensitive measure of the flooding occurring in the fuel cell.

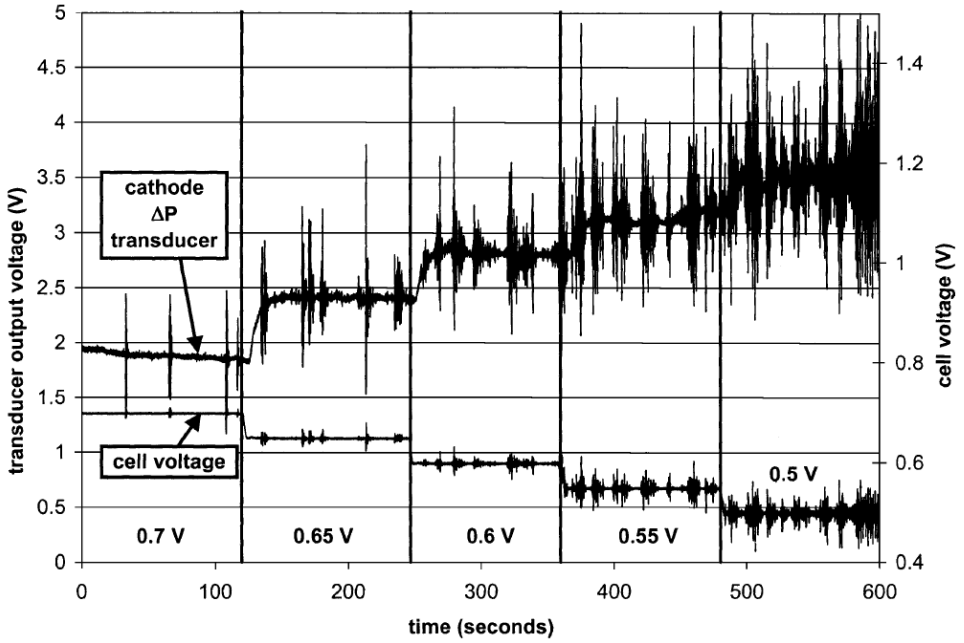

Figure 8. Pressure drop (transducer output voltage) and cell voltage signals as flooding diagnostic tools with an emphasis on the sensitivity of the pressure drop signal (reprinted from Trabold [6] with permission from Elsevier)

This technique can be useful at the cathode, where major flooding can occur, and at the anode, where little flooding occurs. The anode generally sees little variation in the pressure drop but, like the cathode, the expulsion of slugs coincides with spikes in the pressure signal. Pressure drop measurements on the cathode side have also been used to identify flooding in PEM fuel cell stacks [43,44].

The pressure drop signal and voltage signal have also been correlated to show that flow channel flooding in parallel channels lowers voltage and increases instability in the

signal [45]. The voltage loss scaled proportionally to channel plurality divided by the air stoichiometry, and the amplitude of the voltage fluctuations scaled to the channel plurality divided by the air stoichiometry squared. Plurality here is defined as the number of parallel channels per active area.

Pressure drop measurements can be used to determine the ideal gas velocity for water removal at a given current density, as shown by Ma et al. [22]. The pressure measurement was compared with photographs in the cell, which showed that as water accumulated, the pressure drop increased. When the water was finally expelled, the pressure drop decreased. As the gas velocity was increased, the magnitude of the fluctuations decreased since droplets did not have adequate time to form in channels and cause a blockage. This type of analysis could help to optimize flow field design and operating conditions. One problem associated with pressure drop measurements is that it does not provide information regarding the possibility of flooding in other layers in the fuel cell. However, combining the analysis of the pressure drop measurements with the performance curves can give more insight into the operating regions where flooding is an issue [36].

2.2.4 Gas reactant flow maldistribution

Typical flow fields for the PEM fuel cell contain multiple channels connected to the same inlet and exit, and non-uniform flow distribution is a major concern. Flow maldistribution in an active fuel cell is considered to be an important factor in reducing the operating lifetime of a fuel cell [46,47]. Therefore, proper gas reactant distribution is critical to ensure high performance and a long lifetime for a PEM fuel cell. A uniform distribution of current density leads to a uniform distribution of temperature and liquid water production, and lower mechanical stresses on the membrane electrode assembly

(MEA) [48]. Flow maldistribution can cause flooding in some channels, leading to a non-uniform distribution of current density and membrane hydration. As a consequence, the pressure drop and current density show erratic fluctuations and the overall power performance decreases.

Figure 9 shows the effects of flooding in a channel [13]. Once the liquid droplet blocked the channel, the cell performance did not recover over the testing period, which impacts the reliability of the PEM fuel cell. The occurrence and the recoverability of channel blockage in parallel channels is directly related to the flow instabilities of the two-phase flow in parallel flow channels and is affected by many parameters such as the channel flow rate and the wall physical properties such as the contact angle.

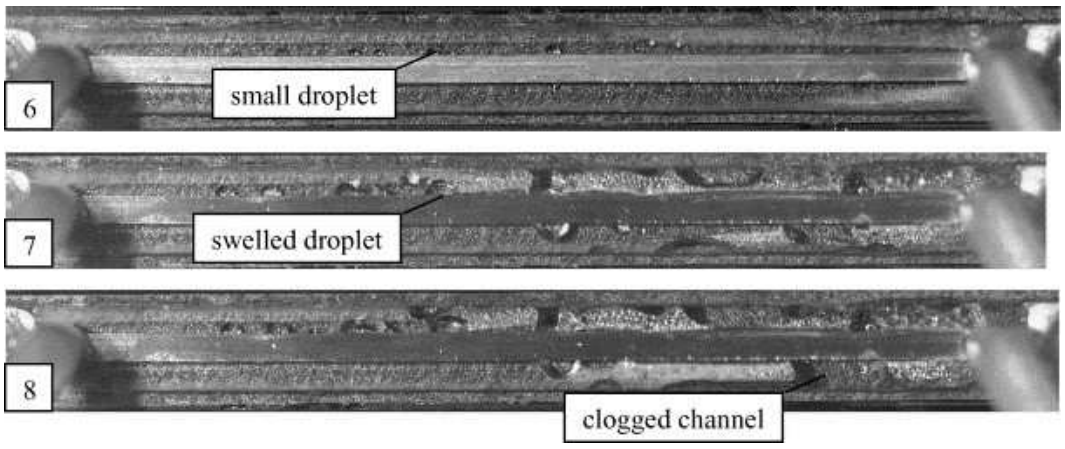

Figure 9. Flow field channel flooding with time (image '6', '7', and '8' at 5, 25, and 30 minutes of operation, respectively) (reprinted from Tüber et al. [13] with permission from Elsevier)

Along with visual observation, residence time distributions may help quantify flow maldistribution in PEM fuel cells [49]. Coupling multiple experimental methods will help to further validate and understand flow maldistribution in fuel cells.

2.3 Ex-situ experimental two-phase flow studies relevant to PEMFCs

Since two-phase flow is a complex phenomenon in PEM fuel cells, ex-situ (non-operating) studies enable one to explore detailed mechanisms behind two-phase flow

behavior at flow conditions relevant to fuel cell operations. In some cases, the work is tied directly to PEM fuel cells, such as droplet emergence and detachment in channels from a GDL surface. Other cases involve non-fuel cell applications, such as heat exchangers, where two-phase flow is also relevant. Ex-situ experiments possess the advantages of easy equipment setups, flexible operating conditions, and the ability to decouple reaction and heat and mass transfer from intricate flow phenomena. This section is an overview of existing ex-situ experimental results related to two-phase flow in minichannels with relevance to fuel cells. These studies have explored the influence of flow conditions, channel wall wettability, channel geometries, and flow media on hydrodynamic parameters such as droplet formation, pressure drop, flow pattern, and liquid hold-up. Additionally, flow distributions are investigated in parallel channels, though few studies are concerned with this phenomenon [50,51].

As noted in Section 2.2, gas-liquid two-phase flow in PEM fuel cells is a unique multiphase flow. Significant differences from conventional two-phase flow are large gas to liquid flow ratios, the method of liquid introduction, and a combination of multiple water transport mechanisms including electroosmotic drag, back diffusion, and water condensation from humidified inlet gases. To simulate an operating fuel cell, the water production rates and total water transport can be taken into account using Faraday's law modified with a water transport coefficient, α, for water transport across the MEA as follows:

$$m_{water} = \frac{(1+2\alpha)iA_{act}}{2F} \tag{40}$$

where m_{water} is the rate of moles of water generated on the cathode side, A_{act} is the active area (cm^2), *i* is the current density ($A\ cm^{-2}$), and F is Faraday's constant (96485

Coulombs mol^{-1}). In ex-situ studies in general, the corresponding superficial velocity of air ranges from 0-10 m s^{-1}, analogous to active fuel cell operations in the current density range of 0-2 A cm^{-2} and gas stoichiometric ratios up to 20. While this is a high stoichiometry, it is useful in establishing potentially relevant hydrodynamic parameters for a PEM fuel cell. Experimental conditions in all two-phase flow studies for fuel cell applications generally fall into these flow conditions, with gas flow channel dimensions typically in the sub-millimeter to millimeter range. Table 2 summarizes ex-situ experimental studies of two-phase flow related to fuel cell operation in the literature.

Table 2 Ex-situ experimental studies of two-phase flow in minichannels and microchannels for fuel cells (reprinted from Anderson et al. [2] with permission from Elsevier)

Authors	Channel Dimensions	Operation Conditions	Remarks
Allen [52]	330 μm circular and 500 μm square	Nitrogen and water, u_G:0-2.4 ms^{-1} and u_L=0-0.035 ms^{-1}	Non-wetting channels with high flow resistance
English and Kandlikar [53]	1.124 mm in width and 0.93 mm in height	Air, water and surfactant Triton DF-12 with concentrations of 0.0208 to 0.1089; u_G, 3.19-10.06 ms^{-1} and u_L, 0.0005 -0.022 ms^{-1}	No significant difference in pressure drop in different surfactant solutions
Lee et al. [54]	0.5 mm in width and 0.2 mm in depth	Air and water; u_G:0 to 20 ms^{-1}; u_L: 0-0.007 ms^{-1}	Flow hysteresis; flow regimes depends on GDL hydrophobicity
Zhang et al. [50,55]	Y-branched parallel channel, 1.6 mm in width and 1.6 mm in height	Air and water, u_G:0-10 ms^{-1}; u_L:0-0.03 ms^{-1};	Flow hysteresis, flow maldistribution occurs at low gas and liquid flow rates
Lu et al. [56]	Parallel channels, 0.7 mm in width and 0.4 mm in height	Air and water; u_G: 0-20 ms^{-1} and u_L:0-0.015 ms^{-1}	Two-phase flow patterns, pressure drop in parallel channels, flow maldistribution
Kandlikar et al. [51]	Parallel channels, 0.7 mm in width and 0.4 mm in height	Air and water; u_G:0-20 ms^{-1} and u_L:0-0.0003 ms^{-1}	Entrance region pressure drop measurement; Flow maldistribution due to different flow resistance

A recent ex-situ method for characterizing two-phase flow in flow channels was designed by Steinbrenner et al. [57] to study how flow patterns change throughout eight injection ports along the length of a serpentine flow channel. This injection is more consistent with the actual mechanism of water injection in an operating fuel cell. As has been seen in other studies, lower pressure drops (parallel channels) and corners (serpentine channels) inhibit water removal from the flow channels. While novel, the water injection ports, where there was often a buildup of liquid water, likely influenced the transitions between flow patterns down the length of the channels. Thus, the flow pattern maps should not be evaluated quantitatively.

2.3.1 Flow patterns

In the ex-situ experiments, flow patterns were also investigated under flow conditions related to fuel cell operation. As in the in-situ case, flow patterns are dependent on the superficial gas and liquid velocities, which are related to gas flow stoichiometric ratios and current densities under active fuel cell operation. In the literature, there are various flow regimes observed in different experiments depending on the flow operating conditions, channel geometries, and liquid water introduction methods. Additionally, channel wettability largely influences the flow regimes in gas flow channels [52].

Similar to the flow regimes identified in the in-situ experiments, typical flow regimes of ex-situ two-phase flow relevant to fuel cells are shown schematically in Figure 10.

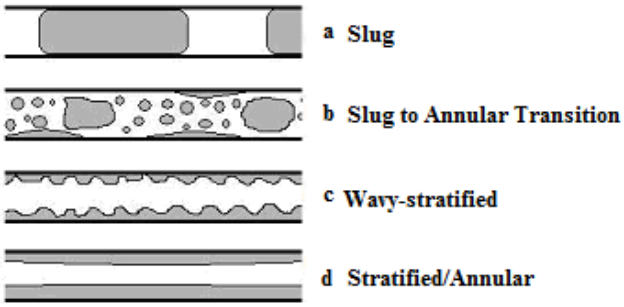

Figure 10. Flow patterns in PEM fuel cell operations a) slug flow b) transition flow from slug to annular c) wavy-stratified d) stratified (annular) flow (reprinted from Anderson et al. [2] with permission from Elsevier)

The gray in the figure represents liquid water while the clear areas represent air. Various researchers have observed the flow regimes shown in Figure 10. These include slug flow (Figure 10a) where a discrete droplet grows to or close to the size of the channel, blocking gas passage [10, 52], transition flow from slug flow to annular flow (Figure 10b) [10], wavy-stratified flow (Figure 10c) [26], and stratified (or annular) flow (Figure 10d) that occurs at high superficial gas velocities with low pressure drop fluctuations [10]. Lu et al. [56] found that at low gas velocities (typically stoichiometric ratios below 5) slugs or semi-slugs are dominant, leading to severe flow maldistribution in parallel channels and large fluctuations in pressure drop. They have also reported a mist flow, which is considered an effective way to remove water because liquid droplets are dispersed in the gas phase and removed convectively. However, mist flow requires high gas velocities, resulting in high parasitic power losses when applied to an operational fuel cell. Film flow or stratified flow is therefore considered to be the most favorable flow pattern for water removal from the gas flow channels because it requires a minimum gas velocity to achieve the desired flow pattern. As previously discussed, Trabold et al. [6] found that a superficial gas velocity of 5-6 m s^{-1} is needed to achieve this flow pattern

while Lu et al. [56] found the superficial gas velocity should be more than 3 m s^{-1}. These results are shown in Figure 11, with the main regimes being slug, film and mist flows.

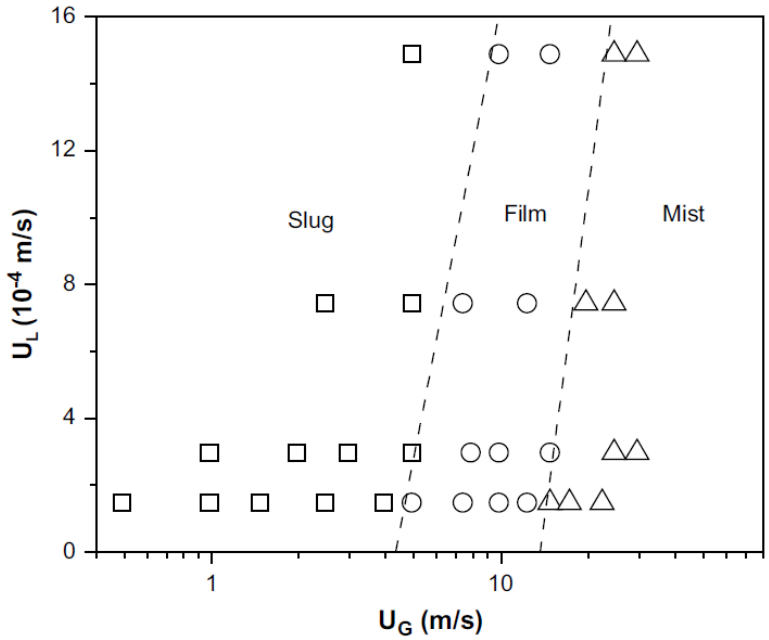

Figure 11. Ex-situ flow patterns in terms of superficial gas and liquid velocities, which change from slug flow to film flow to mist flow as the superficial gas velocity is increased (reprinted from Lu et al. [56] with permission from Elsevier)

Flow pattern maps have been generated in terms of superficial gas velocities and superficial liquid velocities for other applications as well. Examples of flow pattern maps for conventional air and water studies can be found in [58,59,60,61]. While not directly related to the conditions experienced in a PEM fuel cell, these works provide a strong framework from which PEM fuel cell two-phase flow studies can emerge. The bubbly flow pattern is not observed in PEM fuel cells due to the high ratio of gas flow rates to liquid flow rates.

Lu et al. [62] also created additional flow pattern maps in their continuing study on water management in fuel cells. An ex-situ apparatus studied hydrophilic (11^o), uncoated (85^o), and hydrophobic (116^o) channel walls, rectangular, sinusoidal, and trapezoidal channels, and vertical/horizontal orientations. Hydrophilic channels and sinusoidal

channels favor film flow, which is advantageous for operating PEM fuel cells. Vertical channels also help remove water and thus avoid maldistribution and channel flooding.

In microchannels, the surface tension, inertia, and viscosity are important parameters. These forces can be combined to form several dimensionless groups as discussed by Akbar et al. [59], which may help create dimensionless flow region maps with greater relevance to fuel cells.

2.3.2 Gas reactant flow maldistribution and hysteresis

As shown by Section 2.2.4, few attempts have been made to study fuel cell flow fields to address this critical issue due to the complexity of the flow distribution in active fuel cell flow fields. This complexity arises from a number of factors including the presence of the porous gas diffusion layer, where pressure gradients can cause leakage of reactant gas between flow channels, which is particularly relevant when serpentine flow channels are used [1]. Therefore, gas flow rates (and local stoichiometry) can differ from one end of the gas flow channels to the other and differ between channels. Uniform distribution of gas reactants in fuel cell flow fields is important for fuel cell performance, as non-uniform flow distribution can lead to performance losses and non-uniform gradients. Traditional two-phase flow studies on maldistribution in other applications (such as heat exchangers) can be found in [63,64,65]. These studies are useful references for furthering two-phase studies related to PEM fuel cells.

The gas flow rate in the entrance region of individual channels can be used as an indicator of flow distribution in the flow fields. Kandlikar et al. [40] developed an entrance region pressure drop measurement technique to determine instantaneous gas flow rates in individual channels. The method was employed in both an ex-situ and in-

situ experimental setup, and it was found that a porous GDL backing could lead to severe flow maldistribution compared to impermeable backing for the same channels. Under in-situ operating conditions, flow maldistribution was also observed due to water blockage in gas flow channels. One limitation of this method is difficult implementation in operating fuel cells. Nevertheless, it still can provide valuable information of flow maldistribution in parallel channels related to other fuel cell operating parameters such as current density, gas stoichiometry, and gas humidity in a fuel cell with specially designed introduction.

The order of changing gas flow rates also has an impact on flow distributions in parallel channels. Flow hysteresis phenomena were found when the gas flow rate was changed in an ascending or a descending manner. Flow hysteresis is also observed in minichannels bounded with porous walls [54]. In recent work by Zhang et al. [50,55] on gas-liquid flow patterns and flow distributions in two parallel channels, it was found that flow maldistribution occurred at low gas and liquid flow rates, corresponding to low gas stoichiometric ratios, where slug flow patterns were observed.

Figure 12 shows an experimental flow regime map representing the flow patterns in two parallel channels for superficial gas velocities changed in an ascending and descending manner.

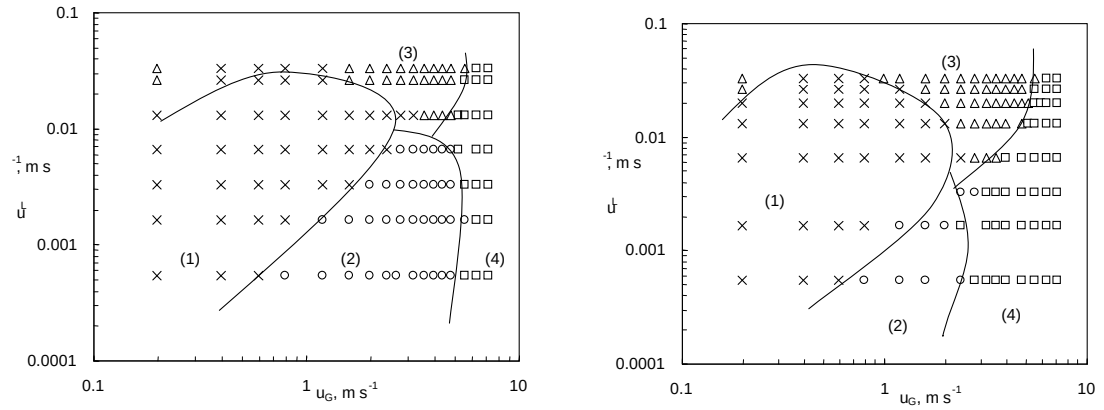

(a) (b)

Figure 12. Flow patterns in parallel channels as observed at different superficial gas velocities and liquid velocities (a) ascending approach and (b) descending approach. (1) ´: slug flow + stagnant liquid; (2) o: stratified flow + stagnant liquid; (3) Δ: slug flow in both channels; (4) : stratified flow in both channels; solid lines are drawn as guides to the eye and define boundaries between flow patterns (reprinted from Zhang et al. [55] with permission from Elsevier)

When the system starts from initial flooding conditions, stratified flow in both channels (regime 4) cannot be reached until very high gas velocities. Slug flow in both channels (regime 3) occurs at medium levels of gas flow rates and high liquid flow rates. Both regime 4 and regime 3 indicate even flow distributions. However, at low gas velocities the gas tends to go through one channel preferentially, leaving the other channel filled with liquid only, as shown in regime 1 and regime 2. This observation is consistent with previous work [66,67] that at low gas velocities both gas and liquid tend to flow in one channel of parallel channel systems, leading to a flow maldistribution. Figure 12b shows the flow pattern distribution identified with decreasing the gas velocity from a stratified flow condition. Compared to the flow patterns obtained in the gas ascending process (Figure 12a), there is a wider region for slug flow and stratified flow in both channels (regime 3 and regime 4) in the gas descending process. In addition, the region of stratified flow and stagnant liquid (regime 2) appears to be much narrower in the gas flow descending process.

Flow hysteresis and flow maldistribution are also observed from the pressure drop data shown in Figure 13, which was a study on the effect of channel inclination angle on ascending and descending pressure drops.

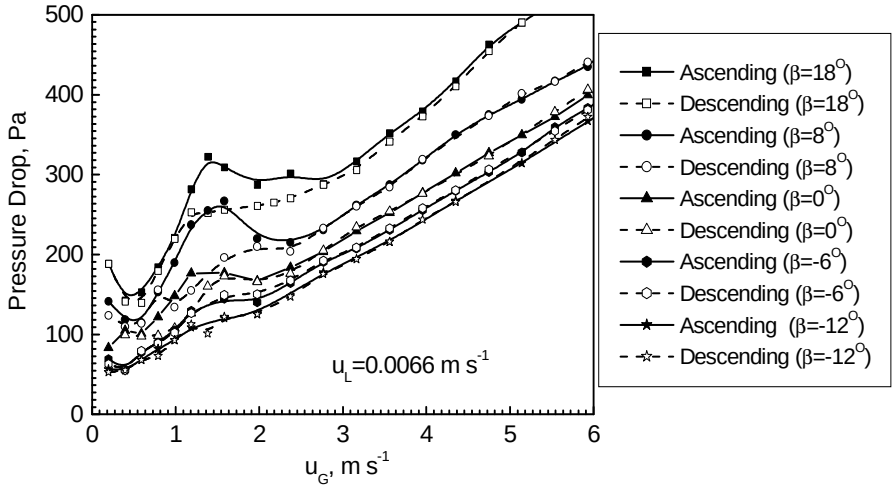

Figure 13. Effects of inclination angles on pressure drop in both ascending (gas flow increasing) and descending (gas flow decreasing) approaches (reprinted from Zhang et al. [50] with permission from Elsevier)

It is seen in Figure 13 that with an increase in inclined angles the total pressure drop increases due to the additional gravitational or static pressure drop. In general, there is a slight decrease in the pressure drop with an increase in the superficial gas velocities, followed by an increase in the pressure drop with further increasing superficial gas velocities. The occurrence of the sudden change in pressure drop indicates a transition from flow maldistribution to even distribution. It was also found that the pressure drop at the peak reflects intrinsic characteristics of the channel design and a lower value is always desirable, indicating that a lower gas flow rate is required to purge water slugs in the gas flow channels. In addition, the pressure drop hysteresis zone still exists in parallel channels inclined with a positive angle, whereas flow hysteresis disappears at negative angles with even flow distribution achieved at lower gas velocities. This result indicates

that it might be beneficial to position flow fields downwards during real fuel cell operation.

While it has been recognized that the presence of liquid slugs in the gas flow channels leads to flow maldistribution [36,51], theories or models to interpret instability-induced flow maldistribution are still lacking in the literature. An attempt was made recently to analyze the stability of possible solutions of gas and liquid flow distributions in parallel channels for fuel cells with a one-dimensional momentum balance equation across the channels [50]. All possible combinations of gas and liquid flow distributions must satisfy the equal pressure drop across all channels if they share a common inlet and outlet. Theoretically, even flow distribution is one default solution of the equal pressure drop requirement, but experimental results show that an even distribution is not always observed. Instead, flow maldistribution appears as a stable solution, indicating that flow distributions of two-phase flow in parallel channels depend on not only pressure drop but also flow stability. If the two-phase flow is operated at an unstable condition, a small perturbation will shift the flow to the nearest stable conditions. A more rigorous theoretical analysis should be conducted over a wide range of operating conditions in the future.

2.3.3 Droplet generation and removal

In the fuel cell, water can enter the gas flow channels from the gas diffusion layer (GDL) media, and the behavior of these droplets is important in understanding the development of two-phase flow. Schillberg and Kandlikar [68] provided a detailed review of water droplet detachment mechanisms, summarizing relevant operating variables such as the channel dimensions, droplet sizes, Reynolds number, GDL

properties, temperature, water introduction rate, and gas flow conditions. Their review also covered the approaches taken to study the type of flow, drag forces, and surface adhesion forces reported in the literature. A static force balance on a droplet emerging from a GDL into a flow field is given by

$$F_P + F_{shear} + F_{drag} = 0 \tag{41}$$

where F_P is the pressure force from the flow field pressure gradient, F_{shear} is the shear force exerted on the top wall by the fluid, and F_{drag} is the drag force exerted on the droplet by the bottom GDL, which is equal and opposite to the surface tension/adhesion force before the droplet detaches from the GDL [69]. If the drag force balances the adhesion force, the droplet will not be removed and the droplet is considered stable. Increasing the drag force until it is greater than the adhesion force can cause instability, allowing the droplet to be detached from the GDL. The droplet growth can increase the force of gravity or the shearing of the liquid by the gas to overcome the surface adhesion force between the droplet and the pore [68]. Kumbur et al. [69] further developed equations for these forces and provided a final macroscopic force balance containing relevant parameters such as the contact angle hysteresis (difference in advancing and receding contact angles), flow velocity, droplet height, chord length, and the channel height. The results of their analysis are in good agreement with experimental results. An important conclusion of this study is that for a constant droplet size and channel width, a lower channel height aids in droplet removal.

The liquid water droplets appear in preferential areas, rather than uniformly along the channel [48, 53, 70]. Once detached, the droplet moves along the GDL surface, where it can combine with other droplets to form slugs [71]. Also, droplets have been identified in

two categories: land-touching and non land-touching, and those that touch the lands grow faster and to a larger size [11]. The location where water droplets are first observed also changes over long operating time (3000 hrs). Observed at 161 hrs, 2036 hrs, and 3092 hrs, the emergence of droplets moved toward the exit with time [72]. However, most ex-situ two-phase flow studies are carried out over short time periods (typically < 1 hr at each data point), and conclusions drawn from these ex-situ studies on droplet dynamics may not be accurate for fuel cells with long expected lifetimes, such as 5000 hrs for cars, due to cell degradation [73]. Another ex-situ study used a permeation cell to determine the breakthrough pressure in a GDL as a function of thickness and PTFE content. The breakthrough pressure increased with both thickness and PTFE content. The inclusion of an MPL was not considered. The results also changed when the GDL was dried between trials, which could be attributed to surface degradation, micro-structural deformation, or residual nano-sized water droplets since the drying was only done at 70^{o}C. Importantly, once breakthrough occurs, water would continue to flow from the column through the GDL even without the syringe pumping in more water to maintain the same hydrostatic pressure [74].

It has been established experimentally that the droplet formation and critical detachment diameter on the cathode side GDL are a function of the air flow rate, water injection rate, and material contact angles [75]. For instance, a standard Toray carbon fiber paper (without PTFE treatment) is highly wettable, which facilitates water spreading instead of forming droplets. The static droplet behavior under hydrophilic and hydrophobic GDL conditions is schematically illustrated in Figure 14.

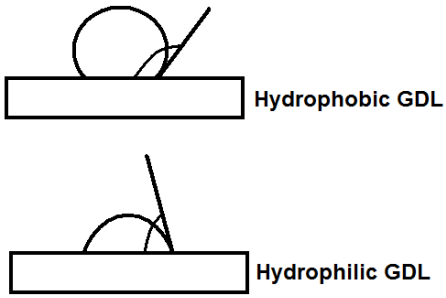

Figure 14. Effect of GDL hydrophobicity on contact angle where water spreads on a hydrophilic surface and beads on a hydrophobic surface (reprinted from Anderson et al. [2] with permission from Elsevier)

When the contact angle is less than 90^o, the surface is hydrophilic and the droplet wets the surface; when the contact angle is greater than 90^o, the surface is hydrophobic and the droplet beads up on the surface. The hydrophobic cases allow a droplet to reach a critical diameter (depending on the gas and liquid flow rates) and then detach, which is a benefit of using a PTFE treated GDL. However, when the surface is hydrophilic, the droplet does not detach and remains on the surface, blocking oxygen diffusion into the GDL and starving the electrochemical reaction. The contact angle of the channel wall is also an important parameter. Theoretically, water film formation along the channel is dictated by the Concus-Finn condition [76]:

$$\theta + \alpha < \pi / 2 \tag{42}$$

where θ is the contact angle of water on the channel and α is the half-angle formed by the channel corner. For a rectangular channel, α is equal to 45^o. The wall contact angle has to be lower than 45^o in order to achieve film formation along the flow channels. In PEM fuel cells, the channel walls are usually hydrophilic, and more hydrophilic channel surfaces are desired for proper water management since film flow is considered to be a preferable flow pattern for water removal in fuel cells.

Ous et al. [11] showed that the air velocity that caused detachment is inversely proportional to the droplet size, i.e., smaller droplets detached at higher velocities. Taller droplets are easier to remove than flatter droplets due to a greater drag force relative to the surface adhesion force. Greater deformation of the droplet decreases the surface tension between the water and carbon fiber paper, leading to detachment. Temperature is also an important variable in the droplet detachment process. As the temperature increases, the surface tension decreases, which allows droplets to be removed from the GDL at lower velocities [18]. Recently, an innovative approach used fluorescence microscopy to monitor droplet movement, where a stagnant drop on a hydrophobic GDL moved quasi-statically across the GDL with a dynamic solid surface to mimic the landing area [77]. The hydrophobic landings remove water more effectively under the landing areas, facilitating quick water detachment into the flow channel.

The effect of advancing and receding contact angles are also important. The definitions of hydrophilic and hydrophobic surfaces given above are in reference to a static droplet. However, when the air flows over the droplet, the droplet deforms and two contact angles are created. These are referred to as advancing (A) and receding (R) contact angles and are also called contact angle hysteresis, which must be considered when modeling droplet detachment from a GDL surface [13]. Polytetrafluoroethylene (PTFE) loading on the GDL causes the droplet to bead up, which can increase contact angle hysteresis and therefore more deformation occurs. A schematic of the dynamic behavior of a droplet with contact angle hysteresis is shown in Figure 15.

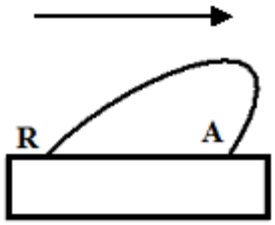

Figure 15. Contact angle hysteresis showing direction of flow and the resulting advancing and receding contact angles (reprinted from Anderson et al. [2] with permission from Elsevier)

Fang et al. [78] further showed the importance of contact angle hysteresis in a numerical simulation, where the contact angle hysteresis is found to impact slug elongation and detachment. The model agreed well with the deformation of droplets measured in microchannels.

The capillary number, which ratios the viscous forces exerted on a drop by the air to the surface tension, has been used to characterize the deformation of a droplet. The capillary number, Ca, is defined as:

$$Ca = \frac{\mu v}{\gamma} \tag{43}$$

where μ is the viscosity and v is the velocity of the continuous phase (in this case air) and γ is the interfacial surface tension. Over the range of Ca from 0.014 to 0.219, droplet deformation was studied numerically on a solid surface and it was found that the deformation was a strong function of Ca when it is large [79]. Droplet detachment can also be characterized by a critical Ca, which corresponds to the point that the advancing and receding contact angles reach an observable limit [18]. These results were studied numerically and experimentally on GDL surfaces relevant to fuel cells.

Different fabrication techniques can alter the surface roughness, which is often only reported from the manufacturer as an average value [80]. The surface roughness is especially important for channels with small hydraulic diameters (0.62-1.067 mm), as the

pressure drop and heat transfer can be increased with increased surface roughness [81]. The work of Dunbar et al. [26] suggested that the slugs of liquid water in the channels (monitored by MRI) often move from surface defect to surface defect. These findings suggest the surface roughness plays a role in two-phase flow in PEM fuel cells.

Addition of water to the anode channel can also affect cell performance. After a long time (> 1 hr) and at low current densities ($i < 0.2$ A cm^{-2}) water can move into the anode due to a concentration gradient across the membrane. Characterizing two-phase flow in the anode channel may also be important when a micro-porous layer (MPL) is used on the cathode side. The MPL on the cathode GDL can create a pressure barrier, which forces water to the anode side rather than to the cathode side [16], and this is discussed further in Section 2.4.2.1.

2.4 Water mitigation strategies

Since water in the PEM fuel cell is an unavoidable product of the electrochemical reaction between oxygen and hydrogen, water mitigation will always be an issue for PEM fuel cells. In general, even if steps are taken to avoid two-phase flow issues there is some parasitic power loss associated with implementing water mitigation strategies. The main purposes of these strategies are to maintain a water balance inside the cell and to reduce the damages associated with two-phase flow inside the flow field channels, the gas diffusion layers, and the catalyst layers (CL). Some of the methods used to improve water management are based on modifying the operating conditions of the fuel cell. The different components of a fuel cell system can also be individually designed to mitigate the overall water management issues. However, many water management approaches

lead to increased system volume and complexity, so continued study into two-phase flow and its applications to water management is still essential.

2.4.1 Operating conditions

Key operating conditions that determine the water accumulation (or water dehydration) inside a fuel cell are gas flow rates, pressure, temperature, relative humidity, and the specific current load at which the fuel cell is running.

Usually, gas flow rates are based on stoichiometry, which is defined in Eqn. 35. Since most of the water is accumulated on the cathode side of the fuel cell, much attention has been paid to the effect of high air/oxygen flow rates on the removal of water. When pure oxygen is used, the required stoichiometry is typically between 1.2 to 1.5, and when air is used the stoichiometry is 2.0 or higher [82]. Higher gas flow rates increase the cell performance, but also increase the total parasitic losses since the air compressor would consume more power [39]. Through the use of a transparent fuel cell, Liu et al. [10,83] observed how the accumulated water droplets and slugs in the flow field channels are removed efficiently when higher air flow rates are used. However, Natarajan et al. [84] demonstrated that high flow rates affect the local current densities and ohmic resistance of the membrane due to membrane dehydration.

The use of high gas flow rates can also be used in order to purge accumulated liquid water inside the channels, GDL and the catalyst layer. Normally, dry gas purging is performed for < 1 minute [85, 86] to ensure the membrane does not dehydrate excessively. Introducing humidity to the purging gas can reduce the degradation of the membrane without significantly affecting the removal of water from the cell [87]. Purging strategies have also been refined to use less power. Cho and Mench [88] studied

evaporative strategies at various flow rates with various landing width to channel width ratios (L/C). This ex-situ work led to a multi-step purge validated in-situ that varied from high to medium to low flow rates. The composite purge was able to remove as much water with time as the high flow rate purge but led to less membrane resistance and less parasitic energy consumption.

A visualization cell with 1 straight channel, 3 parallel channels, and a single serpentine channel also studied the correlation between channel flooding and voltage dynamics [89]. In each flow field design, the onset of flooding was coupled with a decline in the voltage. When the flooding plugged the entire channel, the voltage would quickly decrease. After a purge, the voltage would recover and the process would repeat. This general description applied to all the flow channel configurations, but the time and magnitude associated with the voltage decrease depended on the configuration. The single straight channel was most prone to flooding and performed worst while the serpentine channel relied on higher convective water removal in the GDL and flow channels to maintain higher performance. A schematic of the flooding and voltage response is shown in Figure 16.

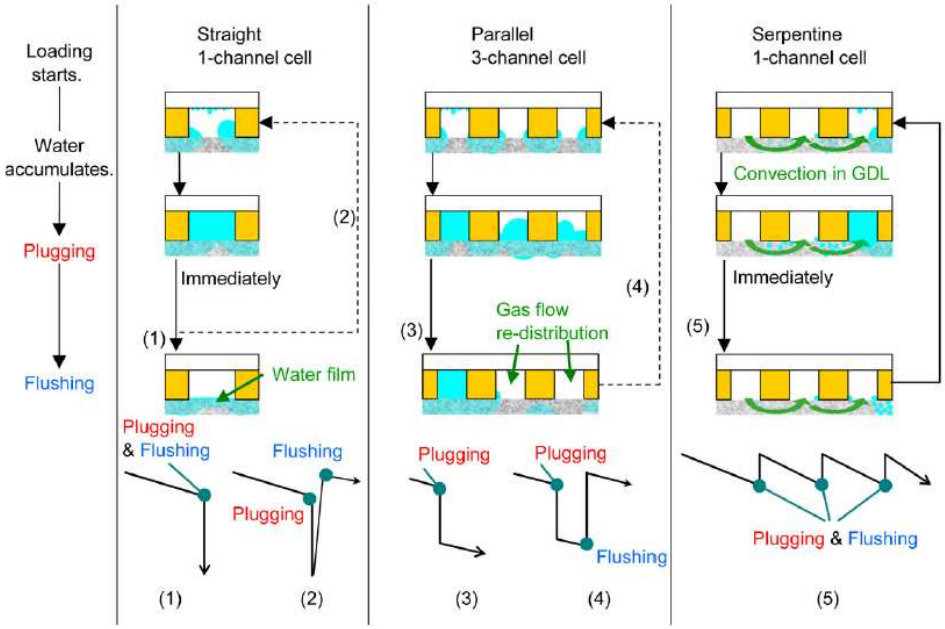

Figure 16. Schematic of channel flooding and voltage response for 3 flow channel configurations (straight 1-channel, parallel 3-channel, and serpentine 1-channel) (reprinted from Masuda et al. [89] with permission from Elsevier)

The pressure of the gases, the pressure drop within the flow field plates, and the pressure difference between the anode and cathode sides are vital parameters that can be manipulated in order to improve the water removal inside fuel cells (details about flow field designs and their pressure drops are given in Section 2.4.2.2). Anode water removal, proposed by Ballard Power Systems [90,91,92], exploits the anode pressure drop to modify the water concentration gradient across the proton exchange membrane, which increases the back diffusion rate of water from the cathode towards the anode. The pressure of the anode gas stream decreases along the flow channel at high fuel flow rates (high stoichiometries) of the fuel gas. As the hydrogen stoichiometry increases, the pressure drop draws more water from the cathode side towards the anode through the membrane. The cell voltage increases with higher fuel flow rates until a peak in performance is reached (Figure 17), where the cell's internal resistance begins to increase

with high flow rates due to membrane dehydration [91]. This topic is further explored experimentally in Chapter 6.

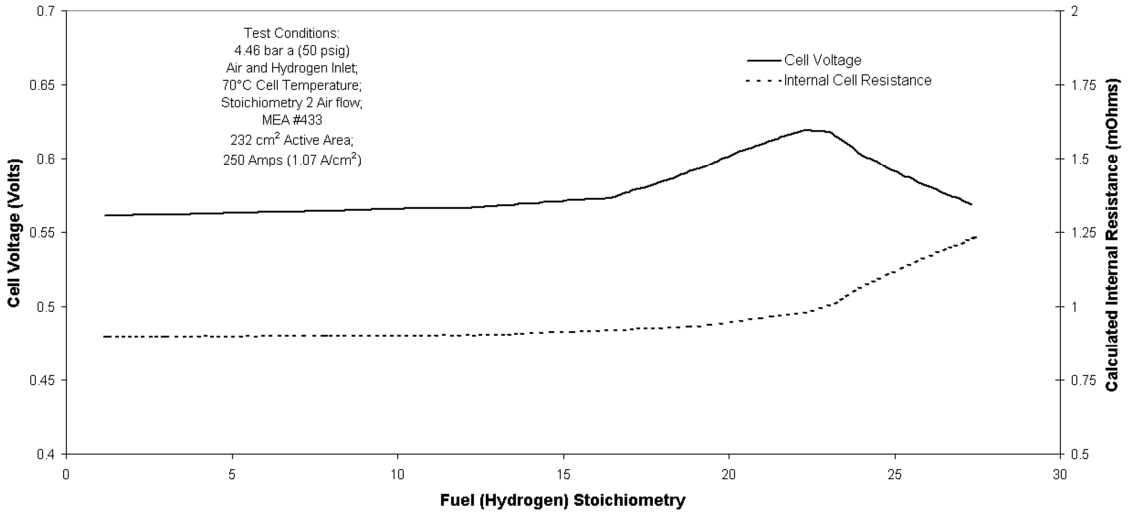

Figure 17. Example of the improvement of a single cell performance due to the anode water removal method where a high fuel flow rate increase cell voltage (reprinted from Voss et al. [91] with permission from Elsevier)

The temperature of the fuel cell has a great effect on the overall cell performance and on the water accumulation inside the flow field channels. At low temperatures, more liquid water accumulates in the channels, which blocks the air flow and decreases the cell's performance due to the lack of oxygen reaching active sites in the catalyst layer. Once the temperature is increased, the amount of liquid water in the channels is reduced since the vapour condensation rate at high temperatures is slower than at low temperatures [83]. Therefore, the flow channels are substantially less blocked with water and the cell's performance improves. In addition, when the cell temperature is increased the cathode pressure drop may decrease since there is less liquid water present in the gas diffusion layers and subsequently the flow channels [93]. Chuang et al. [94] observed that even slight changes in the cell temperature (76 to 80°C) are enough to decrease the amount of liquid water accumulated in the channels and in the GDLs, especially at high

current densities. Higher temperatures also decrease the surface tension and viscosity of liquid water, facilitating more convective water removal in the flow channels [93]. Increasing the temperature between the cathode inlet and outlet to establish a thermal gradient has been shown to be an effective method for water management as well [95]. This can be accomplished through the use of a coolant flow field that can create such temperature gradients. In general, the use of temperature gradients in order to control the water migration from one side of the membrane to the other (from low to high temperature), also referred to as thermo-osmosis, is important in resolving water management issues [96, 97]. A number of researchers have studied this temperature driven flow, but more work is needed so it can be fully understood and used efficiently in future fuel cell designs [98, 99].

The relative humidity is another important operating condition that can be manipulated to mitigate water flooding and two-phase flow inside fuel cells. Bernardi [100] discussed how the water balance in fuel cells is more sensitive to changes in the relative humidity at the inlet of the air stream than at the inlet of the fuel side, leading most studies to deal with the relative humidity on the cathode side. Büchi et al. [101] performed tests with dry gases and showed the performance of the cell was lower compared to the same cell with humidified gases. This performance loss was attributed to increased membrane resistance due to dehydration. Figure 18 shows an example of a single fuel cell with and without humidified gases. It is evident with no humidification that at high current densities (greater than 2000 mA cm^{-2}) the membrane is likely dehydrated, causing the cell performance to quickly deteriorate. Although at the mid-range current densities the cell with dry gases performs similarly to the humidified gases,

it is important to note that after prolonged hours of operation a number of failures are encountered with the dry gases (i.e., dehydration due to lack of water content in the fuel cell). As a water management control strategy, Hussaini and Wang proposed a dynamic RH control to avoiding flooding while maintaining membrane hydration [102]. In general, there should be a proper water balance inside the fuel cell, and the ideal humidity for a specific fuel cell design and operating condition(s) should be the one that achieves such balance.

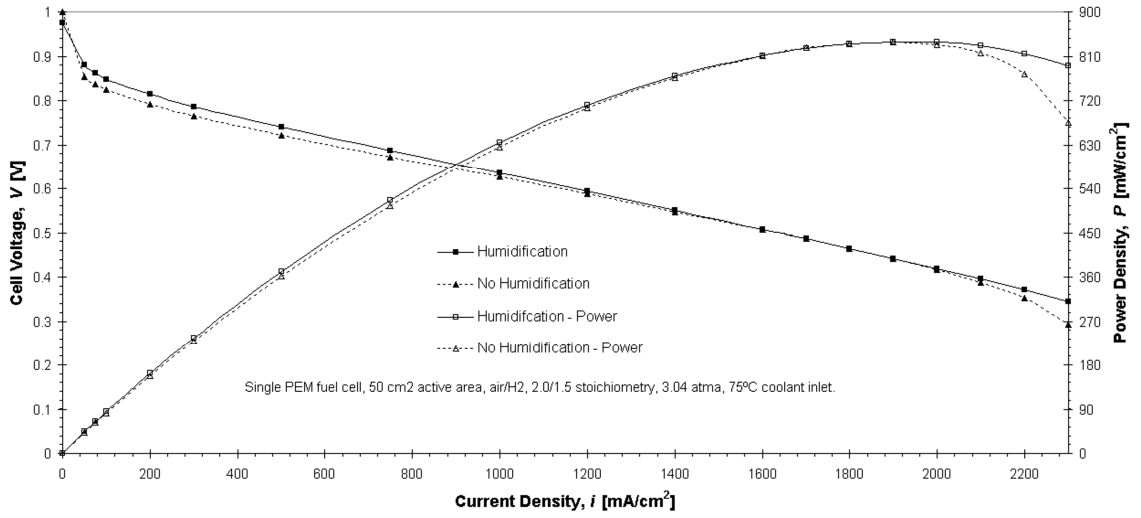

Figure 18. Comparison between humidified gases (100% relative humidity) and no humidified (dry) gases. The MEA was composed of a Gore 5510 Primea Series membrane (0.4 mg Pt cm^{-2} in each side), SGL 25 BC GDLs for both anode and cathode sides. The active area was 50 cm^2. Schematic of a typical transparent PEM Fuel Cell (reprinted from Anderson et al. [2] with permission from Elsevier)

2.4.2 Fuel cell design

Manipulating the proton exchange membrane, the catalyst layer, the gas diffusion layers, and the flow field channels to improve the overall water management inside fuel cells are all valid water mitigation strategies that have been studied and developed. The focus of this section is on the GDL, microporous layer, and flow field designs.

2.4.2.1 Gas diffusion layer design

Designing and modifying each component of the MEA is a common strategy to reduce water accumulation and two-phase flow inside the flow field channels and the whole fuel cell. Though novel methods exist for optimizing the catalyst layer and membrane for water management, this section focuses on the gas diffusion layer. Owejan et al. [103] also provided a review of the various transport mechanisms in GDLs. An example of two different GDLs is shown in Figure 19 [104], which highlights the random orientation of the carbon fibers and the relative thickness of the GDL compared to the MPL.

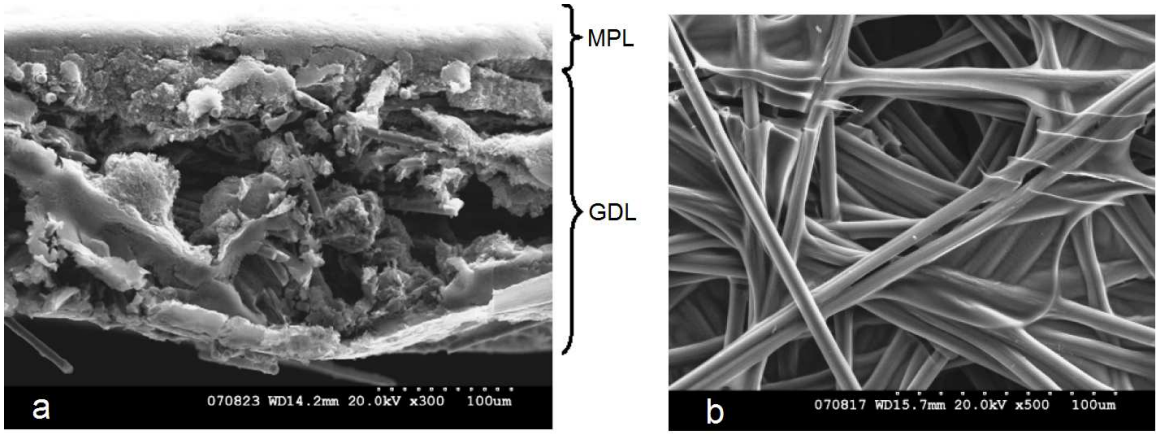

Figure 19. SGL SIGRACET 25 BC GDL(5% PTFE) showing the GDL and microporous layer (MPL) and b) plain (no PTFE) Toray TGPH-060 showing the random orientation of carbon fibers (modified from [104] with permission from Blanco)

As discussed in Section 1.3, gas diffusion layers are normally treated with an agent such as PTFE to increase hydrophobicity. For cathode GDLs, this coating is vital since most of the water produced and accumulated inside the cell exits through the cathode side. For the anode GDL, this coating is not as critical but is still important when dealing with back diffusion of water and to give more structural strength to the GDL. The most common loadings of PTFE are from 5 to 30-wt%. Lin et al. [105] did an extensive study on the effect of the PTFE content on the performance of Toray and SGL SIGRACET

carbon fiber papers. It was observed that increasing the hydrophobicity of the GDL enhanced both the gas and water transport when the fuel cell was operated with high levels of humidity. However, excessive amounts of PTFE reduced the amount of hydrophilic pores, deteriorating the water flow out of the catalyst layer and the GDL. Through the use of a transparent fuel cell, Spernjak et al. [16] observed that with treated GDLs the water produced at the cathode side emerged as droplets on the surface of the material over the entire visible area. With the untreated GDLs, water preferred to be in contact with the sidewalls of the channels, and the water formed films and slugs near the walls. This behavior caused greater water management issues and lowered gas transport towards the active areas.

Normally, the hydrophobic content in the GDLs is constant throughout; however, if certain parts of the GDL have different PTFE content, then the water behavior can be manipulated. A method to vary the PTFE content of a GDL was developed by Mathias et al. [106], leaving high and low PTFE particle density regions around the GDL. Another way of manipulating the GDL in order to overcome water issues is by varying the GDL porosity in specific areas [107]. For instance, grooves or holes can be inserted in the carbon fiber paper in areas where water flooding is a major issue [108]. The location and size of the holes depends on the current densities and the other operating conditions at which the fuel cell will be used. Using carbon cloth materials, which are more porous, in locations of greater water flooding and using carbon fiber paper in the remaining active areas can also create differences in GDL porosity. GDL modification has also been proposed as a mechanism for stabilizing fluctuations in local current density [113]. When water was directed to under the lands as opposed to under the channels, water tended to

flow in the channels on the sidewalls, which allowed for more stable current densities. Controlling the water direction was accomplished by creating a single large pore (400 μm) in the GDL. These modifications can be varied depending on the conditions, such as at low or high humidity.

The compression ratio is also a controllable parameter that can improve fuel cell performance [109]. The compression ratio is the change in MEA thickness divided by the sum of the original thickness of the CCM, anode GDL, and cathode GDL. In the compression ratio range of 10-35%, peak power was found at a compression ratio of 30% for the GDLs with and without an MPL.

Cho et al. [110] also studied voltage stability during transient responses to a change in load. The group found that aged GDLs have lower performance than new GDLs due to increased hydrophilicity in the GDL with aging. This increase in hydrophilicity leads to water 'lakes' in the GDL, which increase mass transport problems and lead to more unstable voltage signals. A similar study could be done with the anode water removal (AWR) [111] technique to see how the voltage responds with new and aged GDLs.

Visualization of the water in the flow channel has also been coupled with photographs of frozen GDL cross-sections to reveal where water is under specific operating conditions [112]. The study focused on using GDLs with a fiber orientation, which were aligned either parallel or perpendicular to the gas flow direction in the serpentine flow field channel. It was found that the perpendicular orientation had higher performance. The perpendicular orientation facilitated sidewall droplets, which facilitated water removal, while the parallel orientation created large droplets on the GDL surface. These flow patterns are due to water being removed from under the landing width with

the perpendicular fibers. With the parallel fibers, water accumulates under the land, leading to higher GDL saturation and lower electrochemical performance. These results are likely due to the direction/magnitude of cross-channel air communication through the GDL. These results are consistent with the GDL modification work (large GDL pores under the channel vs. land) by Kimball et al. [113].

Another strategy for improving the water transport inside fuel cells is by using a thin microporous layer (MPL) on the surface of the GDL that faces the catalyst layer and the membrane. This layer is made with carbon black particles and PTFE (i.e., the layer is hydrophobic), and is usually deposited only on one side of the GDL surfaces, forming a double-layer diffusion layer. The MPL forms smaller pores and acts as another mechanism to reject water, which is critical when the fuel cell is operated at high humidity levels [114]. Microporous layers are now commonly used to improve the overall performance and voltage stability of fuel cells [115].

However, it is still unclear exactly how the MPL affects the water transport mechanism inside the GDL and the MEA. Kim et al. [119] used electrochemical impedance spectroscopy to study the effect of the MPL by analyzing the cases where the anode and cathode both had an MPL, only the cathode had an MPL, and neither anode nor cathode had an MPL. These results were coupled with water collection to determine the crossover rate. These results showed that the MPL on the cathode only pushed more water from the cathode to the anode. This result is due to the small pore radius and high hydrophobicity, which increases the capillary pressure on the cathode, creating a pressure differential between anode and cathode. Neutron radiography has also validated the role of the MPL as a barrier to water transport when using serpentine flow channels. At

current densities of 750 and 1000 mA cm^{-2}, not all of the water could pass through the MPL and water was forced toward the anode [116]. Sasabe et al. [117] also found this conclusion by soft X-ray radiography with parallel channels. The MPL functioned as a capillary barrier that prevented liquid water in the large pores of the GDL from reaching the hydrophilic catalyst layer. A carbon cloth GDL was also examined with an MPL and had better performance than the carbon fiber paper GDL with MPL. This result was due to water concentrating at the weaves (large pores) of the carbon cloth, which allowed for effective water removal and diffusion of oxygen through the small pores of the cloth fibers. An important result from Owejan et al. [118] showed that the influence of the MPL was to allow water vapor to pass from the cathode catalyst layer toward the cathode flow field channel but also act as a liquid water barrier to prevent condensed water in the GDL from reaching the catalyst layer. The thermal conductivity of the GDL thus played a central role, where temperature gradients across the GDL ranged from 2 to 9 K at high current densities depending on the specific GDL used. Kim et al. [119] provide a table with different experimental/modeling approaches to determining the role of the MPL, along with qualifying comments where appropriate. More experimental work is necessary in order to investigate how the MPL helps the performance of the fuel cell [120].

Figure 20 shows the performance of a fuel cell with and without an MPL on the cathode GDL. It is obvious that at most current densities (and at the peak power density) the MPL has a significant influence on the performance of the cell due to improved water removal and management.

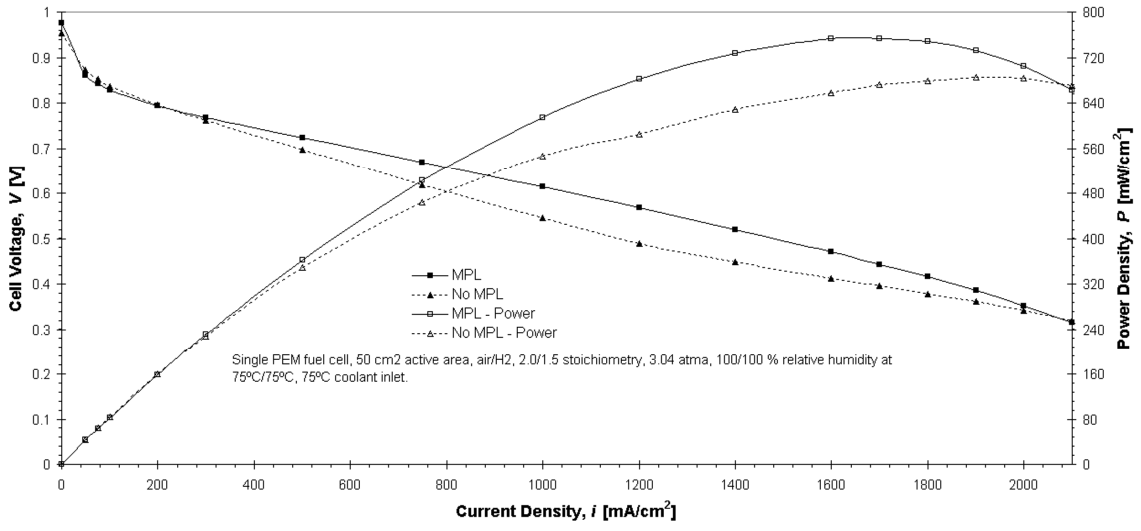

Figure 20. Comparison between gas diffusion layers (GDLs) with and without micro-porous layers. The MEA was composed of a Gore 5510 Primea Series membrane (0.4 mg Pt cm^{-2} in each side), SGL 25 BD GDL for the anode side, and the cathode GDLs were SGL 25BC (with MPL) and 25BA (without MPL). The active area was 50 cm^2. Schematic of a typical transparent PEM Fuel Cell (reprinted from Anderson et al. [2] with permission from Elsevier)

The hydrophobic particles in the MPL can be distributed along the GDL surface such that certain areas have more (or less) hydrophobicity, creating a gradient that can manipulate the water transport. Chen et al. [120] designed a non-uniform MPL that was able to keep the relative humidity inside the whole MEA stable within a specific range instead of letting it increase between the inlet and outlet regions. Thus, the proton exchange membrane was kept uniformly hydrated, which resulted in superior performance at high current densities.

Another approach to MPL design is to create a microstructure in the MPL and spray catalyst onto this layer. This increase in available surface area allows performance to increase at higher current densities because the water surface inside the catalyst layer can extend more towards the MPL [121]. The MPL may also benefit this process by not letting condensed water in the GDL reach these sites as well [116,117].

In addition to MPLs, liquid water barriers have also been used to extend the fuel cell's operating time under dry conditions (no humidity for the anode or cathode gases) [122]. A stainless steel sheet with perforations placed between the GDL and flow field channel was able to increase cell lifetime by ~ 5 hours. This is significant as the cell voltage approached zero after ~1.5 hrs when the GDL had no MPL and ~2 hrs when the GDL did have an MPL. These barriers exacerbated flooding in the dry cell, which allowed for better catalyst layer and membrane hydration and thus longer operating times. The material and design (number of holes, open area) of the liquid water barriers need further optimization before its full potential is realized.

2.4.2.2 Flow field design and configuration

The flow field channels distribute the reactant gases over the electrode surfaces as uniformly as possible in order to utilize as much of the active catalyst area as possible. These channels also have to collect and remove the product water in order to minimize any water flooding. In addition, the flow fields have fixed channel geometries and fixed active areas, which determine the reactant flow characteristics over the operating range of the fuel cell.

The most common flow field designs are parallel, serpentine, and interdigitated channels [123,124,125,126]. The parallel design is made of a number of straight channels connected to common inlet and outlet headers. One issue associated with this design is that the pressure drop is too low to remove the water, and water tends to accumulate in the channels [82,124]. This issue leads to the maldistribution of the reactant gases in the flow field, causing reactant starvation in some channels and an excess of reactant in other channels.

Serpentine flow fields have one or more continuous channels connected to an inlet and outlet header and typically follow a path with several bends. These flow fields generally have longer channel lengths and a greater pressure drop along the channels due to the bends, which facilitates water removal. Multiple serpentine channels are used for large active areas in order to avoid excessively high pressure drops [125]. Li et al. [127] presented a method for designing serpentine flow fields based on an appropriate flow channel pressure drop so that all of the liquid water is evaporated and removed from the cell through the flow fields. However, it is important to note that the cells designed through this method exhibited inferior performance compared to similar cells found in the literature and that the pressure drop can result in a significant parasitic loss for the fuel cell system. New serpentine flow fields can also be designed in light of recent results in two-phase flow literature. Donaldson et al. [128] studied the radius of curvature of the serpentine channel bend in an air-water system where liquid water was the continuous phase. Though this phase configuration is opposite that of the PEM fuel cell flow channel, the results indicate that the Weber number can be used to determine bubble breakup and that a smaller radius of curvature enhanced breakup. Similar studies should be pursued in systems more relevant to PEM fuel cells to aid in the design of serpentine channels, especially considering flooding often occurs in the bends of the flow channels.

In interdigitated (or discontinuous) flow fields, there are a number of parallel discontinuous channels (i.e., the channels are discontinuous from the inlet header to the outlet header). The reactant gases are forced to flow through the porous GDL in order to reach the channels connected to the outlet manifolds. Since the gases are forced along a short path through the GDL and catalyst layer, the liquid water is removed more

efficiently, resulting in better performance at higher current densities. However, these flow fields do not remove the water located at the inlet of the channels properly, and the voltage stability at low loads (current densities) is very poor [126]. In general, this flow field type is most ideal for high current densities, but it increases the parasitic losses due to larger pressure drops.

It is important to note that the direction in which the flow fields (coolant included) of a fuel cell are placed also has an influence on the overall water management and performance of the cell. Depending on the application, it may be desirable for the coolest region of the coolant channels to coincide with the area in which the oxygen concentration in the cathode channels is the highest and where there is the least amount of water in the cell. Wilkinson et al. [95] used this approach to create a thermal gradient from cathode inlet to outlet to keep the product water in the vapor phase. They also operated a fuel cell with dry gases by using the cathode and coolant flow field in co-flow and the anode in counter-flow. Similarly, cross-flow operation between the fuel and the oxidant channels may be preferred to co-flow or counter-flow configurations (see Figure 21).

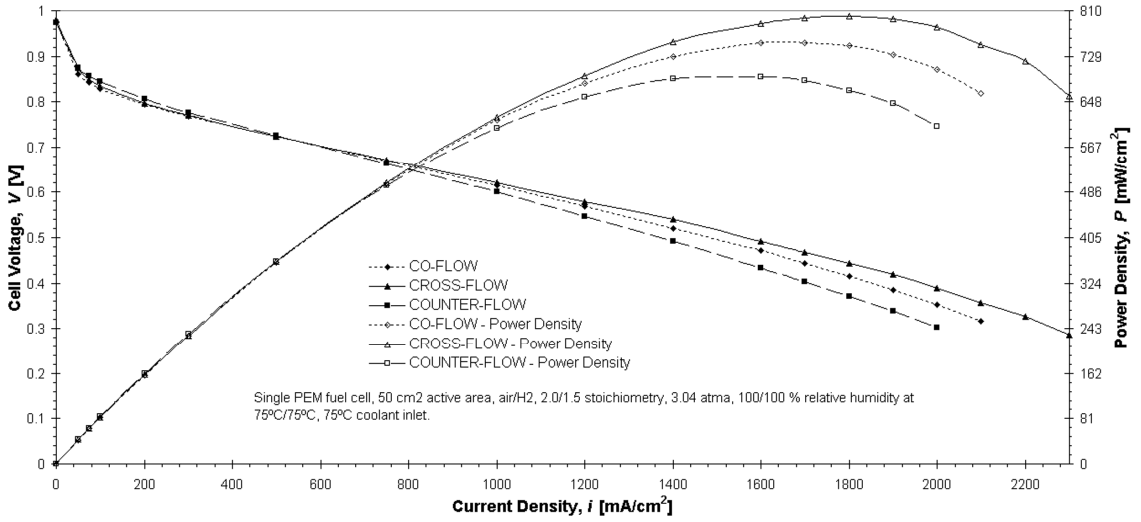

Figure 21. Comparison between co-flow, cross-flow and counter-flow configurations between the anode and cathode flow fields. The MEA was composed of a Gore 5510 Primea Series membrane (0.4 mg Pt cm^{-2} in each side), SGL 25 DC GDL for the anode and SGL 25 BC GDL for the cathode. The active area was 50 cm^2. Schematic of a typical transparent PEM Fuel Cell (reprinted from Anderson et al. [2] with permission from Elsevier)

The cross sectional shape of the flow field channels also plays a key role in the effective water removal inside the flow field plates. For example, Trabold et al. [129,130] demonstrated how triangular shaped flow field channels can have designated localized water collection regions. The water then accumulates away from the gas diffusion layer, which allows more gas to reach the catalyst layer. In addition, the cross section of the channels can be designed to change gradually along the length of the channel, modifying the pressure drop and gas distribution along the active area [131]. Johnson et al. [132] developed a differential pressure flow field for water removal by changing the shape of the flow field channels with respect to each other. In micro-fuel cells, Metz et al. [133,134] developed a passive water management system by using capillary microstructures as flow field channels in the cathode plate. These channels are hydrophilic with a tapered cross-section, allowing them to remove liquid water from the GDL.

The flow field channels can also be modified with respect to their hydrophobicity. Hydrophilic channels may improve the transport of gases to the reactant sites by facilitating the water transport on the edges and surfaces of the channels [200]. However, very hydrophilic channels result in greater pressure drops due to liquid water blockage. The wetting capabilities of the channels can be modified by using different cross-sectional geometries or by altering the surface characteristics of the bipolar plate materials [135], as discussed in Section 2.3.3.

2.5 Summary and outlook

Water management is a critical issue to PEM fuel cell performance and has received substantial attention in the literature. This review focused specifically on water management related to gas-water flow in the flow field channels.

Visualization cells allow an observer to see the liquid water form and serve as a basis for understanding and characterizing two-phase flow in fuel cells. However, the results are often mainly specific to a given system. Often, the specific contact angles for the flow field plate, GDL material, and transparent plate of a visualization cell are dissimilar to those in a typical graphite bipolar plate fuel cell. Since surface properties are important to two-phase flow on this scale, the specificity of the results must be considered. Steps should be taken, perhaps through dimensionless correlations, to make the results of these novel systems applicable to other fuel cells.

In-situ studies have covered a wide range of variables including the PTFE content of the GDL, the inclusion of an MPL, flow field design, reactant gas stoichiometry, gas relative humidity, and temperature. While the influence of these parameters on fuel cell performance has been well documented, less attention has been paid to the flow field

channel hydrodynamics. Thorough analysis of the channel hydrodynamics is still lacking in terms of two-phase flow regimes, two-phase flow distribution, and two-phase pressure drop. These studies are important because the flow regime affects the behavior of the water and access of reactant to the catalyst sites, and a large two-phase pressure drop represents a parasitic power loss in fuel cell operation. Furthermore, flow maldistribution must be considered as some flow field channels may receive insufficient reactant for the electrochemical reaction, causing starvation and underutilization of the active catalyst area. Hydrodynamics will thus play an increasingly important role in PEM fuel cell water management studies.

The current ex-situ experimental studies have been carried out to understand flow distributions, pressure drop, flow patterns, droplet formation, and water removal in flow field channels under flow conditions relevant to fuel cell operation. In the literature, typical two-phase flow patterns found in ex-situ experiments are slug flow, slug to stratified flow, and stratified/annular flow. Among those, stratified flow or annular flow is desirable in terms of water management and operating stability of a real fuel cell. Slug flow should be avoided in operation since it can lead to channel blockage and flooding as well as pressure fluctuations. Therefore, high gas stoichiometry is required to achieve the desired flow pattern. Flow instability, flow maldistribution, and flow hysteresis have been found in both ex-situ and in-situ studies on two-phase flow in parallel channels due to many factors such as channel geometry, intrusion of the compressed GDL in channels, and gas/liquid flow rates. In order to achieve even flow distribution and to overcome flow hysteresis phenomena, high gas velocities are desirable. However, high gas flows are not desirable in practical systems because of the parasitic power loss.

A unique aspect of two-phase flow phenomena in fuel cell flow fields is that the liquid water emerges from porous GDLs and accumulates along the flow channels. Therefore, the two-phase flow pressure drop of such flow systems is not accurately predicted by most of the existing correlations or models. Consequently, these correlations should be revisited for two-phase flow in the fuel cell. There has been some success in obtaining information on instantaneous gas flow rates in individual channels through an entrance pressure drop measurement technique. However, extensive studies are still required to be related to a broader range of operating conditions such as channel dimensions, gas and liquid flow rates (corresponding to current density and gas stoichiometry), and channel surface properties. In addition, a theoretical foundation to elucidate flow distribution in parallel channels is lacking, especially for two-phase flow.

In order to avoid or reduce water management issues inside the fuel cell, a number of water mitigation strategies have been developed. Some of these methods consist of varying the operating conditions of the fuel cell (e.g., temperature, pressure, relative humidities, etc.) or designing the different components inside the cell for water management. Unfortunately, there are no water mitigation methods to date that can deal with water management effectively without affecting other components, especially the membrane and catalyst layers. Thus, more research has to be performed in order to achieve ideal designs and mitigation strategies specific for certain operating conditions and fuel cell applications.

Overall, water management studies are shifting from parametrically based studies that couple water behavior with overall fuel cell performance to specific studies on water management in the catalyst layer, GDL, and flow field channels. These more specific

studies provide an understanding of the hydrodynamics in a fuel cell. To study the two-phase flow in PEM fuel cell flow field channels, work must continue in all of the major research areas: ex-situ approaches, in-situ testing, and numerical simulation. A combined effort of ex-situ and in-situ experiments can help to validate current numerical simulations and help numerical simulations more accurately reflect the actual two-phase flow phenomena that occur. A greater understanding of two-phase flows experimentally and numerically will allow more effective water management strategies to be developed and implemented. Specific areas that need to be better understood include work on flow patterns, pressure drops, flow maldistribution, and two-phase flow hysteresis. Improvements in these areas will eventually lead to higher overall PEM fuel cell performance and efficiency, making the PEM fuel cell a more viable technology for the future.

2.6 Research objectives and thesis layout

It is clear from the literature review that PEM fuel cell water management is an active and important area of research. This work focuses on these issues by addressing the hydrodynamics in the cathode flow field channels, investigating the specific two-phase flow phenomenon of pressure drop hysteresis, and exploring the anode water removal method to diagnose cathode GDL flooding. The specific aims and parameters in these studies are explained here.

To establish a relevant baseline, this work firstly aims at understanding the hydrodynamics of air and liquid water in the cathode flow field channels, and the following central question was posed:

1. What are the relevant hydrodynamics in an operating and non-operating PEM fuel cell based on flow rates (stoichiometry), GDL properties, and temperature?

The parameters listed in this question have an effect on the two-phase flow pressure drop and the two-phase flow patterns. Specific considerations include measuring and predicting (via the Lockhart-Martinelli approach) the two-phase pressure drop. This overall hydrodynamic characterization is done in conjunction with the following more specific question relating to two-phase flow in PEM fuel cell flow channels:

2. What is the mechanism of pressure drop hysteresis in a PEM fuel cell and how does it change with respect to main fuel cell operating parameters such as GDL, air flow rate, and temperature?

Pressure drop hysteresis is the central topic of Chapter 4 and Chapter 5. Chapter 4 focuses on a non-operating (ex-situ) approach where water is injected externally (not produced electrochemically) to simplify the system to better understand the fundamental hydrodynamics. Section 4.1 focuses on ambient temperature and pressure conditions with dry air, while Section 4.2 focuses on temperatures and relative humidities relevant to operating PEM fuel cells. Chapter 5 studies this topic in the operating PEM fuel cell where water is produced electrochemically. Other studies relevant to pressure drop hysteresis are examined as well in these chapters.

The second specific topic related to PEM fuel cell water management investigates the anode water removal method (AWR), and the results are explained in Chapter 6. The central question this study aims to answer is:

3. How can AWR be used to understand cathode GDL flooding in a PEM fuel cell?

A series of tests were performed varying relevant variables in the AWR process, including: cathode relative humidity, GDL properties, and temperature. To further explore this method, flooding was intentionally exacerbated in the GDL layer and flow field channel by placing an extra GDL on the cathode side and injecting water into the flow field channel, respectively. Through this combination of tests, it was determined that AWR is strongly suited to determine when cathode GDL flooding is lowering PEM fuel cell performance.

Chapter 7 presents conclusions and recommendations. The recommendations focus on specific considerations for pressure drop hysteresis, anode water removal, and overall water management in PEM fuel cells.

Schematically, the thesis is shown in Figure 22.

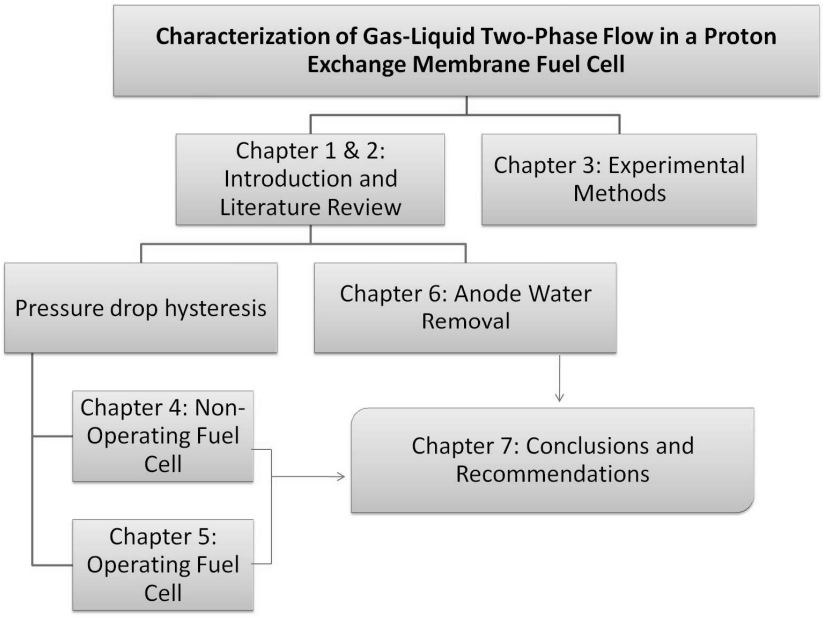

Figure 22. Thesis outline of 'Characterization of Gas-Liquid Two-Phase Flow in a Proton Exchange Membrane Fuel Cell'

3 Experimental approach

This chapter first focuses on the visualization fuel cell designed for the pressure drop hysteresis study. It then discusses the experimental approaches for the non-operating cold model, the non-operating hot model, and the operating PEM fuel cell, all of which relate to pressure drop hysteresis. The last section explains the experimental approach to anode water removal.

3.1 Visualization fuel cell design

A novel diagnostic fuel cell was designed, and fabrication was completed by Tandem Technologies Ltd. and VACCO Industries Inc (flow field plates). An exploded view of the fuel cell is shown in Figure 23.

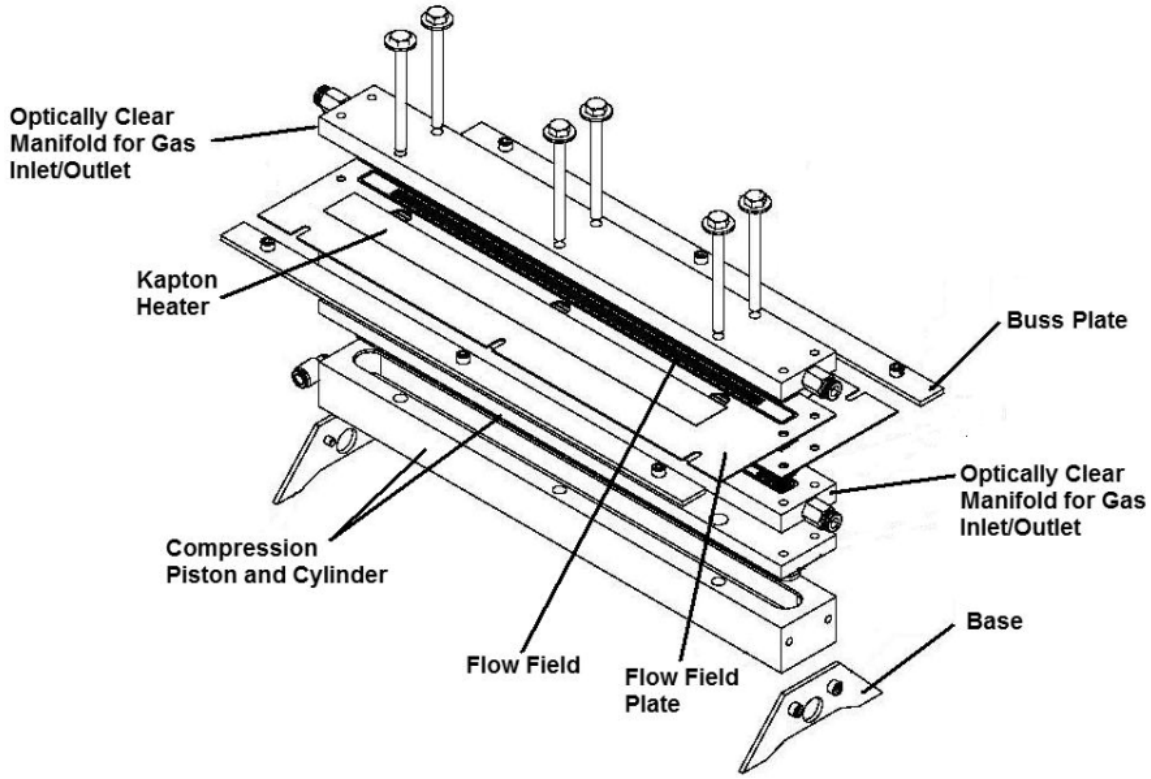

Figure 23. Visualization PEM fuel cell schematic showing an exploded view of all relevant components

The anode and cathode flow field design incorporates 4 parallel channels with dimensions 1 mm x 1 mm x 300 mm. Each flow-field plate is identical and is made of

stainless steel, which is then coated with 5 microns of gold on top of 2 microns of silver. These materials are typical of visualization fuel cells [2]. Etching through the 1mm thick piece of stainless steel creates the 1 mm x 1 mm flow field channels. The length of each flow-field channel is 300 mm. At the beginning and end of the flow field channel are 20 mm long half-etched grooves, which correspond to the gas entrance areas in the manifold above. This area helps facilitate fully developed flow upon entering the flow channels and also serves as the exit connection to the manifold. Thus, the total length of the cell is 378 mm. The landing widths, which contact the GDL for current collection, are also 1 mm wide. A 2 mm seal groove runs around the four channels, which defines the active MEA area, which is 35.7 cm^2. These components are shown in Figure 24. MEA fabrication is detailed in Appendix B.1.

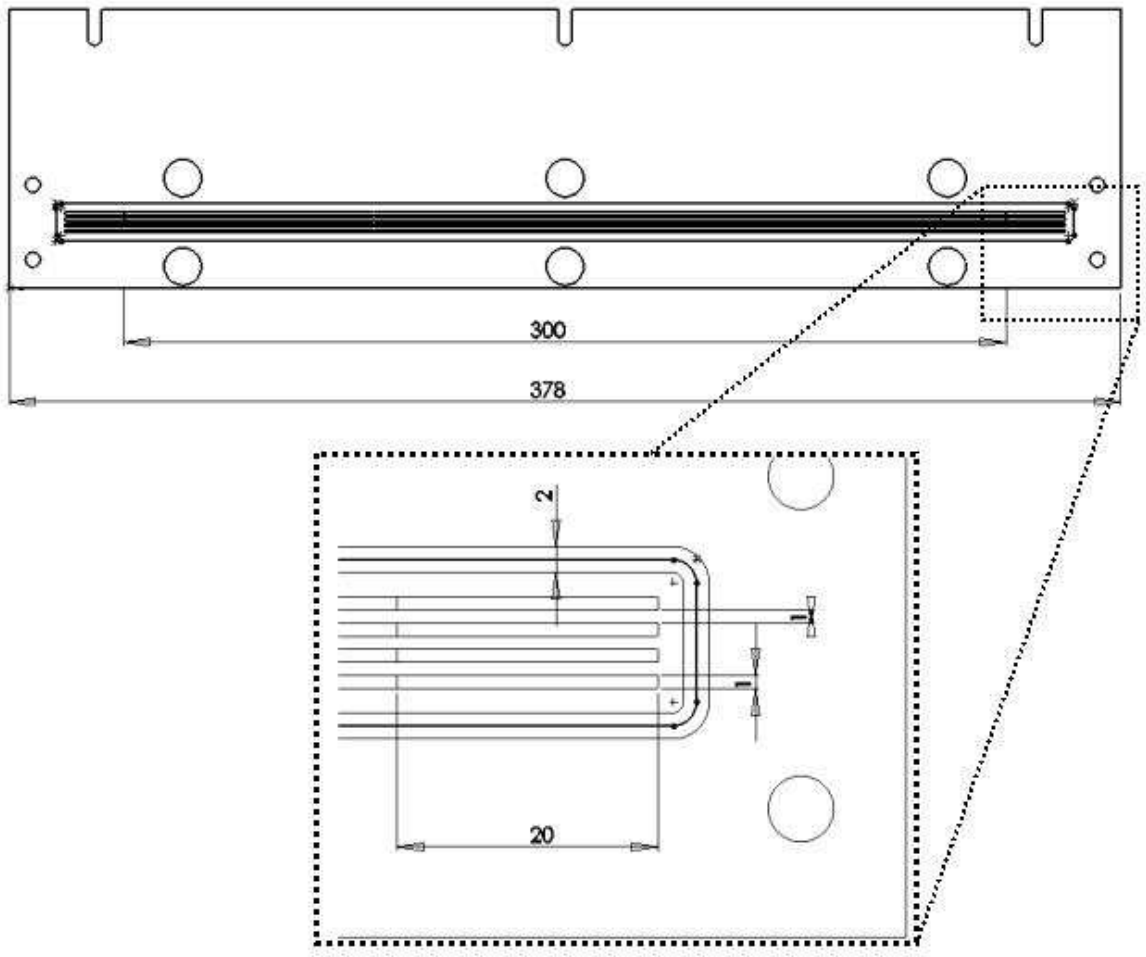

Figure 24. Flow field design showing the overall plate with the entrance area zoomed in to show the channel dimensions and flow development region that contacts the manifold entrance (all measurements are in millimeters)

The anode and cathode manifolds are identical pieces of acrylic, which allow them to be optically transparent to thus allow visualization into the cell. The visualization fuel cell was utilized to observe two-phase flow in the cathode flow field channels. A Pixelink PL-A774 camera with an Edmund Optics VZM 300 lens and a MI-150 high intensity illumination system was used to capture images of the two-phase flow. The manifold is shown in Figure 25.

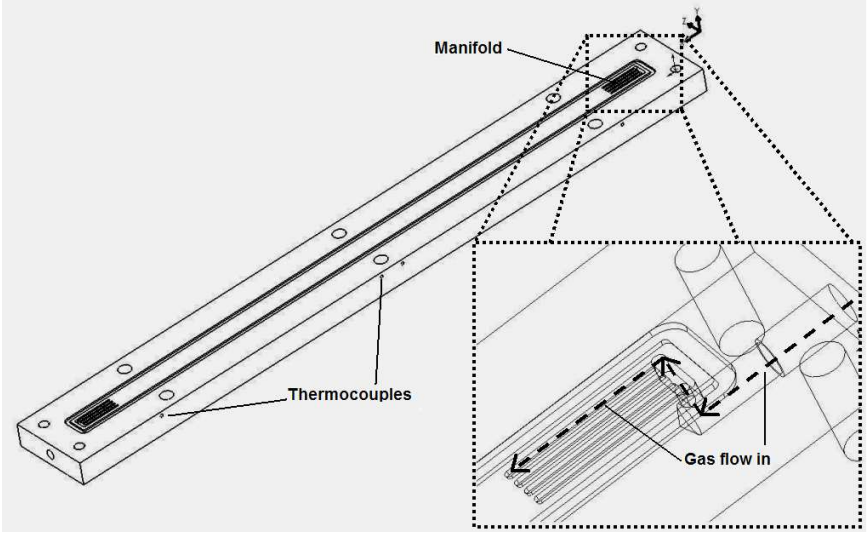

Figure 25. Transparent manifold for anode and cathode showing the gas entrance region and thermocouple ports

The reactant gases enter via a common inlet, which has been magnified in Figure 25. The manifold then contains four channels, which distribute the gases individually to the flow channels' entrance area in the flow-field plates (as described above in Figure 24). The dashed arrows show the path of the gas. The manifold also contains four ports for thermocouples, which are used to measure an approximate temperature in the flow field: one in the entrance, two in the middle evenly spaced around the compression screws, and one at the exit.

Kapton heaters (Omega KH Series) are added to the external area of each flow field plate to ensure proper heating. Each plate has two heaters, one on each side, which connect to a common connection for use in the test station. The test station controllers are able to keep these heaters at a set point based on a thermocouple in the flow field buss plate

Compression is obtained with a piston and cylinder system. Nitrogen displaces the piston upward over the base of the cell. Six bolts that screw directly into the compression cylinder after passing through the manifolds and flow field plates also hold the cell

together. The guide rods ensure proper alignment of all the components. Finally, an additional steel bar is placed on top of the cathode manifold (not shown) so the acrylic manifold does not crack under compression. The bar is machined so the flow channels are still completely visualized. For the non-operating experiments, a compression pressure of 105 psig is used, while for the operating experiments, a compression pressure of 90 psig is used. The reduced pressure helps minimize damage to the membrane. The operating compression pressure was obtained experimentally by plotting the voltage and overall resistance vs. the compression pressure, shown in Figure 26.

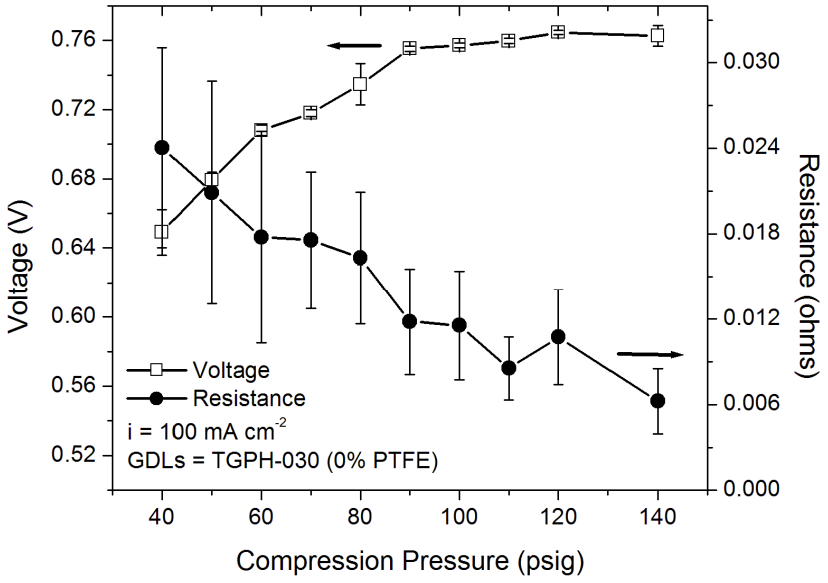

Figure 26. Cell voltage and resistance at constant current vs. compression pressure to determine the ideal compression pressure (TGPH-030 GDLs)

Above 90 psig, there is little gain in electrochemical performance with increased compression. Also, an attempt was made to minimize the compression pressure to ensure the manifold would not be overstressed, which could lead to manifold damage.

A buss plate is used for current collection and can be easily added/removed to/from the cell to simplify cell assembly. Current can be collected at three locations along the length of the channel (entrance, middle, exit). These also correspond to the areas in the

manifold where the temperature is monitored. For simpler setup in the test station, the current is collected at the exit location.

The actual assembled cell is shown in Figure 27. This fuel cell was used in all pressure drop hysteresis studies, the results of which are in Chapter 4 and Chapter 5.

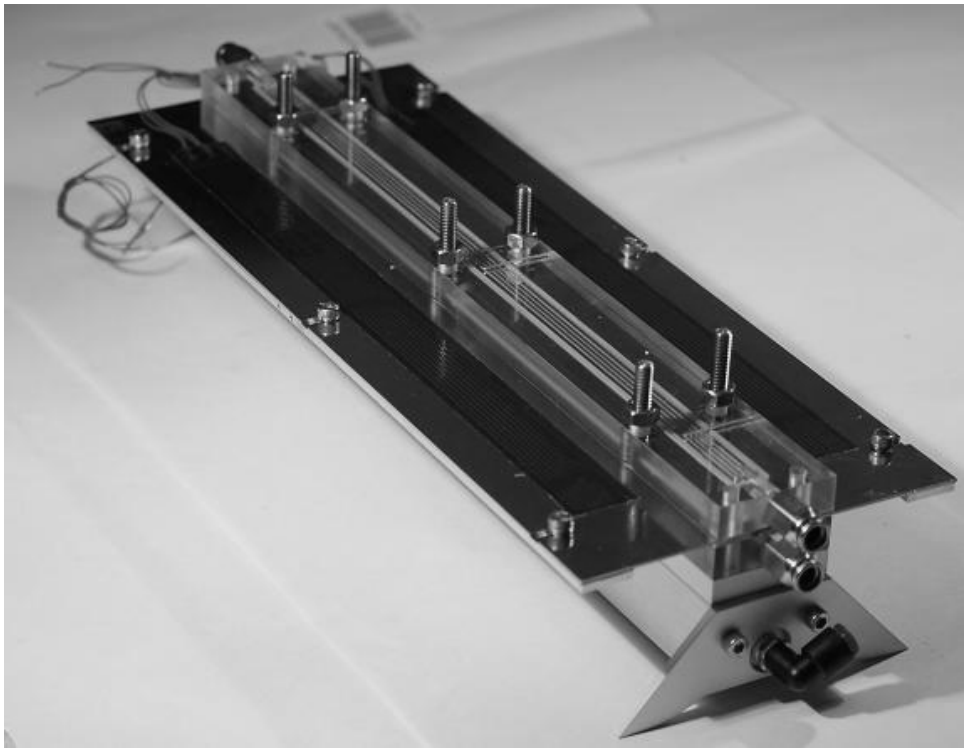

Figure 27. Assembled visualization fuel cell from the schematic in Figure 23

3.2 Pressure drop hysteresis testing: Non-operating cold model

These experimental conditions were used for the tests in Section 4.2. The non-operating cold model cell was run at ambient temperature (hence 'cold model'), the cathode exit was at atmospheric pressure, and the cell was compressed to 105 psig. Air (Praxair Al 0.0XD Extra Dry) was not humidified or heated, with its flow rate controlled by a rotameter and measured by a digital mass flow meter (AALBORG GFM17; 0-5 SLPM). The air entered the cathode manifold where it was distributed to the flow field channels before leaving from the cathode manifold exit. A GDL was placed between the

anode and cathode flow field plates to mimic the actual water injection methods and surface properties of an operational fuel cell. The water was pumped into the anode flow field via a syringe pump (Cole-Parmer 780100C), and it then was forced through the GDL as the syringe pumped at a given volumetric flow rate (mL hr^{-1}). The anode exit was closed, allowing the water pumped into the anode to reach the cathode. A schematic of the non-operational experimental setup is shown in Figure 28.

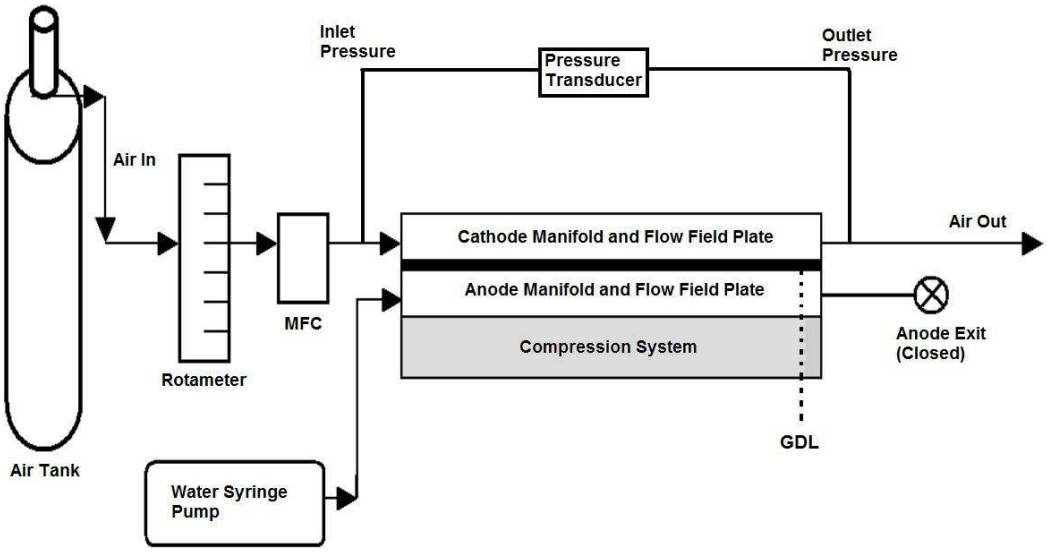

Figure 28. Non-operating cold model experimental setup where the anode flow field channels are utilized as a chamber to inject water through a GDL into the cathode flow field channels, simulating electrochemical water production (reprinted from Anderson et al. [142] with permission from Elsevier)

The GDLs and relevant specifications considered in this set of experiments are shown in Table 3. These vary the inclusion of a microporous layer, PTFE content, and thickness.

Table 3 Gas diffusion layers and specifications relating to MPL inclusion, PTFE content, and thickness (reprinted from Anderson et al. [142] with permission from Elsevier)

Company	GDL	MPL	PTFE Content	Thickness (μm)
SGL Carbon	25 BC	Yes	5%	235
SGL Carbon	25 BA	No	5%	190
SGL Carbon	25 DC	Yes	20%	231
Toray	TGPH-030	No	20%	110
Toray	TGPH-030	No	0%	110

Faraday's Law governs the water injection rate and needed gas flow rates at each current density, as discussed in Section 1.4. In this way, the corresponding water injection rate and necessary cathode air flow rate were set for a given simulated current density (simulated since the cell is not electrochemically active). To determine the needed air flow rate from the needed oxygen flow rate, the oxygen flow rate is divided by the concentration of oxygen in air (0.21). The air stoichiometry, λ_{air}, was utilized to define the actual gas flow rate. For example, a stoichiometry of 2 uses the same liquid water injection rate at a given current density as a stoichiometry of 1, but with twice the air flow. All stoichiometries here refer only to air on the cathode side (no hydrogen was used in the non-operating tests). Table 4 shows the water production rates associated with each current density typically used in these experiments for an active cell area of 35.7 cm^2.

Table 4 Water injection rates for simulated current densities based on an active area of 35.7 cm^2 (reprinted from Anderson et al. [142] with permission from Elsevier)

Current Density ($mA\ cm^{-2}$)	Volumetric liquid water injection rate ($mL\ hr^{-1}$)
50	0.6
100	1.2
200	2.5
400	4.9
600	7.4
800	9.9

The air flow rate and water injection rates for the simulated current densities in Table 4 were run in both an ascending and descending manner to determine the extent of hysteresis in the two-phase pressure drop. In each case, the gas was first increased in the ascending manner and then decreased along the same path. The term ascending approach describes the path by which the simulated current density is increased, which is as

follows: 50, 100, 200, 400, 600, 800 mA cm^{-2}. The descending approach is this path in reverse, which is: 600, 400, 200, 100, 50 mA cm^{-2}. The flows at each current density were held for approximately 8 minutes (approximate due to manually changing the flow rate of air and water), which gives the pressure drop sufficient time to reach a steady state. An Omega 164PC01D37 pressure transducer (0-2,500 Pa) was used to measure the cathode flow channels' pressure drop. The single-phase pressure drop is from the same gas flows but without the water injection.

This experimental setup was used to study pressure drop hysteresis in terms of: the air stoichiometry, the GDL properties, the range of current densities, the effect of decreasing step size, and the effect of initial state (dry vs. flooded flow field channels). These are further detailed in Section 4.2. Triplicate experiments were done at each current density, and these are the values reported experimentally.

3.3 Pressure drop hysteresis testing: Non-operating hot model

These experimental conditions were used for the tests in Section 4.3. In the non-operating hot model, a Hydrogenics™ test station (Model no. G100) was used to control relevant operating variables including air flow rate, air temperature (hence 'hot model'), air dew point temperature, and cell temperature. The cell was compressed to 100 psig. Since these experiments are non-operating, the liquid water was injected externally via a syringe pump (Cole-Parmer 780100C). As in the non-operating cold mode, a GDL was placed between the anode and cathode flow field plates. The anode end was blocked and the syringe pump injected water via the anode inlet. The water was forced through the GDL, where it reached the cathode flow field channel to simulate water injection of an operating fuel cell. The air inlet and outlet lines were insulated and dry air was used

between trials to remove excess water and ensure a dry initial condition. This setup is shown schematically in Figure 29.

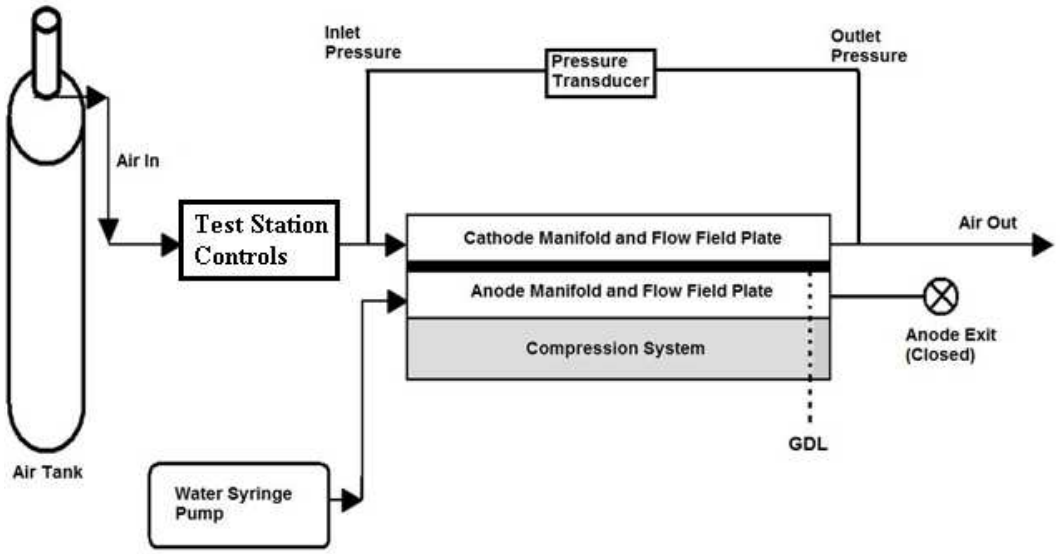

Figure 29. Non-operating hot model (no electrochemical reaction) experimental setup schematic where a fuel cell test station is utilized to control the air humidity and temperature (reprinted from Anderson et al. [144] with permission from Elsevier)

The water injection rates and air flow rates are governed at each simulated current density by Faraday's law as discussed previously. Again, since the setup is non-operating, these current densities are referred to as simulated current densities. The water injection rate assumes all water produced moves into the cathode channel (i.e., no back diffusion term). The water injection rate and air flow rate, in accordance with the simulated current density, were run in an ascending manner and then in a descending manner to determine the extent of hysteresis in the pressure drop. The ascending approach, describing the path by which the simulated current density is increased, was: 50, 100, 200, 400, 600, 800 mA cm^{-2}. The following descending approach was: 600, 400, 200, 100, 50 mA cm^{-2}. The ascending and descending path studied here is identical to the one done in the non-operating cold model pressure drop hysteresis study. Each simulated current was held for approximately 8 minutes to allow the pressure drop to achieve steady

state behavior, and the pressure drop data was sampled at 20 Hz. An Omega 164PC01D37 pressure transducer (0-2,500 Pa) was used to measure the cathode flow channel's pressure drop. Setting the needed gas flow rate but not injecting liquid water obtained the single-phase pressure drop. Unless otherwise noted, the results are an average of three individual trials at each set of conditions.

The gas diffusion layers are the same as those from the non-operating cold model, and their relevant specifications are provided in Table 3. Those GDLs were chosen to study the inclusion/exclusion of the MPL, the PTFE content (hydrophobicity), and thickness. The relevant baseline conditions for all operating variables are listed in Table 5.

Table 5 Baseline conditions for all relevant operating variables in the non-operating hot model (reprinted from Anderson et al. [144] with permission from Elsevier)

Operating Variable	Baseline Value
T_{cell}, T_{gas}, $T_{dew\ point}$	75°C
Relative Humidity	100 %
Gas Diffusion Layer	SGL Carbon 25 BC
Cathode gas	Air
Flow Fields	4 parallel, square channels
Compression pressure	100 psi_g
Air stoichiometry (λ_{air})	2

These experiments focused on the following variables, which are further explained in Section 4.3: the temperature, GDL properties, and air stoichiometry.

3.4 Pressure drop hysteresis testing: Operating fuel cell

A Hydrogenics™ test station (Model no. G100) was used to control and measure relevant operating variables including the air and hydrogen flow rate, operating temperatures, the load, and the voltage. These results are presented in Chapter 5. The cell was compressed to 90 psig. An Omega 164PC01D37 pressure transducer (0-2,500 Pa)

separate from the test station was used to measure the cathode flow channels' pressure drop. The experimental setup is shown schematically in Figure 30.

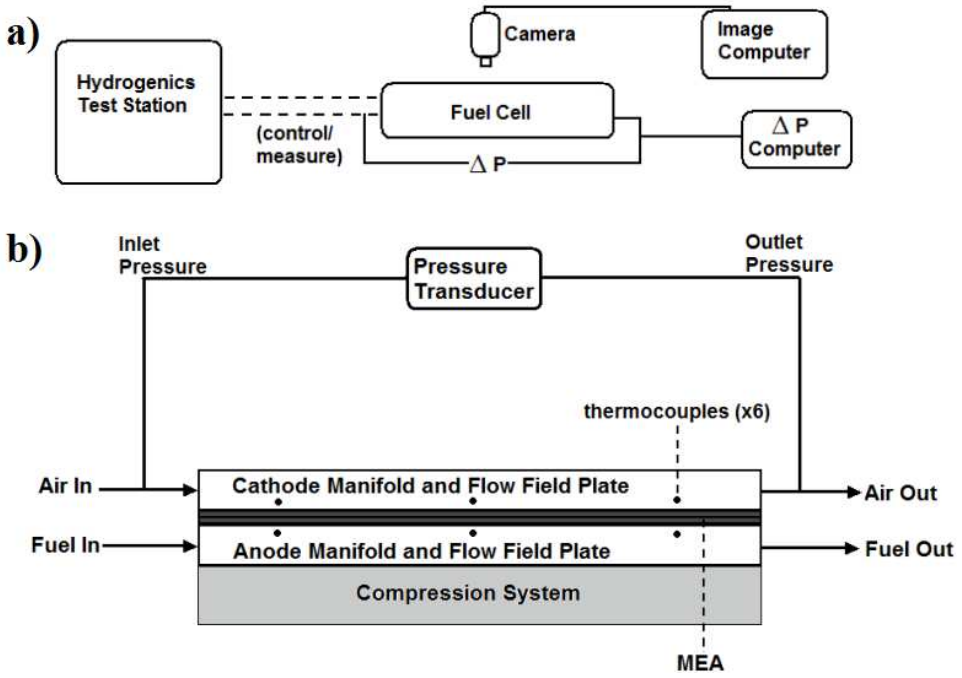

Figure 30. Operating PEM fuel cell experimental schematic focusing on a) General data acquisition schematic; b) Cathode flow ΔP schematic (reprinted from Anderson et al. [148] with permission from Elsevier); all other controls are provided by the Hydrogenics™ test station (Model no. G100)

The current density, i, was run in an ascending manner and then in a descending manner to determine the extent of hysteresis in the pressure drop. The ascending approach was as follows: 50, 100, 200, 400, 600, 800, 1000 mA cm^{-2}. The additional point (compared to the non-operating tests) on the ascending approach to 1000 mA cm^{-2} was done to approach the fuel cell's limiting current density. The descending approach was this path in reverse starting at 800 mA cm^{-2}. Thus, the air and water flow rates were determined via Faradays law and the air stoichiometry for each current density. The single-phase pressure drop at each condition is the gas flow only pressure drop where the fuel cell is held at the open circuit voltage, and the corresponding gas flow rate is increased in accordance with Faraday's law and the stoichiometry.

Each current density was held for approximately 10 minutes. The voltage signal was sampled at 1 Hz and the pressure drop data was sampled at 20 Hz. The gas inlet and outlet lines were insulated, and dry gas was used between trials to remove excess water for a dry initial condition. The results presented are an average of three trials at each set of conditions and indicate that good repeatability was achieved. Examples of the standard deviation from three trials for the pressure drop measurements are shown in Figure 57a and for the electrochemical performance are shown in Figure 59b.

The relevant baseline conditions for all operating variables are listed in Table 6.

Table 6 Baseline conditions for all relevant variables in the operating PEM fuel cell (reprinted from Anderson et al. [148] with permission from Elsevier)

Operating Variable	Baseline Value
T_{cell}, T_{gas}, $T_{dew\ point}$	75°C
Relative humidity (cathode and anode)	100 %
Cathode GDL	SGL Carbon 25 BC
Anode GDL	SGL Carbon 25 DC
Catalyst Coated Membrane (Pt loading)	Gore Primea Series 5510 (0.4 mg Pt cm^{-2})
Air stoichiometry (λ_{air})	2
H_2 stoichiometry	1.5
Cathode gas	Air
Flow fields	4 parallel, square channels
Compression pressure	620 kPag (90 psig)
Gas inlet pressure	206.8 kPag

The temperatures studied were 30, 50, 75, and 90°C and the air stoichiometries studied were 1.5, 2, 3, and 4. These operating conditions are in a narrow range relevant to PEM fuel cells as defined by the US Fuel Cell Council [136]. The gas diffusion layers with their relevant specifications are provided in Table 7. The SGL 25 BC and 25 BA GDLs were chosen to study the impact of an MPL on hysteresis. The SGL 25 DC GDL is used on the anode side for all experiments. Fewer GDLs were used in the operating fuel cell study based on the hydrodynamic results of the non-operating tests (presented in Chapter 4).

Table 7 Gas diffusion layers and specifications focusing on MPL inclusion, PTFE content, and thickness (reprinted from Anderson et al. [148] with permission from Elsevier)

Company	GDL	MPL	PTFE Content	Thickness (μm)
SGL Carbon	25 BC	Yes	5%	235
SGL Carbon	25 BA	No	5%	190
SGL Carbon	25 DC	Yes	20%	231

To ensure the results reached steady state, ascending and descending polarization curves were made at baseline conditions with each current density being held for 15 minutes. The results for the ascending approach are shown in Figure 31. The current densities on the right of the figure are listed in mA cm^{-2}. The dashed lines indicate 5 and 10 minutes. At moderate to high current densities, there is some noticeable dynamics in the voltage signal (sample frequency = 10 Hz; limit of test station). The increased voltage variance with increased current density is consistent with the influence of water at higher current densities, as shown in Figure 8 [6].

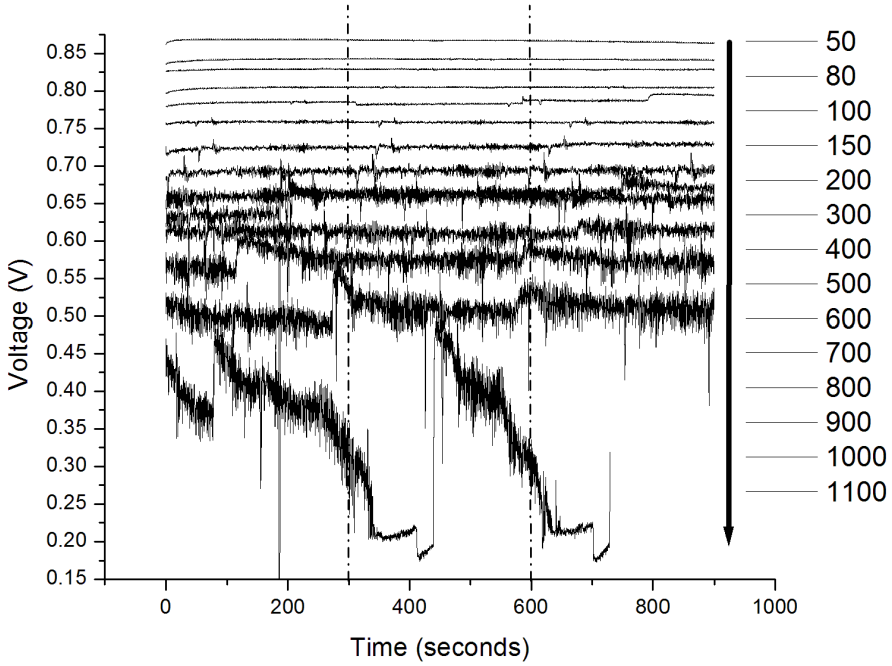

Figure 31. Voltage signals for 15 minutes at each current density of a typical polarization curve (the current densities on the right are in mA cm^{-2})

To see how this dynamic behavior influenced the voltage averages at each current density, the following averages and standard deviations were taken: full 15 minutes, first 10 minutes, first 5 minutes, last 10 minutes, and last 5 minutes. These results are shown in Figure 32. While in some cases the standard deviation is higher if only the first five minutes are averaged (i.e. 700 mA cm^{-2}), the results in each averaging scheme are similar. To ensure a sufficient sampling time while performing reasonably long tests, 10 minutes was chosen as a suitable sampling time and the average of the entire signal is taken. Five minutes of testing was not pursued in the event a particular operating condition had excessively dynamic behavior (such as in a large flooding condition).

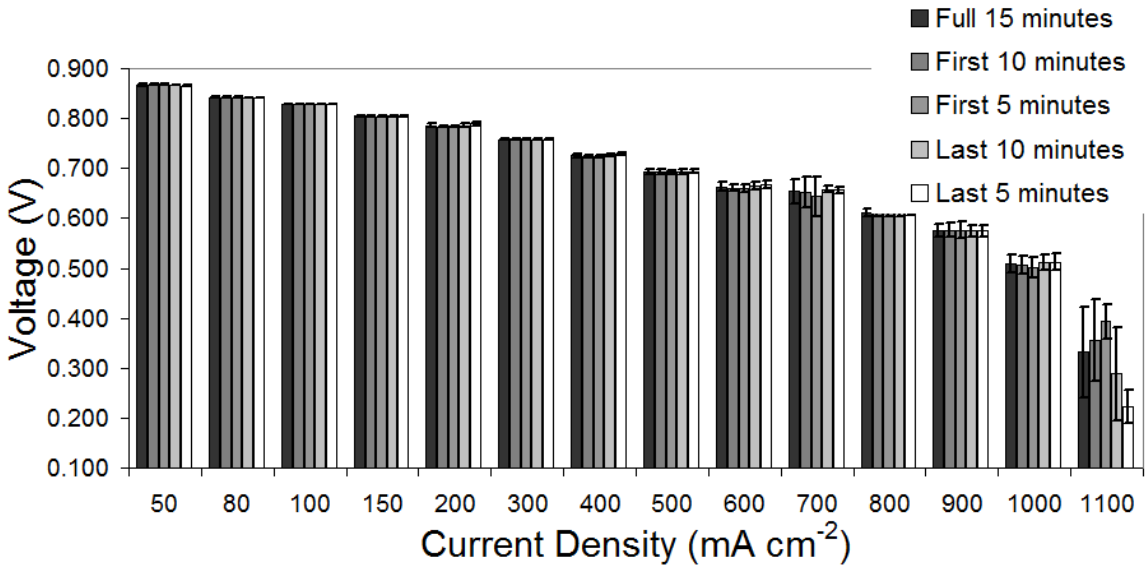

Figure 32. Average voltage at each current density through five averaging schemes to determine the duration of each point when testing

Another example of dynamic voltage data is when the cathode stoichiometry is 1.5 at low current densities (low air flows). At these lower flows, the fuel cell performance tends to fail due to insufficient amounts of oxygen reaching the active catalyst sites and then to recover. An example of this behavior is shown in Figure 33. With this behavior, the average (arithmetic mean) is markedly lower than the values expected on a typical

polarization curve with a large standard deviation. To present more realistic and representative results, the median is used in these cases. Figure 33 shows the difference between the mean and median for both approaches over the course of a ten minute trial. The median is only used in cases of low air flow (current density $\leq$ 100 mA cm^{-2} ; λ_{air} < 2).

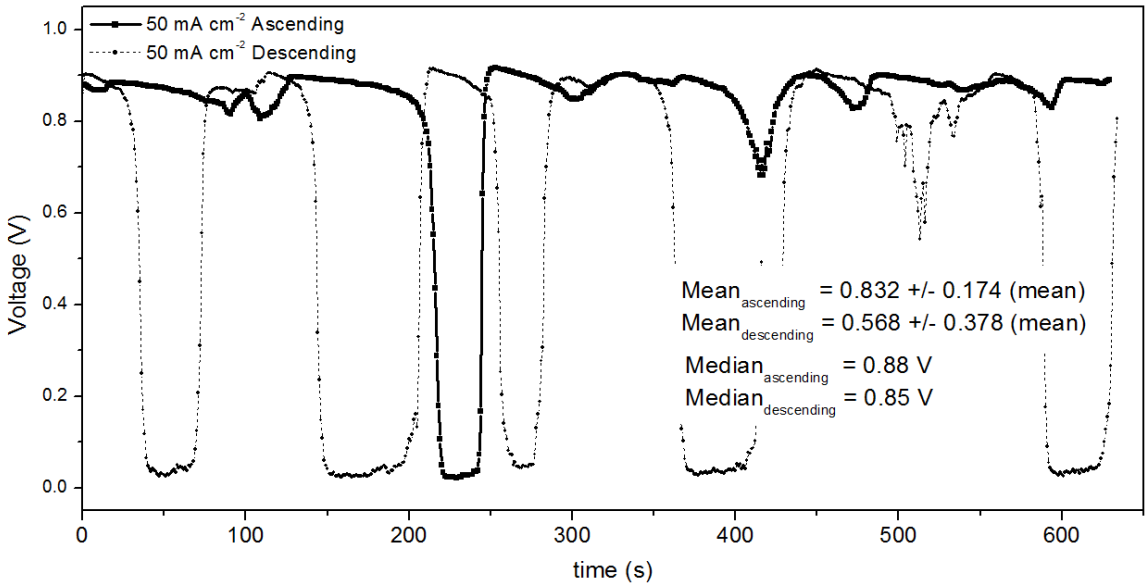

Figure 33. Dynamic voltage behavior at low air flows (λ_{air} = 1.5, i = 50 mA cm^{-2}) showing the difference between the mean and median results; the electrochemical performance is more unstable on the descending approach

As in the non-operating cold studies, majors variables studied include: the air stoichiometry, temperature, and inclusion of a microporous layer (MPL). These are further detailed in Chapter 5. This experimental setup was also used to explore a purging method that can lower the pressure drop hysteresis effect.

3.5 Anode water removal experimental methods

An operating 49 cm^2 fuel cell, TP50 [104], was used for all the tests in this study, and the results are presented in Chapter 6. A Hydrogenics™ test station (Model no. G100) was used to control all fuel cell operating conditions. The conditions for the AWR tests are shown in Table 8.

Table 8 Baseline operating conditions and fuel cell specifications for the anode water removal (AWR) tests

Operating Variable	Baseline Value
T_{cell}, T_{gas}	75°C
Relative humidity (cathode:anode)	100:0 %
Anode GDL	SGL Carbon 25 DC
Catalyst Coated Membrane (Pt loading on both sides)	Gore Primea Series 5510 (0.4 mg Pt cm^{-2})
Active area	49 cm^2
Air stoichiometry (λ_{air})	2
H_2 stoichiometries (AWR)	1.5-15
Cathode gas	Air
Cathode flow field design	Single-serpentine, 27 bends
Cathode channel cross sectional area	Trapezoidal (1.56 mm^2)
Cell compression pressure	110 psig
Gas inlet pressure	206.8 kPag

The inlet cathode gas was fully humidified and the inlet anode gas was completely dry during the AWR tests. Thus, the water concentration gradient favors water transport from the cathode to the anode. This is shown schematically in Figure 34.

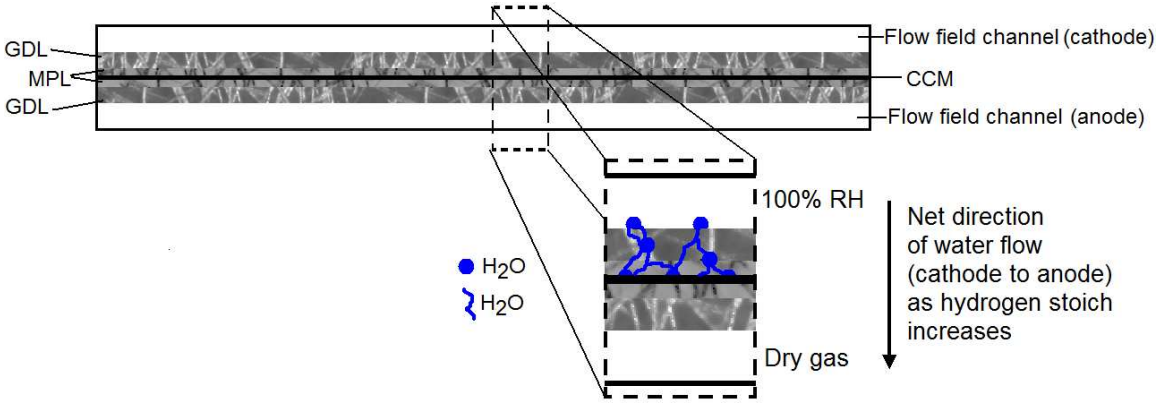

Figure 34. AWR fuel cell schematic showing the net direction of water movement from the cathode toward the anode

The anode stoichiometry was increased throughout the AWR test with all other operating conditions remaining constant, and each anode stoichiometry was sampled for 114 seconds. The test was run until the anode stoichiometry reached 15 or the anode pressure drop exceeded 146.8 kPa. All tests were run at 1,000 mA cm^{-2} with a constant air stoichiometry of 2. This current density was chosen since it represents a reasonably high water production rate. Also, since the anode stoichiometry is increased in the AWR

tests, this high but moderate current density was chosen so a reasonable pressure drop could be obtained at high hydrogen stoichiometries.

The AWR tests used 6 different GDLs on the cathode, which are shown in Table 9. In all tests, the anode GDL was SGL Carbon 25 DC (20% PTFE with an MPL).

Table 9 GDLs used in AWR tests; varying MPL inclusion, hydrophobicity, and thickness

SGL Carbon Cathode GDL	GDL PTFE (%)	MPL	Hydrophobicity	Thickness (μm)
25 BC	5	Yes	Hydrophobic	235
25 BA	5	No	Hydrophobic	190
25 BL	5/0	Yes	Hydrophobic GDL/ Hydrophilic MPL	235
25 BA_{Nitric}	--	No	Mixed Hydrophobic/ Hydrophilic	190
25 AA	0	No	Mixed Hydrophilic/ Hydrophobic; water ingress	190
35 BA	5	No	Hydrophobic	300

The baseline GDL for these tests was the 25 BA GDL, with 5% PTFE and no MPL. The 25 BC GDL has the same properties as the 25 BA GDL but contains an MPL. The 25 BL GDL contains 5% PTFE in the GDL but has a hydrophilic MPL; these tests examine the effectiveness of AWR when the cathode MPL is prone to flooding. The nitric acid treated 25 BA GDL (25 BA_{Nitric}) had a mixed hydrophobicity, with some sections hydrophilic (since the PTFE is removed) and others hydrophobic (due to surface roughness), which promoted some additional flooding in the cathode GDL. The nitric acid treatment was accomplished by immersing the 25 BA GDL in boiling HNO_3 for 1 hour and then rinsing it with DI water. The 25 AA GDL also has mixed hydrophobicity, with small droplets beading up on the surface in a hydrophobic manner and larger droplets quickly entering the GDL (this water ingress causes high GDL saturation).

Tests were also performed with an additional 25 BA GDL placed on top of the existing cathode GDL. This test was done for all of the GDLs in Table 9 to exacerbate the influence of GDL flooding on the fuel cell's performance. The discontinuity in GDL caused by the additional GDL layer can promote additional flooding, and thus more clearly shows how AWR behaves over a range of operating conditions.

Exacerbated flooding was also accomplished by external water injection, which was accomplished by pumping deionized water at ambient temperature with a Masterflex L/S pump (model # 77390-00) through a rotameter. The exit of the rotameter was connected to the cathode gas inlet before the gas entered the cell. The rotameter was utilized to ensure that an accurate water injection rate could be determined. The water injection rate was approximately 145 mL hr^{-1}, which was found to sufficiently reduce the fuel cell's electrochemical performance while still allowing for safe and controlled water injection.

Additional tests were done with the 25 BC and 25 BA GDLs, focused on the effect of temperature (25, 50, 75, and 90^{o}C) and cathode relative humidity (25, 50, 75, and 100%). This was a useful comparison because the only difference between the GDLs was the MPL layer. The temperatures are important because the amount of water in the fully humidified gas stream increases exponentially with temperature, greatly affecting the gradient in the AWR process. The dew points temperatures for the air at 75^{o}C for RHs of 25, 50, 75, and 100% are 45.1, 59.3, 68.3, and 75^{o}C, respectively.

The operating current density was studied as well to determine the effect of the water production rate on AWR (higher current densities produce more water on the cathode). The current densities studied include 100, 500, 750, 1000 (baseline) and 1500 mA cm^{-2}.

For each test, the high frequency resistance (HFR) was studied at a frequency of 1 kHz (GW-Instek LCR-819). These results provided additional data to the voltage data collected during the AWR process (an example is shown in Figure 94). The resistance measurement was taken from the anode and cathode current collectors. The flow field channel pressure drop was measured on both the anode (ΔP_{an}) and the cathode (ΔP_{cat}) by the test station at a sampling rate of 1 Hz.

The AWR performance repeatability was explored using the 25 BC GDL results at 75 ^{o}C and 100 % cathode humidification by running the test five separate times (includes two repeat tests with the same membrane electrode assembly (MEA) and two new MEAs). The percentage error from these five tests was within 2% for the voltage, 10% for the cathode pressure drop, and 8% for the anode pressure drop over the range of hydrogen stoichiometries tested. The error bars shown for the remaining results represent the standard deviation of the signal.

4 Pressure drop hysteresis in a non-operating fuel cell: results for cold and hot studies

Chapter 4 pertains to pressure drop hysteresis in non-operating fuel cell experiments for both cold model (Section 4.2) and hot model (4.3) studies. A brief introduction is given to further explore the relevance of this topic.

4.1 Introduction to pressure drop hysteresis

As discussed, the proton exchange membrane fuel cell has received attention as an energy conversion device due to its high energy efficiency, low operating temperature, and little to zero emissions during operation. As evident from the literature review, one major technical issue that has received extensive research is proper water management. A specific consideration within water management is the impact of gas-liquid two-phase flow in the gas flow channels. A higher pressure drop represents a larger system parasitic power loss [39], prompting additional study into two-phase flow. Another problem associated with two-phase flow in flow channels is reactant maldistribution [56] and current maldistribution [137], which can lower overall cell performance.

To address two-phase flow in flow field channels in a simplified setup, non-operating experiments [70,193 ,75] can be run to mimic the behavior of operational (operating) fuel cells [38, 71,10]. Non-operating experiments possess the advantage of being able to control relevant operating conditions while decoupling reaction and heat/mass transfer from the hydrodynamics. In general, water in non-operating experiments is injected through a GDL into the air flow field channel (simulating the cathode flow field channel) to observe relevant two-phase flow behavior. Operating then refers to running the cell electrochemically to produce water. Borrelli et al. [70] showed that the non-operating experiments exhibit similar droplet behavior to operating cells.

Once the droplets emerge into the flow field channels, non-operating experiments have shown various two-phase flow patterns including slug, film, corner, and mist flows depending on the superficial air velocity and GDL properties [75]. Film flow or stratified flow is considered as a desirable pattern in fuel cells because water is only covering the channel walls, leaving the GDL surface exposed for gas diffusion. However, the superficial velocity needed to achieve this flow pattern varies with experimental setup, with Trabold et al. [6] pointing out that a superficial gas velocity of 5-6 m s^{-1} is needed and Lu et al. [56] recommending more than 3 m s^{-1}. The value of the needed superficial velocity may also change with operating current density [22].

A recently studied two-phase flow phenomenon is pressure drop hysteresis [50, 55]. This behavior occurs when the gas and liquid flow rates (determined by a given current density) are increased along a set path and then decreased along the same path with differing pressure drops. An application exhibiting increasing and decreasing currents is the automobile, where the load varies based on the driving cycle [138, 139]. Since the load varies, the corresponding gas flow rates and water production rate vary as well via Faraday's Law (Eqn. 17 and Eqn. 34). An example automotive load profile studied by Automotive Fuel Cell Cooperation (AFCC) is shown in Figure 35, which shows increases and decreases in the load.

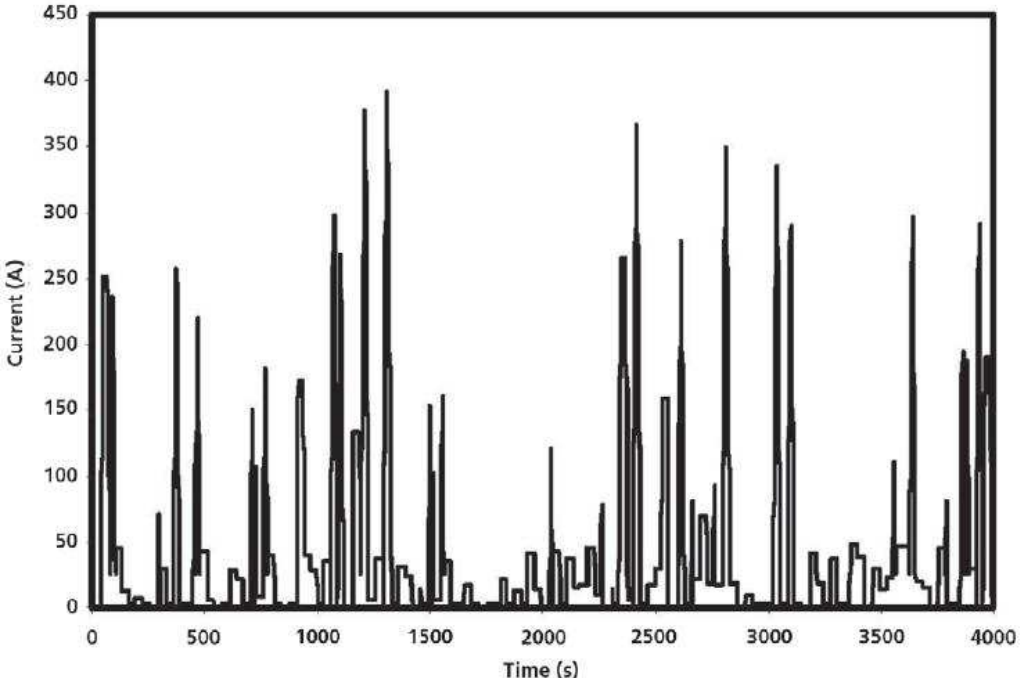

Figure 35. Example automotive load profile from AFCC showing repeated increase and decreases in load, which correspond to increases and decreases in flow rates (reprinted from Kundu et al. [138] with permission from Elsevier)

Additionally, flow regime hysteresis has been observed in minichannels bounded by a porous wall, where the transition between flow regime depended on whether the air flow rate was varied in an ascending or descending manner [54]. This is relevant to PEM fuel cells due to the porous GDL structure defining one wall of the flow field channel.

Previous work examined the pressure drop hysteresis phenomena over a wide range of operating conditions, and an example result of an ex-situ study performed in acrylic channels is shown in Figure 36 [55].

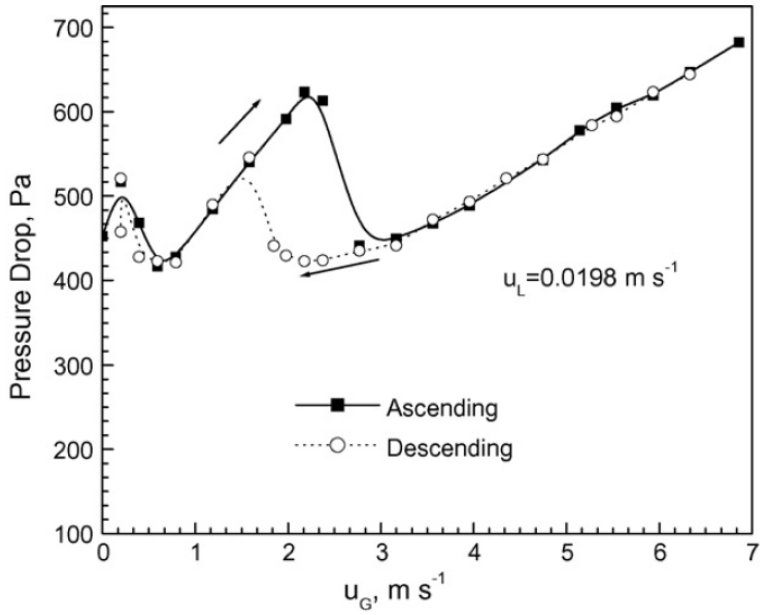

Figure 36. Pressure drop hysteresis with air and water in two parallel minichannels from ascending and descending gas flow rates (reprinted from Zhang et al. [55] with permission from Elsevier)

These results show a clear difference in pressure drop depending on the ascending or descending approach. The pressure drop hysteresis region (superficial gas velocities between ~1.5 and 3 m s^{-1}) occurs here because of flow pattern changes: in the flow descending approach the flow pattern is stratified flow in both channels, but is stratified flow in one channel and stagnant liquid in the other channel during the gas ascending approach. It should be noted this mechanism is not assumed to be the pressure drop hysteresis mechanism in an operating fuel cell, as will be discussed throughout Chapters 4 and 5. It is also important to note that these results could only be confirmed with optical visualization of the flow pattern.

This chapter explores pressure drop hysteresis in two distinct stages: non-operating 'cold' (Section 4.2) and non-operating 'hot' (Section 4.3). Cold and hot refer to the test conditions for the non-operating investigations; cold experiments were studied at ambient temperature and pressure with dry air, while the hot experiments were studied at relevant temperatures with humidified air. The specific test conditions for this chapter are

explained in Section 3.2 (cold) and 3.3 (hot). This progression allowed the establishment of a hydrodynamic baseline, to which results could then be compared as the conditions became more relevant to an operating PEM fuel cell. Pressure drop hysteresis in an operating fuel cell is analyzed in Chapter 5.

The results of this thesis show that pressure drop hysteresis is important at low current densities (both simulated and operating). The pressure drop behavior is important at lower current densities because low loads are often used for high energy conversion efficiency [29,205]. Also, dynamic automotive fuel cells can operate at less than 20% of the rated power, with Barbir [140] noting an average power of 12% of maximum power from the U.S. EPA Urban Dynamometer Driving Schedule (2005), making the regime of lower gas flow important [141]. The compressor work can be related to the pressure drop via Eqn. 44,

$$W_{comp} = \frac{m_{air,in} * c_p * T_1}{\eta_{comp}} \left[\left(\frac{P_2}{P_1} \right)^{\frac{k-1}{k}} - 1 \right] \tag{44}$$

where P_2 is the pressure after compression (including pressure drop), P_1 is the pressure before compression, and k is the ratio of specific heats (1.4 for diatomic gases). A higher pressure drop results in more compressor work, and this work is a parasitic power loss, which lowers overall fuel cell efficiency as discussed [39]. Thus, the pressure drop hysteresis work in Chapter 4 and Chapter 5 is focused on understanding the pressure drop towards the ends of higher total system efficiency, not as a diagnostic tool. By better understanding mechanisms that raise the pressure drop, unnecessary power losses to the compressor can be avoided, raising overall system efficiency. Further discussion on this topic is given in the overall conclusions in Chapter 7.

4.2 Pressure drop hysteresis in a non-operating cold fuel cell[3]

For clarity, the flow approaches are defined again as follows in terms of the 'simulated' current density (the current density defines the relative flow rates of water and air; simulated means the setup is non-operating). The ascending approach is 50, 100, 200, 400, 600, 800 mA cm^{-2}. The corresponding descending approach is: 600, 400, 200, 100, 50 mA cm^{-2}. It should be noted that this simplified approach to the load cycle (compared to Figure 35) is used to combine a typical polarization plot (increasing current density) with an ascending and descending profile that would be seen in automotive applications. While this simplified profile is then artificial, it is a reasonable baseline profile for experimental investigation and is used throughout the pressure drop hysteresis study. The specific operating conditions and fuel cell designs of this motivating application (i.e. the automobile) should not be confused with our experimental setup where simplifications are necessary to understand the complex two-phase flow.

4.2.1 Results and discussion

This section explains pressure drop hysteresis in a non-operating cold fuel cell [142]. The non-operating approach taken here injects water through a GDL into the cathode flow field channel with gases that are neither humidified nor heated. The experimental conditions for these tests are described in Section 3.2. To understand the principles of this pressure drop hysteresis behavior, the non-operating approach examined several variables including: the effect of air stoichiometry (Section 4.2.1.1), the GDL properties (the inclusion of an MPL Section 4.2.1.2.1 and PTFE content Section 4.2.1.2.2), the range of

[3] These results were published in [142]: R. Anderson, D.P. Wilkinson, X. Bi, L. Zhang, Two-phase flow pressure drop hysteresis in parallel channels of a proton exchange membrane fuel cell, J. Power Sources 195 (2010) 4168-4176.

current densities (Section 4.2.1.3), the effect of decreasing step size (Section 4.2.1.4), and the effect of initial state (dry vs. flooded; Section 4.2.1.5).

4.2.1.1 Effect of stoichiometry in the non-operating fuel cell

The ascending and descending pressure drop results for stoichiometries of 1 to 5, which cover a typical range of fuel cell operations [146], are shown in Figure 37a. SGL 25 BC was chosen as the GDL because it is a typical GDL used on the cathode side of the operating fuel cell. Triplicate experiments were done at each current density, and these are the values reported in Figure 37a. Figure 37b and Table 10 show an individual result for the third trial of the 25 BC GDL at a stoichiometry of 2.

Table 10 Pressure drop results for the ascending and descending process for one experimental trial (25 BC GDL, λ_{air} = 2, Trial 3 result) (reprinted from Anderson et al. [142] with permission from Elsevier)

Ascending Process (i_{sim})	**Pressure Drop (Pa)**	**Standard Deviation (Pa)**	**% Error**
50	33	2	7
100	75	2	3
200	159	2	1
400	359	6	2
600	673	70	10
800	1085	36	3
Descending Process (i_{sim})	**Pressure Drop (Pa)**	**Standard Deviation (Pa)**	**% Error**
600	763	32	4
400	532	21	4
200	233	17	7
100	115	24	21
50	61	32	52

The ascending case has a small percentage error (ratio of standard deviation to overall pressure drop). The high percentage error at low simulated current densities during the descending approach is a result of the large oscillations in pressure drop signal due to the flow type. More discussion on the signal fluctuations is in Section 4.2.1.4.

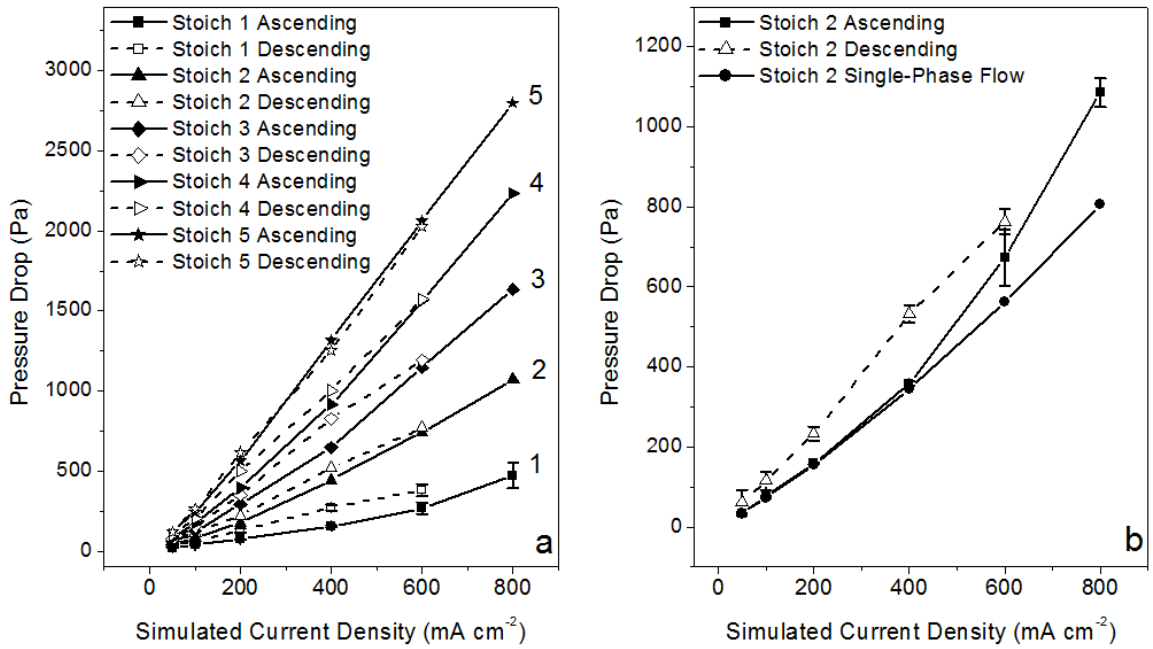

Figure 37. Effect of gas stoichiometry on two-phase pressure drop hysteresis for the 25 BC GDL [P_{gas} = 0 kPag, T_{gas} = 20°C, dry air] (reprinted from Anderson et al. [142] with permission from Elsevier)

The ascending pressure drop and descending pressure drop are not identical for stoichiometries in the range of 1-4. However, at a stoichiometry of 5, the pressure drops from flow ascending and descending approaches match each other. This pressure drop hysteresis effect can be explained by how water enters and leaves the cathode flow field channels. At low simulated current densities, no water is being introduced and the fluid flow in the channels is essentially single-phase air flow. Figure 37b shows the results for single phase flow (air only) with the 25 BC GDL at a stoichiometry of 2, which illustrates how the ascending pressure drop and single phase pressure drop at the same when the simulated current density is $\leq$ 400 mA cm^{-2}. Water breakthrough is evident at a higher simulated current density $\geq$ 600 mA cm^{-2}. In this setup, it is not until these rates that a critical breakthrough pressure is reached, as discussed by Bazylak et al. [193]. As the air flow is lowered in the descending approach, the injected water is unable to be removed from the channels convectively, and the residual water causes a higher pressure drop.

This explanation is true for lower stoichiometries that are less than or equal to four. At a stoichiometry of 5, the air flow is sufficient to remove all injected water and, as a result, residual water is not accumulated. Due to the equilibrium addition and quick removal of water, the ascending and descending pressure drops do not display a hysteresis in this higher stoichiometric range. It is also important to note from other ex-situ work that once breakthrough occurs, water continues to flow through the GDL even without the syringe pumping in more water to maintain the same hydrostatic pressure [74]. Thus, flooding can be greater after breakthrough has occurred.

The extent of pressure drop hysteresis can be quantified by the percentage change between the descending and ascending pressure drops, as shown in Figure 38. This is a useful metric as it relates the two approaches to one another directly; it is a direct comparison of how the descending path changes compared to the ascending path, regardless of how the ascending path's behavior differs from the single-phase flow case. The percentage change is defined as:

$$\% \text{ Change} = \left[\frac{\Delta P_{\text{Descending}} - \Delta P_{\text{Ascending}}}{\Delta P_{\text{Ascending}}} \right] \times 100 \tag{45}$$

i.e. a higher percentage change from ascending to descending pressure drops indicates a more pronounced pressure drop hysteresis. Note the analysis does not rely on the total magnitude of the pressure drop hysteresis. One reason is that the comparison is often inconclusive since such a wide range of overall pressure drops is studied (from approximately 50 to 2500 Pa). Thus, magnitude changes in the pressure drop do not reflect the relative influence of the pressure drop hysteresis, which is more important for finding the relative increase in compressor work at a given current density. Further, since this is a single cell in parallel channels, the magnitude of these differences experimentally

does not increase the compressor work appreciably. However, the magnitude of the pressure drop increase would be more important when considering a full stack where the total flow and total pressure drop would be substantially higher.

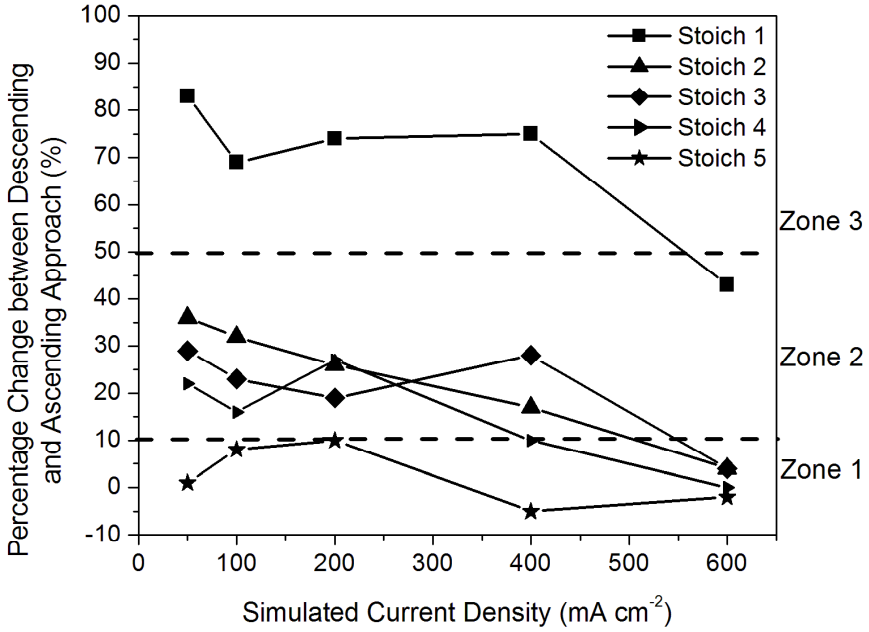

Figure 38. Percentage change in ascending and descending pressure drops showing hysteresis is a larger problem at lower air stoichiometries (lower air flow rates) (reprinted from Anderson et al. [142] with permission from Elsevier)

Three different zones are drawn in this figure for illustrative purposes. At a stoichiometry of 1, the hysteresis effect is large for all simulated current densities because the low air flows are unable to remove the residual water in the descending case (Zone 3). Operation for stoichiometries in the range of 2-4 falls into Zone 2, where the hysteresis effect is not noted at high current densities ($\geq$ 600 mA cm^{-2}). However, at lower simulated current densities, the air is unable to remove residual water in the descending case and two-phase flow hysteresis appears. For a higher stoichiometry of 5 (Zone 1), the hysteresis effect is eliminated because the air flow is sufficiently high to prevent the accumulation of residual water. In this region, the percentage change between ascending and descending pressure drop is consistently below 10%.

These results clearly show higher air flow rates are needed to shear liquid water out of the flow field channels, which relates back to the adhesion forces and shear forces developed in 2.3.3. Droplet removal will only occur if enough force is applied to the droplet to remove it from the channels, a criterion that is met with increasing air flow.

4.2.1.2 Effect of GDL type: MPL inclusion and hydrophobicity

Five different GDLs were tested and compared at a stoichiometry of 2 (the baseline cathode stoichiometry for the operational fuel cell). These GDLs were chosen to investigate the effect of a microporous layer (with and without MPL) and PTFE content (0, 5, 20%) on pressure drop hysteresis. Lee et al. [54] have shown these parameters to have an impact on observed flow regime in fuel cell flow channels. The GDLs used in this research and their relevant specifications are shown in Table 3.

4.2.1.2.1 Effect of MPL

Figure 39 shows the effect of the MPL by comparing SGL 25 BC (with MPL) and 25 BA (no MPL), which have the same PTFE treatment but a different thickness due to the inclusion of an MPL.

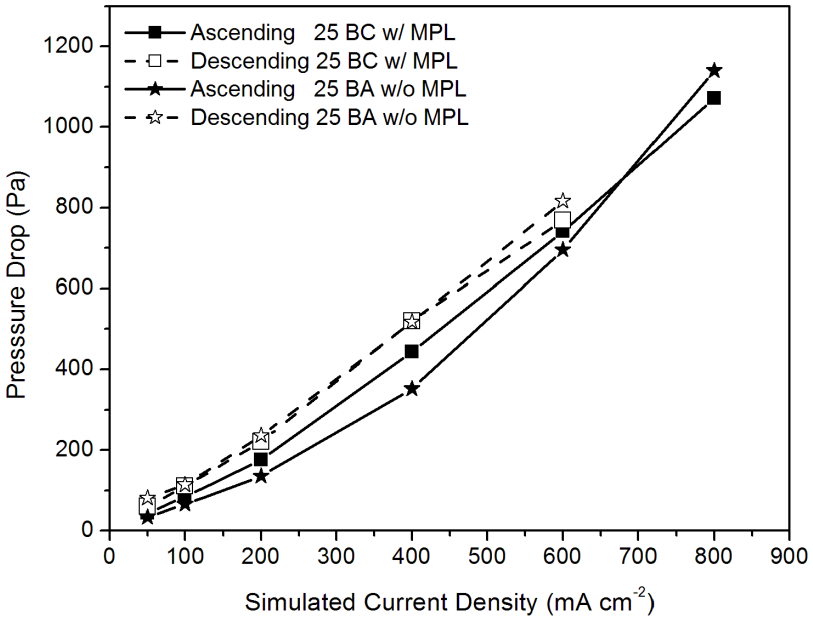

Figure 39. Effect of MPL on pressure drop: 25 BC (with MPL) vs. 25 BA (withouth MPL) at a stoichiometry of 2 [P_{gas} = 0 kPag, T_{gas} = ambient, dry air] (reprinted from Anderson et al. [142] with permission from Elsevier)

These results show that both GDLs share similar descending pressure drops but different ascending pressure drops. At the same descending air flow, the similar capability of expelling the residual water suggests that the droplet detachment/removal dynamics are similar for the two types of GDLs, which have the same PTFE content. The ascending pressure drop for the 25 BA GDL (no MPL) is lower, leading to a larger percentage hysteresis effect when compared with the descending approach (Figure 41). This is a combination of water injection and single-phase pressure drop, as the 25 BC GDL has a higher single-phase pressure drop than the 25 BA GDL (~17% higher on average). Thus, the percentage change appears smaller for the 25 BC GDL due to the higher ascending pressure drop.

The effect of the MPL on two-phase flow hysteresis was also studied by comparing the 25 DC (20% PTFE, MPL) and TGPH-030 with 20% PTFE GDL (no MPL). These results at a stoichiometry of 2 are shown in Figure 40.

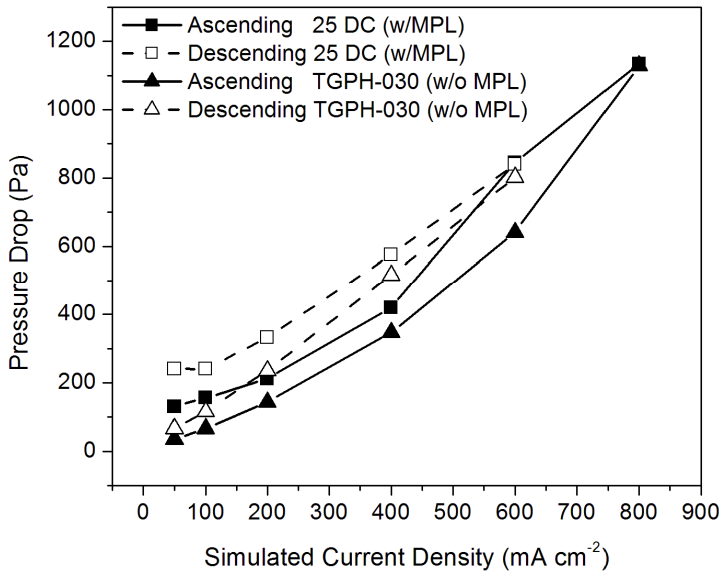

Figure 40. Effect of MPL on pressure drop : 25 DC (with MPL) vs. TGPH-030 20% PTFE (without MPL) at a stoichiometry of 2 [P_{gas} = 0 kPag, T_{gas} = ambient, dry air] (reprinted from Anderson et al. [142] with permission from Elsevier)

Both GDLs exhibit pressure drop hysteresis. In this case, the 25 DC GDL has a higher overall pressure drop in either approach. However, this does not directly show the relative effect of the pressure drop hysteresis. To address this, Figure 41 shows the percentage change between the descending and ascending case for the four GDLs. The data shows that the 25 DC GDL and 25 BC GDL (both with MPL) allow for water breakthrough at a lower simulated current density [143], which reduces the difference between the ascending and descending pressure drop since the water influences both approaches. For the GDLs with no MPL, the later injection during the ascending approach leads to a lower ascending pressure drop and therefore more hysteresis once the water breaks through.

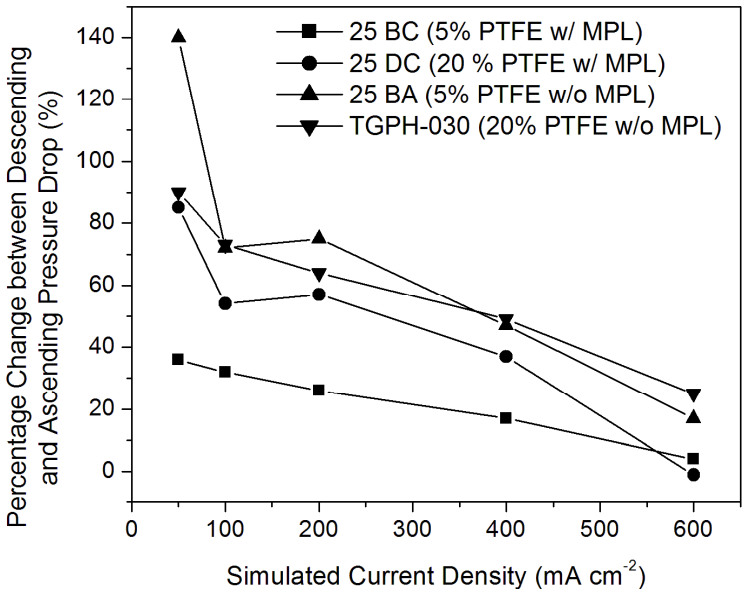

Figure 41. Percentage change in pressure drop for four GDLs varying PTFE and MPL inclusion(reprinted from Anderson et al. [142] with permission from Elsevier)

However, the results for the TGPH-030 20% PTFE GDL (without MPL) and the 25 DC GDL (20 % PTFE with MPL) are quite similar, so it remains uncertain if MPL is a major parameter affecting the extent of pressure drop hysteresis. This is more explicitly addressed in Section 4.2.1.2.3.

4.2.1.2.2 Effect of hydrophobicity

Figure 42 b, c, and d show the effect of PTFE treatment by comparing TGPH-030 with 0% PTFE, TGPH-030 with 20% PTFE, and 25 BA with 5% PTFE respectively (none with MPL). The single-phase pressure drop result for each GDL is also included to show the influence of two-phase flow on the pressure drop.

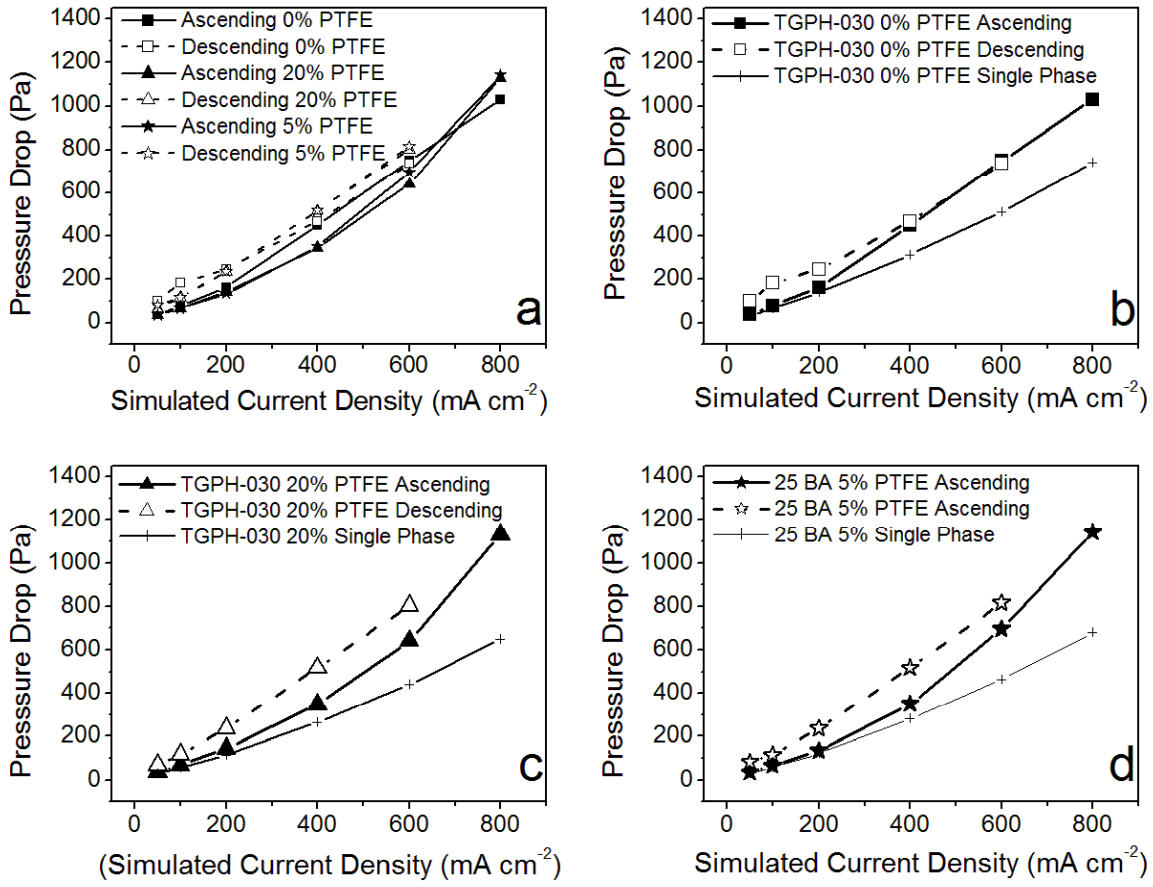

Figure 42. Effect of PTFE treatment on pressure drop: a) Three GDLs b) THPG-030 with 0% PTFE c) TGPH-030 with 20% PTFE d) and 25 BA with 5% PTFE [P_{gas} = 0 kPag, T_{gas} = ambient, dry Air] (reprinted from Anderson et al. [142] with permission from Elsevier)

Water breaks through the plain TGPH GDL at a lower flow rate than the TGPH 20% PTFE coated GDL, leading to a higher ascending pressure drop (Figure 42a). Due to the higher pressure drop in the ascending case, the hysteresis effect is only noted for the plain GDL at simulated current densities of 200 mA cm^{-2} and lower. Water is more efficiently removed from the GDL surface with increasing PTFE, and the TGPH-030 20% PTFE coated GDL led to a lower ascending pressure drop and therefore a wider hysteresis zone when water accumulates in the descending approach. At current densities below 200 mA cm^{-2}, the plain GDL also exhibits a larger pressure drop in the descending approach compared to the TGPH-030 20% PTFE coated GDL. This may be a result of the reduced

PTFE content, which would hinder the droplet's detachment from the GDL surface due to higher hydrophilicity (wetting of the surface) [69]. The 25 BA GDL shows very similar results to the TGPH-030 20% PTFE coated GDL. The percentage difference between these GDLS, defined as:

$$\%\ \text{Change}_{\text{GDLs}} = \left[\frac{\left|\Delta P_{25BA} - \Delta P_{TGPH-030,20\%}\right|}{\Delta P_{25BA}}\right] \times 100 \tag{46}$$

is on average less than 4%. This result indicates that additional PTFE (20% vs. 5%) does not influence the extent of the hysteresis.

The percentage change between the descending and ascending approach pressure drop for the three GDLs in Figure 42 are shown in Figure 43.

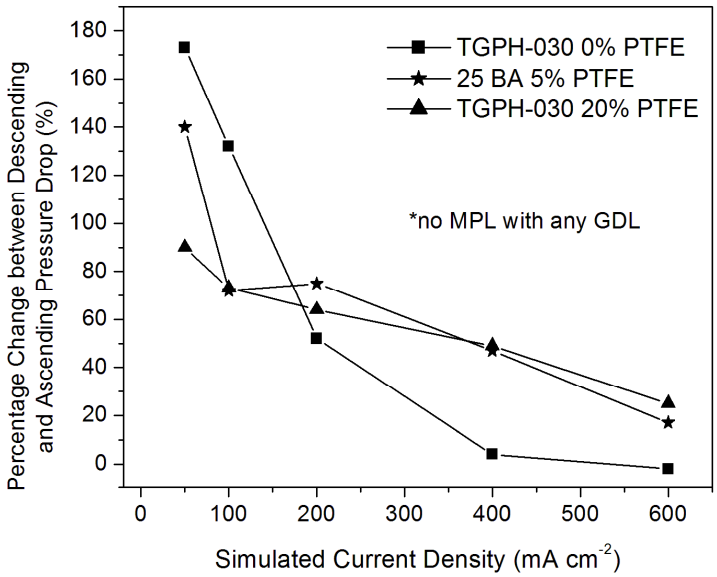

Figure 43. Percentage change between the descending and ascending pressure drop for three GDLs with PTFE content of 0, 5, and 20% (reprinted from Anderson et al. [142] with permission from Elsevier)

This figure shows no clear trend, indicating the PTFE treatment is not a major consideration in pressure drop hysteresis. Thus, it is important to study each GDL individually and evaluate the results in terms of the single-phase pressure drop and the percentage change between approaches.

4.2.1.2.3 Physical interpretation of GDL results

As has been discussed, the hysteresis results depend not only on the amount of accumulation in the descending approach but also the breakthrough point of liquid water. The total amount of water injected into the cathode flow field channels based on the volumetric injection rate in Table 4 is shown in Table 11.

Table 11 Cumulative water injection rates for the entire ascending and descending cycle for simulated current densities based on an active area of 35.7 cm^2

Current Density ($mA\ cm^{-2}$)	**Volumetric liquid water injection rate ($mL\ hr^{-1}$)**	**Cumulative water injection (mL)**
50 (ascending)	0.6	0.1
100 (ascending)	1.2	0.2
200 (ascending)	2.5	0.6
400 (ascending)	4.9	1.2
600 (ascending)	7.4	2.2
800 (ascending)	9.9	3.5
600 (descending)	7.4	4.5
400 (descending)	4.9	5.2
200 (descending)	2.5	5.5
100 (descending)	1.2	5.7
50 (descending)	0.6	5.7

This is important because each GDL can lend itself to a different saturation point before breakthrough occurs. Each GDL has its own specific properties: PTFE loading, thickness, porosity, air diffusivity, MPL inclusion etc. These properties affect how water breaks through from the anode chamber into the cathode flow field channels during the non-operating tests. To study this point, a given i_{sim} was run until breakthrough occurred for the 25 BC and TGPH-030 20% PTFE GDLs. The breakthrough time was noted when the pressure drop signal suddenly changed, and an example is shown in Figure 44.

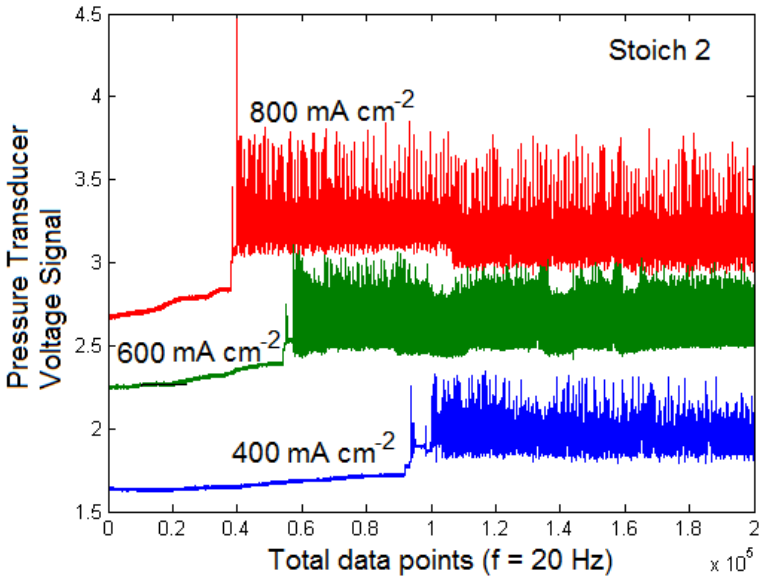

Figure 44. Breakthrough determination from pressure transducer signals for flow rates corresponding to 400, 600, and 800 mA cm^{-2}; the breakthrough point occurs when the signal transitions from relatively stable to high frequency oscillations (25 BC GDL)

The x-axis in this case is total data points collected at a frequency of 20 Hz, which for the analysis is converted into seconds, and the y-axis is the pressure transducer signal in volts. The results shown here make sense; the 400 mA cm^{-2} test takes longer for water to break into the GDL because it has half the volumetric flow rate of the 800 mA cm^{-2} simulated current density. The time until injection plotted against i_{sim} (25 BC GDL, λ_{air}=2, T=ambient, dry gas) is shown in Figure 45.

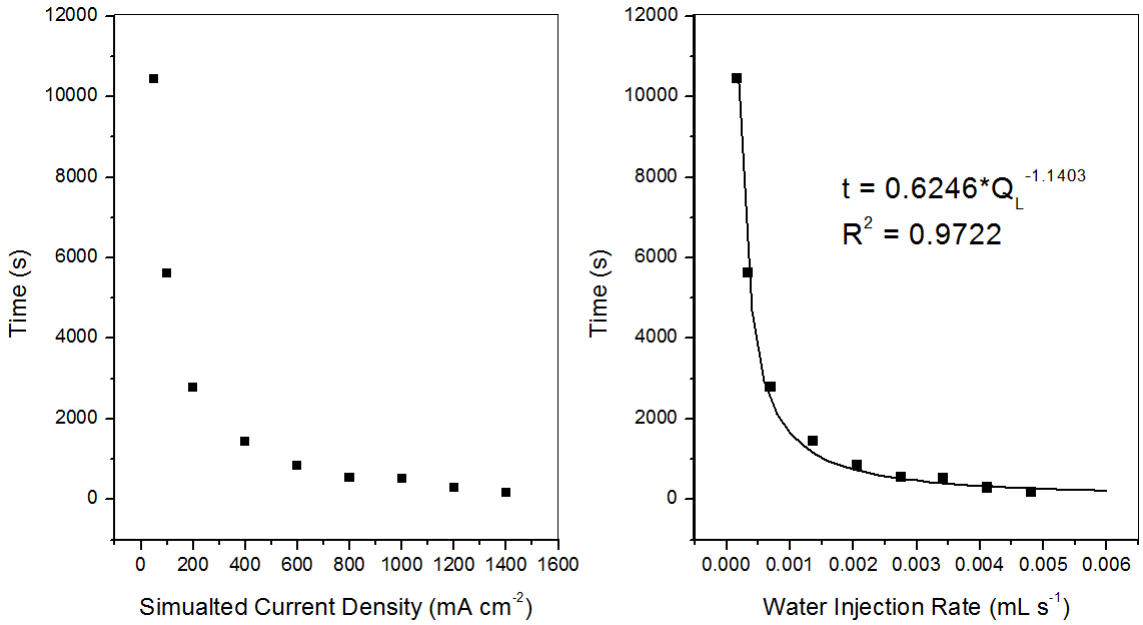

Figure 45. Breakthrough times a) vs. i_{sim} b) vs. water injection rate corresponding to a given i_{sim} with a power law curve fit (25 BC GDL)

The results in a) and b) have the same shape because the i_{sim} and water injection rate are coupled Faradaically. The curve fit shows a power law where the exponent is –1.1403. This exponent is approximately –1, implying that the injection rate x time is a constant value. This result means that each GDL has a specific saturation point (water volume) before water breakthrough will occur under a given set of conditions. The implication to hysteresis is that the two-phase pressure drop is not noted until water injection has occurred. Only then do the removal/accumulation dynamics become important. Experimentally, it was determined on average that the total injected volume before breakthrough was 1.6 mL under these conditions. However, the coefficient on the curve fit (which represents the fitted amount of water injected), is only 0.63 mL. This difference is due to the exponent not being –1 exactly. When refitted with the exponent as –1 and the coefficient set to 1.6 mL, the following plot was found:

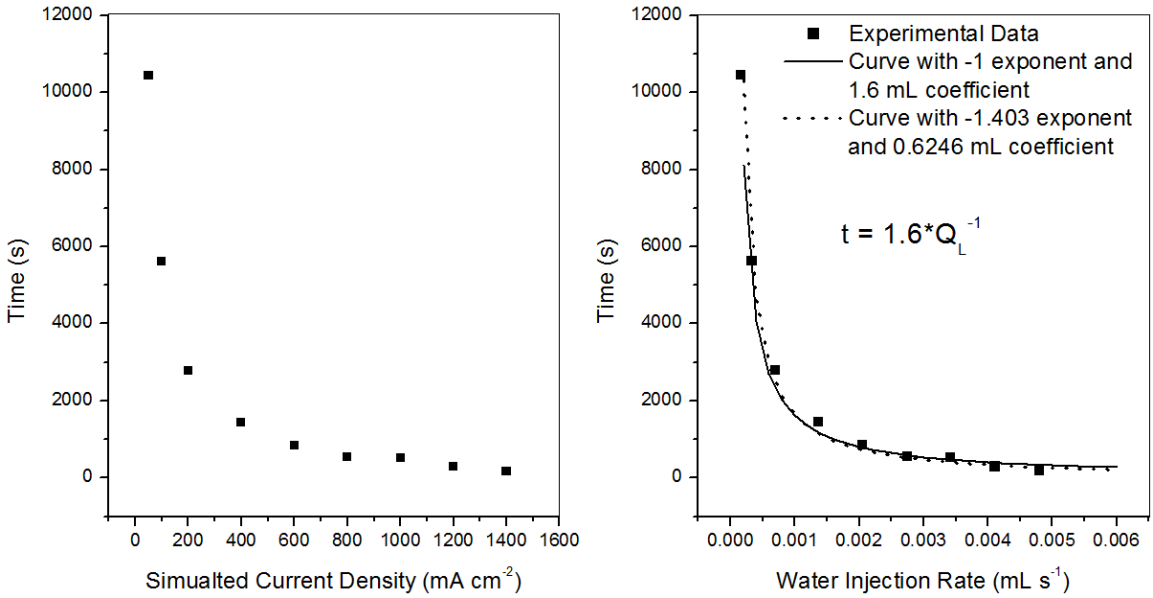

Figure 46. Breakthrough times a) vs. i_{sim} b) vs. water injection rate corresponding to a given i_{sim} with the first power law curve fit and a modified power law curve fit with an exponent of –1 and a coefficient of 1.6 mL (25 BC GDL)

As shown in Figure 46b, the curve fit with an exponent of –1 and a coefficient of 1.6 mL (as found experimentally) is still in good agreement with the data. This agreement means that the physical interpretation of the results is adequate; each GDL has a constant water saturation volume before breakthrough. Physically, the 25 BC GDL can only hold a volume of 0.72 mL (25 BC GDL; *l* x *w* x *h* = 340.1 x 10.4 x 0.235 mm; porosity = 80%), which means that the additional water builds up the pressure on the anode side until breakthrough can occur. This pressure buildup is likely a function of the aforementioned parameters. The pressure drop on the cathode side also increases slightly before the breakthrough, as shown in Figure 44. The flooded GDL may act like an impermeable solid, which would increase the pressure drop (this is discussed in Appendix C.1.1).

This analysis was also done with the TGPH-030 20% GDL with the same result, except the coefficient is 1.95 mL (found experimentally). The exact set of factors that contribute to this constant saturation volume are not clear. Compared to the 25 BC GDL,

the GDL properties are varied (20% PTFE, no MPL, 80% porosity, 0.110 mm thickness), and the breakthrough may also be related to the pressure in the cathode channels, which is a function of the operating conditions. The unique properties of each GDL further highlight why studying pressure drop hysteresis in each GDL is needed and why no dominant trends are noted in the percentage change results for the GDLs (varying MPL and PTFE).

4.2.1.3 Effect of simulated current density range

The range of the simulated current density was varied by studying ascending approaches up to 400 mA cm^{-2} and up to 1600 mA cm^{-2}. The baseline GDL (SGL 25 BC) and baseline operating conditions (dry gas, ambient temperature, $\lambda_{air} = 2$) were used in this study. The results for the final ascending current densities to 1600 mA cm^{-2}, 800 mA cm^{-2} (baseline), and 400 mA cm^{-2} are shown in Figure 47 a, b, and c, respectively.

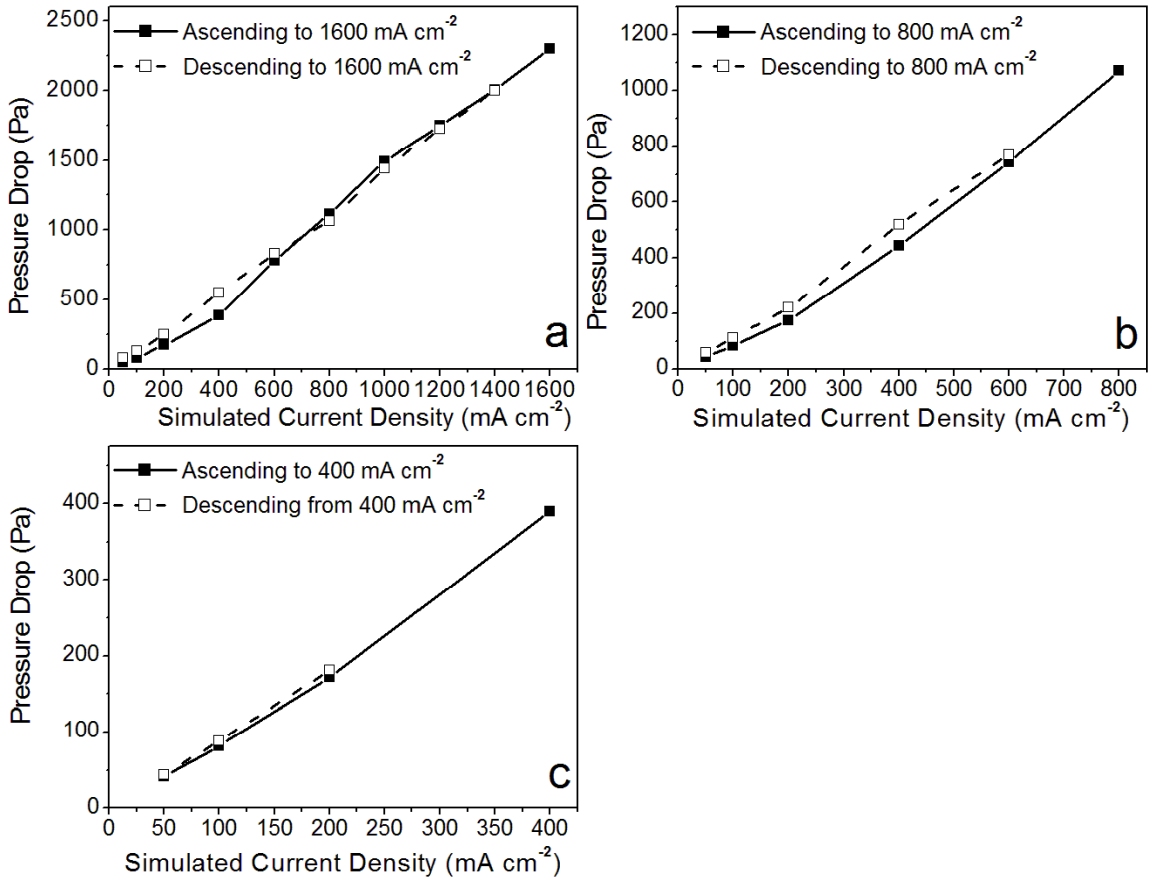

Figure 47. Effect of final current density on pressure drop (three ascending/descending approaches): a) max i_{sim} at 1600 mA cm^{-2}; b) max i_{sim} at 800 mA cm^{-2}; c) max i_{sim} at 400 mA cm^{-2} [P_{gas} = 0 kPag, T_{gas} = ambient, dry air] (reprinted from Anderson et al. [142] with permission from Elsevier)

If a minimum water injection rate is not reached, as in the case of 400 mA cm^{-2}, there is no water breakthrough so no hysteresis is observed. The breakthrough results for 25 BC show a 1.6 mL water injection is needed for breakthrough, which is not reached when the maximum simulated current density is only 400 mA cm^{-2} (Table 11). The average percentage difference between descending and ascending approaches in this case is only 6 +/- 1%. For a final current density of 800 mA cm^{-2}, the breakthrough of water causes accumulation that cannot be removed effectively by the descending airflow, leading to hysteresis. The case of 1600 mA cm^{-2} follows similar hysteresis behavior in the same zone as the 800 mA cm^{-2} case. However, above a current density of 800 mA cm^{-2}, the air flow is able to remove the injected water at a sufficient rate in either approach (similar to

the results of using an air stoichiometry of 5). Thus, there is no hysteresis effect in the high flow rate range. Below 600 mA cm^{-2}, the high air flow does not remove the liquid water, so accumulated water in the channels at lower air flows (below 600 mA cm^{-2}) causes a higher pressure drop in the descending case. This establishes two-phase pressure drop hysteresis. Compared to the same points in the case of 400 mA cm^{-2}, the average percentage change between descending and ascending approach is 56 +/- 12%.

Thus, as explained in the GDL breakthrough section, the hysteresis effect is first explained by breakthrough, which is GDL dependant, and then by the water removal ability of the gas at a given flow rate.

4.2.1.4 Effect of descending step size

In the previous experiments, the simulated current density was incrementally increased to 800 mA cm^{-2} and then descended along the same path (600, 400, 200, 100, 50 mA cm^{-2}). Four experiments were run to analyze the effect of the initial descending step size. Each experiment began at 800 mA cm^{-2} (no ascending approach) and the descending approach step size was changed, with each setting held for approximately 8 minutes. The experimental approaches are given in Table 12.

Table 12 Five descending approach experiments to determine the effect of decreasing step size on pressure drop (reprinted from Anderson et al. [142] with permission from Elsevier)

Trial Number	Descending Approach (mA cm^{-2})
0 (previous baseline)	800→600→400→200→100→50
1	800→400→200→100→50
2	800→200→100→50
3	800→100→50
4	800→50

Each cluster of results in Figure 48 shows the total difference in pressure drop between the pressure drop at 800 mA cm^{-2} and the pressure drop at each current density i.e., ΔP_{800}

$_{mAcm\text{-}2} - \Delta P_{50mAcm\text{-}2}$. For example, 800 → 50 mA cm^{-2} contains five boxes since each trial ended at 50 mA cm^{-2} and 800→600 mA cm^{-2} only has one box since only one trial includes the 600 mA cm^{-2} operating point.

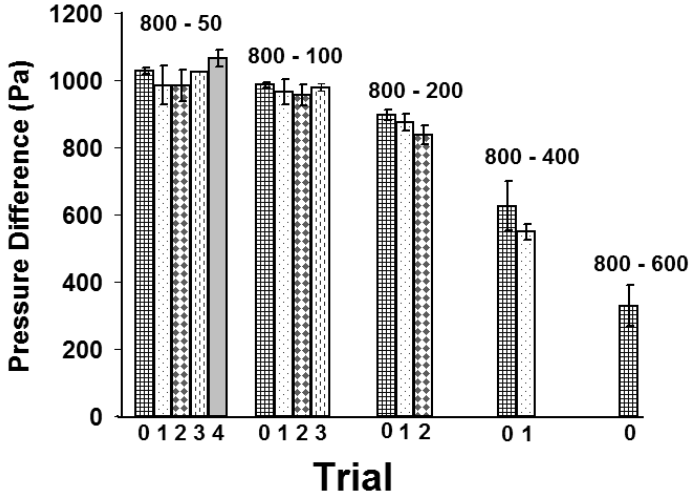

Figure 48. Difference in pressure drop from the 800 mA cm^{-2} pressure drop for the five approaches described in Table 12 (reprinted from Anderson et al. [142] with permission from Elsevier)

The results show that the decrease in pressure drop from the pressure drop at 800 mA cm^{-2} to each lower current density is similar within experimental error regardless of the size of the jump. For example, the pressure drop at 50 mA cm^{-2} is the same whether the path goes from 800→400→200→100→50 mA cm^{-2} or simply from 800→50 mA cm^{-2}. This result implies that the balance of water introduced and subsequently accumulated at each operating condition quickly reaches equilibrium. However, the dynamic behavior of the pressure drop signals is different depending on the size of the descending step change, as reflected in the pressure drop signals shown in Figure 49 for the two cases of Trial 1 and Trial 4 at 50 mA cm^{-2}.

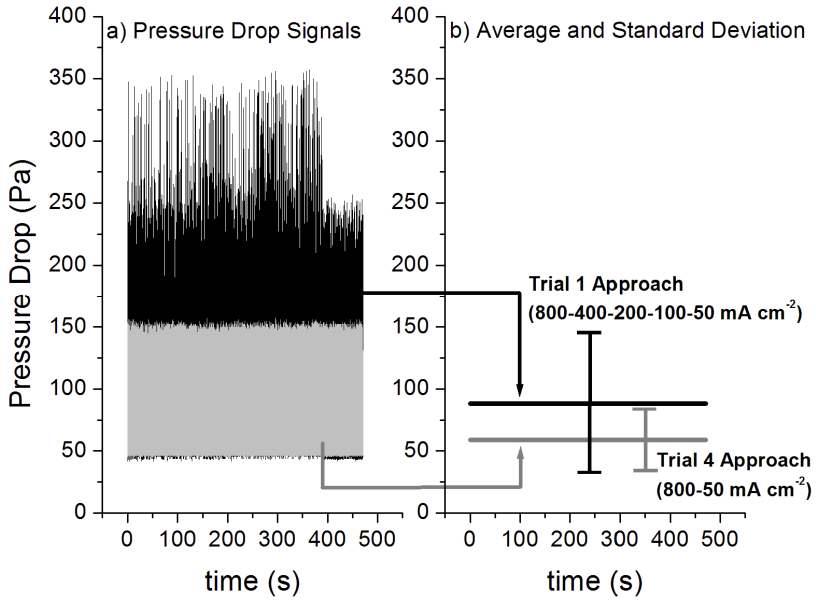

Figure 49. Pressure fluctuation signals for the Trial 1 and Trial 4 approaches (Table 12) to 50 mA cm^{-2} (reprinted from Anderson et al. [142] with permission from Elsevier)

The average pressure drops are within the standard deviation of the data set despite clearly different dynamic behavior. The average value and standard deviations of the pressure signals for both approaches are calculated and shown in Table 13.

Table 13 Pressure drop and standard deviations for Trial 1 and Trial 4 paths (Table 12) to 50 mA cm^{-2} (reprinted from Anderson et al. [142] with permission from Elsevier)

Simulated i (mA cm^{-2})	Pressure Drop (Pa)	Δ P St.dev (Pa)
50	88	57
100	108	37
200	199	26
400	525	23
800	1074	31
Simulated i (mA cm^{-2})	**Pressure Drop (Pa)**	**Δ P St.dev (Pa)**
50	59	25
800	1123	38

The average value of the pressure drop at 50 mA cm^{-2} is similar for both cases. However, when a multi-step approach is used (800 to 400,200,100,50 mA cm^{-2}), the resulting pressure drop at 50 mA cm^{-2} fluctuates much more than the single-step approach to 50

mA cm^{-2} from 800 mA cm^{-2} (standard deviations of 57 and 25 Pa, respectively). From visual inspection using the optical window in the fuel cell, no noticeable/quantitative difference was observed in the flow pattern and no large slugs were noticeable. However, it is likely more water was accumulated with more steps, hence a slightly larger pressure drop and greater oscillations in the pressure drop signal, which is consistent with the work of Ma et al. [32]. This is due to the total amount of injected water in each case, which is shown in Table 14. In the case of the Trial 1 path, nearly 2.5 mL of water is injected vs. only 1.4 mL in the case of the Trial 4 path.

Table 14 Water injection rates and total cumulative injection amount based on 8 minutes per point for Trial 1 and Trial 4 from Table 12 and Figure 49

Current density (mA cm^{-2})-Trial 1 path	Volumetric liquid water injection rate (mL hr^{-1})	Cumulative liquid water injection (mL)	Current density (mA cm^{-2})-Trial 4 path	Volumetric liquid water injection rate (mL hr^{-1})	Cumulative liquid water injection (mL)
800	9.9	1.3	800	9.9	1.3
400	4.9	2.0	50	0.6	1.4
200	2.5	2.3			
100	1.2	2.5			
50	0.6	2.5			

It should be noted that the potential for additional accumulation would be difficult to see visually since the total volume of water injected is so small, but a potential for additional accumulation does explain the observed results.

4.2.1.5 Effect of an initially flooded state

All previous experiments began with dry cathode flow field channels. However, it is also important to explore the pressure drop hysteresis when the channels are already flooded since the current density of an operational fuel cell will likely be changed in either an ascending or descending manner once water is already in the channels. Initial flooding in the channels was accomplished by injecting the cathode flow channel full of water with the syringe pump injecting water through the GDL into the channel. Once air

flow began, the initial condition in all flooding cases quickly became a combination of droplets on the GDL surface, liquid slugs (water droplets touching all four walls), and annular droplets (water film on the gold-coated channel walls).

The initially flooded case exhibited pressure drop hysteresis, but the ascending pressure drop was higher than the descending case. This result is the opposite of the dry start case. A typical case is shown in Figure 50 for the SGL 25 BC GDL at an air stoichiometry of 2.

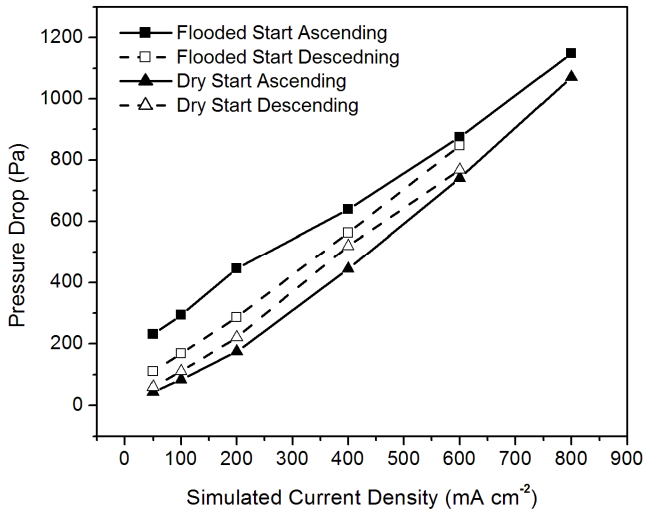

Figure 50. Effect of initial condition on pressure drop: dry vs. flooded for the SGL 25 BC GDL [P_{gas} = 0 kPag, T_{gas} = ambient, dry air] (reprinted from Anderson et al. [142] with permission from Elsevier)

In the dry case, the pressure drop for the ascending case is lower than the descending case because the accumulated water from the descending approach is not removed by the lower air flow rates. Since the amount of water initially present in the flooded channels is greater than the amount accumulating from water breakthrough after a dry start, the ascending pressure drop for a flooded start was higher than the initially dry ascending or descending pressure drop. Once a sufficient air flow is reached in the initially flooded ascending case (e.g. λ_{air}=2, i = 800 mA cm^{-2}), most of the initial water is expelled from the channels, lowering the pressure drop of the subsequent descending approach. Enough

water accumulates in the channel in either case to cause the descending approaches to be higher than the ascending approach from a dry start. The higher descending approach from a flooded start can be attributed to the continuous flow of water through the GDL since the flooded start begins after breakthrough has already occurred. Thus, more total water can enter and subsequently accumulate in the flow field channels in this case.

Similar results were observed with the SGL 25 BA (5% PTFE) and TGPH-030 (20% PTFE) GDLs. In both cases, the ascending pressure drop was higher than the descending pressure drop when the channels were initially flooded. However, a different behavior was observed with the plain TGPH-030 (0% PTFE) GDL. The less hydrophobic nature of this GDL did not facilitate water removal like the others and no hysteresis effect was noted between the ascending and descending cases of the initially flooded experiments.

All of these specific results also depend on the surface wettability of the landings and channel walls. Bazylak et al. [77] studied surface wettability and showed a hydrophilic solid surface, like the gold coated flow field used in this study, favors droplet spreading and liquid water entrapment between the GDL and landing width. These observations help explain why water spreads in the initial startup of the flooded experiments. In addition, land touching droplets tend to grow faster in an operating fuel cell as shown by Ous et al. [11], which complicates the water removal mechanism and can influence the pressure drop.

4.2.1.6 Non-operating cold study conclusions

Two-phase flow pressure drop hysteresis was studied in a fuel cell in non-operating cold model conditions. Hysteresis is noted when the air flow rate and water injection rate (determined from Faraday's law) are increased and then decreased along the same path.

Initially, little water is able to enter the channel because the pressure barrier through the GDL is too high. At sufficiently high current densities, enough water is forced into the cathode flow field channels to cause two-phase flow. As the air flow rate decreases along the same path, the water is not sufficiently expelled and remains in the channels, leading to a higher pressure drop. This results in pressure drop hysteresis between the ascending and descending cases. The following conclusions were drawn from the non-operating experiment:

1. Two-phase flow hysteresis is noted only once a critical simulated current density (water injection rate) is reached to allow sufficient water to enter the channels. Thus, a hysteresis zone is only noted when enough water has entered the channels and the subsequent descending air flow is too low for water to be removed.
2. Two-phase flow hysteresis is eliminated at a stoichiometry of 5. Sufficient air flow is able to remove the same amount of water entering the channels in the ascending and descending case at this stoichiometry, leaving no residual water to induce two-phase pressure drop hysteresis. Stoichiometries less than 5 here lead to accumulation at lower air flow rates, causing pressure drop hysteresis.
3. The inclusion of an MPL and PTFE coating changed the ascending pressure drop. In some cases, water is able to break through the GDLs with MPL at lower ascending current densities, reducing the extent of the hysteresis. While the GDLs with differing PTFE content can have different pressure drops, there is no consistent trend between the pressure drop hysteresis results for the GDLs with 0, 5, and 20% PTFE when no MPL is used. Due to the dissimilar breakthrough characteristics, each GDL should be evaluated individually.

4. The step size in the descending approach does not affect the magnitude of the two-phase flow pressure drop hysteresis. However, the pressure drop signal with a large decreasing step size shows lower fluctuations than the signal with more small steps.
5. The hysteresis effect is inverted when the channel starts as initially flooded for the 25 BA, 25 BC, and TGPH-030 with 20% PTFE GDLs. When water is originally in the channels, the ascending pressure drop is higher than the descending case since the air flow at low current densities is insufficient to remove the initial water. An exception to this is the plain GDL, where no hysteresis is noted for an initially flooded case.

4.3 Pressure drop hysteresis in a non-operating hot model fuel cell[4]

This section explores pressure drop hysteresis in a non-operating fuel cell but at practical fuel cell operating temperatures with fully humidified air [144]. Thus, it is referred to as the non-operating hot model. This section continues the work from Section 4.2 by making the conditions more relevant to an operating PEM fuel cell. The temperature [10,83 ,41], GDL properties [145,16,31], and air stoichiometry [10,83 ,146,38] were chosen for investigation due to their relevance to fuel cell performance [10,146,145,16,31] and two-phase flow pressure drop [83,41,38,69]. This section again focuses on the GDL, specifically the PTFE content and the inclusion of a microporous layer (MPL), since the hydrodynamic conditions in the flow channels differ from those of non-operating cold study (Section 4.2).

[4] These results were published in [144]: R. Anderson, D.P. Wilkinson, X. Bi, L. Zhang, Two-Phase Flow Pressure Drop Hysteresis under Typical Operating Conditions for a Proton Exchange Membrane Fuel Cell, ECS Trans. 28 (2010) 127-137.

4.3.1 Results and discussion

The baseline pressure drop hysteresis results explaining this phenomenon are shown in Figure 51. The same mechanism is noted for hysteresis in these conditions as was discussed in the non-operating cold model case. This is relevant because other pressure drop hysteresis results [55] were based on different flow patterns depending on the direction the gas flow rates were changed. Here, at simulated current densities < 400 mA cm^{-2}, the injected water does not break through the GDL and the pressure drop is similar to the behavior of single-phase flow. Breakthrough is first noted at 400 mA cm^{-2}, and the two-phase pressure drop for 600 mA cm^{-2} and 800 mA cm^{-2} are higher than the single-phase case. As the simulated current density is lowered on the descending path, the pressure drop is greater than both the single-phase case and the ascending approach. This behavior occurs when the air cannot convectively remove the water that enters the channels. As the water is not removed, the descending pressure drop is continually higher than the ascending counterpart. This difference is referred to as the pressure drop hysteresis. Exacerbating this problem is the condensation of liquid water, which must be considered here as an additional water source [10]. This source is a particular problem when fully saturated air is used, since the rate of condensation is much greater than the rate of evaporation when the gas stream is fully humidified [147].

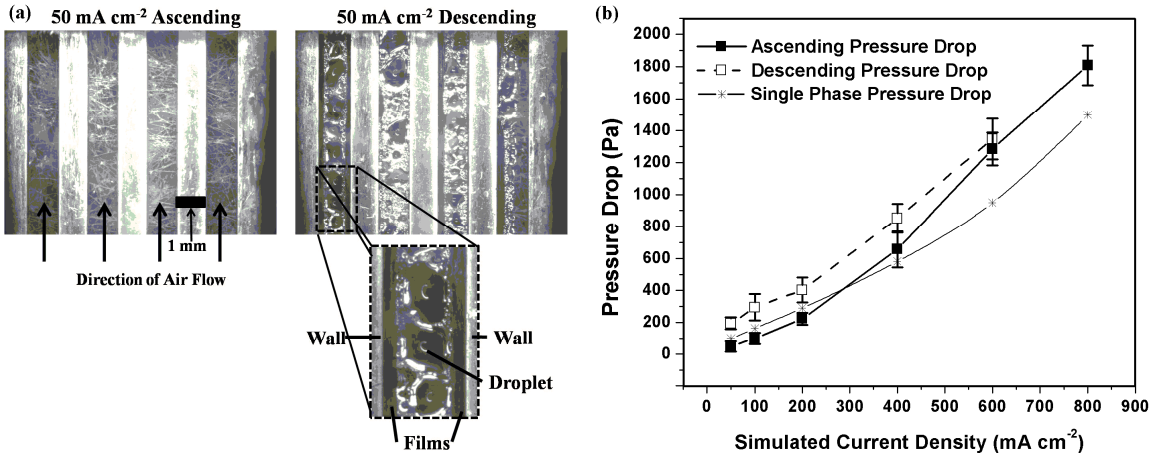

Figure 51. a) Photographs of cathode flow channels at baseline conditions (Table 5) for the ascending and descending case of the 50 mA cm^{-2} simulated current density b) Pressure drop results for the ascending and descending paths depicted in (a) (reprinted from Anderson et al. [144] reproduced by permission from Elsevier)

In the 50 mA cm^{-2} ascending photograph, no liquid water is present due to the low water injection rate not producing breakthrough, and only single-phase behavior is observed. In the 50 mA cm^{-2} descending photograph, water not removed by the air flow has accumulated in the channels. A closer view into the 50 mA cm^{-2} descending case shows a combination of droplets and film flow developing on the channel walls. The liquid water blockage increases the pressure drop, causing the pressure drop hysteresis. In Figure 51b, the error bars represent the standard deviation of the data set for the one trial in Figure 51a. Before water breaks through the GDL (i_{sim} < 400 mA cm^{-2}), the pressure drop signal is steady and the standard deviation is low, while after this point the two-phase flow creates a more oscillatory pressure drop signal, which is indicated in the larger error bars. The results are also repeatable between trials, and the error bars in Figure 53d are the standard deviation from three trials for the baseline operating case.

4.3.1.1 Effect of gas diffusion layer on pressure drop hysteresis

The chosen GDLs (listed in Table 3) address varying the PTFE content (GDL hydrophobicity) and including or excluding a microporous layer (MPL). The remaining operating variables are set to the baseline conditions from Section 3.3. These are similar to the results shown in the non-operating cold model discussion, but are included here since the temperature and relative humidity of the air stream effect the hydrodynamics in the channel. Thus, the droplet detachment behavior may differ, warranting further study into these GDLs. Each GDL also alters the water injection into the flow field channel, as discussed in Section 4.2.1.2.3 on the physical interpretation of the GDL results.

4.3.1.1.1 Effect of PTFE content on pressure drop hysteresis

The PTFE results show that the hydrophobicity alone cannot sufficiently describe the pressure drop hysteresis, and the water breakthrough point must be considered. These results are shown in Figure 52 a-d, which highlights GDLs with 0, 5, and 20% PTFE.

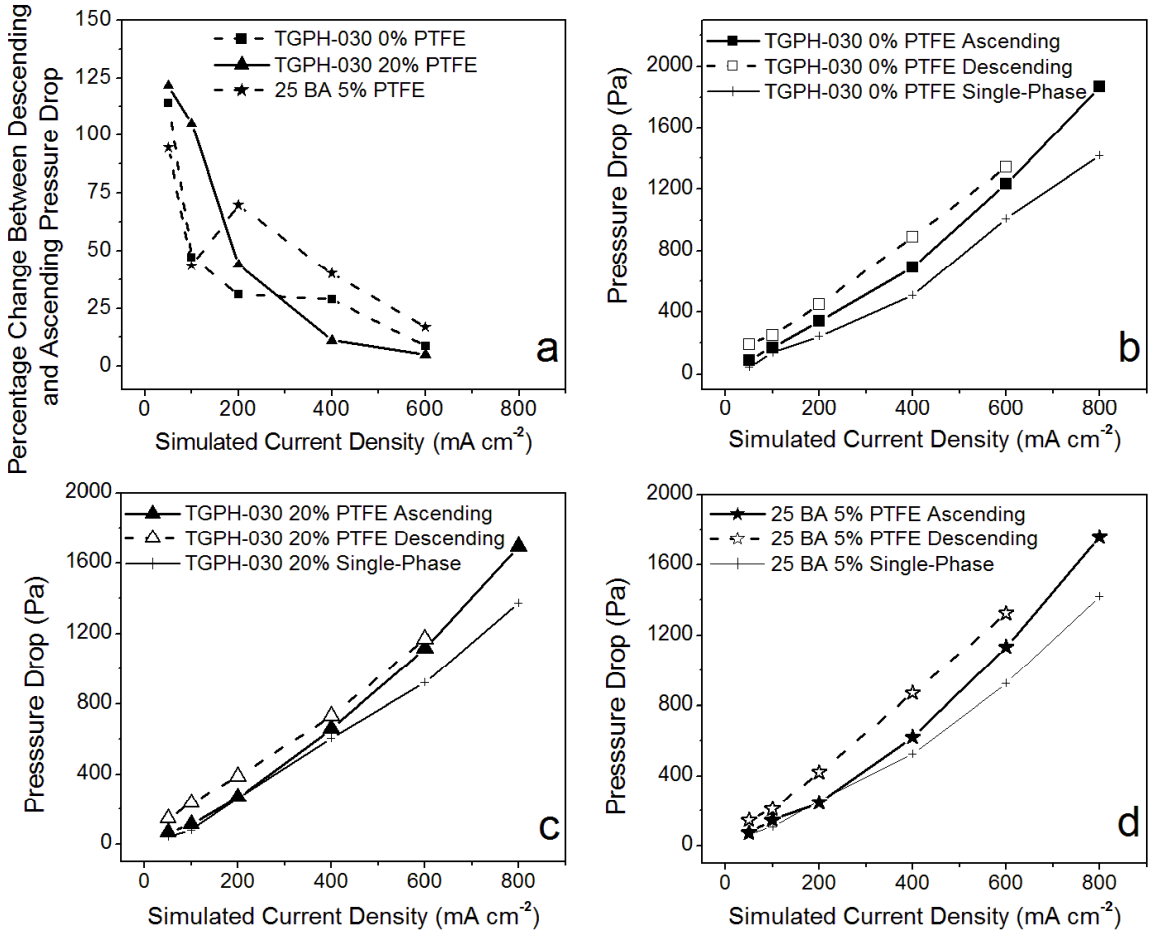

Figure 52. a) Percentage change between descending and ascending approach for 3 GDLS b) Pressure drop hysteresis for TGPH-030 0% PTFE c) Pressure drop hysteresis for TGPH-030 20% PTFE (d) Pressure drop hysteresis for 25 BA 5% PTFE (reprinted from Anderson et al. [144] reproduced by permission of ECS-The Electrochemical Society)

Figure 52a shows the percentage change between the descending and ascending pressure drops for a given simulated current density (Eqn. 45). These results show that the relative degree of pressure drop hysteresis in terms of percentage change is not a function of PTFE content. This is consistent with the results of the non-operating cold model study in Section 4.2.1.2. Also consistent with previous results, the hysteresis effect is lower at higher simulated current densities (higher air flow) due to the convective removal of the injected water and higher at lower simulated current densities due to accumulating water in the descending approach.

Figure 52 b-d show the pressure drop of single-phase flow and two-phase flow for the ascending and descending approach for 0, 5, and 20% PTFE GDLs. These results show how the hysteresis varies between GDLs due to a differing breakthrough point of liquid water, which is apparent when the ascending pressure drop becomes higher than the single-phase pressure drop at a given current density. For the 25 BA GDL with 5 % PTFE and the TGPH-030 GDL with 20% PTFE, breakthrough occurs for $i_{sim} \geq 400$ mA cm^{-2}, while for the TGPH-030 GDL with no PTFE the breakthrough occurs sooner at $i_{sim} \geq 200$ mA cm^{-2}. An earlier breakthrough, as in the case of no PTFE, means the water can increase the two-phase pressure drop earlier in the ascending pressure drop, implying that the relative increase in the descending approach is lower.

4.3.1.1.2 Effect of MPL on pressure drop hysteresis

The inclusion of a microporous layer (MPL) also dictates how water enters the cathode flow field channels. The hysteresis results are highlighted in Figure 53.

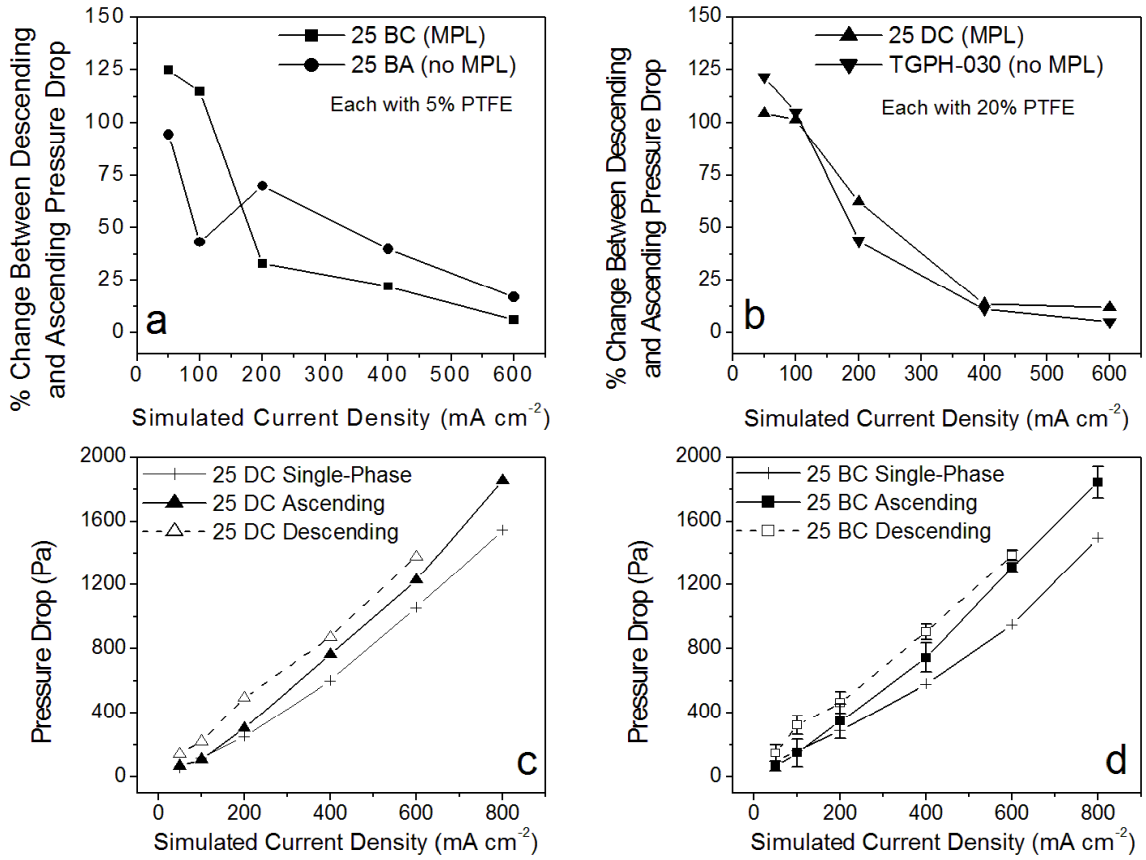

Figure 53. a) Percentage change between descending and ascending approach for 5% PTFE GDLs 25 BA and 25 BC b) Percentage change between descending and ascending approach for 20% PTFE GDLs 25 DC and TGPH-030 20% PTFE c) Pressure drop hysteresis for 25 DC GDL (d) Pressure drop hysteresis for 25 BC GDL (reprinted from Anderson et al. [144] reproduced by permission of ECS-The Electrochemical Society)

Figure 53a and Figure 53b show no correlation between the inclusion of an MPL and the pressure drop hysteresis (with PTFE content held constant in each figure). There is also no clear trend in terms of the point of water breakthrough, which has an influence on the extent of the pressure drop hysteresis. An interesting example of this behavior helps explain the results in Figure 53a, where the percentage change both decreases and increases with i_{sim} for the 25 BA GDL. Particularly interesting is the percentage change for the 25 BA GDL at 200 mA cm^{-2}. The pressure drop results that explain this behavior are shown in Figure 54; the results highlighted in Figure 54a are examined more closely in Figure 54b.

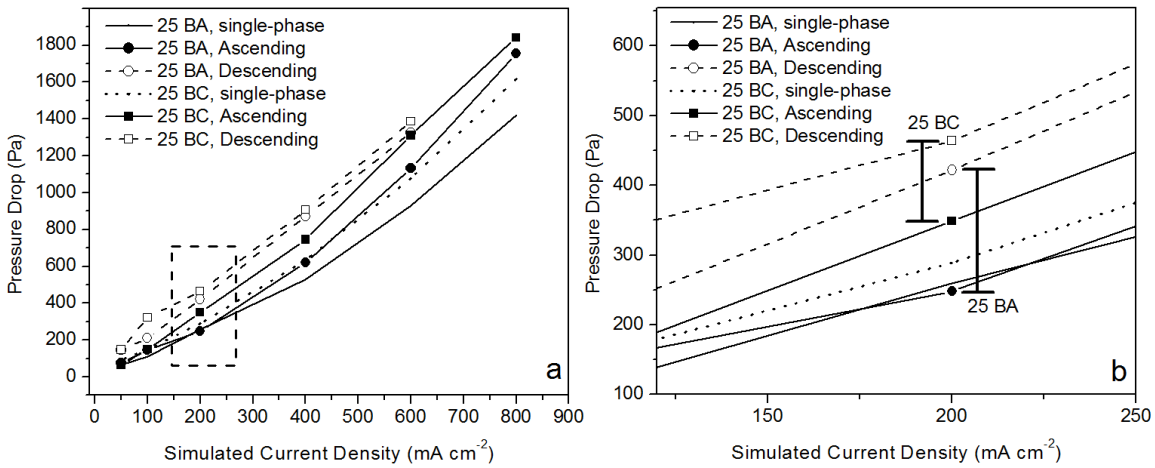

Figure 54. a) Pressure drop for the 25 BC and 25 BA GDLs for single-phase, ascending approach, and descending approach at all simulated current densities and b) pressure drop for the 25 BC and 25 BA GDLs for single-phase, ascending approach, and descending approach at 200 mA cm^{-2} (i_{sim})

The results in Figure 54b show two important points: the 25 BA ascending pressure drop is the same as the single-phase pressure drop while the 25 BC GDL has experienced breakthrough and its ascending pressure drop is higher than the single-phase; the difference between ascending and descending approach is much higher for the 25 BA GDL due to the lower ascending pressure drop. Thus, a large percentage change is noted at 200 mA cm^{-2} with the 25 BA GDL, causing the increased hysteresis noted in Figure 53a. This behavior is consistent over the three trials.

Overall, the pressure drop hysteresis effect must be evaluated for each GDL due to the differing water breakthrough points. These results also suggest that water condensing from the humidified air stream plays a role in the accumulation of liquid water, since this accumulation can occur independently of the MPL or individual GDL properties.

4.3.1.2 Effect of air stoichiometry on pressure drop hysteresis

Air stoichiometry is an important variable in pressure drop hysteresis because a sufficiently high air flow can convectively remove residual injected water, negating the hysteresis [142]. The results for stoichiometries 1-4 are shown in Figure 55. This variable

is important to consider again (having already been established in the non-operating cold model study, Section 4.2.1.1) since the temperature and relative humidity effects alter the water removal abilities of the air steam. The percentage change between the descending and ascending approach is shown in Figure 55a, and the pressure drop hysteresis results for stoichiometries 1 and 4 are shown in Figure 55b. All other variables are held at the baseline conditions.

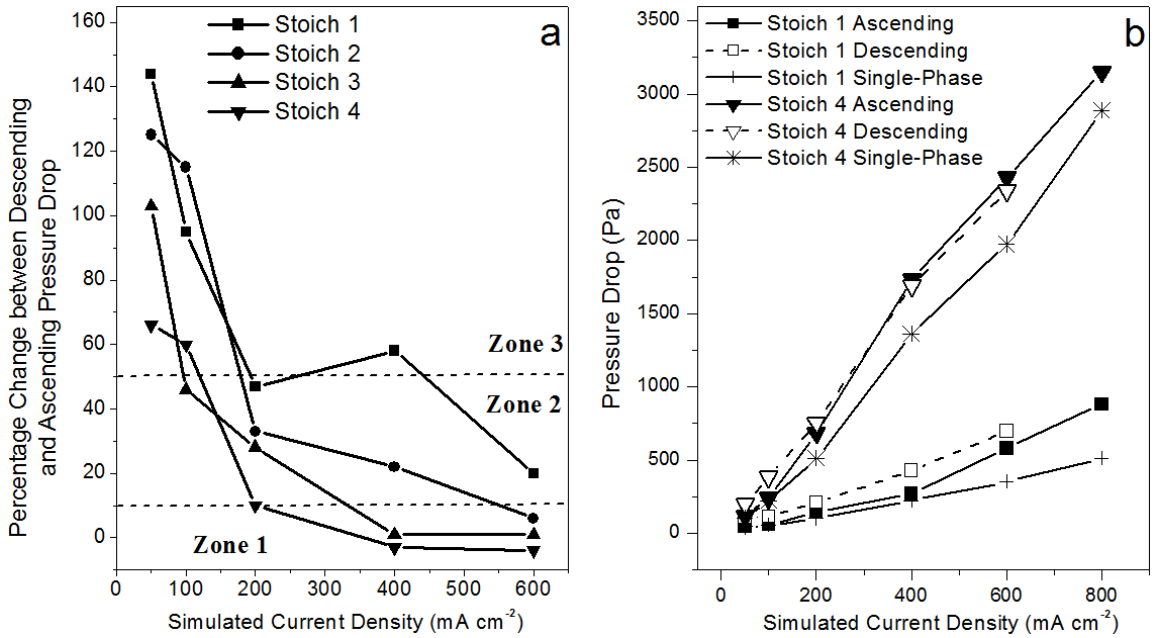

Figure 55. Effect of air stoichiometry on pressure drop hysteresis: a) Percentage change between the descending and ascending pressure drop at baseline conditions for air stoichiometries 1 through 4, b) Pressure drop results for air stoichiometries 1 and 4 (reprinted from Anderson et al. [144] reproduced by permission of ECS-The Electrochemical Society)

To clearly illustrate the relative effect of pressure drop hysteresis, Figure 55a identifies three zones (1, 2, and 3) that represent qualitative levels of hysteresis: zone 1 indicates low hysteresis while 3 represents high hysteresis. These results show that the higher air stoichiometry of 4 is more successful at removing excess water, which reduces the overall degree of hysteresis. For a stoichiometry of 4 at simulated current densities $\geq$ 200 mA cm^{-2}, the hysteresis is low, while for a stoichiometry of 1 the hysteresis is always at least moderate and is high for simulated current densities $\leq$ 400 mA cm^{-2}. The hysteresis

effect is high for i_{sim} < 200 mA cm^{-2} for all stoichiometries studied, even at the higher stoichiometries. While higher flows can reduce the hysteresis, it should be noted that high stoichiometries are coupled with an additional parasitic power loss due to an increased overall pressure drop. Compared to the non-operating cold model (Figure 38), the percentage change is higher due to more water accumulation on the descending approach from condensation.

4.3.1.3 Effect of temperature on pressure drop hysteresis

The effect of temperature is seen on both the overall magnitude of the pressure drop and the extent of the pressure drop hysteresis. The temperatures studied were 30°C, 50°C, 75°C, and 90°C with all other variables at baseline conditions (air stoichiometry = 2, RH = 100%, 25 BC GDL). Figure 56a presents the results for the percentage change between the descending and ascending curves and Figure 56b shows the pressure drop hysteresis results for 30°C and 90°C.

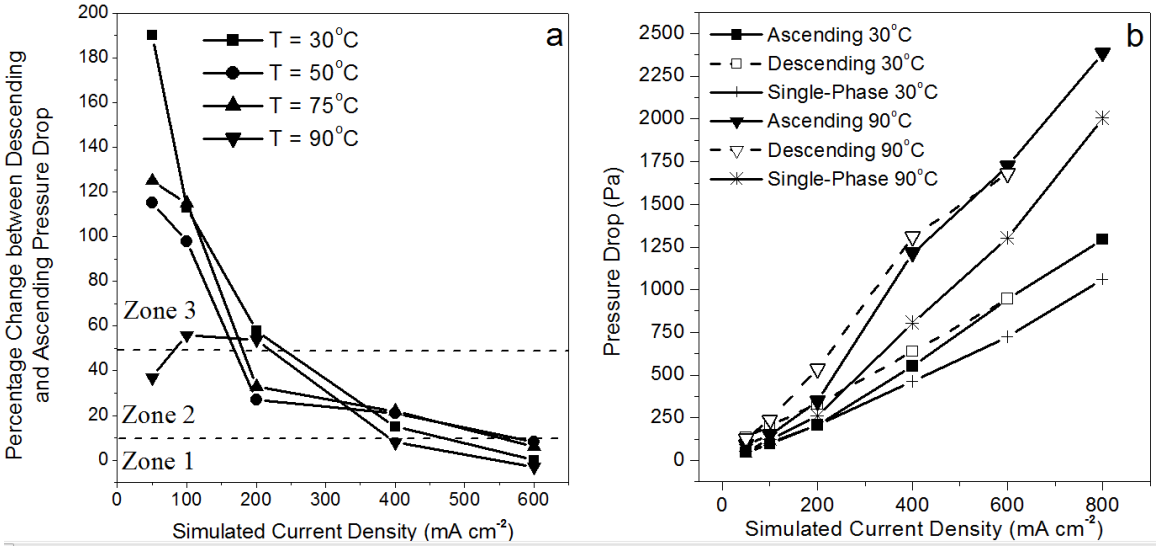

Figure 56. Effect of temperature on pressure drop hysteresis a) Percentage change between the descending and ascending pressure drop at 30, 50, 75, and 90°C, b) Pressure drop results for 30°C and 90°C (reprinted from Anderson et al. [144] reproduced by permission of ECS-The Electrochemical Society)

As shown in Figure 56b, the pressure drop at 90^{o}C in either the ascending or descending approach is higher than at 30^{o}C due to the increased gas viscosity and gas velocity at higher temperatures. Regardless of the temperature used in this study, at a stoichiometry of 2 the Reynolds number of the air is still in the laminar region (for $\lambda_{air} = 2$, $i_{sim} = 800$ mA cm^{-2},T = 90^{o}C, Re $\approx$ 400). Hysteresis is noted in either case, though it is unclear, especially at current densities < 200 mA cm^{-2}, what the relative magnitude of the effect is based on Figure 56b alone. Figure 56a addresses this issue by showing the percentage change between the descending and ascending pressure drop at a given simulated current density for each temperature studied. Lines have again been drawn in Figure 56a for qualitative purposes to divide the figure into three regions, 1, 2, and 3, to further show the extent of hysteresis. In zone 3, the hysteresis has a major effect relative to the ascending pressure drop (>50%). This zone is of particular concern at low temperatures (30^{o}C) and low air flows (i_{sim} < 200 mA cm^{-2}) because the low air flow rate is insufficient to remove excess water and more condensation can occur at lower temperatures. Conversely, zone 1 has a diminished hysteresis effect (<10%) because the air flow rate is sufficiently high to remove residual water injected into the channels. Zone 2 has intermediate hysteresis because the moderate air flows can remove some but not all of the residual water, causing a higher pressure drop for the descending approach.

These results show that at 90^{o}C for $i_{sim} \leq 200$ mA cm^{-2} the percentage increase in pressure drop is between approximately 40 and 60%, while at 30^{o}C the percentage increase is between approximately 60 and 200%. This result means a higher temperature lowers the relative degree of the pressure drop hysteresis at low i_{sim}. However, above 200

mA cm^{-2}, the results in Figure 56a show a similar trend and there is no clear influence of temperature on the relative influence of the hysteresis effect.

These results are consistent with theory about water accumulation in the flow field channel. Firstly, the higher temperature leads to a slight increase in the gas velocity, which increases the convective water removal ability of the air, offsetting accumulation. Secondly, the increase in temperature lowers the surface tension of the water [18], allowing it to be removed more easily from the flow field channels, again lowering accumulation. Finally, the higher temperature gas can evaporate water more readily than the lower temperature gas (both in terms of the rate of evaporation and the total amount of water vapor that can exist in the gas stream). Thus, 30^{o}C is more prone to additional condensation while 90^{o}C is more prone to additional evaporation if there are any local deviations from 100% RH.

4.3.2 Non-operating hot study conclusions

This work is an extension of the hydrodynamic baseline established in the non-operating cold model, and here pressure drop hysteresis was noted over a range of conditions relevant to an operating fuel cell.

- Higher air flow rates (either via higher simulated current density or higher air stoichiometry) can reduce the extent of the hysteresis. This is because the higher air flow rate can convectively remove more water from the descending approach, mitigating the accumulation of liquid water. However, the overall pressure drop is increased and thus increased stoichiometry alone may not be a suitable mitigation strategy.

- While the water detachment mechanism can be influenced by the hydrophobicity of the GDL due to increased PTFE content, the hysteresis is largely related to the mechanism of water accumulation in the descending approach. Condensation, which can occur in the flow field channels regardless of the GDL, plays a large role in addition to the water breakthrough, which is a function of the GDL. The higher two-phase pressure drop occurs once water enters the channels, and the breakthrough point can occur at different i_{sim} depending on the GDL. Thus, each GDL must be studied individually.
- A higher temperature lowers the relative influence of the pressure drop hysteresis, but more energy is needed to sustain higher temperatures, which represents another potential parasitic power loss. Greater pressure drop hysteresis at lower temperature is due to increased condensation, higher surface tension, and lower gas flow rates at lower temperatures, which increases the accumulation of liquid water on the descending approach.

5 Two-phase flow pressure drop hysteresis in an operating proton exchange membrane fuel cell[5]

The hydrodynamic baseline for pressure drop hysteresis was established in Chapter 4. This chapter explores pressure drop hysteresis in an operating fuel cell at practical fuel cell operating conditions [148].The current density is no longer 'simulated' since the water is produced electrochemically. This is an extension of the work done in the non-operating setup (Sections 4.2 and 4.3).

5.1 Introduction

As in Chapter 4, pressure drop hysteresis is explored in ascending and descending approaches. The ascending approach was as follows: 50, 100, 200, 400, 600, 800, 1000 mA cm^{-2}. The descending approach was this path in reverse beginning at 800 mA cm^{-2}. This includes an additional point on the ascending approach (1000 mA cm^{-2}) compared to the path studied in the non-operating setup. This was taken as the approximate maximum current density since under these baseline conditions it is close to the limiting current density, thus the range covers all current densities possible in this experimental setup. The experimental conditions are described in Section 3.4.

As in Section 4.3, variables studied include the air stoichiometry, temperature, and inclusion of a microporous layer (MPL). The temperature [10,83 ,41], GDL properties [145,16 ,31], and air stoichiometry [10,83 ,146 ,38] were chosen for investigation due to their relevance to fuel cell performance [10,145 ,16 ,31 ,146] and two-phase flow pressure drop [83,41 ,38 ,69]. An empirical approach to predicting the two-phase pressure drop based on the Lockhart-Martinelli approach is presented. A purging method is also

[5] Portions of these results were published in [148]: R. Anderson, D.P. Wilkinson, X. Bi, L. Zhang, Two-phase flow pressure drop hysteresis in an operating proton exchange membrane fuel cell, J. Power Sources 196 (2011) 8031– 8040.

presented that can lower the pressure drop hysteresis. This chapter also includes a summary and comparison of the three experimental approaches (non-operating cold through operating) with a focus on dimensionless correlations. This work concludes with a preliminary study into pressure drop hysteresis in a more typical (non-visualization) fuel cell.

5.2 Experimental results and discussion

Pressure drop data and polarization curves are presented for the variables studied. It should be noted that while the ascending and descending approaches show differences in pressure drop, the electrochemical performance in either approach is generally within 10 mV at a given current density. Thus, only the ascending approaches of the electrochemical polarization curves are presented for clarity unless otherwise noted. Also, in the visualization cell, the limiting current density is approached or reached at approximately 1000 mA cm^{-2}, leading to low repeatability and accuracy at these points. These data points are included only to indicate that the fuel cell has reached the limiting current density. The results also indicate that this fuel cell performs as well as or better than other visualization cells with parallel channels in the literature [10], where it is noted that visualization cells have lower performance than traditional fuel cells [149]. These losses are often attributed to ohmic losses due to the novel materials used in transparent cells. However, this effect is not limiting behavior here since the gold coating of the flow field plates provides sufficient conductivity. For the visualization cell in this thesis, there are losses at higher current densities due to reactant movement between flow field channels due to imperfect sealing and compression between the optical manifold and the flow field plate. Since the transparent fuel cells allow direct observation of the water in

the cathode channels, the reduction in performance towards higher current densities is considered acceptable.

The pressure drop data is presented as the percentage change between the descending and ascending approach (Eqn. 45) and also as the two-phase flow multiplier (Eqn. 37). The two-phase flow multiplier is utilized in the operating fuel cell pressure drop analysis because the overall pressure drop is closely tied to the overall efficiency of the fuel cell. Thus, the relevance to the PEM fuel cell is more clearly highlighted.

5.2.1 Causes of pressure drop hysteresis in an operating fuel cell

Pressure drop hysteresis results for air stoichiometry 1.5 are shown in Figure 57a. A stoichiometry of 1 was not considered due to unstable electrochemical performance. The highlighted area focuses on the hysteresis, where the descending pressure drop is higher than the ascending pressure drop at current densities < 200 mA cm^{-2}. The magnitude of the pressure drop is consistent with fuel cell literature for parallel channels [149,150]. Figure 57b shows the ratio of the descending pressure drop to the single-phase pressure drop at all stoichiometries studied and at each current density (descending two-phase flow multiplier). The fitted surface plot is provided for visualization purposes. It is apparent that there is a sharp increase in pressure drop at lower current densities and stoichiometries. The pressure drop behavior is important at lower current densities because low loads are often used for high energy conversion efficiency [205] and dynamic automotive fuel cells often operate at less than 20% of the rated power, making the regime of lower gas flow important [151]. Lu et al. [62] also showed that flow fluctuation is greatest at low flow and the two-phase flow multiplier (in the range of 1.5-2.5) is also higher at lower air flow.

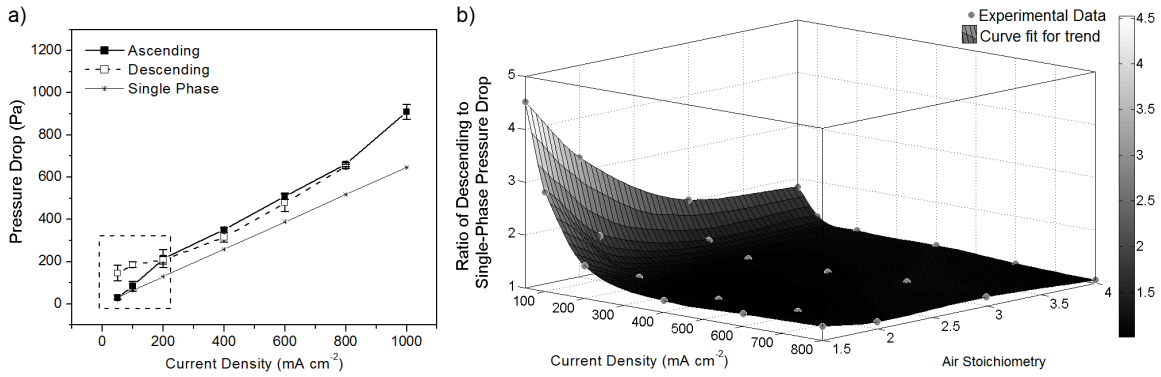

Figure 57. a) Pressure drop results for λ_{air} = 1.5; b) Ratio of the descending pressure drop to single-phase pressure drop at λ_{air} = 1.5, 2, 3, 4 for all current densities (reprinted from Anderson et al. [148] with permission from Elsevier)

At an air stoichiometry of 1.5, the two-phase pressure drop in both the ascending and descending approach is higher than the single-phase pressure drop at current densities ≥ 200 mA cm^{-2}. Also, at i > 200 mA cm^{-2}, the ascending and descending approach exhibit similar behavior, meaning that there is similar two-phase behavior in either approach. However, below 200 mA cm^{-2}, the descending pressure drop is noticeably higher at the lower stoichiometry due to more liquid water accumulating in the descending approach. As in the case of the non-operating hot model, water enters the flow field channels via two mechanisms: i) liquid water breakthrough from the GDL and ii) humidified gas condensation. Condensation is a particular problem since the rate of condensation is greater than the rate of evaporation when the gas stream is at 100% relative humidity [152]. These relative rates of evaporation and condensation mean the liquid water must be removed convectively.

The hysteresis highlighted in Figure 57a is explained by an accumulation of liquid water in the descending approach that is greater than the accumulation in the ascending approach. Water accumulation during the ascending and descending approaches at 50 mA

cm^{-2} at baseline conditions (Table 6) is shown in Figure 58a and Figure 58b, respectively. The same location is photographed in both approaches at the channels' exit.

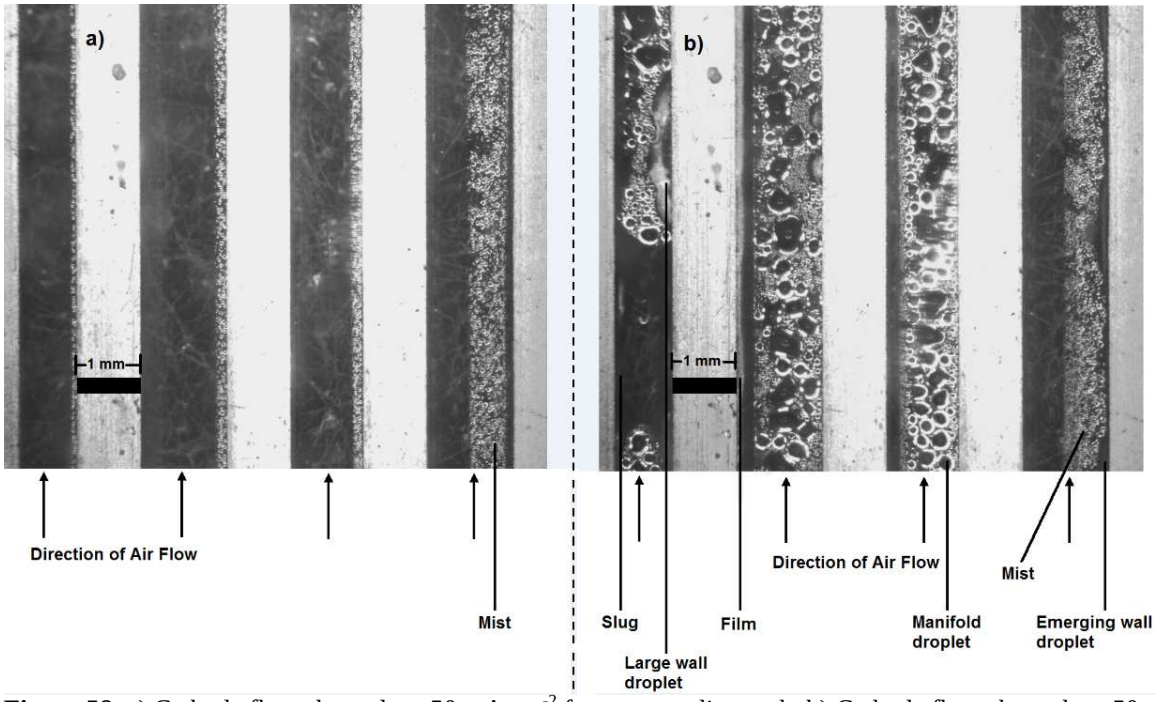

Figure 58. a) Cathode flow channels at 50 mA cm^{-2} for an ascending path; b) Cathode flow channels at 50 mA cm^{-2} for a descending path; λ_{air} = 1.5 with all other conditions at the baseline (Table 6) (reprinted from Anderson et al. [148] with permission from Elsevier)

In the ascending approach, the only two-phase flow pattern is a mist flow that develops on the manifold surface (top wall). In the descending approach, accumulated liquid water led to a combination of slugs, films, wall droplets, and manifold droplets. It is also interesting to note that these descending flow patterns vary with channel, indicative of two-phase flow maldistribution. The increased flooding causes an increase in the pressure drop, resulting in pressure drop hysteresis. Spernjak et al. [149] found a similar flooding mechanism in parallel channels via neutron imaging, where stationary droplets grew over time to form slugs before expulsion. Cathode water accumulation is also noted by Kimball et al. [71] when the cathode is facing 'up', where gravity acts to pull the droplet onto the GDL perpendicular to the direction of flow. By a similar mechanism, the slightly

higher ascending pressure drop (at 400 and 600 mA cm^{-2}) is likely due to some water condensation at the lower flow rates. This water is convectively removed by higher air flow rates later in the ascending approach (800 mA cm^{-2}) and does not re-accumulate in the descending approach at the moderate to high current densities (at $i \geq 400$ mA cm^{-2} the higher flow rates are less prone to this condensation).

The mechanism described here qualitatively matches the experimental results from the non-operating studies [142,144]. A comparison between the current operating study and the non-operating hot model fuel cell results are shown in Figure 59a and Figure 59b, respectively. Both experiments are with the 25 BC GDL at 75^{o}C with fully humidified air and an air stoichiometry of 2. However, in the non-operating case, the pressure is ambient (vs. 206.8 kPag in the operating cell) and water was injected externally into the cathode to simulate water production under the assumption that all of the water would enter the cathode. As that assumption is removed in the operating fuel cell, the hysteresis zone changes but is still a relevant consideration. In the non-operating case, the overall pressure drop increases due to the increased gas velocity (no increased backpressure). GDL saturation and water breakthrough dynamics can also be alerted in the operating case since electrochemically produced water is distributed with the current distribution. Also in the operating cell, water can move toward the anode, which limits the amount of water entering the cathode, reducing the impact of two-phase flow. However, this transport mechanism is likely small when both anode and cathode gas streams are fully humidified. Thus, in fuel cells experiencing little anode water removal, cathode pressure drop hysteresis may be a greater concern.

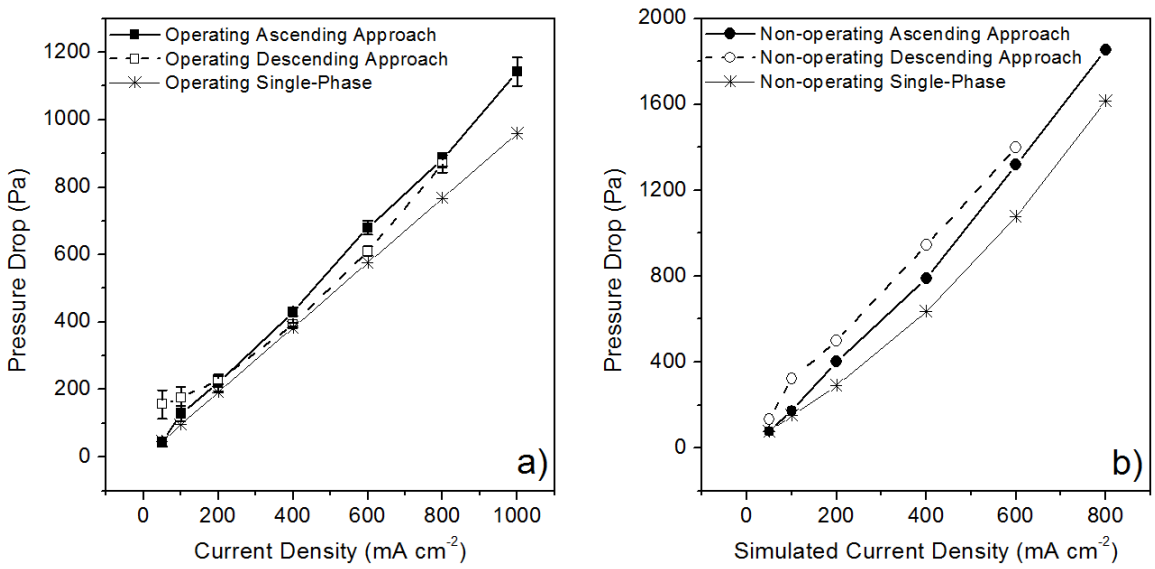

Figure 59. Pressure drop results at the baseline conditions for a) the operating fuel cell (baseline conditions from Table 6); b) the non-operating hot fuel cell (T = 75°C, RH = 100%, GDL = SGL 25 BC, P_{gas} = 0 kPag) (reprinted from Anderson et al. [148] with permission from Elsevier)

These results are also relevant to fuel cells with typical graphite bipolar plates. The water emerging from the hydrophobic GDL surface can spread to the hydrophilic walls as shown in Figure 58b. In this study, the contact angles of the gold-coated flow field plates and the clear manifold are both ~60°. These values are comparable to typical graphite plates where the contact angle is between 70-80° [23], with some experimental graphite plates measured lower at 46° [77]. Graphite plate fuel cells thus approximately match the wetting properties of the experimental apparatus utilized in this study. Preliminary pressure drop hysteresis results in typical graphite plates are discussed in Section 5.5.

5.2.2 Effect of stoichiometry

The additional accumulation of water between descending and ascending approaches depends on the ability of the air to convectively remove the liquid water, which is dependent on the gas velocity and therefore gas stoichiometry. Air stoichiometries of 1.5, 2, 3, and 4 were studied as practical fuel cell stoichiometries. This variable is again studied in pressure drop hysteresis (having previously been explored in Chapter 4)

because the increased backpressure reduces the velocity of the air, altering the hydrodynamics in the flow field channels. The remaining operating conditions were set to the baseline conditions described in Table 6. To gauge the extent of the hysteresis, the percentage change between the descending and ascending approach is used, which is defined previously in Eqn. 45.

The results of this analysis are shown in Figure 60a along with the electrochemical performance results shown in Figure 60b. The pressure drop hysteresis is clearly noted at current densities < 200 mA cm^{-2}. In this region, the percentage change between approaches is most noted for the lowest stoichiometry, 1.5, and is reduced with each increase in air flow rate. The increasing air flow rate (and therefore increasing convective water removal ability) allows less accumulation of liquid water in the descending approach, causing the hysteresis to diminish; the air velocity at a stoichiometry of 1.5 is 0.08 m s^{-1} and at a stoichiometry of 4 is 0.21 m s^{-1}. The Reynolds number for this situation is discussed in greater depth in Section 5.3.1 (Figure 77).

A percentage change less than zero (200-600 mA cm^{-2}) indicates the descending pressure drop is lower than the ascending pressure drop, which is the result of slight condensed water accumulation on the ascending approach that is subsequently removed before the descending approach. However, this is a minor effect compared to the lower current densities.

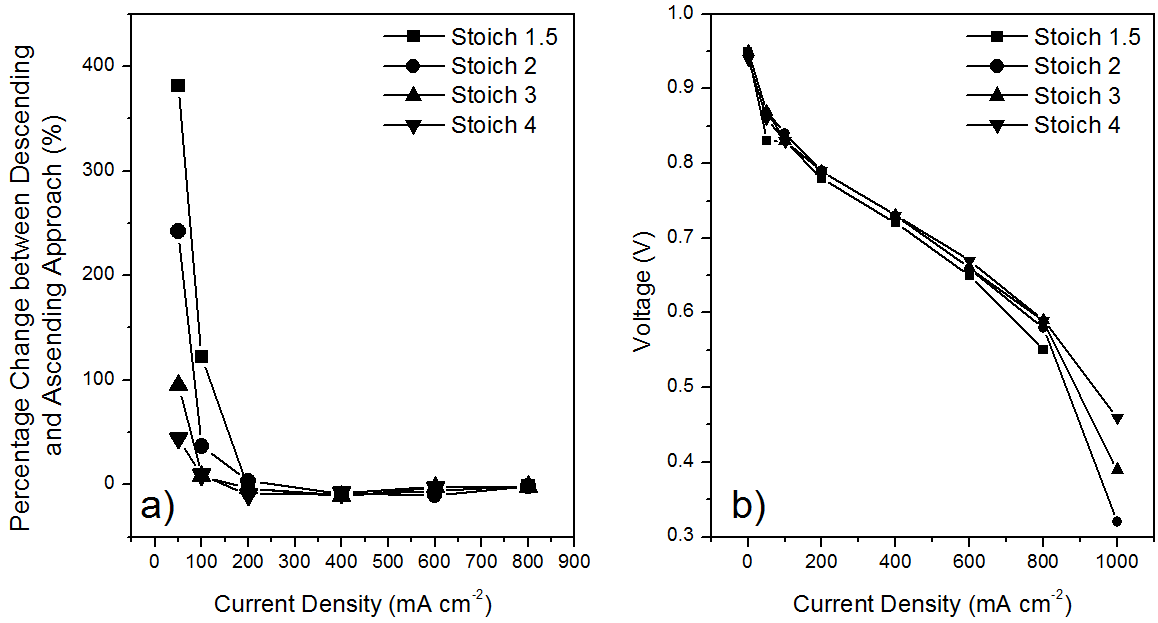

Figure 60. a) Percentage change between descending and ascending pressure drop for λ_{air} = 1.5, 2, 3, 4; b) Ascending polarization curves for λ_{air} = 1.5, 2, 3, 4 (reprinted from Anderson et al. [148] with permission from Elsevier)

The two-phase flow multiplier for the ascending and descending approaches is highlighted in Figure 61a and Figure 61b, respectively. The ascending approach highlights the increased pressure drop due to two-phase flow, meaning that the product water and condensation are increasing the pressure drop. This influence is seen at all stoichiometries, which implies that the product water represents an inevitable parasitic power loss for the system due to an increased pressure drop. The descending approach two-phase flow multiplier shows a large increase in the multiplier in the hysteresis zone (< 400 mA cm^{-2}). As discussed, it is at these lower current densities where additional water accumulates since the low air flow cannot convectively remove the liquid water. The descending two-phase multiplier is also shown in Figure 57b for describing the general mechanism of pressure drop hysteresis.

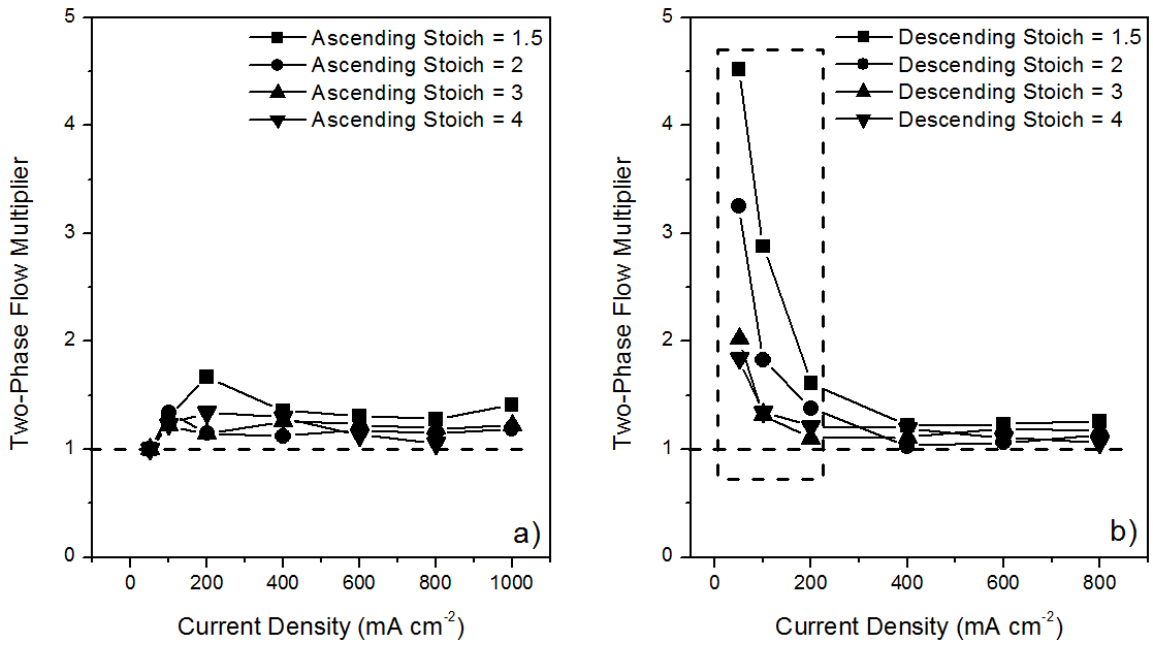

Figure 61. Two-phase flow multiplier for air stoichiometries of 1.5-4 for a) the ascending approach and b) the descending approach with the higher two-phase flow multiplier at low air flow rates highlighted (reprinted from Anderson et al. [148] with permission from Elsevier)

In addition to larger pressure drop hysteresis, the fuel cell does not perform as well electrochemically at an air stoichiometry of 1.5 compared to higher stoichiometries. The lower performance is further exacerbated by voltage signal fluctuations at low current densities, which improve with increasing air stoichiometry as shown in Figure 62. The voltages signals at 100 mA cm^{-2} are shown in Figure 62 for the stoichiometries studied.

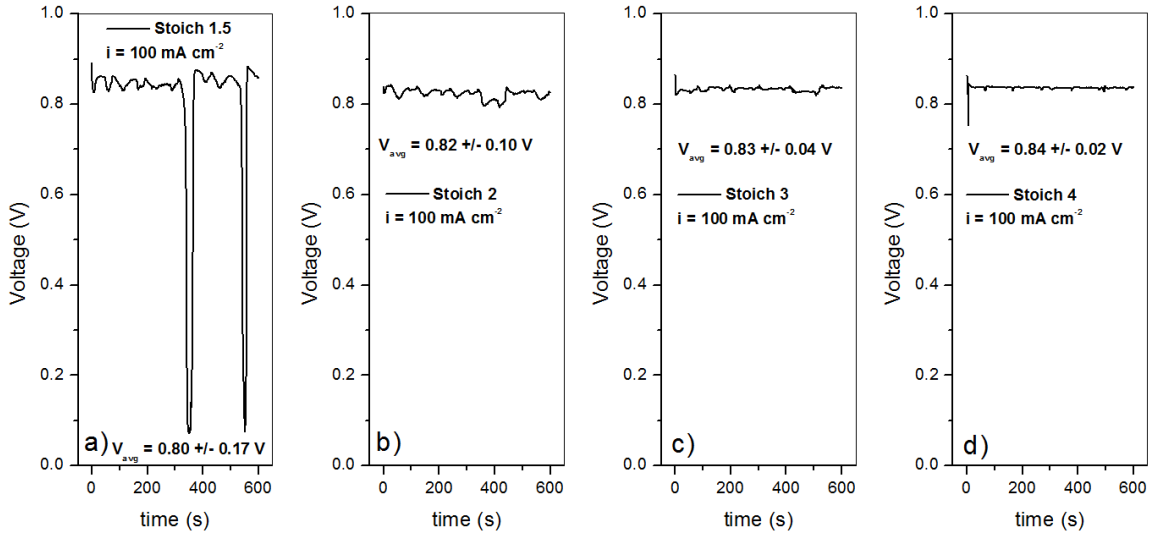

Figure 62. Voltage signals at 100 mA cm^{-2} at a) λ_{air} =1.5; b) λ_{air} = 2; c) λ_{air} = 3; d) λ_{air} = 4 showing improved stability with stoichiometry (reprinted from Anderson et al. [148] with permission from Elsevier)

While there is not a direct relationship between the pressure drop hysteresis behavior and the overall voltage signal, increased flooding at lower flow rates clearly affects the overall stability of the voltage signal. Lower flows can also cause maldistribution in flow field channels and from cell to cell in stacks. A stable signal is advantageous in operation, so mitigating flooding in either approach (ascending or descending) is a priority.

5.2.3 Effect of temperature

The pressure drop hysteresis and cell performance were measured at 50, 75, and 90^{o}C. All other operating conditions were set to the baseline conditions in Table 6. The percentage change between the descending and ascending approaches at these temperatures and the electrochemical performance are shown in Figure 63a and Figure 63b, respectively. It should be noted that at high current densities (around 1000 mA cm^{-2}) the voltage oscillations were very large and not every trial was able to sustain the voltage. Thus, the accuracy of these high current density values is reduced and the data is shown only to point out the limiting current density behavior.

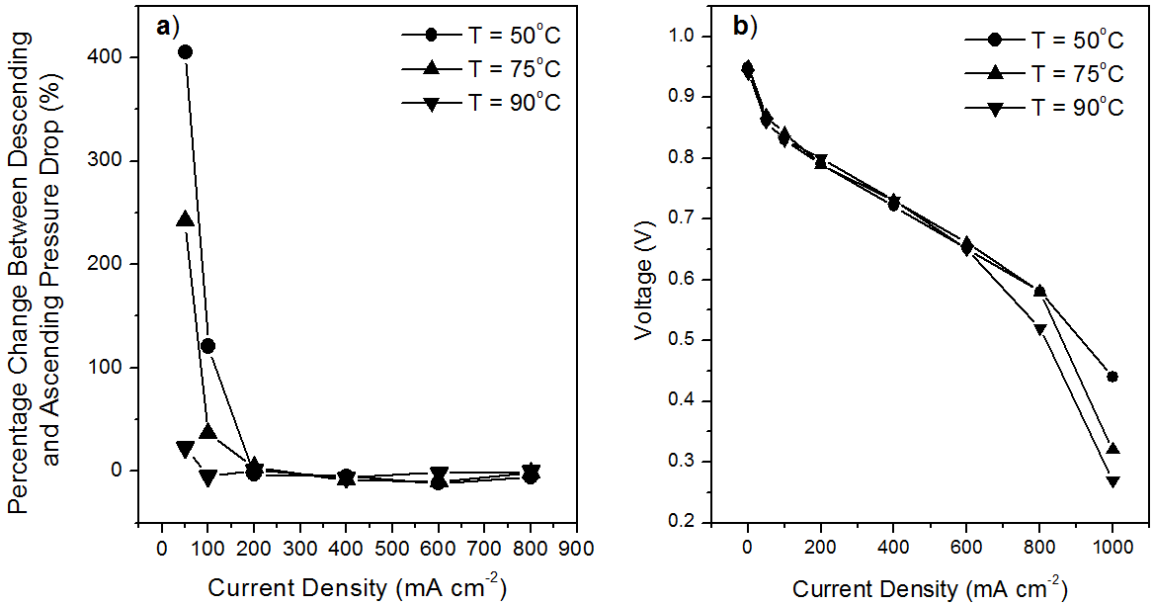

Figure 63. a) Percentage change between descending and ascending approaches for T = 50, 75, 90°C and b) Ascending polarization curves for T = 50, 75, 90°C (reprinted from Anderson et al. [148] with permission from Elsevier)

The lowest temperature has the highest extent of hysteresis, and the hysteresis is reduced with increasing temperature until at 90°C there is little hysteresis. These results are due to the increased air velocity and lower surface tension at higher temperatures, which results in higher convective removal abilities. The increased hysteresis at lower temperatures is also due to the increased condensation rates at lower temperature, resulting in more liquid water accumulation. Also, air at 90°C can evaporate liquid water (if the RH drops below 100% locally) at a faster rate than 50°C [152], which lessens the accumulation at higher temperatures. The higher overall pressure drop at 90°C also means more water can exist in the vapor phase in the gas stream, lowering the effect of condensation in the channels. More liquid water present in the flow channels at lower operating temperatures also agrees with the work of Liu et al. [10] and Owejan et al. [151], who noted liquid water is a problem for automotive applications traveling short distances where lower temperature operation is expected.

As with the stoichiometry, the two-phase flow multiplier provides additional insight into the influence of the two-phase flow pressure drop. Figure 64a and Figure 64b show the two-phase flow multiplier for the ascending and descending approaches, respectively, at 50, 75, and 90°C. For all the temperatures during the ascending approach, the value of $\varphi_{2\text{-phase}}$ stays less than 2 and in some cases is approximately 1. This increase in pressure drop from the single-phase is caused by the two-phase flow resulting from water breakthrough and humidified gas condensation. However, in the descending approach at these temperatures, additional water accumulates and increases the pressure drop, shown by the increased $\varphi_{2\text{-phase}}$ for current densities < 400 mA cm^{-2}. This corresponds directly with the hysteresis zone in Figure 63a.

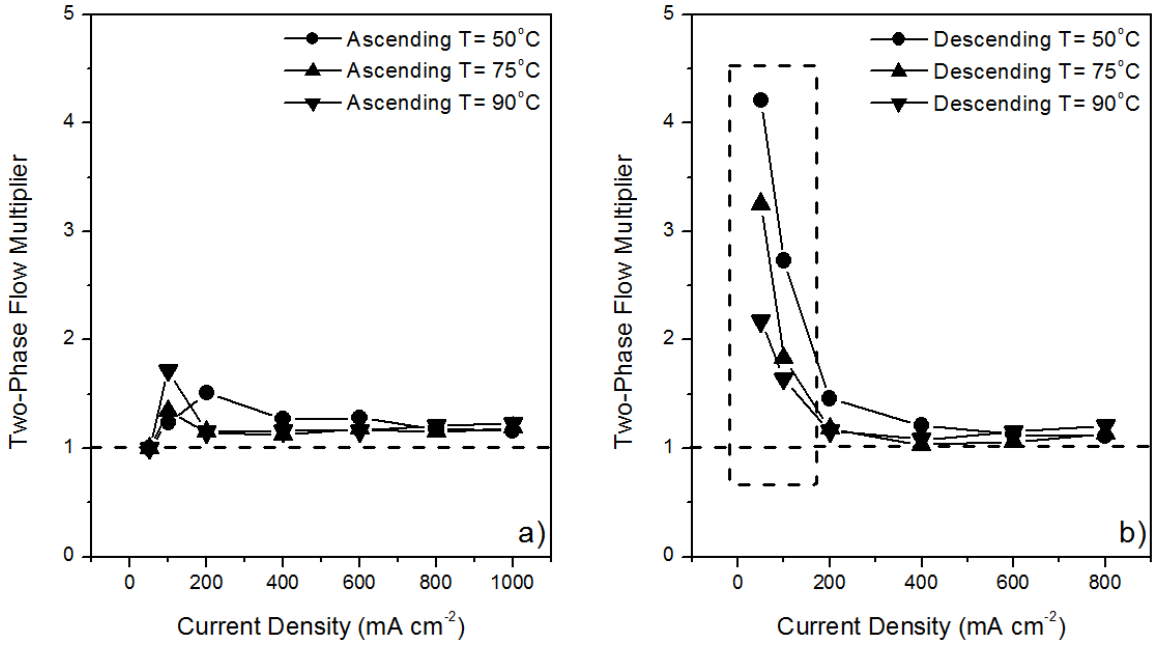

Figure 64. a) Two-phase flow multipliers for a) the ascending approach; b) the descending approach with the higher multipliers at low air flow rates and low temperatures highlighted (reprinted from Anderson et al. [148] with permission from Elsevier)

5.2.3.1 Hysteresis at low temperatures, 30°C

The value of the two-phase flow multiplier for 30°C rises higher than the other temperatures on the ascending approach due to the increase in the cell temperature caused

by the heat of reaction. This issue is further noted in the descending case where the two-phase flow multiplier at 30°C ranges from 2-5, highlighting the combined effects of higher temperature gas and liquid water accumulation. The temperature profiles for the 30°C trial and the 75°C baseline are shown in Figure 65, indicating that the heat from the reaction heats the fuel cell even though the temperature is set at 30°C (the surrounding air is unable to remove the additional heat). A higher current produces more heat, and thus the temperature rises and falls with an increase and decrease in the operating current. Dillet et al. [137] noted significant thermal gradients in their visualization cell as well. The additional heat increases the air temperature, causing an increase in the air viscosity and velocity, which results in a higher pressure drop.

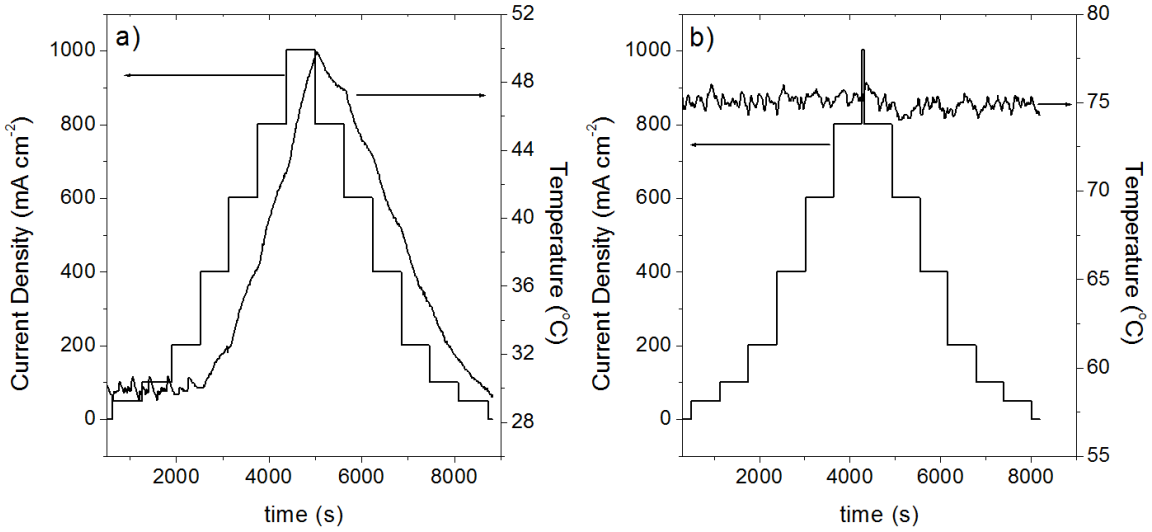

Figure 65. Effect of heat of reaction with an increase in current density on cathode plate temperature: a) Cathode plate temperature profile for $T_{setpoint}$ = 30°C b) Cathode plate temperature profile for $T_{setpoint}$ = 75°C

Since the temperature at 30°C could not be controlled, the results were not further analyzed, and no other electrochemical studies were performed at 30°C.

5.2.4 Effect of microporous layer (MPL)

Lu et al. [153] studied the breakthrough and two-phase flow characteristics of GDLs with and without a microporous layer. Their work shows that GDLs with an MPL exhibit

lower GDL saturation and that the MPL promotes stable water paths with fewer water entry points into the GDL. Conversely, GDLs without an MPL exhibit greater saturation and dynamic breakthrough locations into the flow channels. The observed effect on two-phase flow in the flow channels was that GDLs without an MPL had more uniform water breakthrough over the GDL surface, leading to film flow on the channel walls, while the GDLs with an MPL tend toward the formation of slug flow.

The results for SGL 25 BC (with MPL) and SGL 25 BA (without MPL) on the cathode side are presented in Figure 66. All other operating conditions are at the baseline conditions shown in Table 6. While the 25 BC GDL outperforms the 25 BA GDL electrochemically, which is consistent with the literature [16,31], there is no clear difference in the pressure drop hysteresis, which is consistent with the results of the non-operating hysteresis studies in Section 4.2 and 4.3. The percentage change shows similar behavior between descending and ascending pressure drop for the two GDLs, with each GDL exhibiting hysteresis behavior at current densities < 200 mA cm^{-2}.

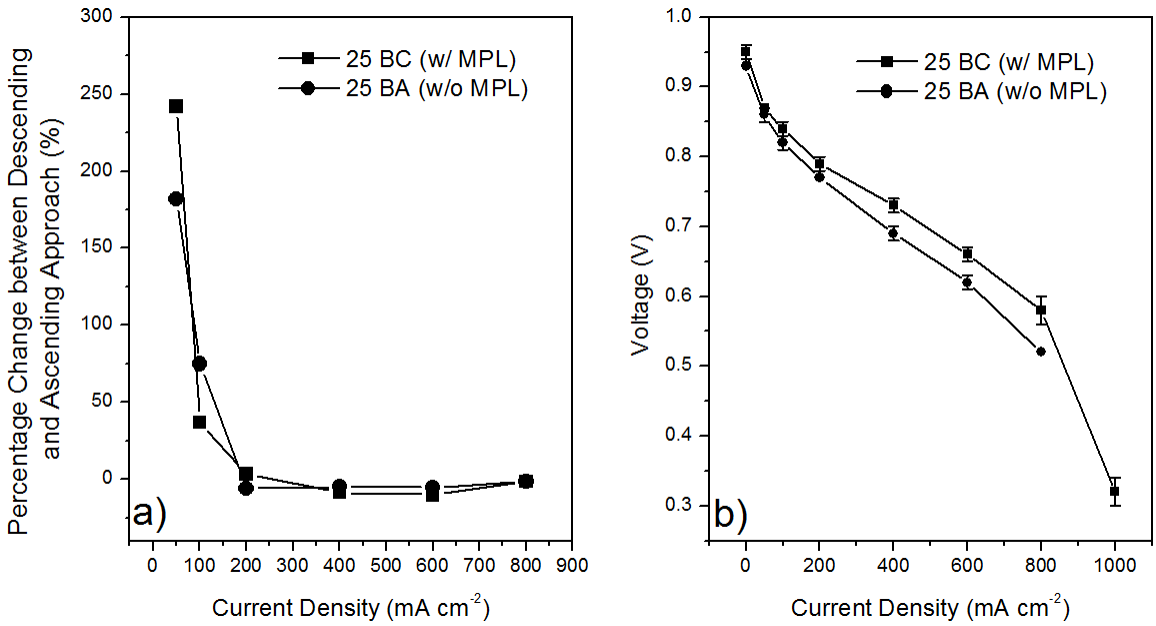

Figure 66. Effect of MPL on a) Percentage change between descending and ascending pressure drop for 25 BC (MPL) and 25 BA (no MPL) and b) Polarization curves at baseline conditions for 25 BC (MPL) and 25 BA (no MPL) (reprinted from Anderson et al. [148] with permission from Elsevier)

With or without MPL, Figure 67b shows both GDLs exhibit similar single-phase behavior (gas-phase only with no electrochemical reaction) and show similar ascending and descending pressure drop behavior. This result means that while the method of water injection may differ, the bulk influence of the liquid water on the two-phase flow pressure drop is similar. The similar influence of the two-phase flow is highlighted in Figure 67a, where the two-phase flow multiplier is similar for either GDL for both the ascending and descending approach, with the major influence of the liquid water being consistently noted below 200 mA cm^{-2}. These results do not necessarily contradict the MPL influence/flow pattern developments discussed previously by Lu et al. [153] because for the superficial gas and liquid velocities in this work, our results are consistent with their flow pattern map, where slug flow is expected with either the 25 BC or 25 BA GDL. It should also be noted that those results were obtained with an ex-situ apparatus (no electrochemical reaction, external water injection), and Lu et al. [153] pointed out

that in-situ results [23,154] have shown more droplets on the GDL surface due to water vapor being transported from the active catalyst layer through the MPL, which is consistent with this work.

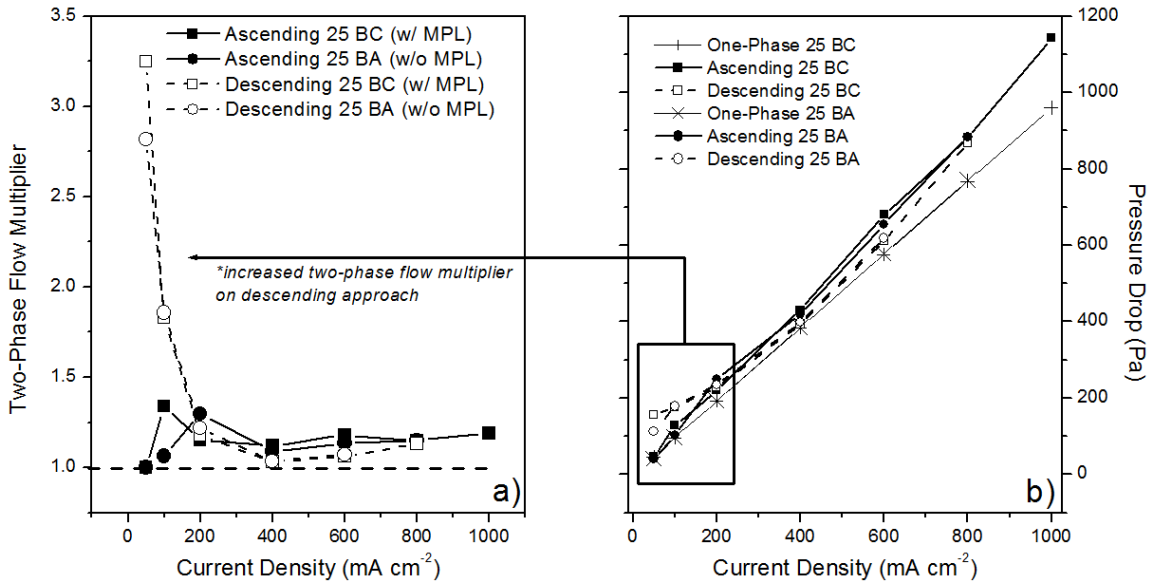

Figure 67. Effect of MPL on a) Two-phase flow multiplier and b) Pressure drop results for 25 BA and 25 BC for single and two-phase flow (reprinted from Anderson et al. [148] with permission from Elsevier)

5.2.5 Further investigation into low current densities

As the hysteresis effect is not large at higher current densities, additional current densities were studied below 200 mA cm^{-2}. These results are presented here in Figure 68, which shows the percentage change between descending and ascending approach for the baseline case and the case with additional data points at low current densities. The behavior in both tests is similar with the inclusion of the additional data points.

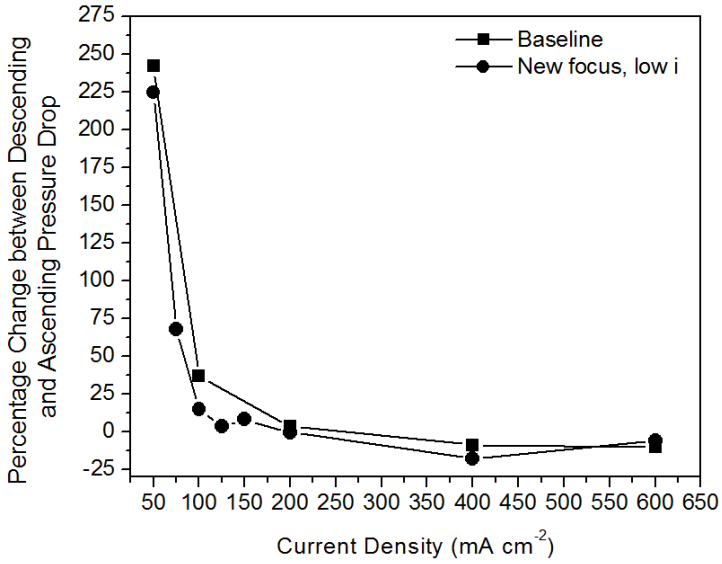

Figure 68. Percentage change between the descending and ascending pressure drop for the baseline case (50, 100, 200, 400, 600 mA cm^{-2}) and the case with more low current densities (50, 75, 100, 125, 150, 200, 400, 600 mA cm^{-2})

Since the magnitude of the pressure drop can be path dependant, the two-phase flow multiplier for the baseline and path with additional low current densities is shown in Figure 69.

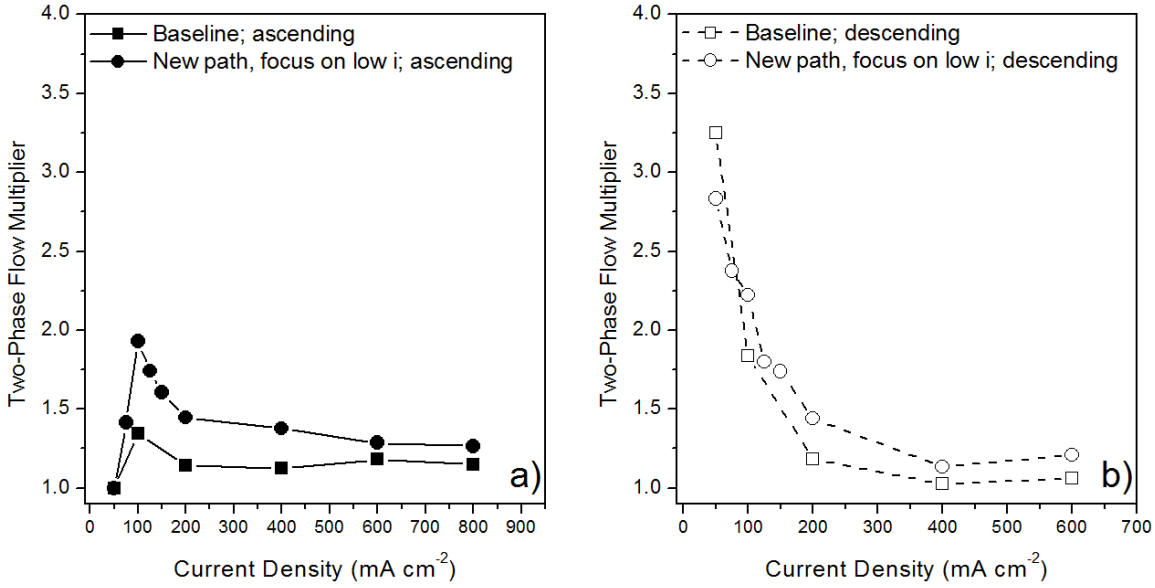

Figure 69. Two-phase flow multiplier comparing the baseline path (50, 100, 200, 400, 600 mA cm^{-2}) to the new path (50, 75, 100, 125, 150, 200, 400, 600 mA cm^{-2}) for a) the ascending approach and b) the descending approach

The new path raises the pressure drop more than the baseline path in both the ascending and descending cases. This is due to more water breaking through the GDL at the lower current densities and additional water condensation from humidified reactants. This is particularly relevant in the ascending approach.

5.2.6 Two-phase flow pressure drop prediction

While the single-phase pressure drop in laminar conditions is well predicted and understood, predicting the two-phase pressure drop relies on empirical approaches. The Lockhart-Martinelli (LM) approach is often used to predict the two-phase flow pressure drop. The LM approach uses the two-phase flow multiplier, which is the ratio of the two-phase pressure drop to the single-phase pressure drop as discussed in the experimental results (Eqn. 37). The two-phase multiplier is correlated to the Martinelli parameter, χ^2, which is defined by:

$$\chi^2 = \frac{\Delta P_l}{\Delta P_g} \tag{47}$$

Chisholm correlated $\varphi_{2\text{-phase}}$ as a function of χ^2 with a constant, C, where C is a flow-regime dependant parameter.

$$\varphi_{2-\text{phase}} = 1 + C\chi + \chi^2 = \frac{\Delta P_{gl}}{\Delta P_g} \tag{48}$$

For laminar liquids and gases, a value of C = 5 is typically used, though English and Kandlikar [53] modified C for non-circular minichannels.

However, Zhang et al. [155] found that this correlation did not match experimental data when permeable walls were considered. Thus, these correlations are not appropriate for fuel cells due to the porous GDL. To correct this problem, they proposed a variation

of liquid water velocity along the channel, which should more closely resemble the actual water flow in a PEM fuel cell. This type of flow is shown in Figure 70.

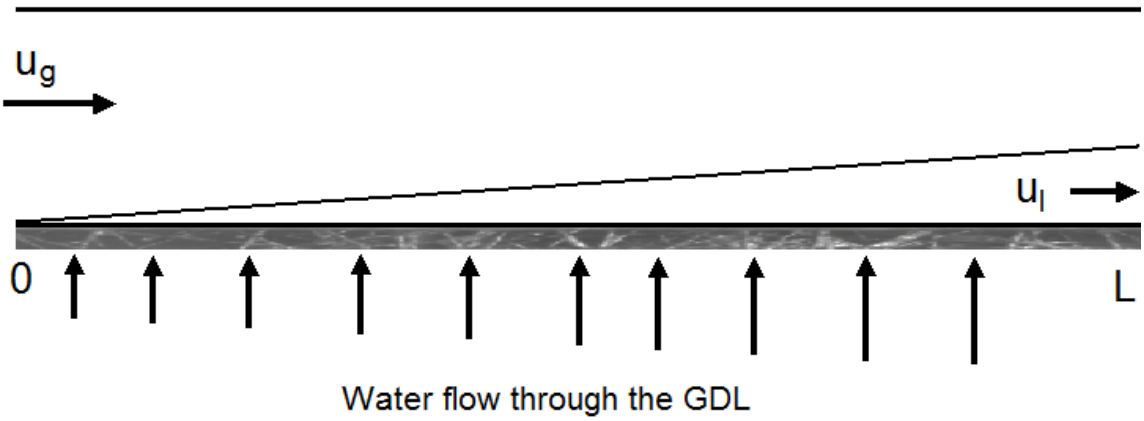

Figure 70. Fuel cell water injection schematic showing water injection rate as a function of channel length (reprinted from Anderson et al. [148] with permission from Elsevier)

Assuming liquid is introduced continuously from a permeable wall, the pressure drop can be expressed as:

$$P_x - P_{x+dx} = \varphi_2 \Delta P_g dx = (1 + C\chi + \chi^2)_x \Delta P_g dx \tag{49}$$

where the χ^2 parameter is determined by the local liquid velocity:

$$\chi^2|_x = \frac{u_L|_x \, \mu_L}{u_g \mu_g} \tag{50}$$

where μ refers to the viscosity and *u* refers to the velocity of the respective fluids. In theory, the liquid velocity should follow a linear relationship with the pressure difference assuming the water flowing through the porous media obeys Darcy's law. Integrating the above expression for a uniform and non-uniform (linear relationship with pressure) case, the expressions for the two-phase pressure drop predications for both uniform and non-uniform injection are [156]:

uniform:

$$\Delta P_{gl} = \Delta P_g \left(1 + (2/3)C\chi + (1/2)\chi^2\right) \tag{51}$$

non-uniform:

$$\Delta P_{gl} = \Delta P_g \left(1 + (1/2)C\chi + (1/3)\chi^2\right) \quad (52)$$

The Martinelli parameter is particularly interesting in fuel cells because for a given set of conditions it is constant at every current density due to the coupling of the gas and liquid flow rates via Faraday's law. For typical fuel cell operating conditions, $\chi^2 < 0.1$. For the operating conditions studied during the electrochemically active hysteresis experiments (T = 50-90 ^oC, λ_{air} = 1.5-4), typical values were $\chi^2 < 0.02$. The results of this analysis are shown in Figure 71 with the classic approach, uniform injection approach, and non-uniform injection approach highlighted. The two-phase flow multiplier presented here is the average multiplier at a given condition for the ascending approach, excluding the initial 50 mA cm^{-2} data point since this is confirmed as single-phase flow ($\varphi_{2\text{-phase}}$ = 1). The liquid water velocity is calculated from the volumetric water production rate divided by the cross sectional area of the channels, which assumes all product water enters the cathode channels.

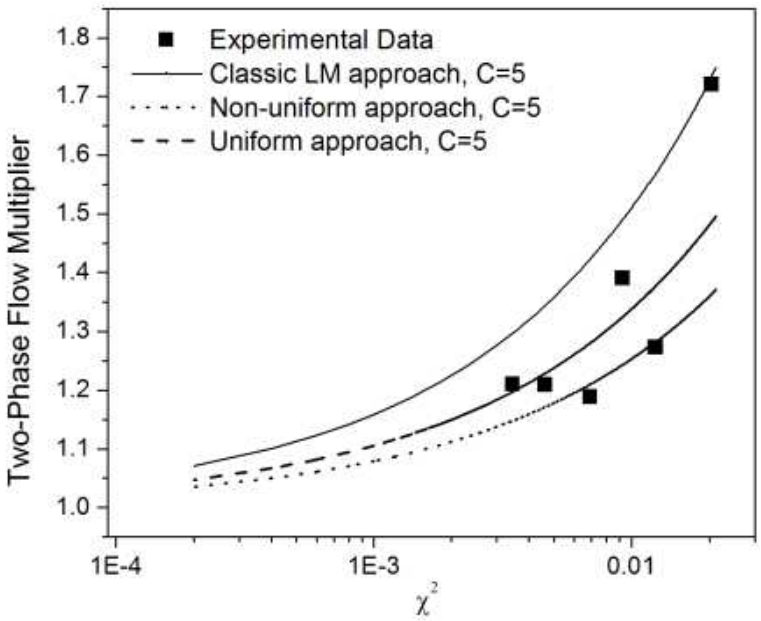

Figure 71. Ascending approach experimental data and two-phase flow pressure drop prediction for the classic, non-uniform, and uniform approaches (reprinted from Anderson et al. [148] with permission from Elsevier)

There is some agreement between the data and the modified predictions for non-uniform and uniform water introduction. Generally, the classic approach over-predicts the data. The descending approach is currently neglected since the models do not take into account the additional accumulation of liquid water in the flow field channels during the descending approach, which greatly raises the experimental values of $\varphi_{2\text{-phase}}$. Two-phase flow multipliers reaching as high as 10 at low gas velocities (where liquid water accumulation is highest) [157] have been studied in ex-situ experiments, though it should be noted that study only had reasonable agreement with the LM approach at high gas flow rates, and the multiplier values are high compared to other studies [38].

While the prediction here is satisfactory on the ascending approach, the model fails to capture all of the water transport phenomena occurring within the fuel cell. In particular, it neglects the effect of condensation on the total amount of water in the channel. Also, the magnitude of the constant C may be optimized for fuel cell applications, where

multiple and changing flow patterns can exist. These results illustrate a method to establish expected two-phase pressure drop values due to the unavoidable influence of liquid water in the fuel cell.

5.3 Comparing the three hysteresis sections

The three hysteresis sections increased in complexity and relevance to PEM fuel cells from external water injection at ambient conditions to electrochemical water production at typical PEM operating conditions. The sections were analyzed separately due to the largely different operating conditions. These differences included water injection/production method, gas temperature and pressure (therefore gas velocity), and gas humidification (another potential water source term). Furthermore, no dimensionless analysis (such as using the gas-phase Re) was able to normalize the data for a direct comparison. However, it is still useful to compare the results together to further understand the results and differences. Two common variables studied in each case are air stoichiometry and GDL. This section focuses on the baseline air stoichiometry of 2 (most typical of fuel cell operation) and the 25 BC vs. 25 BA GDL (MPL vs. no MPL).

The single-phase pressure drop at the baseline conditions and an air stoichiometry of 2 are shown in Figure 72. These results show the inherent differences in flow conditions between the three hysteresis studies.

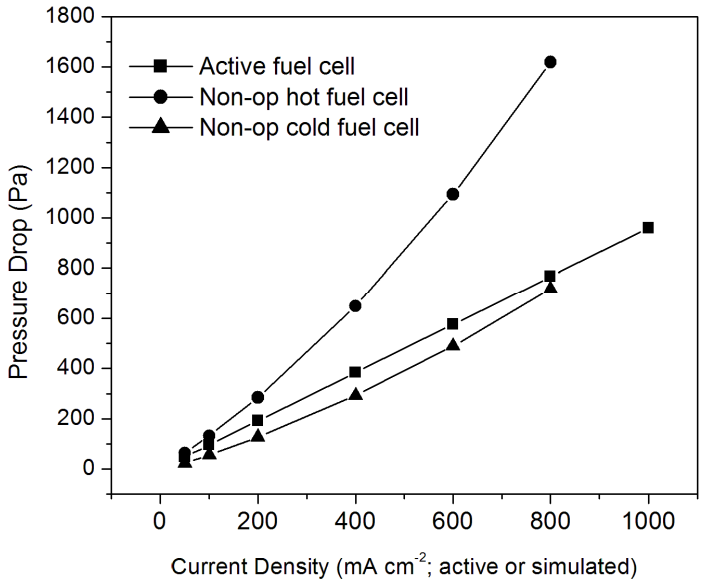

Figure 72. Comparing the pressure drop at baseline conditions for the three hysteresis sections (non-operating cold model, non-operating hot model, and operating); all at λ_{air} = 2 with the 25 BC GDL

The non-operating cold fuel cell (ambient conditions) has the lowest pressure drop. When the gas was heated and humidified, as was the case of the non-operating hot fuel cell, the change in gas properties and the potential for condensation caused the pressure drop to greatly increase. However, since the operating fuel cell operates at 206.8 kPag backpressure, the gas velocity decreases. The lower velocity decreases the pressure drop back to a value near the non-operating cold fuel cell. These variables factor into the single-phase Reynolds number. Any changes in the hysteresis behavior have to be analyzed with this context in mind.

The percentage change between descending and ascending approach along with the two-phase flow multiplier for each approach is shown in Figure 73. Lu et al. [62] show results of similar magnitude for two-phase flow multiplier in an ex-situ approach (in the range of 2-3 at low flow rates). In each case here, the same air stoichiometry, GDL, and flow field is used.

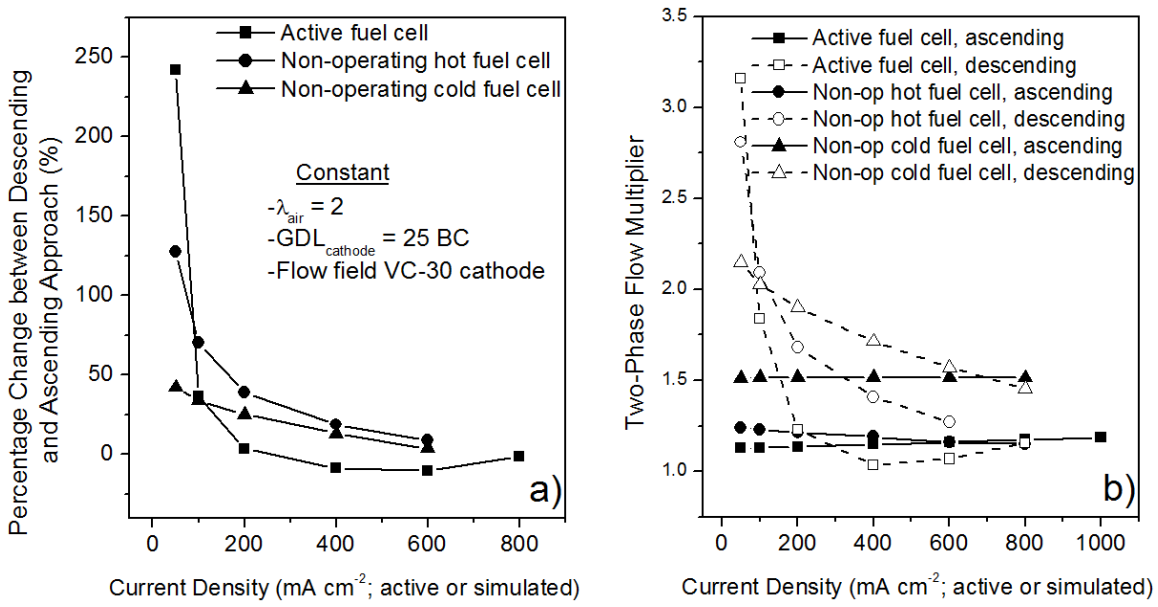

Figure 73. Comparing the three hysteresis studies (non-operating cold model, non-operating hot model, and operating) in terms of: a) Percentage change between descending and ascending approach b) two-phase flow multiplier for the ascending and descending approach

The two-phase flow multiplier is highest in the ascending approach for the non-operating cold model fuel cell. This result can be explained by the lowest experimental single-phase pressure drop in Figure 72. Since the single-phase pressure drop is so low, the influence of the injected liquid water is more pronounced. Also, the descending approach two-phase flow multiplier is the lowest in this study. Thus, the percentage change between approaches is diminished. Conversely, in the active fuel cell the ascending two-phase flow multiplier is lowest and the descending two-phase flow multiplier is highest. The higher descending multiplier is explained by the low air velocity, which causes an increase in condensation and a decrease in the convective removal abilities (increase in accumulation). Thus, the percentage change between approaches appears very high. These results stress the importance of initial condition, single-phase pressure drop, and water injection/accumulation method.

Each study also compared the 25 BC and 25 BA results. In each case, the effect of MPL was ambiguous. Comparing the results in terms of percentage change between descending and ascending approach, Figure 74 shows no clear trends. As with the case of the stoichiometry, each study changed the gas properties and velocities, which had an influence on the results. The effect of the MPL was not consistent between trials.

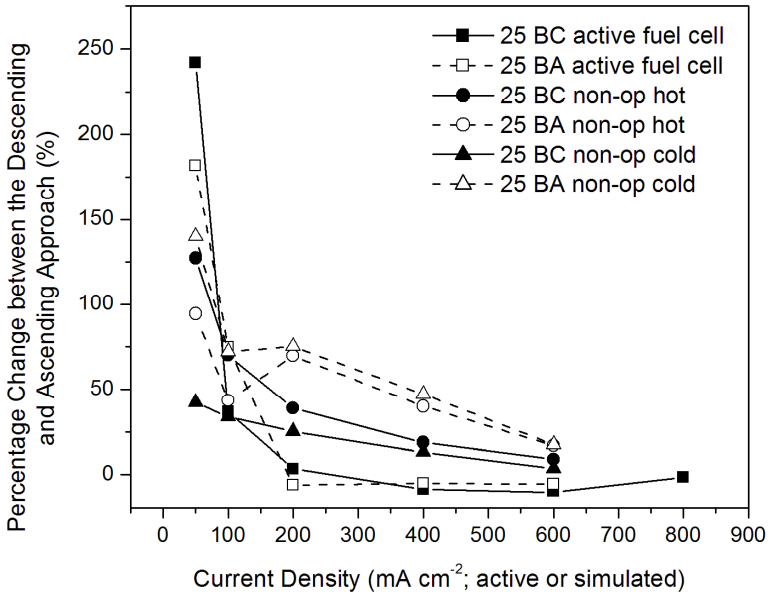

Figure 74. Percentage change results for all three studies (non-operating cold model, non-operating hot model, and operating) for the 25 BC GDL vs. 25 BA GDL

This may be due to the changes in water injection method, changes in GDL saturation, and changes in the resultant flow patterns in the channel. The spread in the data does not seem to support any consistent trend, showing the complexity and often debated effects of the MPL.

5.3.1 Additional dimensionless groups

The Quraishi-Fahidy method is a simplified dimensional analysis procedure that is useful when the equations involved contain a large number of parameters [158,159]. Quraishi-Fahidy used this method for the single-phase continuity equation and the equation of motion as governing equations. They note several dimensionless variables relevant to

Newtonian fluid flow, including the Reynolds number (Re), Froude number (Fr), Weber number (We), friction factor (f), and Euler number (Eu). Algebraic combinations of these groups can then form other dimensionless groups, including the Bond number (Bo i.e. Eötvös number), Laplace number (La), and Capillary number (Ca). An explanation of dimensionless groups studied in literature relevant to PEM fuel cells is shown in Table 15.

Table 15 Relevant dimensionless groups in fuel cell flow channel analysis including the relevant forces considered and typical values in PEM fuel cells

Dimensionless Group	Equation	Forces in Ratio	Explanation/Values
Reynolds (Re)	$Re = \frac{\rho D\bar{v}}{\mu} = \frac{D\bar{v}}{\eta}$	Inertia: Viscous	Stoich 2, ambient conditions Re < 500
Bond (Bo)	$Bo = \frac{\rho g L^2}{\sigma}$	Body: Surface tension	Liquid water holdup is a concern for low Bond number ($10^{-4} \leq Bo \leq 10^{-1}$) numbers [10]
Weber (We)	$We = \frac{\rho \bar{v}^2 L}{\sigma}$	Inertia: Surface tension	Plug to stratified transition ~0.25 (specific GDL setup) [54]
Capillary (Ca)	$Ca = \frac{\mu \bar{v}}{\sigma}$	Viscous: Surface tensions	0.014 to 0.219, droplet deformation was a strong function of Ca when it is large [79]
Laplace (La)	$La = \frac{\sigma \rho L}{\mu^2}$	Surface tension: momentum	Liquid water holdup is a concern for low La numbers: ($10^3 \leq La \leq 10^5$) [10]

As was discussed in the literature review, these numbers are particularity difficult to introduce into the fuel cell flow channel because 1) the gas-liquid ratio is so large 2) the contact angles vary 3) the GDL is porous and the water introduction is from this GDL surface. The various contact angles used in this study are displayed in Figure 75.

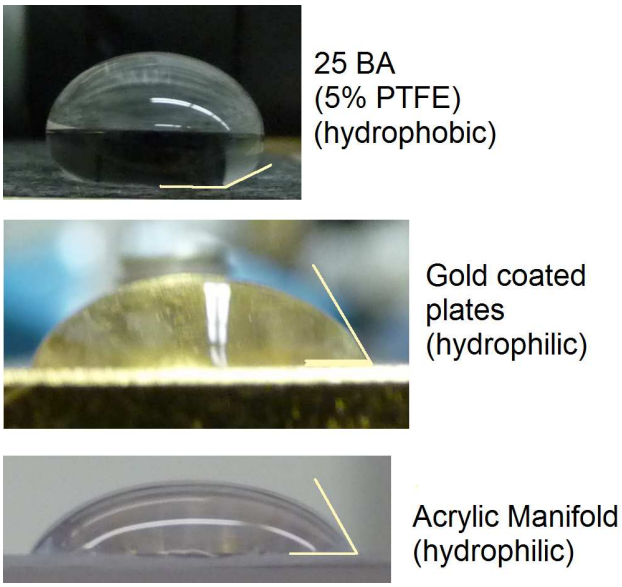

Figure 75. Schematic of the hydrophobicity of the materials in the visualization cell flow channels including the GDL ('bottom' wall), gold coated flow field plate ('side' walls), and acrylic manifold ('top' wall)

The visualization cell has shown that the water often collects on the gold sidewalls and the top acrylic manifold. This problem is in addition to water breaking through the GDL. Thus, dimensionless numbers relying on surface tension are not directly applicable to the PEM fuel cell to help normalize the three sets of experiments, suggesting the pressure drop hysteresis should be examined on a case-by-case basis depending on the experimental setup.

The results for the Re vs. the percentage change between approaches are shown in Figure 76, as they do not rely on the surface tension.

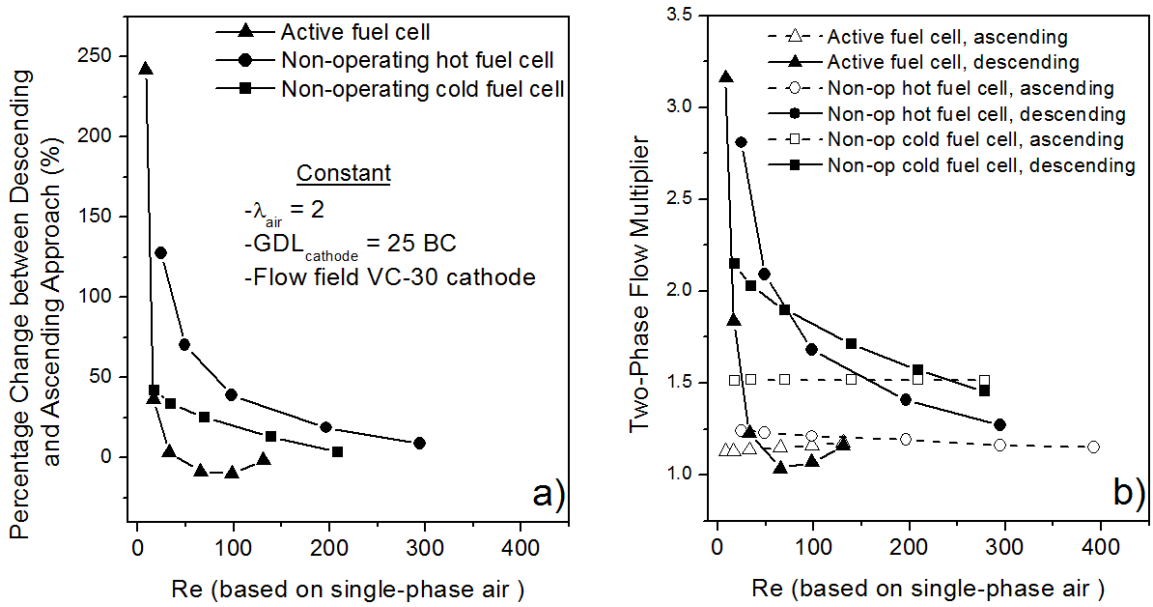

Figure 76. Comparing the three hysteresis studies (non-operating cold model, non-operating hot model, and operating) in terms of: a) Percentage change between descending and ascending approach b) two-phase flow multiplier for the ascending and descending approach

These values refer to the baseline testing conditions for each of the three hysteresis studies. As can be seen, the Re does not predict the results. This is because the two-phase behavior is not captured by this dimensionless parameter.

While it is difficult to use dimensionless numbers to compare the three approaches (active, non-operating hot, non-operating cold), the Re number analysis is very consistent between the 4 stoichiometries studied in the active cell (1.5, 2, 3, and 4) and is somewhat consistent between the three temperatures (50, 75, and 90^{o}C). The percentage change between descending and ascending approaches at the gas-phase Re for each of these trials is shown in Figure 77.

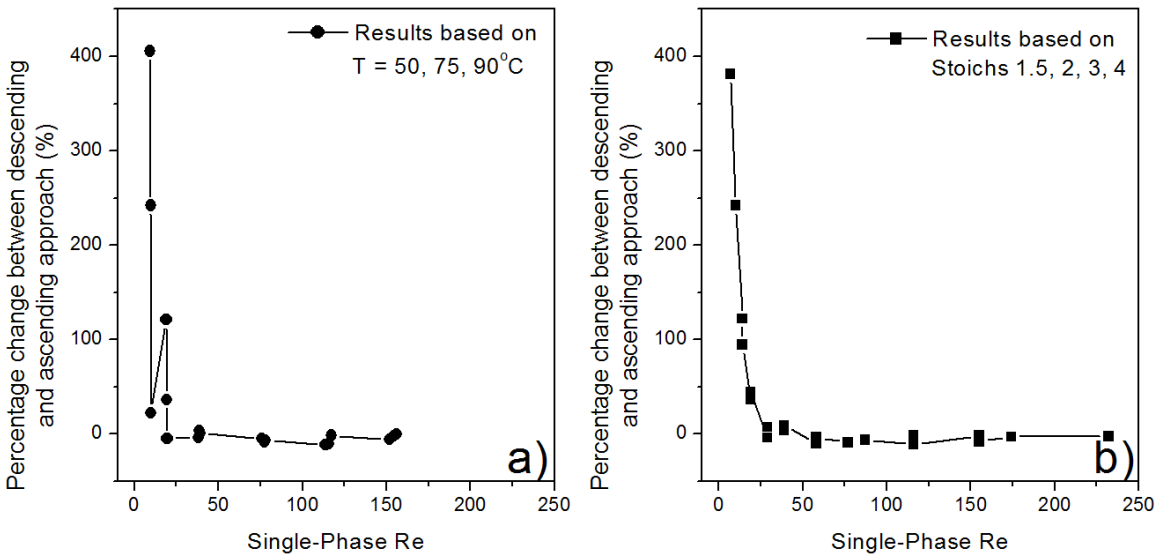

Figure 77. Percentage change between approaches vs. gas-phase Re for a) temperatures studied b) stoichiometries studied

In Figure 77b, the percentage change clearly follows the Re. In some cases, the same Re occurs twice (ex. stoichiometry of 2 at i = 400 mA cm^{-2} and stoichiometry of 4 at i = 200 mA cm^{-2}), and the percentage change results are very similar. However, in Figure 77a at Re < 50, the percentage change between approaches does not exactly follow Re. This is because the condensation/evaporation rates and the surface tension change with temperature, where lower temperatures exacerbate the flooding problem. Thus, the hysteresis problem cannot be analyzed in terms of the Re in these cases.

5.4 Operating fuel cell: Mitigation via purging

A purging strategy is proposed that can reduce the two-phase flow hysteresis for the baseline operating conditions in the operating fuel cell. The purge consists of temporarily increasing the gas stoichiometry to remove accumulated water in the flow field channels. This strategy works because the drag force on the liquid water in the channels increases with the gas velocity, which can cause droplet instability and eventually detachment [69]. However, an excessively long purge will increase the overall pressure drop, while too short of a purge will not remove enough liquid water. Longer purges can also dry out the

membrane, which would cause an undesirable increase in the membrane resistance [86,102,85]. While several purging strategies were examined (varying duration and flow rate), not all were able to reduce the pressure drop hysteresis, and only one successful strategy is presented in this section.

A stoichiometry of 5 was used at each current density for both air and hydrogen during the purge. Since the water produced by electrochemical reaction can also proceed to the anode side, a preemptive purge on the anode side was utilized to mitigate possible water accumulation in conjunction with the air purge. As each current density is held for 10 minutes, the middle purges refer to $t_{min:sec}$ = 4:40-5:00 and the end purges refer to $t_{min:sec}$ = 9:40-10:00. The gas is switched from fully humidified to dry 10 seconds before each purge and remains dry only for the duration of the purge, which adds an additional water removal mechanism via evaporation [102]. This total purge duration (40 seconds) represents purging for 6.7% of the total 10 minute operating time. The resulting Reynolds number in the cathode flow field channels under these conditions are presented in Table 16, which shows that the Reynolds number at each current density is increased by a factor of 1.6. It was important to maintain such a small increase as not to increase the single-phase (gas) pressure drop too much, which would have the undesirable effect of raising the net pressure drop over 10 minutes.

Table 16 Air Reynolds numbers on the descending approach for the baseline (Table 6) and purging method

Descending Current Density (mA cm^{-2})	Reynolds Number Baseline	Reynolds Number Purging
600	98	152
400	65	101
200	33	51
100	16	25
50	8	13

Tests revealed that a 20 second purge of dry gas with both anode and cathode stoichiometries at 5 during only the descending approach significantly lowered the ΔP hysteresis, as shown in Figure 78. This result is due to the accumulating water being convectively removed during the purge, which lowers the net pressure drop over the 10 minutes. Shorter purge times and only a single purge were unable to have the same effect. It was also found that the purge had to be done at each current density on the descending approach to ensure less water accumulation at the lower current densities.

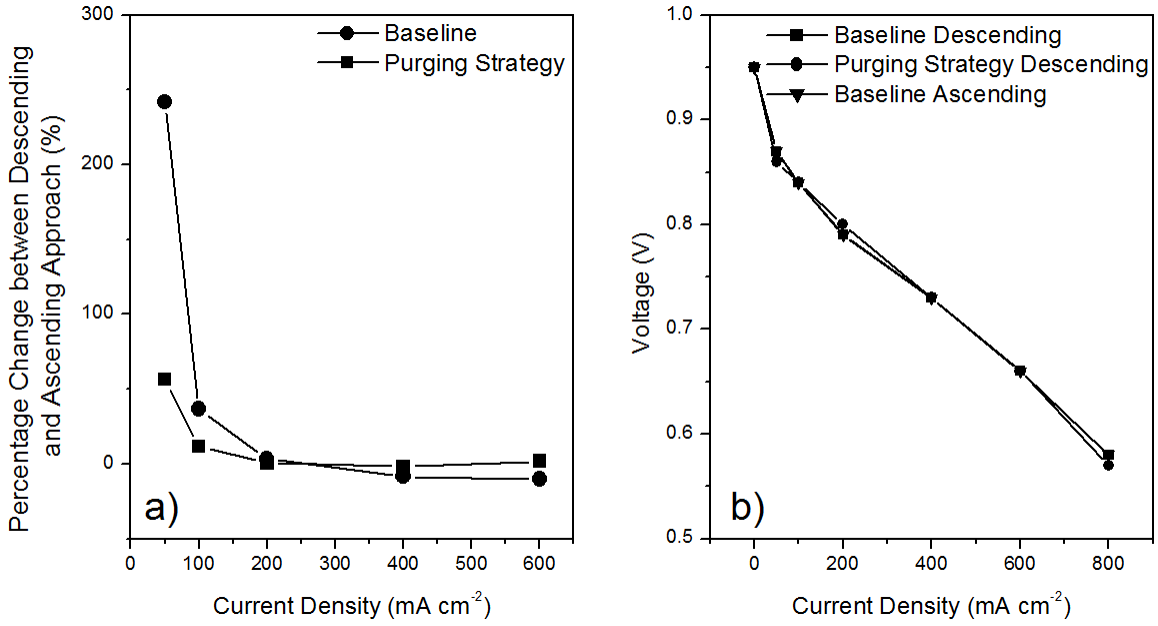

Figure 78. a) Percentage change between descending and ascending approach for the baseline and the purging strategy; b) Ascending and descending approach polarization curve for the baseline and descending approach polarization curve for the purging strategy

This purging strategy on the descending approach lowered the percentage change between descending and ascending pressure drop at 50 mA cm^{-2} from 242 % to 56 %. Purging on only the descending approach also has the benefit of not increasing the ascending pressure drop unnecessarily, since the influence of two-phase flow is not as pronounced in the ascending approach. The results show that the short purges on the descending approach do not dry out the membrane since the electrochemical performance

is the same as the baseline results (Figure 78b). This strategy is a recommendation that would have to be optimized for a particular system/set of conditions to be successful.

5.5 Pressure drop hysteresis in a serpentine channel fuel cell

As has been explained, the results in Chapter 4 and previous results in this chapter were studied in a visualization fuel cell with a specialized design. To further confirm the relevancy to realistic PEM fuel cells, preliminary tests were carried out in a larger fuel cell with traditional plates in serpentine flow fields. The remaining conditions were at the baseline operating conditions from the operating hysteresis study in parallel channels (Table 6; 25 BC GDL on the cathode, T = 75^{o}C, RH = 100%, P_{gas} = 206.8 kPag).), which are consistent with standard protocols [136]. An ascending and descending polarization curve was performed in a TP50 fuel cell (the same fuel cell as the AWR results in Chapter 6 [104]). This fuel cell uses a 27-pass serpentine flow channel on both the anode and cathode and reaches limiting current densities at approximately 2,000 mA cm^{-2}. The channels are machined into traditional graphite plates. The pressure transducers on the Hydrogenics station (model no. G100) are not as accurate at low flows, so a curve fit has been used in both approaches for the pressure drop data. The results were tested in constant flow and constant stoichiometry mode.

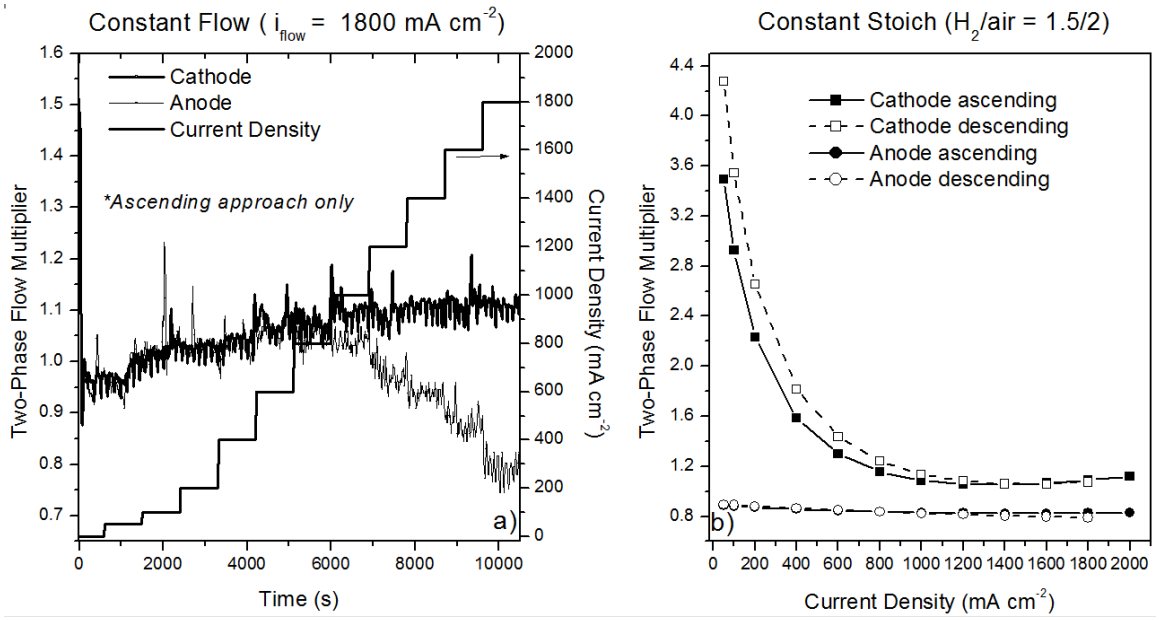

Figure 79. Two-phase flow multiplier results for serpentine flow field channels in graphite at: a) Constant air flow and b) constant air stoichiometry

The results in Figure 79a show that under constant flow conditions (based on i = 1800 mA cm^{-2}, λ_{air} = 2, λ_{H2}= 1.5) the cathode two-phase flow multiplier steadily increases as the influence of the liquid water becomes more relevant. On the anode side, since the hydrogen is a pure gas and the stoichiometry is relatively low, the consumption of the gas causes the two-phase flow multiplier to be less than one. Thus, two-phase flow is a relevant consideration in this traditional fuel cell. The results in Figure 79b show the results under constant stoichiometry operation (λ_{air} = 2, λ_{H2}= 1.5) to compare the two-phase flow multipliers in an ascending and descending approach. On the anode side, the two-phase flow multiplier is always less than one due to consumption in the reaction. However, on the cathode side, both the ascending and descending approaches show large two-phase flow multipliers. These results corroborate with the parallel channel visualization cell because the descending approach multipliers are higher than the ascending approach multipliers.

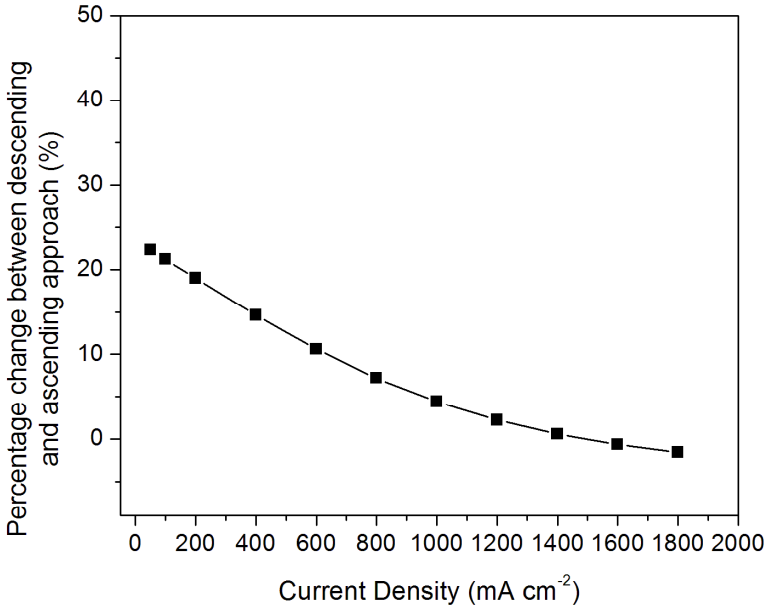

Figure 80. Percentage change between descending and ascending pressure drop in graphite flow fields with serpentine channels

Figure 80 shows the percentage change in pressure drop between descending and ascending approach. While the percentage change is not as high at low current densities as was seen in the visualization cell, the change is still approximately 22% higher. Though visualization was not accomplished in these channels, the hysteresis is likely due to water accumulation in the descending approach in the serpentine bends where flooding is most common. Flooding in these bends may also be responsible for the high two-phase flow multiplier in the ascending approach. The lower percentage change is attributed to the larger convective water removal abilities of the single serpentine channel, where the single-phase air Reynolds number is approximately 77 at 50 mA cm^{-2}, which is much higher than the Reynolds number in the visualization cell (Re = 10 at 50 mA cm^{-2}; Figure 77). Also, the total magnitude of the pressure drop hysteresis is higher with the serpentine channels, so the system efficiency may still decrease via additional compressor work (Eqn. 44) even at lower percentage changes. Thus, pressure drop hysteresis is a relevant consideration in PEM fuel cells.

5.6 Operating fuel cell conclusions

Two-phase flow pressure drop hysteresis occurs when the pressure drop differs depending on the path by which the current density is changed in an operating fuel cell. When the current density is increased, water from the electrochemical reaction and condensation of humidified air enters the cathode flow field channels and causes the pressure drop to increase over the single-phase pressure drop. However, when the current density is subsequently decreased, additional water accumulates in the flow field channels, causing the pressure drop at low current densities (generally < 400 mA cm^{-2}) to be higher than both the single-phase and ascending two-phase pressure drop. The water accumulates further in the descending approach since the lower air flow rate cannot remove as much residual water (from the previous current density) convectively. This mechanism was confirmed with direct visual observation of the cathode flow field channels and is consistent with the non-operating results in Sections 4.2 and 4.3. Main observations include:

1. Increased air stoichiometry (in the range of 1.5-4) decreases the extent of the pressure drop hysteresis. This behavior occurs because the ability of the gas to convectively remove water increases with increased flow rate, causing the ascending and descending pressure drops to be the same. However, higher air flow rates cause the total magnitude of the pressure drop to increase.
2. Increased operating temperature (50-90^{o}C) decreases the extent of the pressure drop hysteresis. This result occurs because the increased air temperature increases the convective water removal capabilities of the gas (higher velocity and lower surface tension), and the condensation rate is lower at higher temperatures when

fully humidified reactants are used. Conversely, lower temperatures increase the condensation rate and decrease the gas velocity, which increases the accumulation of liquid water on the descending approach.

3. The inclusion/exclusion of an MPL does not change the pressure drop hysteresis. Though the mechanism of water injection may differ, liquid water entering the channels increases the two-phase pressure drop in a similar manner due to the same flow patterns.
4. A modified Lockhart-Martinelli (LM) approach can be used to moderately predict the two-phase pressure drop hysteresis. The modification takes into account how liquid water enters the flow channels from a porous GDL wall, which leads to deviations from the classic LM approach. Further work is needed to predict the descending approach due to the accumulation of liquid water along this path.
5. Dimensionless numbers that rely on surface tension are difficult to use in practical PEM fuel cells due to multiple surfaces in the flow field channels. Furthermore, the single-phase Re number is unable to normalize the hysteresis results between the three experimental approaches (non-operating cold, non-operating hot, operating). However, the single-phase Re number does show consistent results in a given experimental approach (e.g. operating) when comparing the hysteresis effect at different stoichiometries and temperatures.
6. A purging strategy has been developed that relies on two short purges during each current density during the descending approach. These short purges can remove residual water, lowering the overall pressure drop at a given current density during the duration of the test. The purge was able to lower the percentage change

between descending and ascending pressure drop to 56% from 242% at 50 mA cm^{-2}.

6 Anode water removal in an active PEM fuel cell

The pressure drop hysteresis work fits into the broad category of PEM fuel cell water management. In a similar theme, this study on anode water removal (AWR) furthers the understanding of water management in fuel cells. Anode water removal was used as a diagnostic tool to determine maximum performance in the absence of cathode mass transport limitations.

6.1 Introduction

To have a better understanding of how different conditions and fuel cell components (e.g., the GDL and MPL) improve the water management of the fuel cell, researchers have developed a number of diagnostic tools designed to visualize water transport inside the cell. These techniques include neutron radiography [160,161], magnetic resonance imaging (MRI) [162], x-ray micro tomography [163], and direct optical visualization [164,165]. Unfortunately, most of these techniques are expensive and/or require the fuel cell to be designed differently from practical fuel cells. Therefore, there is a need for a diagnostic technique that is easily used and allows the researcher to have a better idea of where the liquid water accumulation is occurring, depending on the conditions and fuel cell components.

To achieve this goal, Wilkinson et al. at Ballard Power Systems first proposed a method called anode water removal (AWR), which was used to understand mass transport issues inside fuel cells [166,167,168]. In this method, water in the cathode is drawn by a concentration gradient across the membrane to a dry anode stream. Therefore, the effects due to water accumulation in the cathode are reduced or eliminated, consequently separating mass transport from other effects. This diagnostic technique is accomplished by creating a pressure gradient along the anode flow field channel in order

to increase the ability of the fuel stream to carry water vapor [167]. By observing how the cell voltage increases with higher fuel flow rates, conclusions can be made regarding the different components used in the cell, especially on the cathode side. A schematic of this voltage increase with hydrogen stoichiometry is shown in Figure 81 with previous literature results noted in Figure 17.

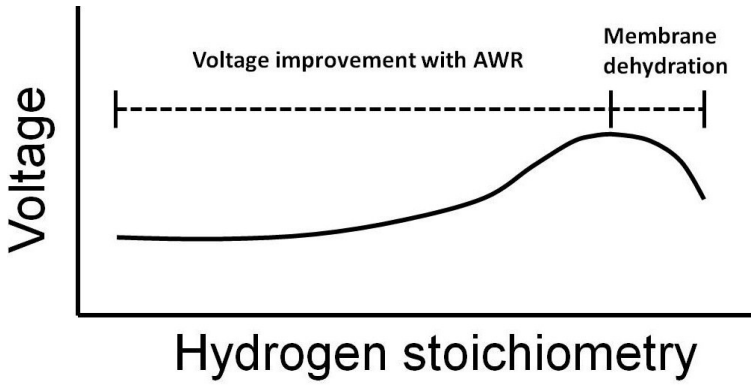

Figure 81. Schematic of AWR voltage results where the increase in dry hydrogen stoichiometry leads to an increase in voltage until membrane dehydration becomes limiting

A clear advantage of this method, especially if the fuel cell system recycles the hydrogen, is that it does not increase the parasitic losses involved with the use of high air flow rates. However, one concern with this approach is the possible degradation (and possible rupture) of the membrane caused by the pressure differences between the anode and cathode sides. Another issue with this method is the parasitic losses involved with the increase of the hydrogen flow rate and the direct impact that this has on the overall fuel efficiency in the system.

This chapter describes in detail how the anode water removal method can be used as a simple diagnostic tool to understand liquid water accumulation and transport within a PEM fuel cell. In particular, it is found that this method is effective at determining when cathode GDL flooding is lowering the cell voltage. Variables studied include various cathode GDLs (with and without MPLs), operating temperature (25, 50, 75, and 90^{o}C),

and cathode relative humidity (25, 50, 75, and 100%). An additional GDL layer on the cathode side was also used to exacerbate GDL flooding to determine how AWR isolates GDL flooding. Injecting water into the cathode flow field also exacerbated flooding to further gauge the effectiveness of AWR.

The analysis examines the change in voltage during the AWR process (i.e. Figure 81) and also utilizes the pressure drop multiplier. The pressure drop multiplier is defined here as a separate parameter from the two-phase flow multiplier of Eqn. 37. The two-phase flow multiplier isolates the effect of liquid water on the pressure drop. Here, the pressure drop multiplier ($\Phi_{\Delta P}$; Eqn. 53) is used since the AWR pressure drop may increase due to the addition of water vapor to the dry anode stream or decrease due to the removal of liquid water from the cathode flow channels:

$$\Phi_{\Delta P} = \frac{\Delta P_{AWR,\lambda_{hydrogen}=1.5\rightarrow 15}}{\Delta P_{OCV,\lambda_{hydrogen}=1.5\rightarrow 15}} \tag{53}$$

This multiplier is the ratio of the pressure drop during the AWR test (at constant current density i.e. 1000 mA cm^{-2}) to the pressure drop of the single-phase gas at the same flow rates (run at the open circuit voltage). This pressure drop multiplier is calculated based on both the anode and cathode pressure drops. As will be noted, the anode pressure drop multiplier in the AWR experiments tends to level out with an increase in anode stoichiometry, indicative of saturation but not necessarily anode channel flooding.

The experimental details for these tests are described in Section 3.5. It should be noted that the fuel cell used in the AWR tests is not the visualization cell from Chapters 4 and 5. This uses the TP50 (no visualization) with serpentine flow field channels on both the anode and cathode. This was chosen for continuity with previous work [104], the

ability to operate over a larger range of current densities (i_{lim} > 2000 mA cm^{-2}), and the higher pressure drop associated with serpentine channels on the anode, which aids in the AWR process.

6.2 Results and discussion

Anode water removal can be utilized by increasing the pressure drop in the anode. The water vapor content in a gas stream (fraction by volume), r_{H2O}, is given by:

$$r_{H_2O,Vol} = \frac{\varphi_{gas} * P_{vs}}{P} \tag{54}$$

where φ_{gas} is the relative humidity of the gas stream, P_{vs} is the saturated vapor pressure, and P is the total pressure. As the flow rate of hydrogen is increased, the pressure drop increases. Thus, the average pressure in the channels, P, is decreased, leading to an increase in the volume fraction of water vapor in the gas stream. Also, as the hydrogen stoichiometry is increased, the volumetric flow rate of the hydrogen gas increases. Combined with the increasing volume fraction from Eqn. 54, the water removal ability of the gas increases exponentially. Furthermore, the saturation pressure (in Pa) increases exponentially with temperature, as shown in Eqn. 55. Thus, an increase in the operating temperature leads to an exponential increase in r_{H2O}.

$$P_{vs} = e^{aT^{-1}+b+cT+dT^2+eT^3+f\ln(T)} \tag{55}$$

An example of the amount of water vapor that can be removed by the hydrogen stream is shown in Figure 82. The water production rate, assuming the water is in the vapor phase, is also depicted. In this case, the hydrogen stream can remove all of the product water (fully humidifying the hydrogen steam) at a stoichiometry of approximately 6.

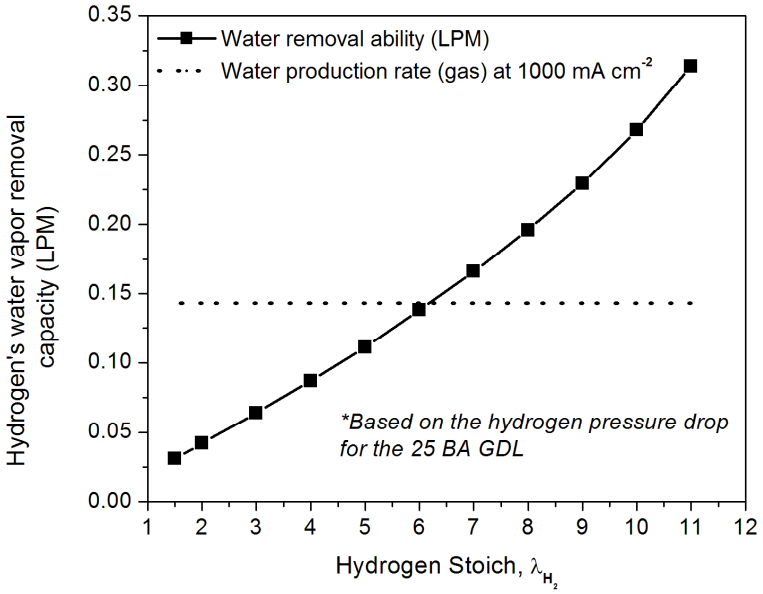

Figure 82. Water removal capability of the dry hydrogen stream as a function of hydrogen stoichiometry. The dashed line is the water production rate at 1000 mA cm^{-2} (assuming vapor is formed). The pressure drop results are from the 25 BA GDL results (Figure 84).

However, while the hydrogen has the capacity to remove product water in the vapor phase, it is limited by resistance to mass transfer. The rate of convective mass transfer into the gas phase can be described by:

$$\dot{m}_{H_2O} = h_m(\rho_s - \rho_v) \tag{56}$$

where ρ_s is the density of saturated vapor on the membrane surface assuming the water and vapor are in equilibrium in saturated gas, ρ_v is the density of water vapor in the bulk gas stream, and h_m is the convective mass transfer coefficient. This expression is analogous to convective heat transfer, and as such, the Sherwood (Sh) number is described analogously to the heat transfer Nusselt number:

$$Sh = \frac{h_m l}{D} \tag{57}$$

where l is a characteristic length and *D* is the water vapor diffusivity in the gas. Several empirical relationships exist for the Sherwood number as a positive function of the Reynolds (Re) number and the Schmidt (Sc) number.

$$\mathrm{Re} = \frac{\rho_g D_h u_g}{\mu_g} \tag{58}$$

$$\mathrm{Sc} = \frac{\mu_g}{\rho_g D} \tag{59}$$

As the gas velocity increases with an increase in hydrogen stoichiometry, the Reynolds number increases. This in turn increases the Sherwood number and thus the mass transfer coefficient. Thus, AWR is a function of removal potential and convective water removal ability. Additionally, while the hydrogen stream has the potential to remove water vapor, it must overcome the resistances in individual layers of the MEA as water from the cathode must be drawn through the cathode catalyst later, membrane, and anode catalyst layer.

6.2.1 Effect of cathode GDL properties on voltage

The GDLs, listed in Table 9, vary with the inclusion/exclusion of an MPL, the GDL hydrophobicity, the MPL hydrophobicity, and thickness. The polarization curves (non-AWR results) for each GDL studied are shown in Figure 83. Each curve was produced at the same baseline operating conditions listed in Table 8, except the anode gas is humidified and the anode stoichiometry is constant at 1.5. These tests were done to ensure reasonable electrochemical performance of each GDL before further study in the AWR tests.

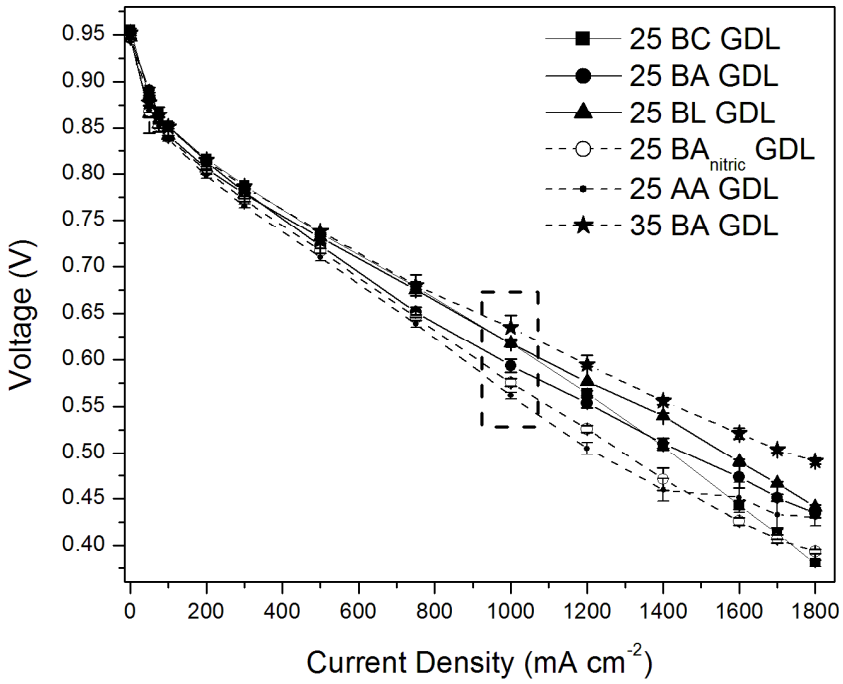

Figure 83. Polarization curves for the 6 GDLs studied to determine baseline electrochemical performance; N.B. the anode and cathode relative humidities are both set to 100%, which is different than the AWR tests where the anode humidity is 0% (dry gas)

These GDLs show similar performance in the kinetically controlled regime but differ in the ohmic and mass transfer limiting regimes of fuel cell operation (for these tests $i_{kinetic}$ < 150 mA cm^{-2}; 150 mA cm^{-2} < i_{ohmic} < 1400 mA cm^{-2}; $i_{mass\ transfer}$ > 1400 mA cm^{-2}). In general, the 25 BA nitric acid treated GDL (25 BA_{nitric}) and 25 AA GDLs performed worse due to the hydrophilic nature of the GDL. The 35 BA GDL performed best in these baseline conditions, and this may be due to reduced overall GDL saturation due to a larger total volume in this thicker GDL. This MEA would be considered as the optimum of the six GDLs for those particular operating conditions. Highlighted in the figure are the results at 1000 mA cm^{-2}, where the baseline AWR tests were subsequently performed. This voltage was chosen for a reasonably high water production rate. Also, since the anode stoichiometry is increasing in the AWR tests, this moderate current density was chosen so a reasonable pressure drop could be obtained at high hydrogen stoichiometries.

The change in voltage (ΔV) during the AWR process for each GDL is shown in Figure 84.

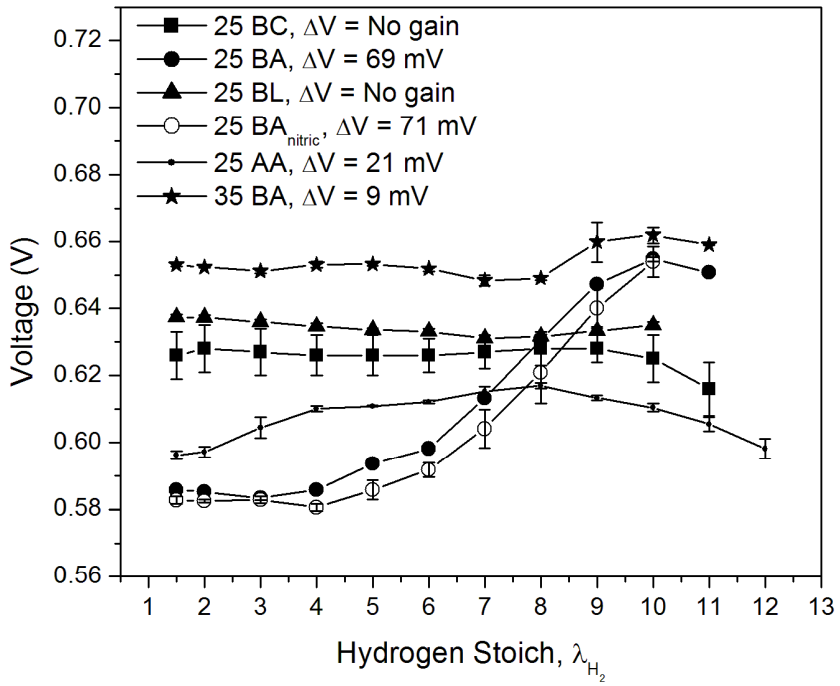

Figure 84. Anode water removal voltage results comparing the effect of GDL properties (Table 9) on cell voltage at 1000 mA cm^{-2}

At 1000 mA cm^{-2}, the GDLs with the higher initial electrochemical performances show inherent enhanced water management capabilities (35 BA, 25 BC, 25 BL) and reduced ohmic resistance. These GDLs with superior water management capabilities (in this setup) underwent little improvement through the AWR process. However, the GDLs with relatively poor water management capabilities (25 BA, 25 BA$_{nitric}$) show a much larger response to the AWR process, and improved performance by approximately 70 mV. Neutron radiography has shown that at moderate current densities, such as at 1,000 mA cm^{-2}, the water produced at the cathode cannot permeate through the cathode MPL towards the cathode flow field channel, and instead water is forced through the membrane toward the anode [169]. The MPL may also act as a liquid water barrier to prevent liquid water in the cathode GDL from reaching and flooding the cathode catalyst

layer [118]. This helps explain why the GDLs with MPL have higher cell performance and show little response in the AWR process. Conversely, without an MPL, more water is likely to enter the cathode GDL and flood the cathode MEAs. Since these GDLs without MPL have such a large increase in voltage with the AWR process, the poor performance initially at lower hydrogen stoichiometries is attributed to GDL flooding. The 25 AA GDL shows modest improvement (~20 mV), which shows that this GDL suffers some flooding issues, but the water ingress and high saturation is not entirely mitigated by the AWR process.

At the end of the AWR process, the GDLs without MPL tend to have higher performance (35 BA, 25 BA, 25 BA_{nitric}). This is attributed to better oxygen access to the catalyst later when there is no water blockage and no additional resistance to gas transport from the MPL.

These results can also be evaluated in the absence of ohmic losses via a resistance correction for each MEA. The average gain in voltage from ohmic correction for the six GDLs studied is 14 +/- 6 mV. While this is a small gain, it can mask the AWR effect in the cases where there is little observed voltage gain such as with the 25 BL GDL.

Table 17 Change in voltage via the AWR process for all six GDLs (Table 9) comparing the non-resistance corrected data to the corrected resistance data

	25 BC	**25 BA**	**25 BL**	**25 BA_{nitric}**	**25 AA**	**35 BA**
Initial voltage (V)	0.626	0.586	0.637	0.583	0.596	0.653
Peak voltage (V)	0.628	0.655	0.637	0.654	0.617	0.662
Uncorrected ΔV (mV)	No gain	69	No gain	71	21	9
Corrected ΔV (mV)	9	83	18	87	26	31

It is important to note these results with the correction for ohmic losses match the trend of the results without the resistance correction. For example, there is little voltage gain for the 25 BC GDL in either case, and a very large change in voltage for the 25 BA and 25

BA_{nitric} GDLs in either case. It is interesting to note that the 25 BL and 35 BA GDLs show a modest voltage improvement with AWR when the data is corrected for resistance losses. This shows that these GDLs had larger resistance losses that masked the voltage gain via AWR. The voltage gain is due to AWR overcoming flooding issues due to the hydrophilic MPL (25 BL) and utilizing a GDL without MPL (35 BA). Once corrected, the results are consistent with GDLs without an MPL being more susceptible to flooding and thus voltage improvement during the AWR process and GDLs with an MPL exhibiting enhanced water management capabilities and thus showing little voltage improvement during the AWR process.

These GDL results are consistent with Lu et al. [153], who have shown that GDLs without an MPL have higher water saturation than GDLs with an MPL, which is schematically shown in Figure 85.

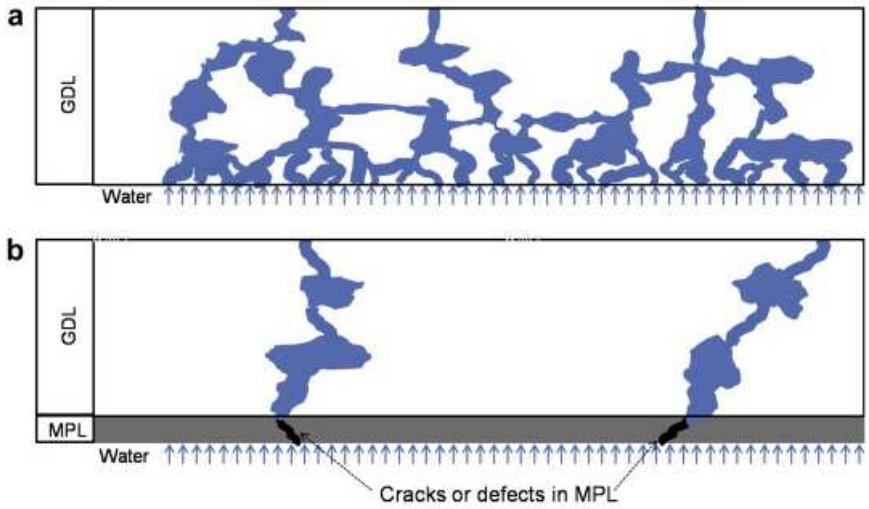

Figure 85. GDL saturation for a) a GDL without MPL and b) a GDL with MPL (reprinted from Lu et al. [153] with permission from Elsevier)

The AWR process is thus a good diagnostic tool to identify whether cathode GDL flooding is an issue. It also shows how well a fuel cell can perform in the absence of

cathode GDL flooding, which aids in the design of novel MEAs. Thus, AWR can be a valuable design tool for GDL/MEA development that is easy to implement and test.

6.2.2 Effect of multiple cathode GDL layers and external water injection

The 25 BA GDL was used as an additional layer on top of the existing MEA structures to test the effect of multiple GDLs on the AWR results. By creating a discontinuity in the GDL, this additional layer can exacerbate the influence of GDL flooding, further confirming the role of GDL water in the AWR process.

The voltage results and pressure drop multiplier results for one and two 25 BA cathode GDLs are shown in Figure 86 and Figure 87, respectively.

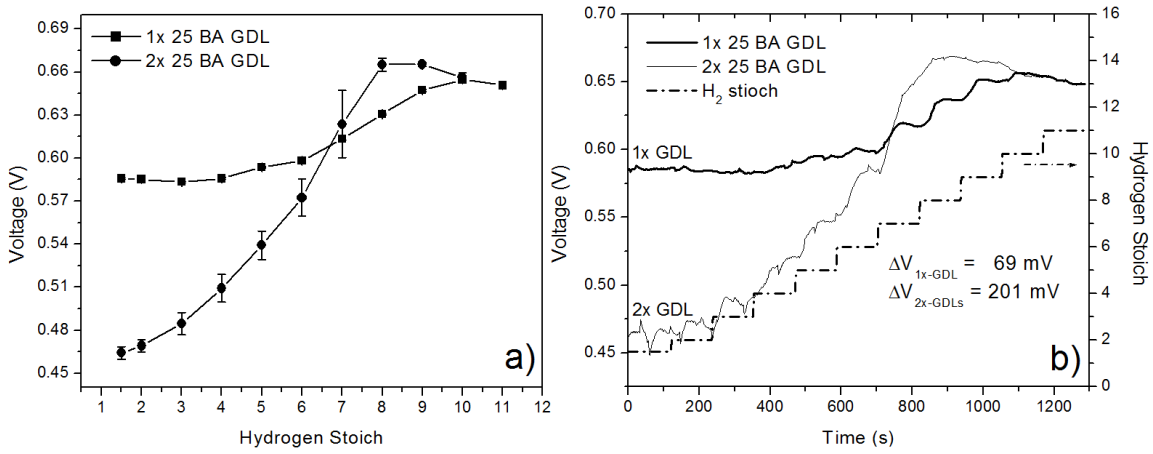

Figure 86. a) Comparison of the AWR voltage results for one and two 25 BA GDLs on the cathode side b) Comparison of the AWR voltage signals for one and two 25 BA GDLs on the cathode side

When using the 25 BA GDL, the use of an additional GDL layer initially lowers the voltage substantially due to mass transport limitations. Through the AWR process, the voltage increases by 201 mV compared to 69 mV with only one GDL. The nearly identical final voltages through AWR mean that the voltage loss with the two GDLs at low hydrogen stoichiometries mainly resulted from GDL flooding, i.e. the dry anode removes the excess cathode GDL water, resulting in comparable final voltages. Further confirming the mass transport differences between these two cases, the total cell ohmic

resistance on average over the course of the entire AWR process is nearly identical for one or two GDLs. It is also interesting to compare the voltage signals for one versus two GDLs, as shown in Figure 86b. With two GDLs, the voltage instability due to GDL flooding at low hydrogen stoichiometries is consistent with the work of Cho et al. [110]. With 2 GDLs, the voltage signal also increases substantially at hydrogen stoichiometries 3-7. This leads to the larger error bars depicted at those points in Figure 86a.

The pressure drop results further confirm this analysis. At higher anode hydrogen stoichiometries (≥9), the pressure drop multipliers are similar, indicating the AWR process removes a similar amount of water in either case. At hydrogen stoichiometries > 9, the voltage results are similar as well (Figure 86a), suggesting the absence of GDL flooding in either case. Initially, the pressure drop multiplier for 2 GDLs is lower. This is because the 2 GDLs lead to more cathode GDL flooding, so less water goes to the anode (initially lessened influence of water on the anode pressure drop). Above a hydrogen stoichiometry of 6, the anode can remove this water, which means more total water is going to the anode with 2 GDLs than with 1 GDL above that point. This leads to the higher pressure drop multiplier with 2 GDLs above a hydrogen stoichiometry of 6. It should be noted that this analysis refers to the transient response of the system to the changes in hydrogen stoichiometry.

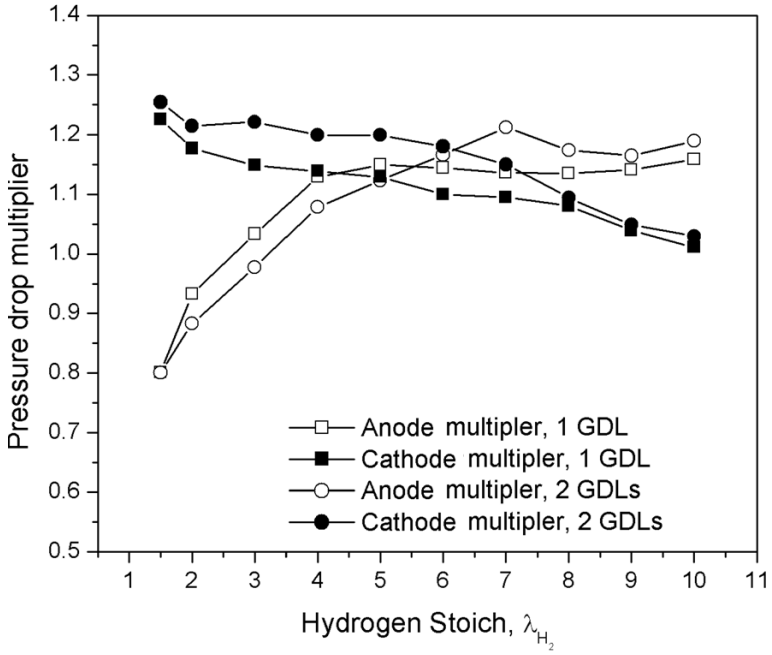

Figure 87. Pressure drop multiplier for one and two 25 BA GDLs on the cathode side (all at $RH_{cathode}$ = 100%)

It is also interesting to note that in general the anode pressure drop multiplier values level off after the initial increase. This is likely related to the point where the anode has removed all of the product water in the system (above the dashed water production line in Figure 82), thus the influence of water on the anode side would have already reached a maximum.

This exacerbated GDL flooding has a much larger effect when using GDLs without an MPL. When an extra 25 BA layer is placed on top of a 25 BL layer, the increase in voltage with peak AWR is only ~8 mV, and when an extra 25 BA layer is placed on top of a 25 BC layer, the increase in voltage is ~22 mV. The results for an additional 25 BA GDL on the 25 BC GDL are shown in Figure 88. It is interesting to note that the cathode GDL thickness plays a more important role in this setup than the inclusion of an MPL layer alone. The cases of the 25 BC with a 25 BA GDL (425 μm thick with MPL) and the 35 BA (300 μm thick without MPL) both show improved performance with AWR when

compared to a single 25 BC (with MPL) GDL (235 μm thick with MPL). The 25 BC/25BA double GDL and the 35 BA GDL both show signs of GDL flooding, since they both increase in voltage during the AWR process. The peak voltages with AWR for these GDLs are also similar to the peak voltage results from the single and double 25 BA GDLs, shown in Figure 86. It should be noted that the difference in performance between the 35 BA GDL and the 25 BC GDL are not ohmic alone; resistance correction does not lead to similar voltages for the two GDLs.

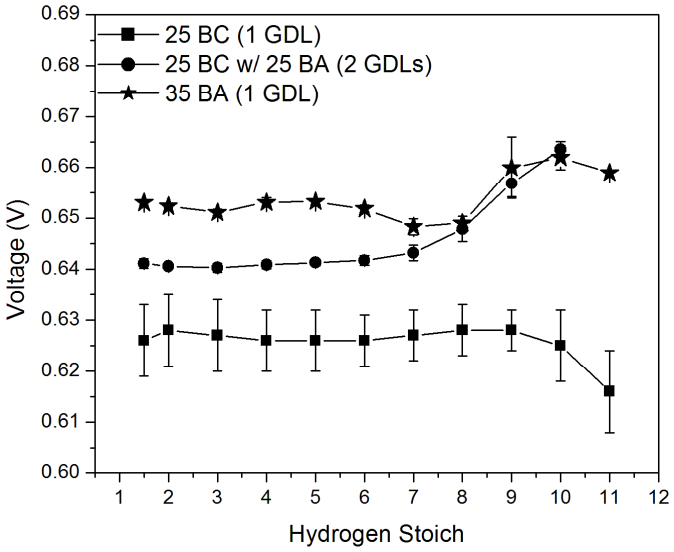

Figure 88. AWR voltage results for 25 BC with 1 GDL and 2 GDLs (an additional 25 BA layer on top on the cathode side), and the results for the 35 BA GDL

To further understand the extent to which AWR can remove water from the cathode to the anode, water was externally injected into the cathode flow field channels. The work was studied with the 25 BA GDL, where AWR has a more significant effect due to higher GDL saturation. These results are shown in Figure 89a and Figure 89b. The water injection clearly lowers the electrochemical performance compared to the case of no water injection, but the AWR process is able to increase the voltage substantially (48 mV) by removing water from the flooded GDL. The voltage oscillations are also lowered

through AWR (Figure 89b), showing the AWR process is overcoming the flooding process.

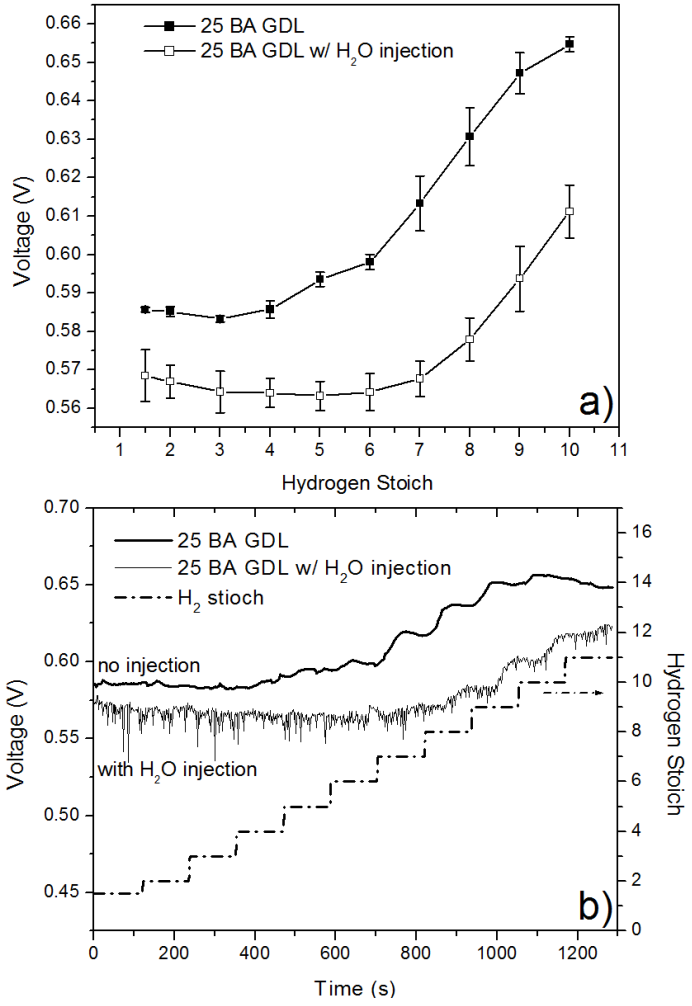

Figure 89. AWR voltage results for the 25 BA GDL (without MPL) with and without external water injection, and b) AWR voltage signals for the 25 BA GDL with and without external water injection

However, the AWR effect does not necessarily reach the cathode flow field where the water was injected. The pressure drop multipliers for anode and cathode for the cases with and without injection are shown in Figure 90.

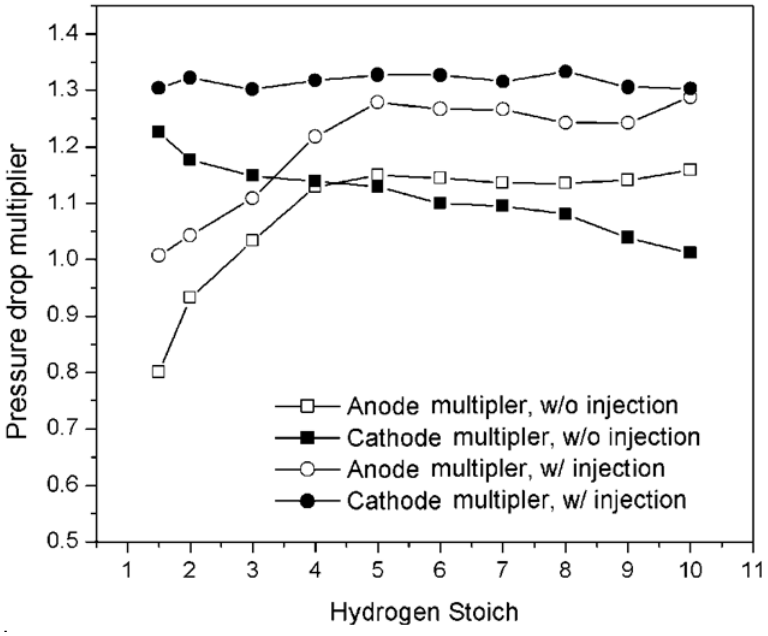

Figure 90. AWR pressure drop multiplier results for the anode and cathode for the 25 BA GDL (without MPL) with and without external water injection

The multiplier is higher on the anode when the water injection happens, indicating the anode does remove more water. However, not enough water is removed to clear the cathode flow field channels of water since the cathode pressure drop multiplier remains constant with the injection (though, the amount of injected water was much higher than the removal ability of the dry anode stream, even at the highest hydrogen stoichiometries). The injected water keeps the cathode GDL saturated (hence the lower final voltage), but the AWR process helps remove some saturation, hence the gain in voltage through AWR. This further confirms the AWR process helps determine the extent to which cathode GDL flooding hinders fuel cell performance.

6.2.3 Effect of relative humidity (RH)

The water vapor content in the gas is directly proportional to the relative humidity (Eqn. 54). Since the AWR process depends on the water concentration gradient between the anode and cathode, the relative humidity of the cathode gas stream is important in the

AWR process. When liquid water is formed, some of it can enter the vapor phase when the cathode RH is less than 100%. Cathode RHs of 25, 50, 75, and 100% were studied at 75^{o}C with the results presented here focusing on the case with the 25 BC (MPL) and 25 BA (no MPL) GDLs. The anode inlet relative humidity remained 0% (dry) in all cases.

The voltage results in Figure 91 for the 25 BC GDL with an MPL do not show much voltage improvement due to AWR. Furthermore, as the membrane dries, the voltage drops, and the voltage drop is greater for drier cathode streams (i.e. the lower cathode RH dries out the membrane more). When the cathode gas stream is not fully saturated (RH < 100%), the cathode gas can remove some of the product water, and the voltages are similar.

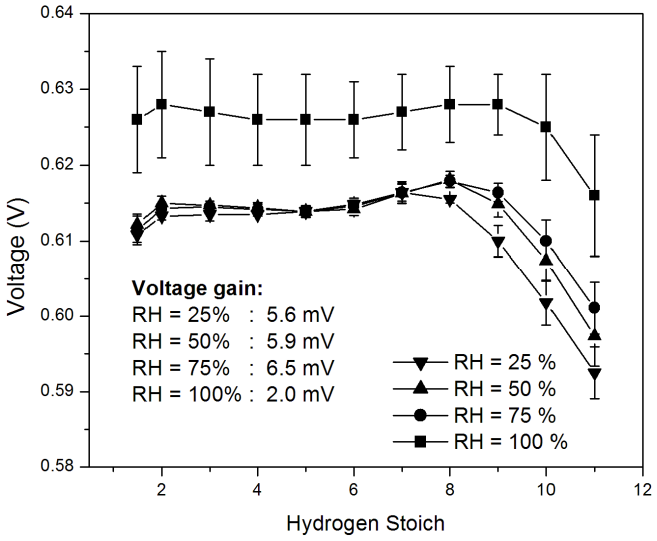

Figure 91. Anode water removal cell voltage results with the 25 BC GDL (w/MPL) for cathode RH = 25, 50, 75, and 100%

The AWR results are much more dramatic with the 25 BA GDL (without the inclusion of the MPL layer), indicating GDL flooding is a problem. The results in Figure 92a show the voltages at each RH begin at a comparable level and all rise with increasing hydrogen stoichiometry.

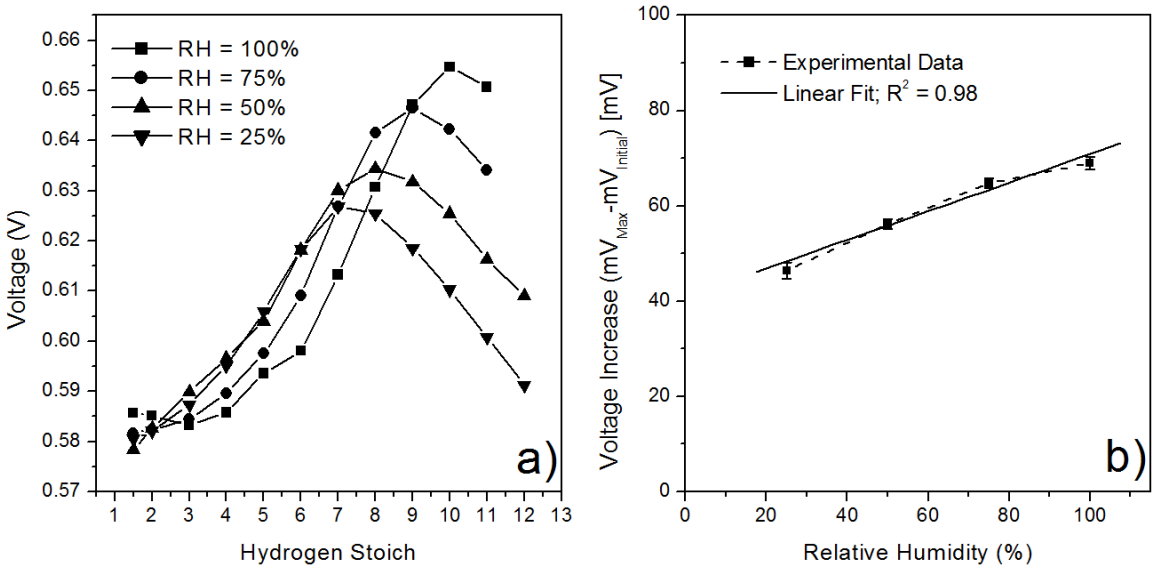

Figure 92. a) Anode water removal cell voltage results with the 25 BA GDL (w/o MPL) for cathode RH = 25, 50, 75, and 100% b) maximum voltage increase as a function of cathode relative humidity

The maximum change in voltage achieved via AWR increases linearly with RH, as shown in Figure 92b. This is because the increased water content with increased cathode RH allows the membrane to maintain hydration longer, which extends the useful range of the AWR improvement. Also, the voltage improvement occurs more quickly at lower cathode RH (Table 18). This is because there is more water removal potential on the cathode with lower RH, so the cathode GDL flooding can be reduced at a lower hydrogen stoichiometry. This potential is further explained in Figure 93, where the removal capabilities are based on the pressure drops using the 25 BA GDL. A relatively drier cathode stream (i.e. 25% RH vs. 100% RH) can remove product water in addition to the anode. Thus, a lower anode stoichiometry is needed to completely remove all of the product water. Thus, the rate of voltage improvement in Figure 92 is higher when a lower cathode relative humidity is utilized.

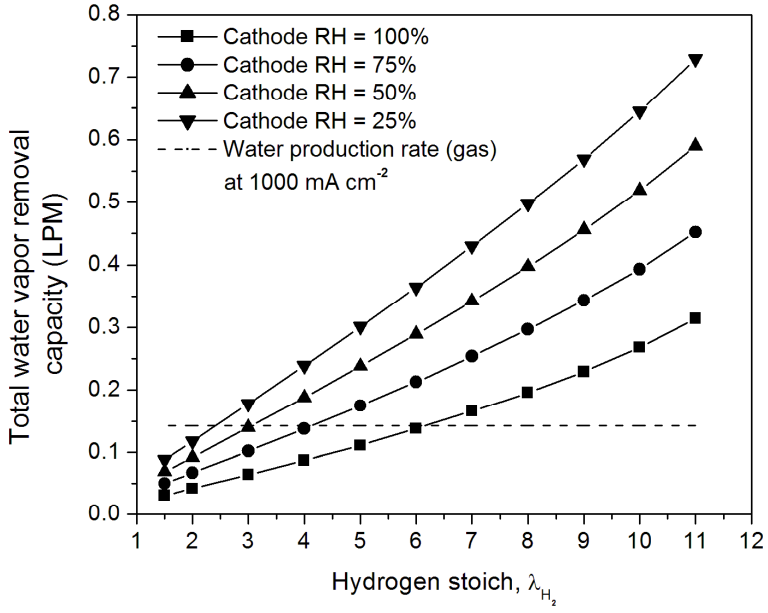

Figure 93. Total water vapor removal capacity with a dry hydrogen steam and varying cathode humidification along with the electrochemical water production rate (vapor phase) at 1000 mA cm^{-2} with all other conditions at the baseline (25 BA GDL)

The voltage at lower cathode RHs reaches a maximum at a lower hydrogen stoichiometry due to increased membrane resistance with the dry anode and a relatively drier cathode. The ratio of resistance at each stoichiometry to the initial resistance for a given RH is shown in Figure 94a. This ratio is utilized to highlight the magnitude of the change in resistance. The first hydrogen stoichiometry after the maximum voltage, where the resistance offsets the AWR impact, is labeled in the figure. The overall cell resistance data for these ratios are shown in Figure 94b.

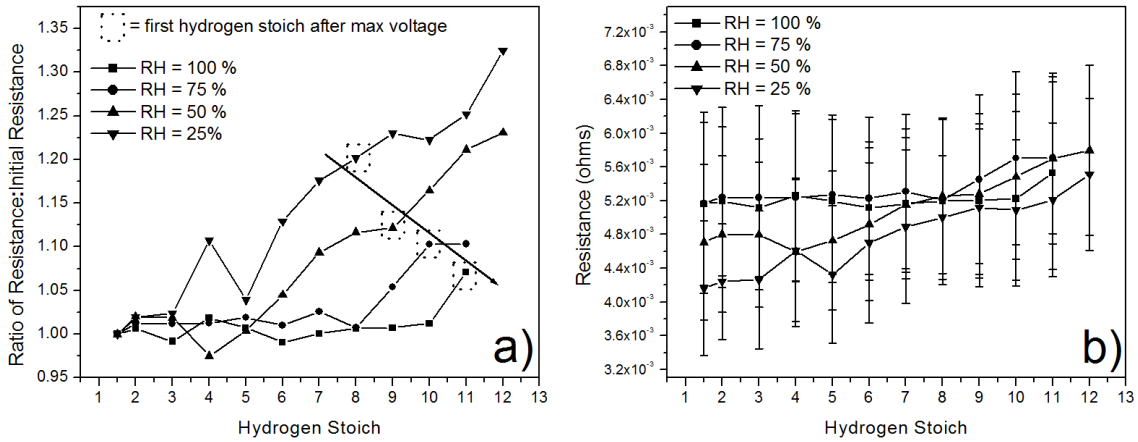

Figure 94. a) Ratio of resistance at a given hydrogen stoichiometry to initial resistance for the 25 BA GDL at cathode RH = 25, 50, 75, and 100% b) experimental resistance measurements at cathode RH = 25, 50, 75, and 100%

When corrected for resistance losses, the gain in voltage during the AWR process is very similar at each RH, 79 +/- 5 mV, as shown in Table 18. Thus, in the absence of mass transport losses in the cathode GDL and in the absence of resistance losses, the peak voltages are comparable. This result makes sense since the MEA is constant for each cathode RH studied, so the peak corrected voltages should be similar.

Table 18 Change in voltage via the AWR process for four cathode relative humidities comparing the non-resistance corrected data to the corrected resistance data

	25 %	**50 %**	**75 %**	**100 %**
Initial voltage (V)	0.581	0.578	0.582	0.586
Peak voltage (V)	0.627	0.635	0.647	0.655
Uncorrected ΔV (mV)	46	56	65	69
Corrected ΔV (mV)	82	83	78	72
Hydrogen stoich at peak voltage	7	8	9	10

Figure 95a and Figure 95b show the anode and cathode pressure drop multipliers, respectively. The general trend is that the higher RH values have a higher pressure drop multiplier, which is indicative of the additional water entering the fuel cell via the humidified gas stream at higher cathode relative humidities. Particularly interesting is at

high hydrogen stoichiometries (≥10) the cathode pressure drop multipliers are all approximately equal, while on the anode side the multipliers generally increase with increasing relative humidity. This is because more water is available for transport from the cathode to anode at higher cathode relative humidities, which increases the amount of water transport to the anode side.

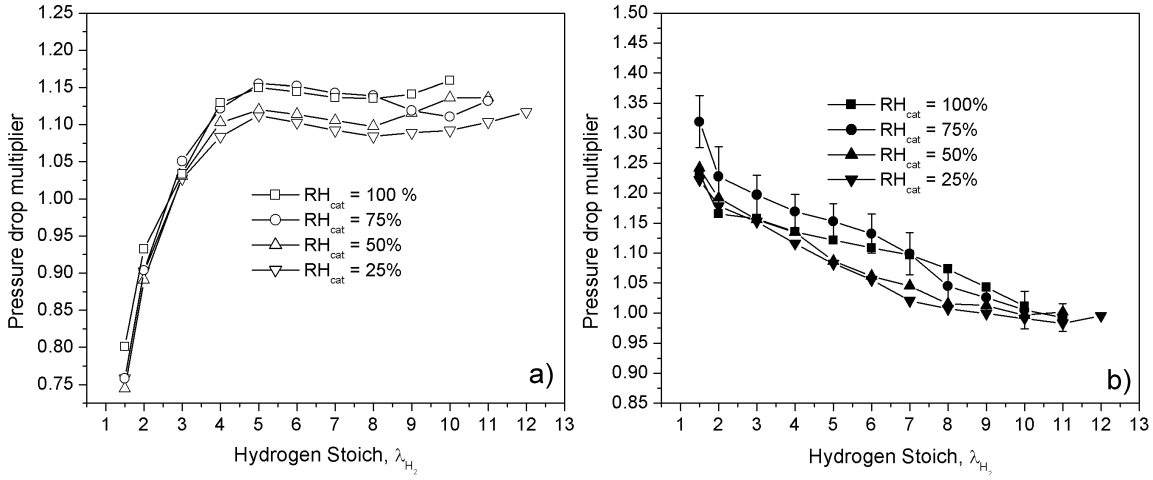

Figure 95. a) Anode pressure drop multiplier results for cathode RH = 25, 50, 75, and 100% b) Cathode pressure drop multiplier for cathode RH = 25, 50, 75, and 100% (baseline conditions with 25 BA GDL)

6.2.4 Effect of temperature

The temperature influences the water concentration gradient since the water volume capacity in the gas stream increases exponentially with temperature. At 90°C the water volume content in the air stream is nearly 6 times more than at 50°C. This has a significant effect on the gas properties and the AWR water vapor gradient. As with the RH section, the results presented here focus on the case of the 25 BC and 25 BA GDLs with all material properties held constant except for MPL inclusion.

For the 25 BC GDL, the increased water concentration gradient at 90°C causes an initial increase in the voltage compared to the lower temperatures (Figure 96). The voltage gain at 75°C was 2 mV and the gain at 90°C was 14 mV. The cases at 25 and

50°C show no influence of the AWR process on voltage, and instead the increased hydrogen stoichiometry lowers the voltage due to the membrane drying out.

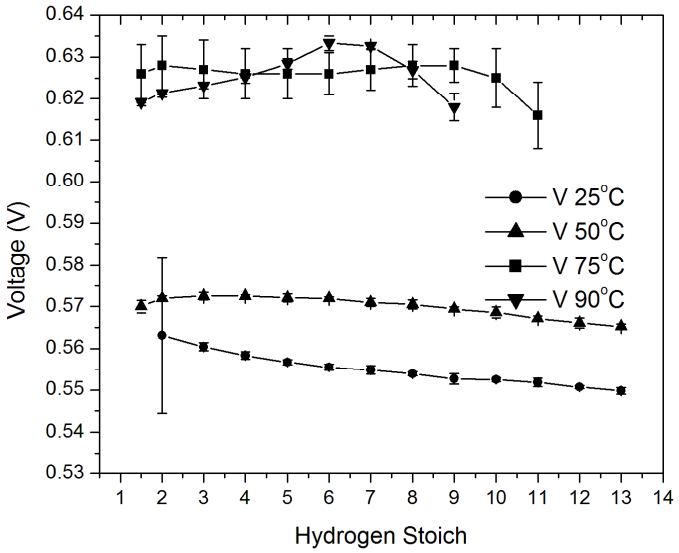

Figure 96. AWR voltage results at T = 25, 50, 75, and 90°C for the 25 BC GDL (all at $RH_{cathode}$ = 100%)

The voltage results with the 25 BA GDL at 75 and 90°C are shown in Figure 97a. Results at 25 and 50°C are not shown because a steady voltage signal could not be achieved at the lower hydrogen stoichiometries.

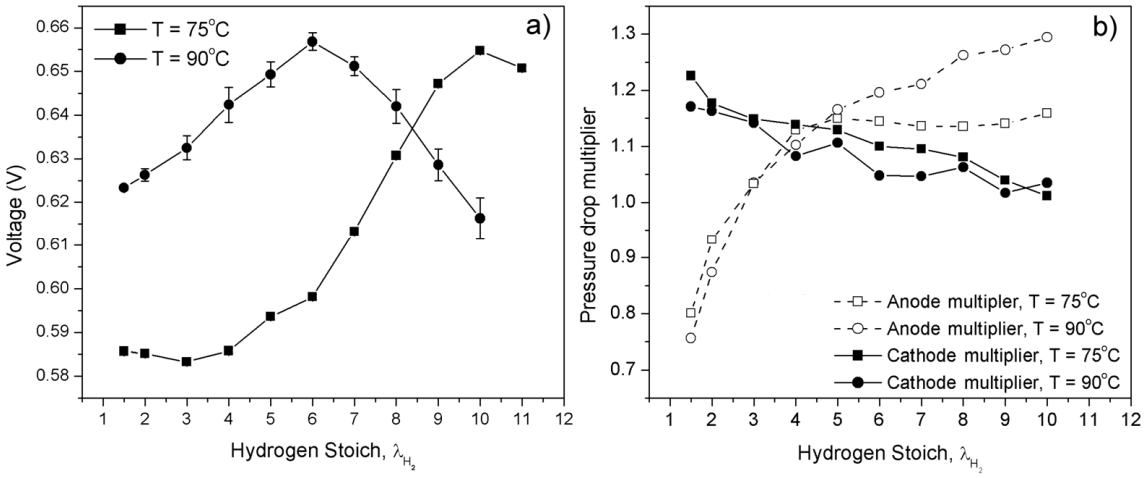

Figure 97. a) Voltages results for the 25 BA GDL at T = 75 and 90°C b) Anode and cathode pressure drop multiplier results for the 25 BA GDL at T = 75 and 90°C (all at $RH_{cathode}$ = 100%)

As in the case of the 25 BC GDL, the higher temperature leads to a greater water concentration gradient between the anode and cathode, and a higher anode carrying

capacity for water vapor (Eqn. 55). The total water removal ability of the hydrogen stream at 75°C and 90°C is shown in Figure 98, and it should be noted the amount of water vapor that can be removed at 90°C is 1.96 +/- 0.02 times more than the amount at 75°C over the range of hydrogen stoichiometry studied. The hydrogen stream at 90°C has the ability to remove all of the product water at a much lower stoichiometry than at 75°C (~3 vs. ~6, respectively). Thus, the results in Figure 97a show a much quicker response to the AWR process at 90°C.

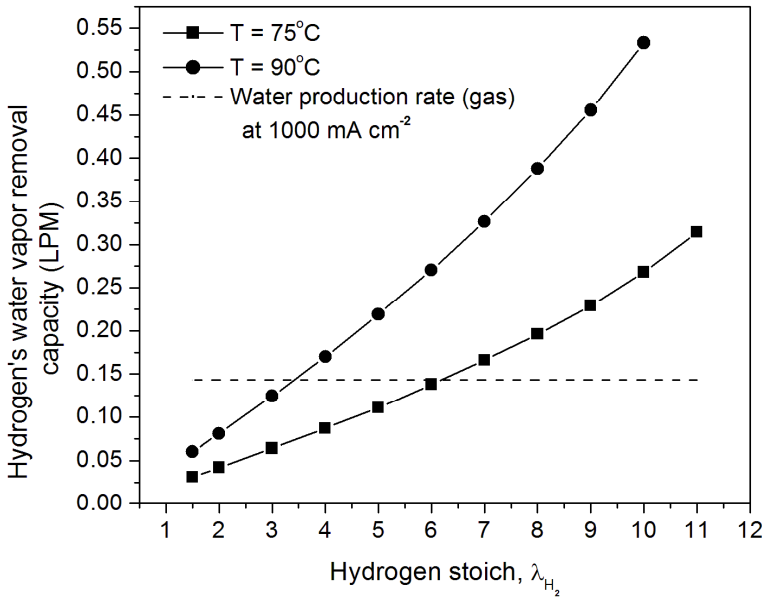

Figure 98. Water vapor removal capability of hydrogen at 75°C and 90°C for the pressure drops at baseline conditions and the 25 BA GDL

However, there is increased membrane drying at higher stoichiometries at 90°C. This leads to a decrease in voltage after a hydrogen stoichiometry of 6 (Figure 97), which is similar to results with 25 BC at 90°C. The resistance at 75°C shows very little increase with an increase in the hydrogen stoichiometry (same resistance value for the cathode RH = 100% case in Figure 94a). However, the resistance at 90°C increases with hydrogen stoichiometry and is 8% higher than the initial resistance at a hydrogen stoichiometry of 7 and is 15% higher than the initial resistance at a hydrogen stoichiometry of 10.

The anode and cathode pressure drop multipliers are shown in Figure 97b. As the hydrogen stoichiometry increases, the cathode pressure drop multiplier decreases, which shows the influence of water in the cathode channels is reduced during the AWR process. The anode pressure drop multiplier is higher at 90^{o}C compared to 75^{o}C above a hydrogen stoichiometry of 5, which is due to the increased ability of hydrogen to remove water at higher temperatures and more water entering the cell via the fully humidified air stream. Water is likely also coming from the membrane itself, as evidenced by the large drop in voltage due to membrane dehydration. This leads to the larger pressure drop multiplier in the anode.

6.2.5 Effect of operating current density

Changing the current density changes both the air flow rate and the water production rate, influencing the water gradient for the AWR process. Figure 99 shows the results for the 25 BA GDL at several current densities, including the baseline results at 1000 mA cm^{-2}.

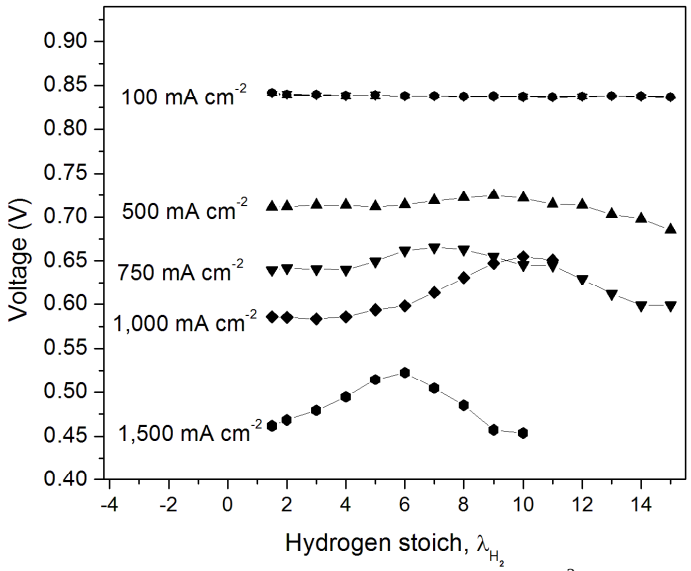

Figure 99. AWR voltage results at 100, 500, 750, 1000, and 1500 mA cm^{-2} for the 25 BA GDL (without MPL)

It can be seen that there is no increase in voltage for the 25 BA GDL when the current density is low (100 mA cm^{-2}). This result is because not enough water is produced to

substantially reduce performance through mass transfer losses. This result is also true for the 25 BC GDL (results not shown). These results are consistent with low current density voltage losses being due to kinetic effects from slow oxygen reduction. Tests were also performed with the 25 BA GDL at 500, 750, 1000, and 1500 mA cm^{-2} where more water is produced, which can increase GDL saturation and reduce performance. The voltage gains from the AWR process for these four current densities were approximately 13, 26, 69, and 61 mV, respectively. Increased water production is associated with higher GDL flooding, which is removed by AWR, leading to larger gains in voltage.

6.3 Conclusions

Anode water removal (AWR) is a powerful diagnostic tool to evaluate cathode GDL flooding. By using a dry anode stream and increasing the water removal capability with increasing anode stoichiometry, liquid water saturating the cathode GDL can be removed via the anode. This reduces voltage losses due to water flooding in the cathode GDL. The major results from this study are:

1. The largest voltage gains with AWR occur with the use of GDLs without an MPL. GDLs without MPL are more prone to flooding, and this water is removed during the AWR process. Multiple GDLs on the cathode result in more flooding/GDL saturation when GDLs without an MPL are used. This leads to a steep drop in cell voltage that is fully recovered with the AWR process. Thus, when the AWR process shows a large voltage gain, the voltage failure mechanism can be attributed to cathode GDL saturation.
2. The cathode air RH plays a key role in the AWR process when the GDL does not have an MPL. A lower cathode RH can also remove water in addition to the

anode, so the peak voltage is reached at a lower hydrogen stoichiometry. While the lower RH leads to additional resistance losses, correction for resistance shows a similar voltage gain for all four cathode RHs studied (25%, 50%, 75%, 100%).

3. An increase in temperature from 75^{o}C to 90^{o}C causes the voltage to improve faster with increasing hydrogen stoichiometry. This can be attributed to the larger water removal capability of the anode at higher temperatures. However, membrane dehydration occurs at moderate hydrogen stoichiometries with higher temperatures.
4. At lower current densities (100 mA cm^{-2}), not enough water is produced electrochemically to flood the GDL, and no gain in voltage is noted. However, as the current is increased, and thus the water production rate, the AWR process can increase the voltage. These results are due to mass transport limitations being a greater factor at higher current densities, which are then removed in the AWR process.

The AWR method can be used to evaluate and design novel GDL structures to minimize mass transport losses in the GDL. The maximum voltage from this AWR process indicates how well a fuel cell can perform in the absence of cathode GDL mass transport issues.

7 Conclusions and recommendations

The conclusions and recommendations here reflect the work done on pressure drop hysteresis (Chapters 4 and 5) and anode water removal (Chapter 6). Both studies are important in PEM fuel cell water management, and the major results are highlighted.

7.1 Conclusions

Our group has studied a new problem within the field of PEM fuel cell water management: pressure drop hysteresis. This study is the first time this phenomenon has been examined in PEM fuel cells, and the results are relevant to water management as a whole.

- Pressure drop hysteresis occurs when the gas and liquid flow rates, uniquely coupled in a PEM fuel cell via Faraday's law, are increased along a set path and then decreased along the same path but show a different pressure drop. The general mechanism for the pressure drop hysteresis is unique to PEM fuel cells. When starting from dry initial conditions, low flows of water are not able to break through the GDL. When water breakthrough does occur at moderate flows (current densities), the air flow rate is high enough to remove the water convectively. This leads to a larger two-phase flow pressure drop, but not necessarily accumulation. As the load is subsequently decreased, water can accumulate in the flow channel. Thus, the pressure drop in the descending approach can be higher than in the ascending approach.
- Three distinct experimental approaches to this hydrodynamic problem allowed us to understand the problem fundamentally and then apply the results to the most realistic system. The first approach explored this phenomenon in a fuel

cell's flow channels under non-operating conditions at ambient temperature and pressure to establish the hydrodynamic baseline. The results were then explored in a non-operating setup with humidified and heated gases to understand the pressure drop hysteresis in terms of more relevant fuel cell operating conditions. Finally, the pressure drop hysteresis was studied in an operating PEM fuel cell in a narrow range of most relevant conditions. This phenomena was explored through several variables relevant to PEM fuel cells, including: GDL properties, MPL inclusion, gas stoichiometry, and temperature.

- In general, the GDL properties are not a main factor in pressure drop hysteresis. While the mechanism of water reaching the cathode can change depending on the GDL and MPL, the bulk influence of water in the flow channels in terms of accumulation for pressure drop hysteresis is similar.
- The gas stoichiometry is the most important parameter as it largely defines the convective removal abilities of the cathode air stream. Higher air flow rates (such as at an air stoichiometry of 5) can remove the same amount of water in either ascending or descending approach, removing the pressure drop hysteresis.
- The temperature also plays an important role, especially with fully humidified air, as condensation can exacerbate the flooding problem, and the condensation occurs more readily at lower temperatures. Also, the gas velocity decreases and the surface tension of water increases with lower

temperatures, causing more water accumulation. Thus, more hysteresis is noted at 30^{o}C than at 90^{o}C.

The problems associated with excess water accumulation are well documented: increased parasitic power losses due to an increased pressure drop, gas maldistribution, and decreased reactant transport to active catalyst sites. These concepts can also be problems in fuel cell stacks, where low cells in particular can lower system performance in stacks. Thus, research groups considering applications where the load cycles should be aware of this problem. A practical consideration would be to measure the pressure drop during actual operation of a load cycle to determine if any differences in pressure drop exist. From this thesis, it is likely that an increase in pressure drop would be due to additional liquid water accumulation, not just flow pattern changes. This mechanism of hysteresis is distinctively different, which is important for an operator to know for long term stability and durability.

Anode water removal was also studied as an important issue in PEM fuel cell water management. By increasing the flow rate of a dry anode stream, the water removal capabilities of the anode increase. As water is removed from the cathode by the anode, the voltage of the cell can increase, giving an indication of maximum performance in the absence of mass transfer limitations.

- Larger voltage gains occur during the AWR process with the use of GDLs without an MPL. GDLs without MPL are more prone to flooding/high saturation, which is removed during the AWR process. Cathode GDL flooding can be exacerbated when multiple GDLs are used on the cathode side and when water is injected externally into the cathode flow field channels. These

lead to a drop in cell voltage that is recovered with the AWR process. Thus, the performance failure mechanism when large voltage gains are noted can be attributed to cathode GDL saturation.

- The cathode air relative humidity is an important parameter in the anode water removal process when considering a GDL without an MPL. A reduced cathode gas RH (< 100%) can remove water in addition to the anode gas, so the peak voltage without mass transfer limitations is reached at a lower hydrogen stoichiometry.
- An increase in temperature from 75^{o}C to 90^{o}C causes the voltage to improve faster with increasing hydrogen stoichiometry. This result is attributed to the larger water vapor removal ability of the anode gas at a higher temperature. However, membrane drying can occur faster at the higher temperatures, and thus the voltage decreases from the peak value at moderate hydrogen stoichiometries.
- The operating current density dictates the water production rate and is thus an important consideration in AWR. At low current densities (100 mA cm^{-2}), not enough water is produced to substantially flood the GDL so no voltage improvement is noted. As the current density is increased, the GDL flooding can increase, which is followed by increasingly larger voltage gains during AWR.

The AWR method is well suited to determine if GDL flooding mass transport limitations are causing a decrease in cell voltage. By knowing the maximum performance in the absence of GDL flooding problems, novel GDLs can be further understood and

advanced. Thus, AWR is a useful and quick diagnostic tool for an operator when considering performance losses associated with GDLs.

7.2 Recommendations

Recommendations are provided for pressure drop hysteresis, anode water removal, and water management studies in general.

7.2.1 Pressure drop hysteresis

- Explore purging methods in more depth to mitigate the effect of the hysteresis. Purges on the descending approach can raise the pressure drop significantly for a short period, but then remove the accumulated liquid water in the flow field channels. The overall pressure drop is then reduced and additional accumulation on the descending approach is substantially lessened. However, this method requires potentially unrealistic controls, and thus more study is needed.
- Now that the mechanism of pressure drop hysteresis in a PEM fuel cell is understood, it would be interesting to study these results in a serpentine flow field, where the overall pressure drop, and thus parasitic loss, is much higher. Preliminary results show some pressure drop hysteresis does exist at baseline conditions in the TP50 fuel cell, which is discussed in Section 5.5. More accurate pressure transducers should be used with the Hydrogenics™ station if this work is to be done accurately. The transducers for the parallel channels will not be suitable due to the very large pressure drops at higher current densities in the serpentine channels.
- It would be useful to perform the pressure drop hysteresis tests in a PEM fuel cell stack, particularly in one that employs parallel channels since this flow field type

has already been characterized in this work. The magnitude of the pressure drop difference is low in a single cell with parallel channels, thus the potential parasitic power loss is not well characterized. Operating with an entire fuel cell stack where the total pressure drop is higher would further quantify the relevance of this topic in PEM fuel cell water management.

- The two-phase flow pressure drop has not been predicted via the Lockhart-Martinelli equation for the descending approach. A modification is needed to take into account water accumulation at low air flow rates, which greatly increases the two-phase flow multiplier. Quantifying the amount of water accumulating in the channel during the descending approach would help form this parameter. One method to accomplish this would be to perform the pressure drop hysteresis test and then purge the cell quickly to a water collection chamber. If purged fast enough, only accumulated water will be collected and additional condensation from the humidified air can be avoided. This would be time consuming though since one collection test would be needed for each point on the descending approach for each operating condition. Then, the process would have to begin again from the first point in the ascending approach.

7.2.2 Anode water removal

- Perform the AWR tests with parallel channel flow fields. Graphite plates for the TP50 have been fabricated already with the same channel cross-sectional dimensions as the cathode's serpentine channels, but the serpentine bends were connected to act as flow distributors to form parallel channels. However, this plate cannot be used in conjunction with the serpentine anode channels because the

larger pressure drop on the anode causes an unsafe pressure differential between the parallel channel cathode and the serpentine channel anode. A parallel channel anode is needed before this test can be performed.

- Perform the AWR tests in the transparent visualization cell used during the pressure drop hysteresis tests. It would be interesting to see how AWR effects a flooded cathode flow field channel. While tests were done to inject external water, it would be interesting to see any flow patterns changes in the cathode during AWR. Also, the anode could be visualized to see if more liquid water enters the anode flow field.
- Perform the AWR tests with an anode GDL that does not contain an MPL. It would be interesting to see how the anode MPL affects the overall water balance. The current anode GDL is the 25 DC GDL, which contains 20% PTFE and an MPL. A suitable anode GDL to test next would be the 25 DA GDL, which would keep the PTFE content at 20% but exclude the MPL.

7.2.3 PEM fuel cell water management

- Current work is being done by our group on flow maldistribution mitigation in parallel, non-operating channels. Numerical simulations have looked at putting small connections in the channel divider (i.e. the landing width) of two-parallel channels. The simulation results have suggested that when the communications are close to the channel size, 1 x 1 mm for instance, the maldistribution problem becomes worse since the gas phase utilizes the communication instead of the liquid. However, at smaller connection sizes, 0.25 mm x 1 mm, the liquid water fills the connection completely to bridge the two channels, allowing water to more

evenly distribute between two channels. This then reduces the gas maldistribution. Work is ongoing to validate the numerical results experimentally via entrance pressure drop measurements to quantify the maldistribution.

References

[1] R. O'Hayre, S-W. Cha, W. Colella, F.B. Prinz, Fuel Cell Fundamentals, John Wiley and Sons Inc., New Jersey, 2006.

[2] R. Anderson, L. Zhang, Y. Ding, M. Blanco, X.Bi, D.P. Wilkinson, A Critical Review of Two-phase Flow in Gas Channels of PEM Fuel Cells, J. Power Sources 195 (2010) 4531-4553.

[3] J. Benziger, Fan the flame with water: current ignition, front propagation, and multiple steady states in polymer electrolyte membrane fuel cells, AIChE J. 55 (2009) 3034-3040.

[4] K. Jiao, X. Li, Water transport in polymer electrolyte membrane fuel cells, Prog. Energy Combust. Sci. 37 (2011) 221-291.

[5] H. Li, Y. Tang, Z. Wang, Z. Wang, Z. Shi, S. Wu, D. Song, J. Zhang, K. Fatih, J. Zhang, H. Wang, Z. Liu, R. Abouatallah, A. Mazza, A review of water flooding issues in the proton exchange membrane fuel cell, J. Power Sources 178 (2008) 103-117.

[6] T.A. Trabold, Minichannels in polymer electrolyte membrane fuel cells, Heat Transfer Eng. 26 (2005) 3-12.

[7] Springer, T. E., T. A. Zawodzinski, S. Gottesfeld, Polymer electrolyte fuel cell model, J. Electrochem. Soc. 138(8) (1991) 2334-2342.

[8] D. M. Bernardi, M. W. Verbrugge, Mathematical model of a gas diffusion electrode bonded to a polymer electrolyte, AIChE Journal 37(8) (1991) 1151-1163.

[9] F.Y. Zhang, X.G. Yang, C.Y. Wang, Liquid water removal from a polymer electrolyte fuel cell, J. Electrochem. Soc. 153 (2006) A225-A232.

[10] X. Liu, H. Guo, F. Ye, C.F. Ma, Flow dynamic characteristics in flow field of proton exchange membrane fuel cells, Int. J. Hydrogen Energy 33 (2008) 1040-1051.

[11] T. Ous, C. Arcoumanis, Visualisation of water droplets during the operation of PEM fuel cells, J. Power Sources 173 (2007) 137-148.

[12] H. Masuda, K. Ito, T. Oshima, K. Sasaki, Comparison between numerical simulation and visualization experiment on water behavior in single straight flow channel polymer electrolyte fuel cell, J. Power Sources 177 (2008) 303-313.

[13] K. Tüber, D. Pocza, C. Hebling, Visualization of water buildup in the cathode of a transparent PEM fuel cell, J. Power Sources 124 (2003) 403-414.

[14] A. Hakenjos, H. Muenter, U. Wittstadat, C. Hebling, A PEM fuel cell for combined measurement of current and temperature distribution, and flow field flooding, J. Power Sources 131 (2004) 213-216.

[15] F-B. Weng, A. Su, C.Y. Hus, C-Y. Lee, Study of water-flooding behavior in cathode channel of a transparent proton-exchange membrane fuel cell, J. Power Sources 157 (2006) 674-680.

[16] D. Spernjak, A.K. Prasad, S.G. Advani, Experimental investigation of liquid water formation and transport in a transparent single-serpentine PEM fuel cell, J. Power Sources 170 (2007) 334-344.

[17] S. Ge, C.Y. Wang, Liquid water formation and transport in PEFC anode, J. Electrochem. Soc. 154 (2007) B998-B1005.

[18] A. Theodorakakos, T. Ous, M. Gavaises, J.M. Nouri, N. Nikolopoulos, H. Yanagihara, Dynamics of water droplets detached from porous surfaces of relevance to PEM fuel cells, J. Colloid Interface Sci. 300 (2006) 673-687.

[19] R. Shimoi, M. Masuda, K. Fushinobu, Y. Kozawa, K. Okazaki, Visualization of the membrane temperature field of a polymer electrolyte fuel cell, Trans. ASME 126 (2004) 258-261.

[20] H-S. Kim, T-H. Ha, S-J. Park, K. Min, M, Kim, Visualization study of cathode flooding with different operating conditions in a PEM unit fuel cell, Proceedings of the 3rd International Conference on Fuel Cell Science Engineering and Technology, Ypsilanti, USA, 2005, pp. 57-63.

[21] K. Sugiura, M. Nakata, T. Yodo, Y. Nishiguchi, M. Yamauchi, Y. Itoh, Evaluation of a cathode gas channel with a water absorption layer/waste channel in a PEFC by using visualization technique, J. Power Sources 145 (2005) 526-533.

[22] H.P. Ma, H.M. Zhang, J. Hu, Y.H. Cai, B.L. Yi, Diagnostic tool to detect liquid water removal in the cathode channels of proton exchange membrane fuel cells, J. Power Sources 162 (2006) 469-473.

[23] X. G. Yang, F. Y. Zhang, A. L. Lubawy, C.Y. Wang, Visualization of liquid water transport in a PEFC, Electrochem. Solid-State Lett. 7 (2004) A408-A411.

[24] M. Wang, H. Guo, G. Ma, Temperature distribution on the MEA surface of a PEMFC with serpentine channel flow bed, J. Power Sources 257 (2006) 181-187.

[25] J. Cho, H-S Kim, K. Min. Transient response of a unit proton-exchange membrane fuel cell under various operating conditions, J. Power Sources 185 (2008) 118-128.

[26] Z. Dunbar, R. Masel, Magnetic resonance imaging investigation of water accumulation and transport in graphite flow fields in a polymer electrolyte membrane fuel cell: Do defects control transport?, J. Power Sources 182 (2008) 76-82.

[27] P. Chang, J. St-Pierre, J. Stumper, B. Wetton, Flow distribution in proton exchange membrane fuel cell stacks, J. Power Sources 162 (2006) 340-355.

[28] J. St-Pierre, PEMFC in situ liquid-water-content monitoring status, J. Electrochem. Soc. 154 (2007) B724-B731.

[29] J. Sergi, S. Kandlikar, Quantification and characterization of water coverage in PEMFC gas channels using simultaneous anode and cathode visualization and image processing, I. J. Hydrogen Energy 36 (2011) 12381-12392.

[30] K. Takada, Y. Ishigami, J. Inukai, Y. Nagumo, H. Takano, H. Nishide, M. Watanabe, Simultaneous visualization of oxygen distribution and water blockages in an operating triple-serpentine polymer electrolyte fuel cell, J. Power Sources 196 (2011) 2635-2639.

[31] J.P. Owejan, T.A. Trabold, D.L. Jacobson, M. Arif, S.G. Kandilkar, G. Satsih, Effects of flow field and diffusion layer properties on water accumulation in a PEM fuel cell, Proceedings of the Fifth International Conference on Nanochannels, Microchannels and Minichannels, Puebla, Mexico, June, 2007, pp. 401-408.

[32] M.A. Hickner, N.P. Siegel, K.S. Chen, D.N. McBrayer, D.S. Hussey. D.L. Jacobson, M. Arif, Real-time imaging of liquid water in an operating proton exchange membrane fuel cell, J. Electrochem. Soc. 153 (2006) A902-A908.

[33] A. Bazylak, Liquid water visualization in PEM fuel cells: A review, Int. J. Hydrogen Energy, 34 (2009) 3845-3857.

[34] S. Tsushima, S. Hirai, In situ diagnostics for water transport in proton exchange membrane fuel cells, Prog. Energy Combust. Sci. 37 (2011) 204-220.

[35] H-Y. Tang, A. Santamaria, J.W. Park, C. Lee, W. Hwang, Quantification of water in hydrophobic and hydrophilic flow channels subjected to gas purging via neutron imaging, J. Power Sources 196 (2011) 9373-9381).

[36] S.G. Kandlikar, Microscale and macroscale aspects of water management challenges in PEM fuel cells, Heat Transfer Eng. 29(7) (2008) 575-587.

[37] W. Dai, H. Wang, X-Z. Yuan, J. Martin, D. Yang, J. Qiao, J. Ma, A review on water balance in the membrane electrode assembly of proton exchange membrane fuel cells, Int. J. Hydrogen Energy 34 (2009) 9461-9478.

[38] I. S. Hussaini, C.-Y. Wang, Visualization and quantification of cathode channel flooding in PEM fuel cells, J. Power Sources 187(2) (2009) 444-451.

[39] D.P. Wilkinson, H.H. Voss, K. Prater, Water management and stack design for solid polymer fuel cells, J. Power Sources 49 (1994) 117-127.

[40] S-S. Hsieh, Y-J. Huang, B-S. Her, Pressure drop on water accumulation distribution for a micro PEM fuel cell with different flow field plates, Int. J. Heat Mass Transfer 52 (2009) 5657-5659.

[41] X. Liu, H. Guo, F. Ye, C. F. Ma, Water flooding and pressure drop characteristics in flow channels of proton exchange membrane fuel cells, Electrochimica Acta 52(11) (2006) 3607-3614.

[42] K. Ito, K. Ashikaga, H. Masuda, T. Oshima, Y. Kakimoto, K. Sasaki, Estimation of flooding in PEMFC gas diffusion layer by differential pressure measurement, J. Power Sources 175 (2008) 732-738.

[43] F. Barbir, H. Gorgun, X. Wang, Relationship between pressure drop and cell resistance as a diagnostic tool for PEM fuel cells, J. Power Sources 141 (2005) 96-101.

[44] P. Rodatz, F. Buchi, C. Onder, L. Guzzella, Operational aspects of a large PEFC stack under practical conditions J. Power Sources 128 (2004) 208-217.

[45] N. S. Siefert, S. Lister, Voltage loss and fluctuation in proton exchange membrane fuel cells: The role of cathode channel plurality and air stoichiometric ratio, J. Power Sources 196 (2011) 1948-1954.

[46] S.D Knights, K.M. Colbow, J. St-Pierre, D.P. Wilkinson, Aging mechanisms and lifetime of PEFC and DMFC, J. Power Sources 127 (2004) 127-134.

[47] J.P. Mayers, R.M. Darling, Model of carbon corrosion in PEM fuel cells, J. Electrochem. Soc. 153 (2006) A1432-1442.

[48] Al-Baghdadi and Al-Janabi, Effect of Operating Parameters on the hyhro-thermal stresses in proton exchange membranes of fuel cells, Int. J. Hydrogen Energy 32 (2007) 4510-4522.

[49] J. St-Pierre, A. Wong, J. Diep, D. Kiel, Demonstration of a residence time distribution method for proton exchange membrane fuel cell evaluation, J. Power Sources 164 (2007) 196-202.

[50] L.F. Zhang, W. Du, H.T. Bi, D.P. Wilkinson, J. Stumper, H.J. Wang, Gas-liquid two-phase flow distributions in parallel channels for fuel cells, J. Power Sources 189 (2009) 1023-1031.

[51] S.G. Kandlikar, Z. Lu, W.E. Domigan, A.D. White, M.W. Benedict, Measurement of flow maldistribution in parallel channels and its applications to ex-situ and in-situ experiments in PEMFC water management studies, Int. J. Heat Mass Transfer 52 (2009) 1741-1752.

[52] J.S. Allen, Two-phase flow in small channels and the implication for PEM fuel cell operation, ECS Transactions, 3(1) (2006) 1197-1206.

[53] M.J. English, S.G.Kandlikar, An experimental investigation into the effect of surfactants on air-water two-phase flow in minichannels, Heat Transfer Engineering, 27(4) (2006) 99-109.

[54] E.S. Lee, C. Hidrovo, K. Goodson, J. Eaton, Gas-liquid flow in microchannels bounded by a porous wall, 6th International Conference on Multiphase Flow, Leipzig, Germany, July, 2007, Paper No. S7_Thu_A_46.

[55] L.F. Zhang, H.T. Bi, D.P. Wilkinson, J. Stumper, H.J. Wang, Gas-liquid two-phase flow patterns in parallel channels for fuel cells, J. Power Sources 183(2) (2008) 643-650.

[56] Z. Lu, S.G. Kandlikar, C. Rath, M. Grimm, W. Domigan, A.D. White, M. Hardbarger, J.P. Owejan, T.A. Trabold, Water management studies in PEM fuel cells, part II: Ex situ investigation of flow maldistribution, pressure drop and two-phase flow pattern in gas channels, Int. J. Hydrogen Energy 34 (2009) 3445-3456.

[57] J. E. Steinbrenner, E.S. Lee, C. H. Hidrovo, J.K. Eaton, K.E. Goodson, Impact of channel geometry on two-phase flow in fuel cell microchannels, J. Power Sources 196 (2011) 5012-5020.

[58] K. Pehlivan, I. Hassan, M. Vaillancourt, Experimental study on two-phase flow and pressure drop in millimeter-size channels, Appl. Therm. Eng. 26 (2006) 1506-1514.

[59] M.K. Akbar, D.A. Plummer, S.M. Ghiaasiaan, On gas–liquid two-phase flow regimes in microchannels, Int. J. Multiphase Flow 29 (2003) 855-865.

[60] K.A. Triplett, S.M. Ghiaasiaan, S.I. Abdel-Khalik, D.L. Sadowski, Gas–liquid two-phase flow in microchannels Part I: two-phase flow patterns, Int. J. Multiphase Flow 25 (1999) 377-394.

[61] J.L. Xu, P. Cheng, T.S. Zhao, Gas–liquid two-phase flow regimes in rectangular channels with mini/micro gaps, Int. J. Multiphase Flow 25 (1999) 411-432.

[62] Z. Lu, C. Rath, G. Zhang, S. G. Kandlikar, Water management studies in PEM fuel cells, part IV: Effects of channel surface wettability, geometry, and orientation on

the two-phase flow in parallel gas channels, I. J. Hydrogen Energy 36 (2011) 9864-9875.

[63] A. Marchitto, F. Devia, M. Fossa, G. Guglielmini, C. Schenone, Experiments on two-phase flow distribution inside parallel channels of compact heat exchangers, I. J. of Multiphase Flow 34 (2008) 128-144.

[64] Y. Taitel, L. Pustylnik, M. Tshuva, D. Barnea, Flow distribution of gas and liquid in parallel pipes, Int. J. Multiphase Flow 29 (2003) 1193-1202.

[65] M. Tshuva, D. Barnea, Y. Taitel, Two-phase flow in inclined parallel pipes, Int. J. Multiphase Flow 25 (1999) 1491-1503.

[66] G.Hetsroni, A.Mosyak, Z. Segal, E. Pogrebnyak, Two-phase flow patterns in parallel micro-channels, Int. J. Multiphase Flow 29 (2003) 341–360.

[67] L. Pustylnik, D. Barnea, Y. Taitel, Prediction of two-phase flow distribution in parallel pipes using stability analysis, AIChE. J. 52 (2006) 3345–3352.

[68] C. Schillberg, S. Kandlikar, A review of modes for water droplet detachment from the gas diffusion later-gas flow interface in PEMFCs, Proceedings of the Fifth International Conference on Nanochannels, Microchannels and Minichannels, Puebla, Mexico, June, 2007, pp. 299-310.

[69] E.C. Kumbur, K.V. Sharp, M.M. Mench, Liquid droplet behavior and instability in a polymer electrolyte fuel cell flow channel, J. Power Sources 161 (2006) 333-345.

[70] J. Borrelli, T. Trabold, S. Kandlikar, J. Owejan, Water transport visualization and two-phase pressure drop measurements in a simulated PEMFC cathode minichannel, Third Annual Conference on Microchannels and Minichannels', (2005).

[71] E. Kimball, T. Whitaker, Y. Kevrekidis, J. Benziger, Drops, slugs, and flooding in polymer electrolyte membrane fuel cells, AIChE Journal 54 (2008) 1313-1332.

[72] T. Murahashi, H. Kobayashi, E. Nishiyama, Combined measurement of PEMFC performance decay and water droplet distribution under low humidity and high CO, J. Power Sources 175 (2008) 98-105.

[73] J. Wu, X. Z. Yuan, J.J. Martin, H. Wang, J. Zhang, H. Shen, S. Wu, W. Merida, A review of PEM fuel cell durability: Degradation mechanisms and mitigation strategies, J. Power Sources 184 (2008) 104-119.

[74] A. Tamayol, M. Bahrami, Water permeation through gas diffusion layers of proton exchange membrane fuel cells, J. Power Sources 196 (2011) 6356-6361.

[75] Z. Lu, A.D. White, J. Pelaez, M. Hardbarger, W. Domigan, J. Sergi, S.G. Kandlikar, Investigation of water transport in an ex-situ experimental facility modelled on an actual doe automotive target compliant fuel cell, Proceedings of the Sixth International ASME Conference on Nanochannels, Microchannels, and Minichannels. June 23-25, (2008).

[76] P. Concus, R. Finn, On the behavior of a capillary surface in a wedge, Appl. Math Sci. 63 (1969) 292-299.

[77] A. Bazylak, J. Heinrich, N. Djilali, D. Sinton, Liquid water transport between graphite paper and a solid surface, J. Power Sources 185(2) (2008) 1147-1153.

[78] C. Fang, C. Hidrovo, F-M Wang, J. Eaton, K. Goodson, 3-D numerical simulation of contact angle hysteresis for microscale two phase flow, Int. J. Multiphase Flow 34 (2008) 690-705.

[79] E. Shirani, S. Masoomi, Deformation of a droplet in a channel flow, J. Fuel Cell Sci. Technol. 5(4) (2008) 041008-8.

[80] P. Young, T. Brackbill, S. Kandlikar, Estimating roughness parameters resulting from various machining techniques for fluid flow applications, Proceedings of the Fifth International Conference on Nanochannels, Microchannels and Minichannels, Puebla, Mexico, June, 2007, pp. 827-836.

[81] S. Kandlikar, S. Joshi, S. Tian, Effect of surface roughness on heat transfer and fluid flow characteristics at low Reynolds numbers in small diameter tubes, Heat Transfer Eng. 24(3) (2003) 4-16.

[82] F.Barbir, PEM Fuel Cells: Theory and Practice, Elsevier Academic Press, New York, 2005, pp. 119-121.

[83] X. Liu, H.Guo, C.F.Ma, Water flooding and two-phase flow in cathode channels of proton exchange membrane fuel cells, J. Power Sources 156 (2006) 267-280.

[84] D. Natarajan, T.V. Nguyen, Current distribution in PEM fuel cells. Part 1: Oxygen and fuel flow rate effects, AIChE Journal 51 (2005) 2587-2598.

[85] J. St-Pierre, J. Roberts, K. Colbow, S. Campbell, A. Nelson, PEMFC operational and design strategies for sub zero environment, J. New Mater. Electrochem. Syst. 8 (2005) 163-176.

[86] K. Tajiri, C.Y. Wang, Y. Tabuchi, Water removal from a PEFC during gas purge, Electrochimica Acta 53 (2008) 6337-6343.

[87] K.T. Cho, A. Turhan, J.H. Lee, J.S. Brenizer, A.K. Heller, L. Shi, M.M. Mench, Probing water transport in polymer electrolyte fuel cells with neutron radiography, Nucl. Instr. Meth. Phys. Res. A, 605 (2009) 119-122.

[88] K.T. Cho, M.M. Mench, Coupled effects of flow field geometry and diffusion media material structure on evaporative water removal from polymer electrolyte fuel cells, I. J. Hydrogen Energy 35 (2010) 12329-12340.

[89] H. Masuda, A. Yamamoto, K. Sasaki, S. Lee, K. Ito, A visualization study on relationship between water-droplet behavior and cell voltage appeared in straight, parallel, and serpentine channel pattern cells, J. Power Sources 196 (2011) 5377-5385.

[90] D.P. Wilkinson, H.H. Voss, D.S. Watkins, K.B. Prater, US5366818 (1994).

[91] H.H. Voss, D.P. Wilkinson, P.G. Pickup, M.C. Johnson, V. Basura, Anode water removal: A water management and diagnostic technique for solid polymer fuel cells, Electrochimica Acta 40 (1995) 321-328.

[92] H.H. Voss, D.P. Wilkinson, D.S. Watkins, Method and apparatus for removing water from electrochemical fuel cells by controlling the temperature and pressure of the reactant streams, US5441819 (1995).

[93] W. He, G. Lin, T.V. Nguyen, Diagnostic tool to detect electrode flooding in proton-exchange-membrane fuel cells, AIChE Journal 49 (2003) 3221-3228.

[94] P.A. Chuang, A. Turhan, A.K. Keller, J.S. Brenizer, T.A. Trabold, M.M. Mench, The nature of flooding and drying in polymer electrolyte fuel cells, Third International Conference on Fuel Cell Science, Engineering and Technology, (2005) 31-37.

[95] D.P. Wilkinson, H.H. Voss, N.J. Fletcher, M.C. Johnson, E.G. Pow, Electrochemical fuel cell stack with concurrent flow of coolant and oxidant streams and countercurrent flow of fuel and oxidant streams, US5773160 (1998).

[96] R. Zaffou, J.S. Yi, H.R. Kunz, J.M. Fenton, Temperature-driven water transport through membrane electrode assembly of proton exchange membrane fuel cells, Electrochem. Solid-State Lett. 9 (2006) A418-A422.

[97] J.P.G. Villaluenga, B. Seoane, V.M. Barragan, C. Ruiz-Bauza, Thermo-osmosis of mixtures of water and methanol through a Nafion membrane, J. Membr. Sci. 274 (2006) 116-122.

[98] S. Kim, M.M. Mench, Investigation of temperature-driven water transport in polymer electrolyte fuel cell: phase-change-induced flow, J. Electrochem. Soc. 156 (2009) B353-B362.

[99] S. Kim, M.M. Mench, Investigation of temperature-driven water transport in polymer electrolyte fuel cell: thermo-osmosis in membranes, J. Membr. Sci. 328 (2009) 113-120.

[100] D.M. Bernardi, Water-balance calculations for solid-polymer-electrolyte fuel cells, J. Electrochem. Soc. 137 (1990) 3344-3350.

[101] F.N. Buchi, S. Srinivasan, Operating proton exchange membrane fuel cells without external humidification of the reactant gases, J. Electrochem. Soc. 144 (1997) 2767-2772.

[102] I.S. Hussaini, C.Y. Wang, Dynamic water management of polymer electrolyte membrane fuel cells using intermittent RH control, J. Power Sources 195 (2010) 3822-3829.

[103] J.P. Owejan, J. E. Owejan, W. Gu, T.A. Trabold, T.W. Tighe, M.F. Mathias, Water transport mechanisms in PEMFC gas diffusion layers, J. Elec. Soc. 157 (2010) B1456-B1464.

[104] M. Blanco, "Study of selected water management strategies for proton exchange membrane fuel cells" (PhD diss., University of British Columbia, 2011).

[105] G.Y. Lin, T.V. Nguyen, Effect of thickness and hydrophobic polymer content of the gas diffusion layer on electrode flooding level in a PEMFC, J. Electrochem. Soc. 152 (2005) A1942-A1948.

[106] M. Mathias, J. Roth, B. Sompalli, M. Schoeneweiss, D. Wood, Diffusion media, fuel cells, and fuel cell powered systems, US2004137311 (2004).

[107] J. St-Pierre, D.P. Wilkinson, S. Knights, M. Bos, Relationships between water management, contamination and lifetime degradation in PEFC, J. New Mater. Electrochem. Syst. 3 (2000) 99-106.

[108] M.C. Johnson, D.P. Wilkinson, C.P. Asman, M.L. Bos, R.J. Potter, Electrochemical fuel cell with an electrode substrate having an in-plane nonuniform structure for control of reactant and product transport, US5840438 (1998).

[109] H-M. Chang, C-W. Lin, M-H. Chang, H-R. Shiu, W-C. Chang, F-H. Tsau, Optimization of polytetrafluoroethylene content in the cathode gas diffusion layer by the evaluation of compression effect on the performance of a proton exchange membrane fuel cell, J. Power Sources 196 (2011) 3773-3780.

[110] J. Cho, T. Ha, J. Park, H-S. Kim, K. Min, E. Lee, J-Y Jyoung, Analysis of transient response of a unit proton-exchange membrane fuel cell with a degraded gas diffusion layer, I. J. Hydrogen Energy 36 (2011) 6090-6098.

[111] H.H. Voss, D.P. Wilkinson, P.G. Pickup, M.C. Johnson, V. Basura, Anode water removal: a water management and diagnostic technique for solid polymer fuel cells, Electrochim. Acta 40 (1995) 321-328.

[112] K.S.S. Naing, Y. Tabe, T. Chikahisa, Performance and liquid water distribution in PEFCs with different anisotropic fiber directions of the GDL, J. Power Sources 196 (2011) 2584-2594.

[113] E.E. Kimball, J. B. Benziger, Y. G. Kevrekidis, Effects of GDL structure with an efficient approach to the management of liquid water in PEM fuel cells, Fuel Cells 10 (2010) 530-544.

[114] M.S. Wilson, J.A. Valerio, S. Gottesfeld, Low platinum loading electrodes for polymer electrolyte fuel cells fabricated using thermoplastic ionomers, Electrochimica Acta 40 (1995) 355-363.

[115] H.K. Atiyeh, K. Karan, B. Peppley, A. Phoenix, E. Halliop, J. Pharoah, Experimental investigation of the role of a microporous layer on the water transport and performance of a PEM fuel cell, J. Power Sources 170 (2007) 111-121.

[116] M. A. Hickner, N.P. Siegel, K.S. Chen, D.S. Hussey, D.L. Jacbonson, M. Arif, In situ high-resolution neutron radiography of cross-sectional liquid water profiles in proton exchange membrane fuel cells, J. Elec. Soc. 155 (2008) B427-B434.

[117] T. Sasabe, P. Deevanhxay, S. Tsushima, S. Hirai, Investigation on the effect of microstructure of proton exchange membrane fuel cell porous layers on liquid water behavior by soft X-ray radiography, J. Power Sources 196 (2011) 8197-8206.

[118] J.P. Owejan, J. Owejan, W. Gu, T.A. Trabold. T.W. Tighe, M.F. Mathias, Water transport mechanisms in pemfc gas diffusion layers, J. Electrochem. Soc. 157 (2010) B1456-B1464.

[119] T. Kim, S. Lee, H. Park, A study of water transport as a function of the micro-porous layer arrangement in PEMFCs, I. J. Hydrogen Energy 35 (2010) 8631-8643.

[120] J. Chen, T. Matsuura, M. Hori, J. Power Sources 131 (2004) 155-161.

[121] M-S. Lee, T.H. Chen, W.S. Lee, B.S. Lin, B.Y. Lau, P.F. Tsai, G.C. Wang, From microstructure to the development of water and major reaction sites inside the catalyst layer of the cathode of a proton exchange membrane fuel cell, J. Power Sources 196 (2011) 7411-7419.

[122] M. Blanco, D.P. Wilkinson, H. Wang, Application of water barrier layers in a proton exchange membrane fuel cell for improved water management at low humidity conditions, I. J. Hydrogen Energy 36 (2011) 3635-3648.

[123] F.Barbir, PEM Fuel Cells: Theory and Practice, Elsevier Academic Press, New York, 2005, pp. 163-186.

[124] X. Li, Principles of Fuel Cells, Taylor & Francis, New York, 2006, pp. 325-343.

[125] D.P. Wilkinson, O. Vanderleeden, in: W. Vielstich, H.A. Gasteiger, A. Lamm (Eds.), Handbook of Fuel Cells: Fundamentals, Technology and Applications, vol. 3, John Wiley & Sons Ltd., 2003, pp. 316-324.

[126] T.V. Nguyen, W .He, in: W. Vielstich, H.A. Gasteiger, and A. Lamm (Eds.), Handbook of Fuel Cells: Fundamentals, Technology and Applications, vol. 3, John Wiley & Sons Ltd., 2003, pp. 325-336.

[127] X. Li, I. Sabir, J. Park, A flow channel design procedure for PEM fuel cells with effective water removal, J. Power Sources 163 (2007) 933-942.

[128] A.A. Donaldson, D.M. Kirpalani, A. Macchi, Curvature induced flow pattern transitions in serpentine mini-channels, Int. J. Multiphase Flow 37 (2011) 429-439).

[129] T.A. Trabold, J.P. Owejan, Flow field geometries for improved water management, US7087337 (2005).

[130] J.P. Owejan, T.A. Trabold, D.L. Jacobson, M. Arif, S.G. Kandlikar, Effects of flow field and diffusion layer properties on water accumulation in a PEM fuel cell, Int. J. Hydrogen Energy 32 (2007) 4489-4502.

[131] G. Montie, R.B. Redlich, D.E. Leger, Fuel cell cathode flow field, US20080213648 (2008).

[132] M. Johnson, D.P. Wilkinson, J. Kenna, O.Vanderleeden, J. Zimmerman, M. Tabatabian, Differential pressure fluid flow fields for fuel cells, US6586128 (2003).

[133] T. Metz, N. Paust, C. Muller, R. Zengerle, P. Koltay, Passive water removal in fuel cells by capillary droplet actuation, Sens. Actuators, A 143 (2008) 49-57.

[134] T. Metz, J. Viertel, C. Muller, S. Kerzenmacher, N. Paust, R. Zengerle, and P. Koltay, Passive water management for µfuel-cells using capillary microstructures, J. Micromech. Microeng. 18 (2008) 1-10.

[135] N. Akhtar, A. Qureshi, J. Scholta, C. Hartnig, M. Messerschmidt, W. Lehnert, Investigation of water droplet kinetics and optimization of channel geometry for PEM fuel cell cathodes, Int. J. Hydrogen Energy 34 (2009) 3104-3111.

[136] US Fuel Cell Council, Protocol on Fuel Cell Component Testing: Primer for Generating Test Plans (USFCC 04-003A), 2006.

[137] J. Dillet, O. Lottin, G. Maranzana, S. Didierjean, D. Conteau, C. Bonnet, Direct observation of the two-phase flow in the air channel of a proton exchange membrane fuel cell and of the effects of a clogging/unclogging sequence on the current density distribution, J. Power Sources 195 (2010) 2795-2799

[138] S. Kundu, M. Cimenti, S. Lee, D. Bessarabov of Automotive Fuel Cell Cooperation Corp (AFCC), Fingerprint of automotive fuel cell cathode catalyst degradation: Pt band in PEMs, Membrane Technology 10 (2009) 7-10.

[139] B. Li, R. Lin, D. Yang, J. Ma, Effect of driving cycle on the performance of PEM fuel cell and microstructure of membrane electrode assembly, Int. J. Hydrogen Energy 35 (2010) 2814-2819.

[140] F.Barbir, PEM Fuel Cells: Theory and Practice, Elsevier Academic Press, New York, 2005, pp. 343-344.

[141] J.P. Owejan, J.J. Gagliardo, J.M. Sergi, S.G. Kandlikar, T.A. Trabold, Water management studies in PEM fuel cells, Part I: Fuel cell design and in situ water distributions, Int. J. Hydrogen Energy 34 (2009) 3436-3444.

[142] R. Anderson, D.P. Wilkinson, X. Bi, L. Zhang, Two-phase flow pressure drop hysteresis in parallel channels of a proton exchange membrane fuel cell, J. Power Sources 195 (2010) 4168-4176.

[143] U. Pasaopullari, C.-Y. Wang, Two-phase transport and the role of microporous layer in polymer electrolyte fuel cells, Electrochim. Acta 49 (2004) 4359–4369.

[144] R. Anderson, D.P. Wilkinson, X. Bi, L. Zhang, Two-phase flow pressure drop hysteresis under typical operating conditions for a proton exchange membrane fuel cell, ECS Trans. 28 (2010) 127-137.

[145] J-H. Lin, W-H. Chen, S-H. Su, Y-K. Liao, T-H. Ko, Carbon film coating on gas diffusion layer for proton exchange membrane fuel cells, J. Power Sources 184 (2008) 38-43.

[146] F-B. Weng, A. Su, C-Y. Hsu, The study of the effect of gas stoichiometric flow rate on the channel flooding and performance in a transparent fuel, Int. J. Hydrogen Energy, 32 (2007) 666-676.

[147] N. Khajeh-Hosseini-Dalasm, K. Fusinobu, K. Okazaki, Phase change in the cathode side of a proton exchange member fuel cell, J. Power Sources 195 (2010) 7003-7010.

[148] R. Anderson, D.P. Wilkinson, X. Bi, L. Zhang, Two-phase pressure drop hysteresis in an operating proton exchange membrane fuel cell, J. Power Sources 196 (2011) 8031-8040.

[149] D. Spernjak, A.K. Prasad, S.G. Advani, In situ comparison of water content and dynamics in parallel, single-serpentine, and interdigitated flow fields of polymer electrolyte membrane fuel cells, J. Power Sources 195 (2010) 3553-3568.

[150] J. Chen, Experimental study on the two phase flow behavior in PEM fuel cell parallel channels with porous media inserts, J. Power Sources 195 (2010) 1122–1129.

[151] J.P. Owejan, J.J. Gagliardo, J.M. Sergi, S.G. Kandlikar, T.A. Trabold, Water management studies in PEM fuel cells, Part I: Fuel cell design and in situ water distributions, Int. J. Hydrogen Energy 34 (2009) 3436-3444.

[152] N. Khajeh-Hosseini-Dalasm, K. Fusinobu, K. Okazaki, Phase change in the cathode side of a proton exchange member fuel cell, J. Power Sources 195 (2010) 7003-7010.

[153] Z. Lu, M.M. Daino, C. Rath, S.G. Kandlikar, Water management studies in PEM fuel cells, part III: Dynamic breakthrough and intermittent drainage characteristics from GDLs with and without MPLs, Int. J. Hydrogen Energy 35 (2010) 4222-4233.

[154] T. Ous, C. Arcoumanis, The formation of water droplets in an air-breathing fuel cell, Int. J. Hydrogen Energy 34 (2009) 3476-3487.

[155] L. Zhang, X, Bi, D.P. Wilkinson, J. Stumper, H. Wang, Pressure drop of two-phase flow in minichannels bounded with permeable walls, 8th World Congress of Chemical Engineering, August 24-27, 2009, Montreal, Canada, paper no. 145, 1-6.

[156] L. Zhang, X.T. Bi, D.P. Wilkinson, R. Anderson, J. Stumper, H. Wang, Gas-liquid two-phase flow behavior in minichannels bounded with a permeable wall, Chem. Eng. Sci. 66 (2011) 3377-3385.

[157] X.C Adroher, Y. Wang, Ex situ and modeling study of two-phase flow in a single channel of polymer electrolyte membrane fuel cells, J. Power Sources, 196 (2011) 9544-9551.

[158] M. S. Quraishi and T.Z. Fahidy, A simplified procedure for dimensional analysis employing si units, Can. J. Chem. Eng., 59 (1981) 563-566.

[159] E.L. Gyenge, Dimensionless numbers and correlating equations for the analysis of the membrane-gas diffusion electrode assembly in polymer electrolyte fuel cells, J. Power Sources 152 (2005) 105–121.

[160] Bellows RJ, Lin MY, Arif M, Thompson AK, Jacobson D. Neutron imaging technique for in situ measurement of water transport gradients within nafion in polymer electrolyte fuel cells. Journal of the Electrochemical Society 1999;146:1099–103.

[161] Hickner MA, Siegel NP, Chen KS, Mcbrayer DN, Hussey DS, Jacobson DL, et al. Real-time imaging of liquid water in an operating proton exchange membrane fuel cell. Journal of the Electrochemical Society 2006;153(5):A902–8.

[162] Tsushima S, Teranishi K, Hirai S. Magnetic resonance imaging of the water distribution within a polymer electrolyte membrane in fuel cells. Electrochemical and Solid State Letters 2004;7:A269–72.

[163] Sinha PK, Halleck P, Wang CY. Quantification of liquid water saturation in a PEM fuel cell diffusion medium using x-ray microtomography. Electrochemical and Solid State Letters 2006;9:A344-8.

[164] Liu X, Guo H, Ma CF. Water flooding and two-phase flow in cathode channels of proton exchange membrane fuel cells. Journal of Power Sources 2006;156(2):267–80.

[165] Zhang FY, Yang XG, Wang CY. Liquid water removal from a polymer electrolyte fuel cell. Journal of the Electrochemical Society, 153(2) (2006) A225–32.

[166] Wilkinson DP, Voss HH, Watkins DS, Prater KB. Solid polymer fuel cell systems incorporating water removal at the anode. US5366818; 1994.

[167] Voss HH, Wilkinson DP, Pickup PG, Johnson MC, Basura V. Anode water removal: A water management and diagnostic technique for solid polymer fuel cells. Electrochimica Acta 1995;40:321-8.

[168] Voss HH, Wilkinson DP, Watkins DS. Method and apparatus for removing water from electrochemical fuel cells by controlling the temperature and pressure of the reactant streams. US5441819, 1995.

[169] M.A. Hickner, N.P. Siegel, K.S. Chen, D.S. Hussey, D.L. Jacobson, M. Arif, In situ high-resolution neutron radiography of cross-sectional liquid water profiles in proton exchange membrane fuel cells, Journal of the Electrochemical Society, 155 (4) (2008) B427-B434.

[170] A. Z. Weber, J. Newman, Modeling transport in polymer-electrolyte fuel cells, Chem. Rev. 104(10) (2004) 4679-4726.

[171] C. Y.Wang, Fundamental models for fuel cell engineering, Chem. Rev. 104(10) (2004) 4727-4765.

[172] A. BiyIkoglu, Review of proton exchange membrane fuel cell models, Int. J. Hydrogen Energy 30(11) (2005) 1181-1212.

[173] W. Q. Tao, C. H. Min, X.L. Liu, Y.L. He, B.H. Yin, W. Jiang, Parameter sensitivity examination and discussion of PEM fuel cell simulation model validation: Part I. Current status of modeling research and model development, J. Power Sources 160(1) (2006) 359-373.

[174] N. Djilali, P. C. Sui, Transport phenomena in fuel cells: from microscale to macroscale, Int. J. Comput. Fluid Dynam., 22 (1-2) (2008) 115-133.

[175] C. Siegel, Review of computational heat and mass transfer modeling in polymer-electrolyte-membrane (PEM) fuel cells, Energy 33(9) (2008) 1331-1352.

[176] J. J. Baschuk, X. Li, Modelling of polymer electrolyte membrane fuel cells with variable degrees of water flooding, J. Power Sources 86(1-2) (2000) 181-196.

[177] D. Natarajan, T. Van Nguyen, A two-dimensional, two-phase, multicomponent, transient model for the cathode of a proton exchange membrane fuel cell using conventional gas distributors, J. Electrochem. Soc. 148(12) (2001) A1324-A1335.

[178] T. Berning, N. Djilali, A 3D, multiphase, multicomponent model of the cathode and anode of a PEM fuel cell, J. Electrochem. Soc. 150(12) (2003) A1589-A1598.

[179] S. Litster, N. Djilali, in: B. Sunden, M. Faghri, Transport Phenomena in Fuel Cells, WIT Press, Billerica, MA, 2005, pp. 175-213.

[180] Z. H. Wang, C. Y. Wang, K. S. Chen, Two phase flow and transport in the air cathode of proton exchange membrane fuel cells, J. Power Sources 94(1) (2001) 40-50.

[181] V. Gurau, R. V. Edwards, J. A. Mann, T. A. Zawodzinski, A look at the multiphase mixture model for PEM fuel cell simulations, Electrochem. Solid-State Lett. 11(8) (2008) B132-B135.

[182] C.Y. Wang, Comment on “A Look at the Multiphase Mixture Model for PEM Fuel Cell Simulations” [Electrochem. Solid-State Lett., 11, B132 (2008)], Electrochem. Solid-State Lett. 12(2) (2009) S2-S3.

[183] V. Gurau, Response to “Comment on `A Look at the Multiphase Mixture Model for PEM Fuel Cell Simulations' ” [Electrochem. Solid-State Lett., 11, B132 (2008)], Electrochem. Solid-State Lett.12(2) (2009) S4-S6.

[184] C.W. Hirt, B.D. Nichols, Volume of fluid (VOF) method for the dynamics of free boundaries, J. Comp. Phys. 39(1) (1981) 201-225.

[185] P. Quan, B. Zhou, A. Sobiesiak, Z. Liu, Water behavior in serpentine micro-channel for proton exchange membrane fuel cell cathode, J. Power Sources 152 (2005) 131-145.

[186] H. Chen, S. Chen, W. Matthaeus, Recovery of the Navier-Stokes equations using a lattice-gas Boltzmann method, Phys. Rev. A 45 (1992) R5339-R5342.

[187] K. S. Chen, M. A. Hickner, D. R. Noble, Simplified models for predicting the onset of liquid water droplet instability at the gas diffusion layer/gas flow channel interface, Int. J. Energy Res. 29(12) (2005) 1113-1132.

[188] K. S. Chen, Predicting water-droplet detachment from GDL/channel interfaces in PEM fuel cells, ECS Transactions 11(1) (2007) 715-724.

[189] G. He, P. Ming, Z. Zhao, A. Abudula, Y. Xiao, A two-fluid model for two-phase flow in PEMFCs, J. Power Sources 163(2) (2007) 864-873.

[190] Z. Zhan, J. Xiao, M. Pan, R. Yuan, Characteristics of droplet and film water motion in the flow channels of polymer electrolyte membrane fuel cells, J. Power Sources 160(1) (2006) 1-9.

[191] Y. H. Cai, J. Hu, H. P. Ma, B. L. Yi, H. M. Zhang, Effects of hydrophilic/hydrophobic properties on the water behavior in the micro-channels of a proton exchange membrane fuel cell, J. Power Sources 161(2) (2006) 843-848.

[192] X. Zhu, P. C. Sui, N. Djilali, Dynamic behavior of liquid water emerging from a GDL pore into a PEMFC gas flow channel, J. Power Sources 172(1) (2007) 287-295.

[193] A. Bazylak, D. Sinton, N. Djilali, Dynamic water transport and droplet emergence in PEMFC gas diffusion layers, J. Power Sources 176(1) (2008) 240-246.

[194] X. Zhu, P. C. Sui, N. Djilali, Numerical simulation of emergence of a water droplet from a pore into a microchannel gas stream, Microfluidics and Nanofluidics 4(6): (2008) 543-555.

[195] X. Zhu, P. C. Sui, N. Djilali, Three-dimensional numerical simulations of water droplet dynamics in a PEMFC gas channel, J. Power Sources 181(1) (2008) 101-115.

[196] A. D. Le, B. Zhou, A general model of proton exchange membrane fuel cell, J. Power Sources 182(1) (2008) 197-222.

[197] A. D. Le, B. Zhou. Fundamental understanding of liquid water effects on the performance of a PEMFC with serpentine-parallel channels, Electrochimica Acta 54(8) (2009) 2137-2154.

[198] K. Jiao, B. Zhou, P. Quan, Liquid water transport in parallel serpentine channels with manifolds on cathode side of a PEM fuel cell stack, J. Power Sources 154(1) (2006) 124-137.

[199] K. Jiao, B. Zhou, P. Quan, Liquid water transport in straight micro-parallel-channels with manifolds for PEM fuel cell cathode, J. Power Sources 157(1) (2006) 226-243.

[200] P. Quan, M. C. Lai, Numerical study of water management in the air flow channel of a PEM fuel cell cathode, J. Power Sources 164(1) (2007) 222-237.

[201] K. Jiao, B. Zhou, Innovative gas diffusion layers and their water removal characteristics in PEM fuel cell cathode, J. Power Sources 169(2) (2007) 296-314.

[202] K. Jiao, B. Zhou, Effects of electrode wettabilities on liquid water behaviors in PEM fuel cell cathode, J. Power Sources 175(1) (2008) 106-119.

[203] L. Hao, P. Cheng, Lattice Boltzmann simulations of anisotropic permeabilities in carbon paper gas diffusion layers, J. Power Sources 186 (1) (2009) 104-114.

[204] Y. Wang, S. Basu, C. Y. Wang, Modeling two-phase flow in PEM fuel cell channels, J. Power Sources 179(2) (2008) 603-617.

[205] S. Basu, J. Li, C. Y. Wang, Two-phase flow and maldistribution in gas channels of a polymer electrolyte fuel cell, J. Power Sources 187(2) (2009) 431-443.

[206] S. Basu, C.Y. Wang, K.S. Chen, Two-phase flow maldistribution and mitigation in polymer electrolyte fuel cell, J. Fuel Cell Sci. Technol. 6 (2009) 031007-1 - 031007-11.

[207] S. Um, C. Y. Wang, K. S. Chen, Computational fluid dynamics modeling of proton exchange membrane fuel cells, J. Electrochem. Soc. 147(12) (2000) 4485-4493.

[208] S. Mazumder, J. V. Cole, Rigorous 3-D mathematical modeling of PEM fuel cells, J. Electrochem. Soc. 150(11) (2003) A1503-A1509.

[209] X. Zhu, Q. Liao, P.C. Sui, and N. Djilali. Numerical investigation of water droplet dynamics in a low-temperature fuel cell microchannel: Effect of channel geometry, J. Power Sources 195(3) (2010) 801-812.

[210] Y. Ding, H. T. Bi, D.P. Wilkinson, Three-dimensional numerical simulation of water droplet emerging from a gas diffusion layer surface in micro-channels, J. Power Sources 195 (2010) 7278–7288.

[211] A. D. Le, B. Zhou, A generalized numerical model for liquid water in a proton exchange membrane fuel cell with interdigitated design, J. Power Sources 193(2) (2009) 665-683.

[212] X.D. Wang, Y.Y. Duan, W.M. Yan, D.J. Lee, A. Su, P.H. Chi, Channel aspect ratio effect for serpentine proton exchange membrane fuel cell: Role of sub-rib convection, J. Power Sources 193(2) (2009) 684-690.

[213] D.P. Wilkinson, O. Vanderleeden, J. Zimmerman, Flow fields for supporting fluid diffusion layers in fuel cells, US6541145 (2003).

Appendix A CFD literature review[1]

In recent years, several reviews have been published about the fuel cell models. Weber and Newman [170] presented various types of transport and corresponding models in each fuel cell layer. However, their review mainly focused on one-dimensional models and two-phase flow in gas channels was not taken into account. Wang [171] summarized fundamental models for PEM fuel cell engineering but limited the review to computational fluid dynamic (CFD) methods only. Biyikoglu [172] presented a review about different aspects of modeling and simulation, including CFD modeling and flow field design. Tao et al. [173] presented a comprehensive review of mathematical modeling of PEM fuel cells, which especially focused on model validation and parameter influence. Djilali et al. [174] gave a critical discussion about computational strategies for the polymer electrolyte membrane, porous gas diffusion electrodes, and microchannels. Multi-scale strategies were also discussed. Most recently, Siegel [175] presented a detailed literature overview of PEM fuel cell models with a focus on modeling strategies and commonly used model assumptions. However, no review has been written to the authors' knowledge focusing on the presence of two-phase flow in the gas channels of PEM fuel cells.

A.1.1 Gas-liquid two-phase flow models for PEM fuel cells

Empirical models, mechanistic models, and computational fluid dynamics (CFD) models have been developed to study the gas-liquid two-phase flow. In PEM fuel cells, gas-liquid two-phase flow occurs simultaneously with mass transfer, heat transfer, and electrochemical reactions, and is affected by the material properties in different

[1] This section was written by Y. Ding and edited by R. Anderson in the following publication [2]: R. Anderson, L. Zhang, Y. Ding, M. Blanco, X. Bi, D.P. Wilkinson, A critical review of two-phase flow in gas flow channels of proton exchange membrane fuel cells, J. Power Sources 195 (2010) 4531-4553.

components. Therefore, CFD models can be effective tools for the numerical investigation of two-phase flow phenomena in PEM fuel cells. Liquid water transport was first incorporated in fuel cell modeling in early 2000, with these works treating the liquid water as a solid species that only occupies a certain volume fraction [176] or neglecting the convective transport of liquid water [177]. As computational power increased, more complex two-phase flow models have been applied to the PEM fuel cell modeling. In this section, several two-phase flow models applied to PEM fuel cells are reviewed, including the multi-fluid model, mixture model, volume of fraction method (VOF), and Lattice Boltzmann method (LBM). Table 19 summarizes the current literature on CFD simulations of gas-liquid two-phase flow in PEM fuel cells.

The multi-fluid model was first used in PEM fuel cell modeling by Berning and Djilali [178]. In this model, each phase is represented by one complete set of conservation equations (mass, momentum, and energy), and the two phases are coupled by the saturation state. This model has only a few assumptions, but requires the highest number of dependent variables, and the coupling of the phases can lead to unstable solutions [179].

The mixture model was first used to model PEM fuel cells by Wang et al. [180] and uses the same equation set as the multi-fluid model. Each phase is modeled using an individual mass conservation equation, but a single momentum equation is solved to obtain the velocity field of the mixture, of which physical properties are the average of the two phases. Each phase velocity can then be extracted from the mixture velocity in the post processing. Recently, Gurau et al. [181] commented that the mixture model was limited to flows without phase transitions or phase production because the momentum

term due to phase change is neglected. For more complex situations, such as in PEM fuel cells, this model may lead to predictions of unrealistic velocity and scalar fields. Although Wang's group [182] responded that the "missing" term was relatively small compared with the Darcy term, Gurau [183] insisted that the missing term possibly had the same order of magnitude as the Darcy term.

The volume of fraction (VOF) method was developed in the 1970s as a flexible way to simulate complicated free boundaries [184] and this method has become popular in simulating gas-liquid flows in fuel cell gas flow channels since Quan et al. [185] first incorporated it. The model can simulate immiscible fluids by solving a single set of momentum equations and then tracks the volume fraction of each of the fluids throughout the domain. Due to its capacity to consider surface tension and wall adhesion effects, liquid droplet behaviors can be captured and traced. Thus, this model is especially suited for surface tension dominated flows and flows in channels with different wall materials. However, because the specific structure of the flow domain is required this model has been only applied to gas flow channel simulations, and it is difficult to couple to the electrochemical reactions in the fuel cell.

Instead of solving the Navier-Stokes equations like traditional CFD methods, the Lattice Boltzmann method models the fluid as fictive particles, which perform consecutive propagation and collision processes over a discrete lattice mesh. In conventional CFD models, it is difficult to implement microscopic interactions, such as interfaces between gas and liquid phases, into the macroscopic Navier–Stokes equation. However, in the LBM, the particulate kinetics provide a relatively easy and consistent way to consider the microscopic interactions by modifying the collision operator [186].

Thus, this method shows great potential to simulate the two-phase flows in PEM fuel cells. However, as a mesoscopic model, it is difficult to apply this method to large length scales, and coupling this model with heat transfer and reactions is still a challenge.

Table 19 Selected studies on modeling gas-liquid two-phase flow in PEM fuel cells (reprinted from Anderson et al. [2] with permission from Elsevier)

Models	Authors	Research Aspects	Remarks
Mechanistic Model	Chen, Hickner et al. (2005) [187]	Effects of gas flow velocity, flow channel length and height, and contact angle hysteresis on the droplet detachment diameter	No water injected, single sphere droplet
	Chen (2007) [188]	Effects of channel height, contact angle hysteresis and water-droplet size on the critical gas flow velocity	No water injected, single sphere droplet
Multi-fluid Model	He, Ming et al. (2007) [189]	Effects of wettability on the droplet detachment diameter	Single droplet
VOF	Theodorakakos, Ous et al. (2006) [18]	Effects of temperature on the droplet detachment	Single water inject pipe
	Zhan, Xiao et al. (2006) [190]	Effects of gas flow velocity, wettability and flow channels on the droplet removal	Liquid water was injected from the same inlet as gas
	Cai, Hu et al. (2006) [191]	Effects of wettability on the droplet removal.	Liquid droplet was initially attached to the GDL surface
	Shirani and Masoomi (2008) [79]	Effects of gas velocity, the density and viscosity of water, and the surface tension coefficient on the flow pattern	No water injected, single droplet
	Zhu, Sui et al. (2007) [192]	Effects of channel size and pore diameter on the water droplet motion	Single pore, high liquid flow rates
	Bazylak, Sinton et al. (2008) [193]	Effects of GDL microstructure on the droplets motion	Only two water inject pipes
	Zhu, Sui et al. (2008) [194]	Effects of wettability of channel walls, pore diameter, gas velocity, and liquid water velocity	Single pore, high liquid flow rates
	Zhu, Sui et al. (2008) [195]	Effects of air and water velocity, pore diameter and the wettability of the GDL surface	Single pore, high liquid flow rates
	Fang, Hidrovo et al. (2008) [78]	Effects of contact angle hysteresis	Single water inject pipe

Models	Authors	Research Aspects	Remarks
	Le and Zhou (2008) [196]	A 3D general model of PEM fuel cell coupled VOF method	Homogenous GDL and electrode
	Le and Zhou (2009) [197]	Flow behaviors of liquid water in serpentine-parallel flow channels	Homogenous GDL and electrode
	Quan, Zhou et al. (2005) [185]	Behavior of liquid water in a U-shaped serpentine gas channel	Liquid water was initially attached to the GDL surface
	Jiao, Zhou et al. (2006) [198]	Behavior of liquid water in a complex parallel serpentine channel	Liquid water was initially attached to the GDL surface
	Jiao, Zhou et al. (2006) [199]	Air-water flow in a 3D straight micro-parallel-channel	Liquid water was initially attached to the GDL surface
	Quan and Lai (2007) [200]	Effects of channel wettability, channel geometry, and air inlet velocity on water behavior	Homogenous GDL
	Jiao and Zhou (2007) [201]	Investigation on three innovative GDLs micro-structure designs	Homogenous catalyst layer
	Jiao and Zhou (2008) [202]	Effects of electrode wettability	Homogenous catalyst layer
	Ding et al. (2008) [210]	Two-phase flow pattern, Effects of GDL microstructure, surface wettability, liquid flow rates	Multiple pores, simplified GDL surface
LBM	Hao and Cheng (2009) [203]	Effects of gas velocity and GDL wettability	Single pore
Mixture Model	Wang, Basu et al. (2008) [204]	Effects of air stoichiometry and relative humidity	Homogenous electrode and GDL
	Basu, Li et al. (2009) [205]	Effect of GDL intrusion at the edge channels	Homogenous electrode and GDL
	Basu, Wang et al. (2009) [206]	Maldistribution effects in parallel channels	Steady-state and isothermal

A.1.1.1 Droplet behavior

Understanding the liquid water motion in gas flow channels is essential for effective water management in a PEM fuel cell. Early two-phase flow models always assumed the liquid water moving at the same velocity as the gas flow, called mist flow [207-208]. However, as discussed in Section 2.2, in-situ experimental results showed that water emerging from the GDL surface formed droplets rather than mists (Figure 100), especially at a high current density or a low gas stoichiometric ratio. Therefore, the droplet behavior in the gas flow channel must be well understood to accurately characterize two-phase flow in the gas channels.

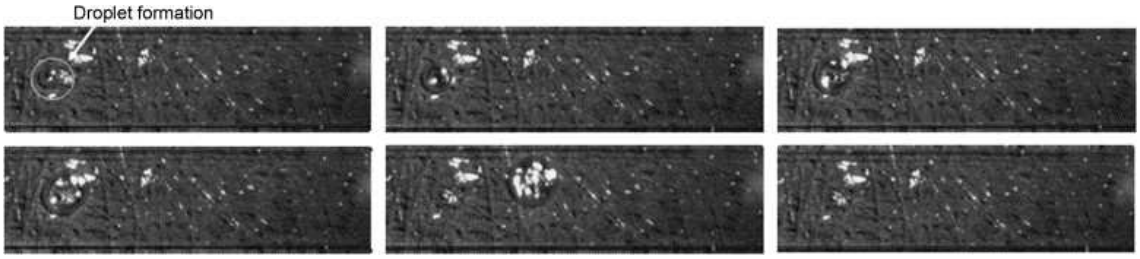

Figure 100. Visualized water droplet formation and detachment from the GDL surface (reprinted from Theodorakakos et al. [18] with permission from Elsevier)

The critical detachment diameter of a droplet is different with respect to changing operating conditions, channel design, or using different materials. Chen et al. [187] developed a two-dimensional simplified cylindrical droplet model to predict the instability of a single water droplet based on macroscopic force balances and a droplet-geometry approximation. Their qualitative results indicated that increasing the flow channel length or mean gas flow velocity, decreasing channel height or contact angle hysteresis, or making the GDL surface more hydrophobic would reduce the critical detachment diameter and enhance the removal of droplets. The same model also predicted the critical gas velocity required for a spherical water droplet to detach from the

GDL surface [188]. It was found that the critical gas velocity varied inversely with water-droplet size (to the 2/3 power), and decreased with increasing GDL surface hydrophobicity, decreasing contact-angle hysteresis, and lowering the channel height. However, the geometry approximation used in this simplified model would result in an inaccurate drag force on the droplet, especially at high gas flow velocity. Parametric studies with the VOF method [192] showed that the height of the channel as well as the width of the pore had a significant impact on the detachment of the water droplet. The critical velocity was found to decrease with increasing droplet size and decreasing GDL pore diameter. Zhu et al. [209] also investigated the effects of channel geometry on the droplet dynamics. Lower aspect ratios reduce the GDL coverage ratio due to droplets attaching to the top wall, but lower aspect ratios also increase the pressure drop. A rectangular channel with a curved bottom wall was found to have a minimum coverage ratio and water saturation, and a moderate pressure drop. However, the liquid flow rates in their simulations were much higher (several orders) than those in a realistic PEM fuel cell, and the droplet motion may be quite different at low liquid flow rates corresponding to real fuel cell operation.

More hydrophobic GDL surfaces aid in droplet detachment because of lower capillary forces, as shown by He et al. [189] using the multi-fluid model. These results are in agreement with Hao et al. [203], who applied a multiphase LBM approach to show that high gas flow velocities and a more hydrophobic GDL surface were beneficial for the water removal. An analytical model based on a force balance was also developed to predict the droplet detachment size. Zhu et al. [194] found that the critical air velocity for detachment decreased with increasing hydrophobicity of the surface and increasing the

initial size of the droplets. Temperature also has an effect on the droplet's detachment [18]. Experimentally measured contact angles and operating conditions were input into a numerical model based on the VOF method where water was injected from a single pipe. The results showed that higher temperatures facilitate the droplet's detachment due to lower surface tension and adhesion forces. Contact angle hysteresis plays a major role in droplet detachment dynamics. Fang et al. [78] investigated the effects of contact angle hysteresis on the droplet detachment height using the VOF method and showed that without considering the contact angle hysteresis, the droplet's detachment height was quite different from what was observed in the experiments. These results are shown in Figure 101. The results also implied that the contact angle distribution along the droplet can be approximated by piecewise linear functions.

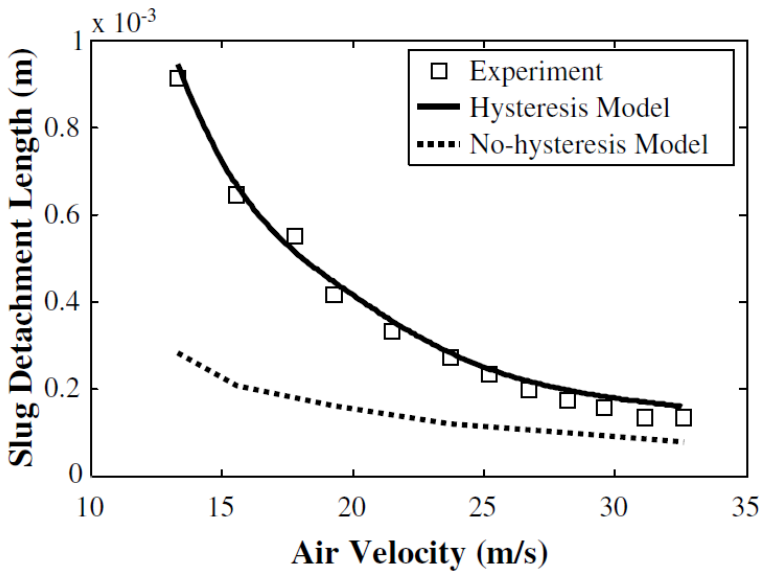

Figure 101. Droplet detachment height versus air velocity; both contact angle hysteresis and non-contact angle hysteresis results are presented for comparison with experimental results, which highlights contact angle hysteresis must be considered (reprinted from Fang et al. [78] with permission from Elsevier)

After detachment, a liquid droplet may have different behavior while moving along the gas flow channel because of different operating conditions or materials (different wettabilities of channel surfaces). A hydrophobic GDL surface and hydrophilic channel

sidewall, which is a common condition in PEM fuel cells, turns dispersed droplets into thin water films attached to the channel sidewalls [191]. Shirani et al. [79] also used the VOF method to investigate the motion of a liquid droplet. By studying the effects of gas velocity, the density and viscosity of water, and the surface tension on the droplet deformation, it was found that the droplet shape strongly depended on the capillary number when the capillary number was large, and it poorly correlated with the Reynolds number.

A.1.1.2 Flow patterns in a PEM fuel cell

In the above section, the focus was mainly on the dynamics of a single droplet. However, in PEM fuel cell gas channels, droplets always emerge from GDL surface at multiple sites. Thus, the two-phase flow pattern can be different from the single droplet behaviors discussed above due to the coalescence of droplets.

Bazylak et al. [193] studied multi-droplet effects by employing two pipes to represent the microstructure of the GDL. With an initially dry GDL and gas channel, slug flow and channel flooding followed the motion of individual droplets. More recently, Ding et al. [210] studied the effect of the GDL surface microstructure by varying the pore diameters and the number of pores with the VOF method. Three stages were identified during the droplet formation: droplets merging on the GDL surface, accumulation on the channel sidewalls, and detachment from the top wall. These results are shown in Figure 102. The results also showed that different GDL surfaces would result in significantly different two-phase flow patterns. However, when the pore size was small enough (and the pore number was large enough), the flow pattern would not change with further reduction in the pore diameter. This result suggested that the GDL surface microstructure could be

simplified by increasing the pore size to reduce the computational time. The material wettability had a strong impact on the two-phase flow pattern and pressure drop, where more hydrophilic sidewalls or more hydrophobic GDL surfaces were beneficial for water removal.

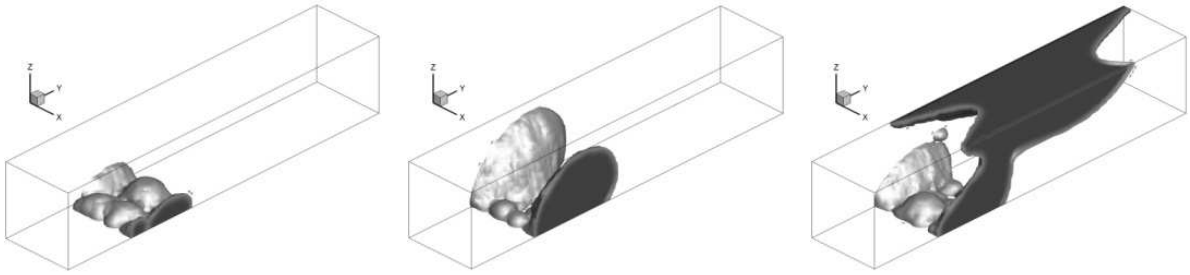

(a) **(b)** **(c)**

Figure 102. Three stages of the emerging water droplet into a single channel: (a) merging, (b) accumulating, (c) detaching (reprinted from Ding et al. [210] with permission from Elsevier)

Jiao et al. [201] used several small cubes or trapezoids with the same volume to represent the pores from which liquid water could emerge from a GDL. The results indicated that the trapezoidal porous holes with the minimum area facing the gas flow channel were beneficial to the liquid removal due to enhanced air flow inside the GDL. Furthermore for these microstructure designs, the hydrophobicity level of the catalyst layer must be greater than or equal to the GDL in order expel liquid water into the gas flow channel [202].

Channel design is another key factor that affects the two-phase flow pattern. In fact, the appropriate design of flow channels has been considered the most successful strategy in addressing water flooding issues [5]. Three commonly used flow fields in PEM fuel cells are parallel/straight channels, serpentine channels, and interdigitated channels.

Zhan et al. [190] showed that straight channels with high air velocities and more hydrophobic surfaces are beneficial to the liquid water removal. However, in this study liquid water was injected with the inlet gas, which is different from droplets emerging from GDL surfaces in real PEM fuel cells. Simulation results using the VOF method indicated that the bend area inside a U-shaped micro-channel played an important role in determining water behavior [185]. Water flooding could occur in the “after-bend” section, and, with larger amounts of water, the water distribution following the U-bend can block the reactant transport inside the flow channel. However, liquid droplets were initially placed in the channel, which is different from an actual PEM fuel cell where the droplets emerge from GDL surfaces. Jiao et al. [198] presented a numerical investigation of two-phase flow in a more complex parallel serpentine channel format with manifolds with water droplets initially placed in the channel. Using the VOF model, the serpentine gas flow channel's “collecting-and-separating-effect” facilitated water drainage, and it was recommended that keeping the area that has the higher amount of water close to the outlet manifold was beneficial for water drainage. Jiao et al. [199] further simulated a 3-D straight micro-parallel-channel format with PEM fuel cell stack inlet and outlet manifolds. It was found that the outflow manifold might be easily blocked by water even if the amount of water was small. A curved channel wall was suggested to prevent water from flowing back to the air inlet, allowing water to move into the flow field channels faster.

Quan et al. [200] numerically investigated the effects of channel surface wettability, channel geometry, and air inlet velocity on water behavior, water content inside the channel, and two-phase pressure drop. The results showed that the pressure drop was

caused by channel blockage and the gas-liquid drag force. A hydrophilic channel surface could benefit the transport of reactants to the reaction sites, but would also introduce a significantly higher pressure drop. A sharp corner channel could be a better design option since it would provide a space for water accumulation and paths for water to climb onto upper surfaces. Increasing the inlet velocity could facilitate water management, but the corresponding pressure drop was also increased linearly.

Non-uniform flow distribution (maldistribution) in multiple channels is another major concern in channel design. Wang et al. [204] developed a mixture model to simulate the simultaneous flow of liquid water and gaseous reactants in straight mini-channels of a PEM fuel cell. The results showed that under fully humidified inlet conditions, liquid water built up quickly at the inlet and was followed by a slow increase downstream. Water was found to stick around the region with a geometrical heterogeneity. They [206] also examined the maldistribution effects in parallel channels of PEM fuel cells, where GDL intrusion into the channels was found to cause severe flow maldistribution. Employing flow splitters in the inlet manifold can mitigate such flow maldistribution. However, their simulation results were steady-state and isothermal, and droplet formation cannot be captured using this two-phase flow model.

A.1.1.3 PEM fuel cell performance

The literature discussed above mainly focused on the hydrodynamic behavior of two-phase flow in the gas channel without considering electrochemical reactions. Although these studies can provide a fundamental view of liquid water evolvement into the flow field channel, the lack of reaction makes it difficult to predict the complicated two-phase phenomena happening in a real PEM fuel cell. The non-uniform reaction in the catalyst

layer results in a non-uniform water generation rate and thus has a great impact on the subsequent two-phase flow in the flow field channels. Meanwhile, non-uniform water distribution in flow field channels also affects the diffusion of reactants, which reduces the PEM fuel cell performance.

A general 3-D model of a PEM fuel cell has been developed by Le et al. [196], which couples the VOF method with electrochemical reaction, heat transfer, and species transport. Liquid droplets were initially located on the side walls of a single serpentine cathode channel and the two-phase flow patterns, effects of channel structure, current density, and temperature distribution were discussed in detail. Furthermore, they applied this model to investigate the flow behavior of liquid water in serpentine-parallel flow channels [197] and in interdigitated flow channels [211]. The results showed that the liquid droplets caused high pressure-drop, decreased the local cell temperature, and blocked the pathway of reactants, but the droplets also increased the ionic conductivity of the catalyst layers and the membrane. However, the GDL, catalyst layer, and membrane were all assumed to be homogenous media, and it is not appropriate to apply the VOF method to a homogenous porous region. To improve the cell performance, the flow channel aspect ratio can be modified to increase the sub-rib convection. This increase resulted in higher reactant velocity, faster liquid water removal, and better cell performance [212]. However, excessive sub-rib convection may also dry out the membrane.

Flow maldistribution is an issue in an operating PEM fuel cell, as shown by Basu et al. [205] via an integrated mixture model with electrochemical reactions. The model was validated against experimental data of the wetted area on the GDL surface and pressure

drop on the cathode side. The effect of GDL intrusion at the edge channels, which can lead to flow maldistribution, was numerically studied and the results are shown in Figure 103.

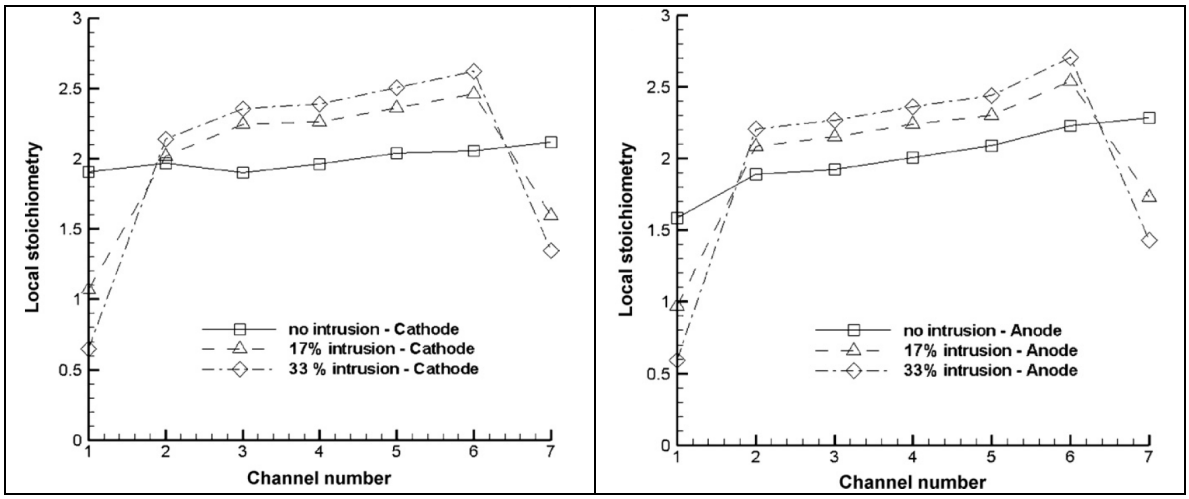

Figure 103. Plots of local stoichiometry for different channels at different GDL intrusion percentages on a) the cathode side and b) the anode side (reprinted from Basu et al. [205] with permission from Elsevier)

At low flow rates, channel intrusion blocks the GDL surface and makes the edge regions starved of reactants. Innovative flow field designs, such as those developed by Wilkinson et al. [213], are required to mitigate this type of flow maldistribution of gas reactants.

Appendix B MEA fabrication and conditioning

This section details both membrane electrode assembly (MEA) fabrication and the needed conditioning steps before the MEA can be used to produce accurate data. Consistent fabrication and conditioning are important to ensure reproducible results.

B.1 MEA fabrication

A Membrane Electrode Assembly (MEA) is formed by combining the membrane, catalyst layers, and gas diffusion layers (GDL). In this case, the membrane is a catalyst-coated membrane (CCM; Gore Primea 5510) and thus the MEA consists of the two GDL layers sandwiching the CCM.

Consistent production of the MEA was guaranteed by designing rule dies to act as cutters for the CCM, GDL, and final MEA. The general procedure is described with a schematic of the steps presented in Figure 104. The schematic is specific to the visualization cell (Section 3.1), but the same method works for other fuel cells (such as the TP50) that would use cutters specific to that fuel cell.

1. Two rectangular steel plates open in the center are covered with a layer of Kapton.
2. Each Kapton film is cut with the GDL cutter
    a. GDL cutter matches the active area of the fuel cell (in this case the area inside the seals)
3. The CCM is cut with the CCM cutter
    a. CCM cutter matches the outer seal dimensions (Active area + seals)
4. The CCM is placed on the Kapton in the open space left by the GDL cutter
    a. A few millimeter clearance (here 2.4 mm) on each side allows sufficient adhesion of the CCM to the Kapton
5. The second layer of Kapton is affixed to the CCM
    a. The CCM is thus sealed inside two pieces of Kapton with the active area of the fuel cell exposed
6. The MEA is cut from this with the MEA cutter
    a. The MEA cutter leaves a MEA the size of the entire fuel cell (defined by the manifold) with holes for the alignment pins and compression screws
7. The GDL cutter is used to cut appropriately sized GDLs
    a. The appropriate size is the active area of the fuel cell

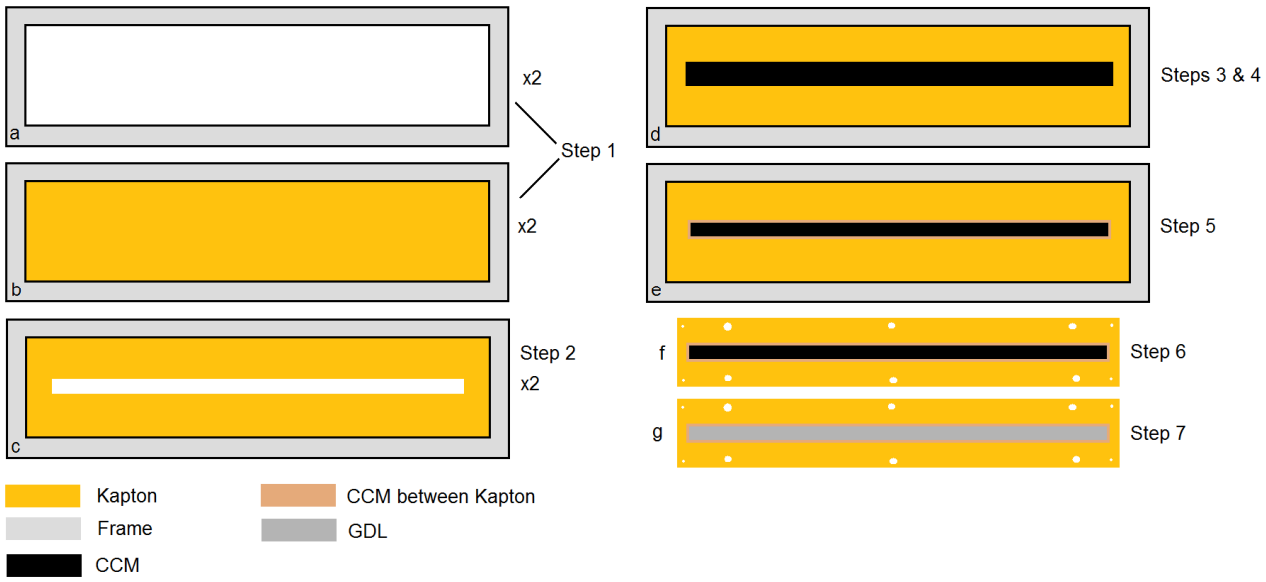

Figure 104. MEA fabrication schematic corresponding to the general procedure described in steps 1 through 7

The GDL layers are not permanently fixed to the CCM piece before entering the fuel cell. Once the cell is operated under the compressed conditions, the GDLs adhere to the CCM and the final MEA piece is created.

The three cutters are 3/4" thick Plexiglas, allowing the operator to see what is being cut. While the CCM and GDL could simply be cut to the size of the cell (defined by the manifold size), the active area is much smaller and thus using CCM and GDL the size of the manifold would waste material unnecessarily.

B.2 MEA conditioning

An unused (new) membrane must be conditioned before testing to ensure proper electrochemical performance. The conditioning test takes place by running the fuel cell at 800 mA cm^{-2} (28.6 A) for 8 hours under the baseline electrochemical operating conditions listed in Table 20, which are specific to the transparent fuel cell. A constant current is chosen so that the voltage does not go below ~0.5 V, which is satisfied by the 800 mA cm^{-2} current density. The conditioning can also be accomplished at 600 mA cm^{-2}

(21.5 A), where the goal is to keep the conditioning voltage between 0.5 and 0.6 V. To satisfy this voltage, a higher current density is used to condition the TP50 fuel cell (up to 1000 mA cm^{-2}).

Table 20 Baseline conditions for all relevant operating variables in MEA conditioning

Operating Variable	Baseline Value
T_{cell}, T_{gas}, $T_{dew\ point}$	75°C
Relative humidity (cathode and anode)	100 %
Cathode GDL	SGL Carbon 25 BC
Anode GDL	SGL Carbon 25 DC
Catalyst Coated Membrane (Pt loading)	Gore Primea Series 5510 (0.4 mg Pt cm^{-2})
Air stoichiometry (λ_{air})	2
H_2 stoichiometry	1.5
Cathode gas	Air
Flow fields	4 parallel, square channels
Compression pressure	90 psig
Gas backpressure	30 psig

Over the 8-hour period, the voltage increases. Generally, a conditioning test is considered complete when the final hour of operating has voltage oscillations are less than +/- 5 mV. For the conditioning results in Figure 105, the final hour voltage is 0.594 V +/- 8 mV. For the electrochemical performance of this novel visualization cell, the 8 mV oscillation is acceptable. The resulting OCV after this conditioning was 0.96 V (measured for 10 minutes).

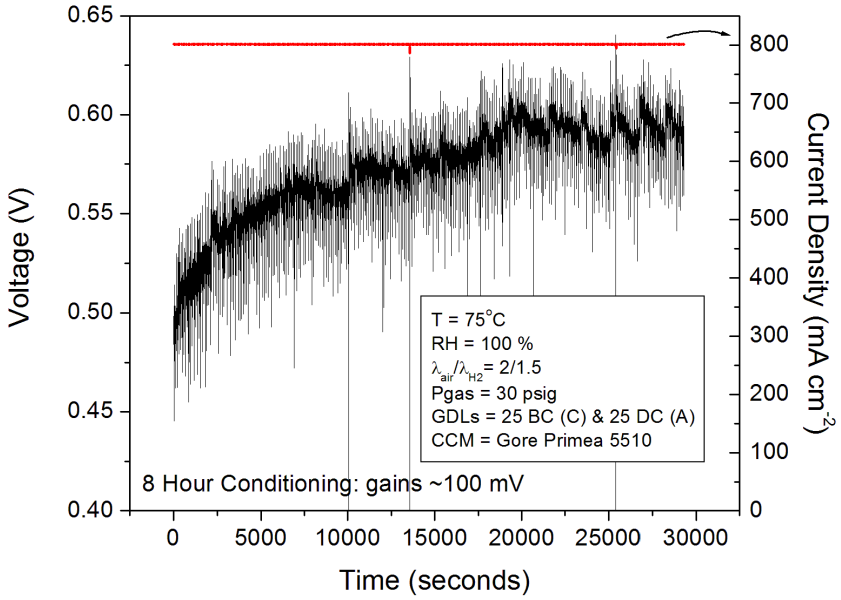

Figure 105. MEA conditioning voltage results over 8 hrs at 800 mA cm^{-2} (all other conditions at the baseline in Table 20)

The MEA must also be reconditioned before starting a new set of electrochemical experiments. It is assumed that the membrane remains conditioned between individual experiments on a given day. To recondition, the same baseline conditions are set as in the conditioning procedure. However, the recondition only needs to run for 0.5- 1 hr to ensure a stable voltage signal.

Appendix C Additional pressure drop hysteresis tests

In addition to the work presented in Chapters 4 and 5, additional studies were examined relevant to pressure drop hysteresis. This includes work from the non-operating cold model, non-operating hot model, and the operating fuel cell. Those results are shown here.

C.1 Work completed in the non-operating cold model

This section discusses supplemental data obtained during the non-operating cold model study. This work focuses on the use of solid (non-porous) GDL inserts.

C.1.1 Non-operating cold model: Solid GDL inserts

Tests were done to see how gas diffusion into the GDL affects the single-phase pressure drop. The open spaces in the GDL offer a path for gas flow in addition to the flow field channels. This increase in area could mean the measured pressure drop is lower than expected based only on the cross section of the channels. To measure this influence, solid inserts of typical GDL thickness were used in place of actual GDLs, which means gas can only flow in the channels. The inserts used were 108, 172, and 226 μm thick (comparable to the thickness of GDLs in Table 3). The experiments used dry gas at room temperature and an air stoichiometry of 2 in the simulated current density range of 50-800 mA cm^{-2}. The cell was compressed with the nitrogen bladder to 100 psig. The solid inserts were made with a polyimide film (Kapton©).

Three scenarios in addition to thickness were analyzed that used the 25 BC GDL (235 μm):

1. The anode chamber open to the atmosphere at both ends
2. The anode chamber closed on both ends with air filling the anode chamber

3. The anode chamber closed on both ends with water filling the anode chamber

These tests were done to see how diffusion into the GDL depends on the anode chamber conditions. These results are shown in Figure 106a.

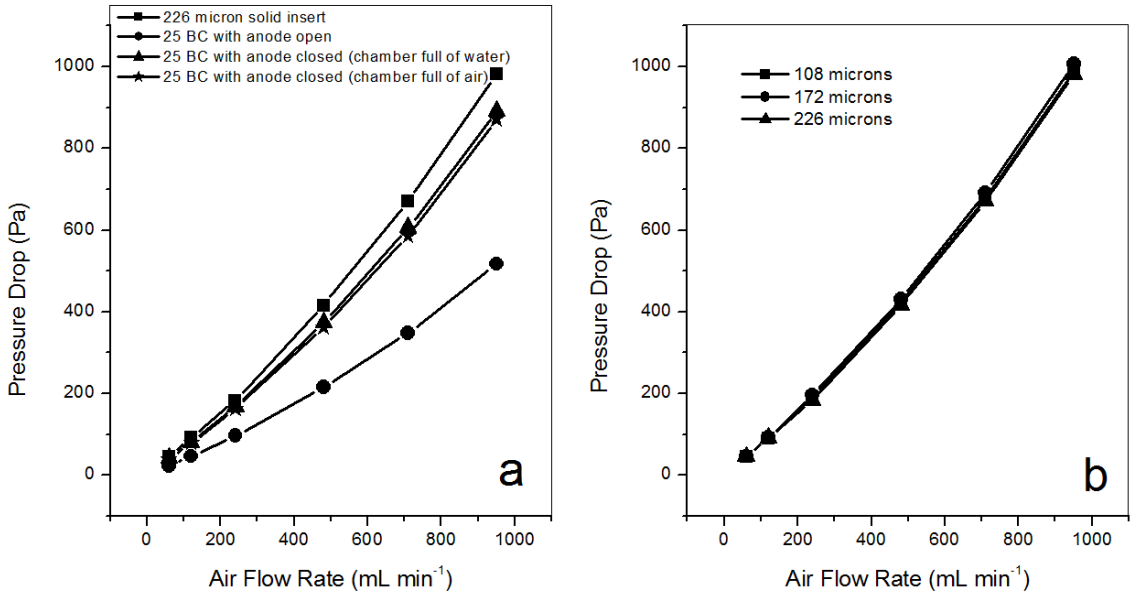

Figure 106. Pressure drop results for a) varying anode configurations from Figure 28 (anode exit open, anode closed and filled with air, anode closed and filled with water) b) effect of solid insert thickness

The results in Figure 106a confirm that the pores in the GDL effectively add to the cross sectional area of the flow channels. The highest pressure drop is found for the solid GDL insert when compared to an actual 25 BC GDL. The lowest pressure drop occurred when both anode ends were open to the atmosphere because air could diffuse through the GDL and exit via the anode manifold. In between these cases are the 25 BC GDL with the anode ends closed but filled with a fluid. It does not matter if the fluid is liquid water or air. Also, the solid insert thickness does not matter, as shown in Figure 106b.

The pressure drop is indicative of the amount of air flowing in the channel. The percentage the pressure drop is lowered due to the GDL pores relates to the rate of air flowing into the pores instead of the flow field channels. These results are shown in Table 21.

Table 21 Percentage difference in pressure drop between solid insert (226 μm) and 25 BC GDL

ΔP 25 BC GDL (235 μm; anode closed with H_2O in chamber)	ΔP solid insert (226 μm)	% Difference
41	45	8
80	92	13
168	183	8
374	416	10
606	672	10
891	982	9

These results show that in general the 25 BC GDL allows an 8-13% reduction of the cathode flow channel pressure drop.

C.2 Work completed in the non-operating hot model

This section explains other experiments performed during the non-operating hot model testing. While the results of temperature, GDL, and stoichiometry were presented at ECS 217 and published by ECST, the scope of the experiments included the effect of backpressure, inclination angle, and the maximum i_{sim}. Each of these studies is addressed in this section. Unless otherwise noted, the baseline conditions from Table 5 are used with fully humidified gas at 75^{o}C with the 25 BC GDL at an air stoichiometry of 2. Each point runs for ~ 8 minutes, and the pressure drop is sampled at 20 Hz. The visualization fuel cell with 4 parallel channels is used in each test.

C.2.1 Non-operating hot model: Backpressure

When run electrochemically, the fuel cell gas pressure is usually set to 206.8 kPa_g for increased electrochemical performance. However, the syringe pump used to inject water from the anode channels to the cathode channels could not overcome the pressure difference caused by the backpressure, and no water could be injected. Thus, the non-operating fuel cell experiments were run without cathode backpressure. This meant that the velocity of the gas changed inversely with the change in backpressure (via the ideal

gas law). To see if there would be a large effect due to backpressure, a pressure of 50 kPag was set as a minimum to hopefully allow water breakthrough. However, several problems were still noted:

- Even at this low backpressure, the syringe pump could not inject any water into the cathode flow field channels due to the large pressure difference between the anode and cathode
- The manifold showed signs of leaking at low flow rates (i_{sim} = 50 mA cm^{-2} and 100 mA cm^{-2} with an air stoichiometry of 2)
    - At 50 mA cm^{-2} with λ_{air}=2, the pressure dropped to 17.3 kPa_g within 5 minutes and settled at the end of the test (~8 minutes) to 16 kPa_g
    - The leak 'confused' the pressure transducer calibration, resulting in negative pressure drops at low air flows

Due to the inaccuracy, this topic was not pursued further.

C.2.2 Non-operating hot model: Inclination angle

The inclination angle was expected to change the droplet detachment dynamics. If the outlet was pointed downward, it was expected that the droplets would more easily be expelled, while if the outlet was pointed upward, the additional gravitational force would hinder droplet detachment. This theory was tested by putting the fuel cell outlet at a ~15^o angle (calculated 13.8^o) downward to facilitate water removal with the goal of lowering the pressure drop hysteresis effect. A schematic of this setup is shown in Figure 107.

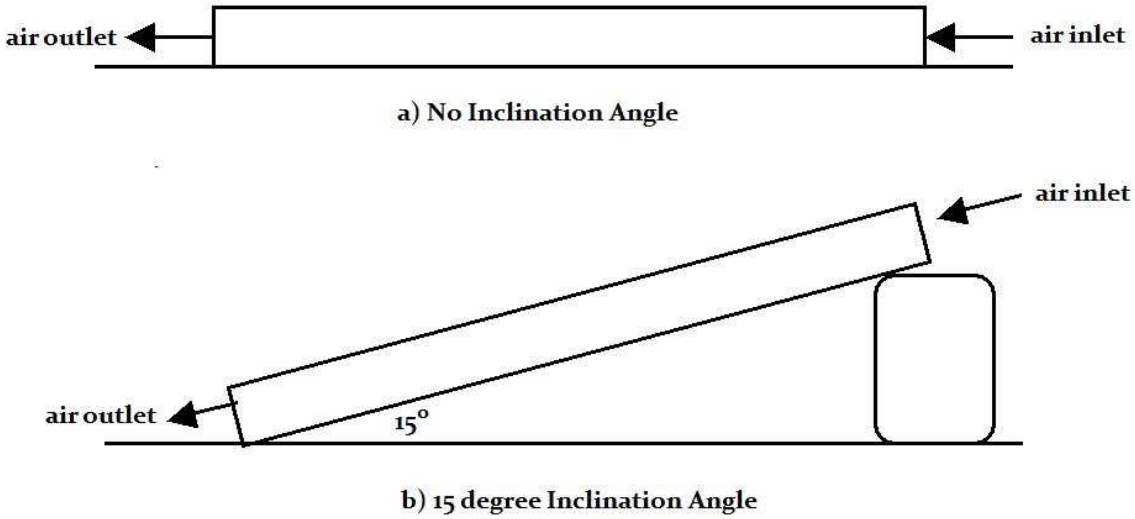

Figure 107. Inclination angle schematics for a) no inclination angle and b) 15^{o} inclination angle with the manifold inlet above the outlet

The results from this experiment are shown in Figure 108, and it is apparent that the hysteresis effect is still noted. The error bars represent the standard deviation of the data set for one trial. Since inclination angle is not a largely studied fuel cell operating variable and these results were not encouraging for hysteresis reduction, further experiments were not performed. It is also unclear how accumulation in the manifold's exit at this angle influences the results. However, by modifying the current apparatus, it would be interesting to see the results of an entirely vertical setup (inclination angle at 90^{o}).

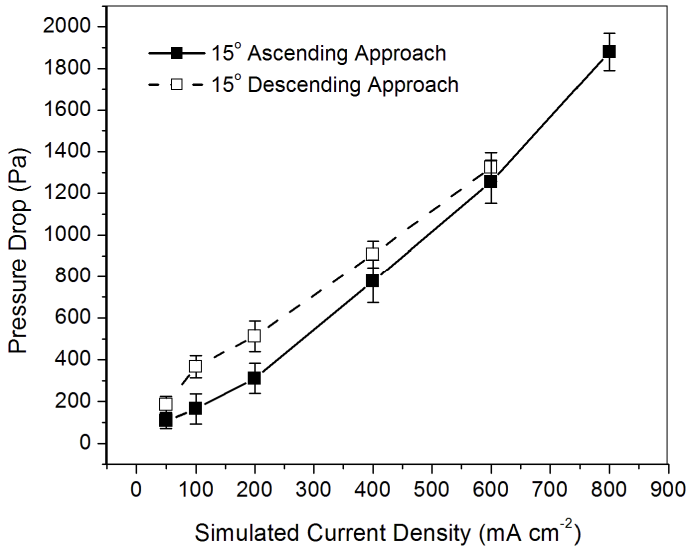

Figure 108. 15° inclination angle pressure results for the ascending and descending approaches

C.2.3 Non-operating hot model: Max i_{sim}

The effect of the maximum value of the i_{sim} on the descending approach was shown to affect the hysteresis in the cold model non-operating experiments. In that study at low maximum i_{sim} (400 mA cm^{-2}), the injected water could not break through the GDL and no hysteresis was observed. At high maximum i_{sim} (1400 mA cm^{-2}), the water could break through the GDL, but the convective water removal capabilities of the higher air flows could remove the same amount of water in the ascending and descending case, which led to no hysteresis in the pressure drop at the higher i_{sim}. In the case of a high maximum i_{sim}, hysteresis was again noted at lower i_{sim} on the descending approach.

These results were also studied in the hot model approach to see if the heated and humidified air altered these results. The maximum i_{sim} was set to 1400 mA cm^{-2}, and the results are shown in Figure 109.

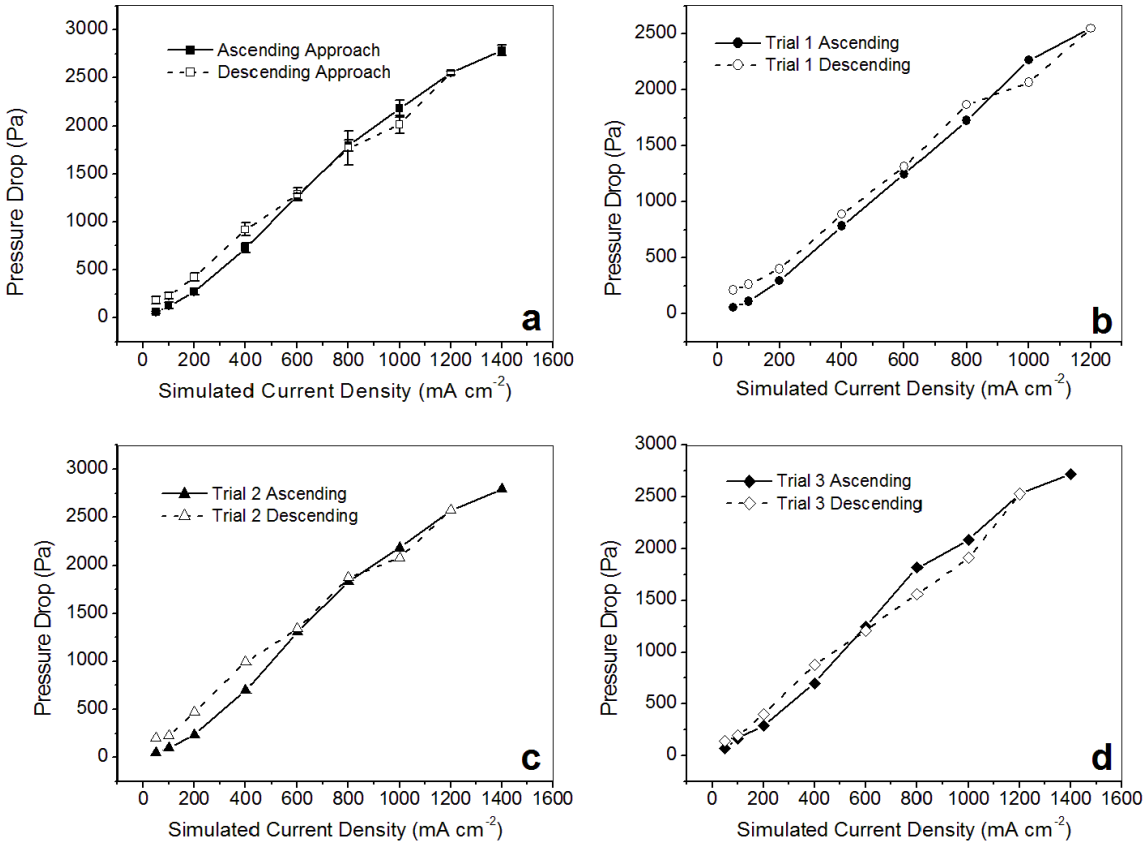

Figure 109. Max i_{sim} results to 1400 mA cm^{-2} including the average results and results of three individual trials: a) Average of three trials b) Trial 1 c) Trial 2 d) Trial 3

The error bars in Figure 109a are from the standard deviation of the three trials shown in Figure 109b-d. The results agree with the analysis from the cold model non-operating testing: no hysteresis is noted at high i_{sim} due to the higher convective water removal abilities of the air but hysteresis is noted at moderate and low i_{sim} due to the accumulation of liquid water in the descending approach.

The varying behavior at higher i_{sim} is likely due to the addition of condensed water in the gas inlet lines. The higher gas flow rates can also convectively bring in liquid water from the gas inlet lines to the fuel cell flow channels. This addition of water can lead to an increased ascending pressure drop, inverting the hysteresis results at higher i_{sim} (Figure 109b and Figure 109d).

As these results agree with the previous cold model non-operating results, further testing was not considered. Also, the visualization fuel cell cannot reach an operating current density of 1400 mA cm^{-2}, so further testing was not warranted.

C.2.4 Non-operating hot model: Ascending/descending i_{sim} cycles

The hysteresis behavior during the descending approach is due to the accumulation of liquid water in the cathode flow field channels relative to the dry channels before breakthrough on the ascending approach. Cycles were performed to see how the second ascending approach would change if the accumulated water was present in the channels and to see what effect this new ascending path would have on the overall hysteresis. The results are shown in Figure 110 with all conditions at the baseline (Table 5).

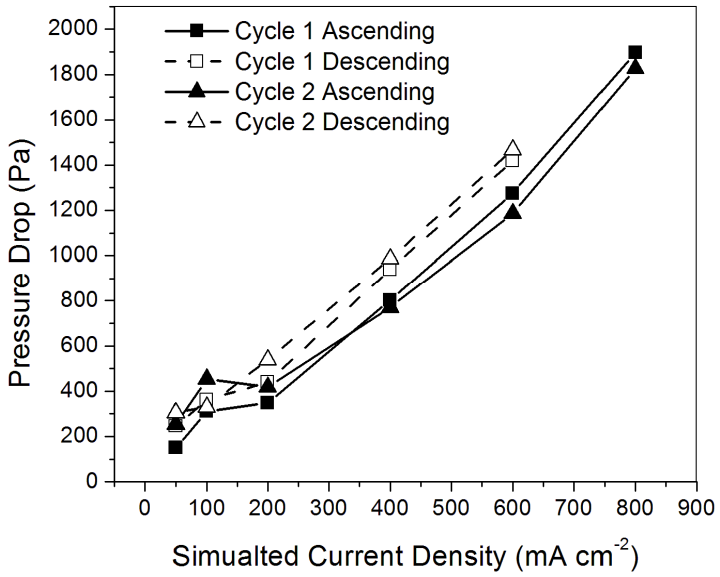

Figure 110. Results of two successive ascending/descending cycles with the 25 BC GDL

The pressure drop for low i_{sim} on cycle 2 ascending is higher than the cycle 1 descending case because of the additional liquid water accumulation. However, by $i_{sim} \geq 400$ mA cm^{-2}, the higher air flow rates convectively remove the water and the pressure drops on the ascending approach for cycle 1 and 2 are similar. The subsequent pressure drop on the

descending approach of cycle 2 is then similar to the descending approach of cycle 1. Thus, cycling is most important at low i_{sim}, which is generally where hysteresis is most prevalent.

C.3 Work completed in the operating fuel cell

In addition to the results in Chapter 5 [148], additional experiments were performed to understand pressure drop hysteresis in an operating PEM fuel cell. These tests included further exploration of the LM approach, mitigation strategies via dynamic RH control, and constant air flow rate vs. constant stoichiometry.

C.3.1 Operating fuel cell: Further exploration of the LM approach

The LM approach results were also used in "Gas-liquid two-phase flow behavior in minichannels bounded with a permeable wall" by L. Zhang et al. [156]. The operating results from Chapter 5 were compared with the results of Lu et al. [56]. Figure 10b from reference [156] is shown in Figure 111, with equation 10 referring to the uniform injection method and equation 11 referring to the non-uniform injection method (discussed in 5.2.6).

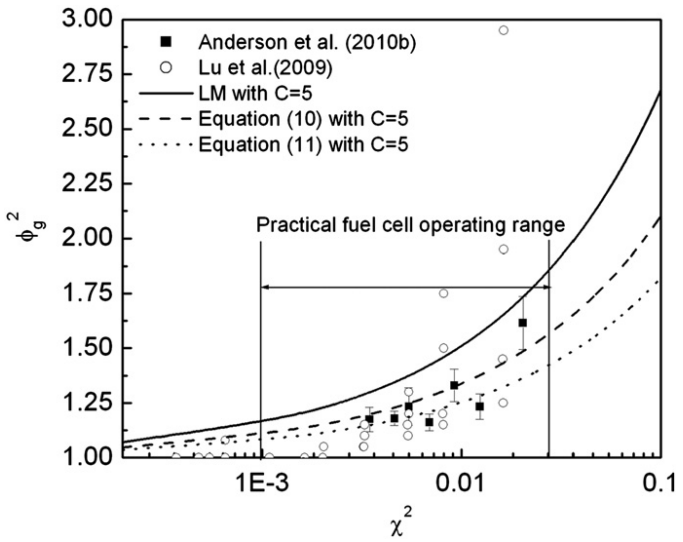

Figure 111. Comparing the LM approach to Lu et al. [56] data and Anderson et al. data (modified from [148]) with three versions of the LM method (modified from Zhang et al. [156] with permission from Elsevier)

This comparison is made here for further validation of the experimental results presented throughout 5.2.6. The values from Lu et al. [56] were from an ex-situ experiment, but they still are reasonably close to the two-phase flow multipliers determined here. The experimental results from Chapter 5 are from an average of the temperature and stoichiometry results (the standard deviation is from the average of all current densities at a given condition since they all have the same χ^2). This reasonable agreement with Lu et al. provides more confidence in the accuracy of the experimental results.

C.3.2 Operating fuel cell: Mitigation via dynamic RH control

Using the dynamic relative humidity control algorithm from Hussaini et al. [102], the times required at 4 distinct cycles (in order: GDL saturation, GDL drying, membrane dehydration, membrane hydration) could be solved for at the baseline experimental operating conditions in this study. The cycles are based on water firstly accumulating in the anode and cathode GDLs due to product water and condensing water from the humidified gases. Dry gases are then used to evaporate this water, but this causes the

membrane to dry, which then results in a loss of voltage. A critical voltage loss (in this case 10 mV) can be used to determine the time it will take for the dry membrane to cause that voltage loss (due to increased resistance) at which point humidified gas is used to re-hydrate the membrane. The total hydration and dehydration times at each current density for the baseline conditions from Table 6 are shown in Table 22. The cycles are repeated throughout the 10 minutes at each current density. If an individual hydration/dehydration cycle was not completed in the 10 minutes, the percentage time remaining of that cycle was continued at the next current density. The ascending and descending approach was used to a maximum of 800 mA cm^{-2}. Beyond this current density, the times at each cycle were too quick to be manually changed reliably.

Table 22 Cycle times for MEA hydration/dehydration based on Hussaini/Wang method [102]

i ($mA\ cm^{-2}$)	Dehydration (s)	Hydration (s)
50	286	202
100	143	101
200	72	50
400	36	25
600	24	17
800	18	13

The pressure drop hysteresis was not mitigated via this method. Thus, further results are not presented here.

C.3.3 Operating fuel cell: Constant flow results

The air has a convective removal ability that carries away the liquid water. In the typical case, a constant stoichiometry is used (cathode stoichiometry of 2), and the coupled gas and liquid flow rates increase and decrease together. To further understand the convective process, a constant air flow test was done at the highest current density (800 mA cm^{-2}) for λ_{air} = 2. The results, shown in Figure 112, show little hysteresis as expected. At all current densities studied, the two-phase pressure drop is higher than the

single-phase pressure drop. This is true even at low current densities where the water production is low, meaning the condensation of liquid water in constant flow experiments is an issue. When compared to the constant stoichiometry case with λ_{air} = 2, the percentage change between approaches is much smaller. This result is because the higher constant air flow case consistently removes the flow channel water convectively, resulting in little accumulation at any current density. Thus, no hysteresis is seen.

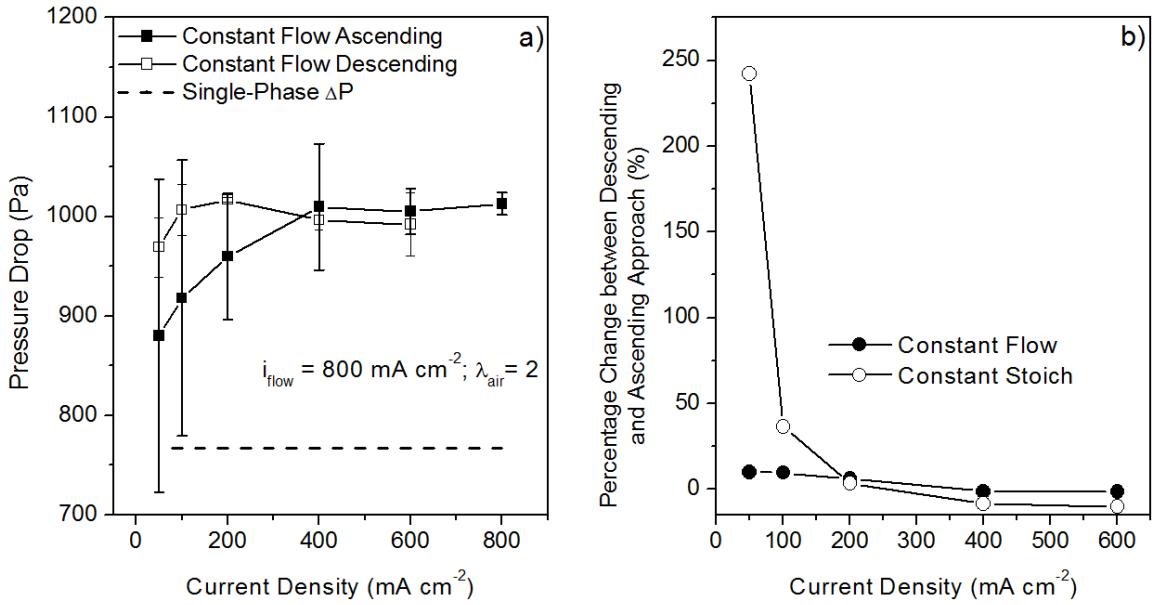

Figure 112. a) Constant flow pressure drop results for the ascending and descending approach b) Percentage change between approaches for constant air flow and constant air stoichiometry methods